University of East Anglia

Development and Fabrication of New Electrode Materials for Hybrid Battery / Supercapacitor Devices

A thesis submitted to the University of East Anglia for the degree of Doctor of Philosophy

April 2022

Sarah Ali Alshehri

Energy Materials Laboratory

School of Chemistry

Norwich

Contents .....

List of figures…….

List of tables……..

List of Abbreviations

AC	Alternating current
AC	Activated carbon
AQ	Anthraquinone
A	Area of Electrode
Bu	Butyl
$^{n}Bu_4N$	Tetra-n-butylammonium
C_{dI}	Double layer capacitance
C_s	Specific capacitance
CF	Carbon fibre
CNTs	Carbon Nanotubes
CE	Counter Electrode
CV	Cyclic Voltammetry
C	Capacitance
DC	Direct current
DCM	Dichloromethane
EDLC	Electric Double layer supercapacitor
EIS	Electrochemical Impedance Spectroscopy
E	Electrode potential
ΔE	The peak potential separation
EQCM	Electrochemical Quartz Crystal Microbalance
FTO	Fluorine-doped tin oxide
F	Faradays Constant (96485.3 $C.mol^{-1}$)
Δf	Frequency change (Hz)

GCE	Glassy carbon electrode
HESS	Hybrid energy storage system
I	Current (A)
i_p	Peak Current (A)
LED	Light Emitting Diodes
LAMPs	Lewis Acid Modified Polymers
Δm	Mass change of the quartz crystal (g)
MeCN	Acetonitrile
m	Mass
PPy	Polypyrrole
POM	Polyoxometalate
P	Power density
R_s	Equivalent Series Resistance
R_{ct}	Charge Transfer Resistance
RE	Reference Electrode
SEM	Scanning Electron Microscopy
t	Time (s)
TEM	Transmission Electron Microscopy
υ	Scan rate (V/s)
ΔV	Potential change
V	Cell voltage
WE	Working Electrode
W	Warburg impedance
XPS	X-ray Photoelectron Spectroscopy

Acknowledgements

I would like to thank my supervisors Dr. John Fielden, Prof. Gregory Wildgoose, and Joseph Wright for their support throughout my PhD.

Many thanks to UEA for providing excellent facilities including an excellent lab environment for PhD students.

Many thanks to the Saudi government and PNU for their generous support during my PhD in the UK.

A big thank you to both John Fielden and the Wildgoose groups for their help and support during my PhD, especially Robin, James, Ahmad, Sarah, Charley, Bethany, and Kevin.

Many thanks to my friends Hind Abdulrahman Al Saud, Anita Morling, Veronica and Duygu for keeping in touch with me and encouraging me throughout all these years, especially in difficult times during Covid-19.

Finally, a huge thank you to my family, especially Mum, Dad and my brother for their support.

Definitions

Cycle life The number of cycles under specified conditions that are available from a secondary battery before it fails to meet specified criteria as to performance.

Capacity The total number of amper-hours that can be withdrawn from a fully charged cell or battery under specified conditions of discharge.

Capacity retention The fraction of the full capacity available from a battery under specified conditions of discharge after it has been stored for a period of time.

Internal impedance The opposition or resistance of a cell or battery to an alternating current of a particular frequency.

Internal Resistance The opposition or resistance to the flow of an electric current within a cell or battery, the sum of the ionic and electronic resistances of the cell components.

Reference electrode Electrode that has a reproducible potential against which other electrode potentials may be measured.

Energy density The ratio of the energy available from a battery to its volume (Wh/L).

Power density The ratio of the power available from a battery to its volume (W/L).

Over discharge Is discharge past the point where the full capacity of the battery has been obtained.

Overvoltage The potential difference between the equilibrium potential of an electrode and that of the electrode under an imposed polarization current.

Specific capacitance The capacitance divided by mass or area of active material.

Hybrid battery/ supercapacitor Type of energy storage system that can store and release electricity. It combines features of both batteries and capacitors.

Chapter 1

Thesis outline

This thesis describes the electrochemical properties of active materials, such as N-pyrrolyle boranes and polyoxometalate-polypyrrole hybrids, and their application as electrodes for use in hybrid battery/supercapacitor devices. The thesis is divided into 7 chapters. The first chapter introduces the background to the research in this thesis. The second chapter describes all electrochemical techniques used throughout this research and all the experimental methods.

Chapter 3 describes development of hybrid battery/supercapacitors based on anthraquinone/lithium for use in hybrid-diffusional battery devices. The investigation was carried out by electrochemical methods including cyclic voltammetry, Electrochemical impedance spectroscopy (EIS), galvanostatic (charge-discharge technique) and electrochemical quartz crystal microbalance (EQCM).

Chapter 4 presents a study of the electropolymerisation of the N–pyrrolyl–bis(pentafluorophenyl) borane monomer and compares the resulting material (poly**1**) with the known conducting polymer poly(pyrrole) by using different electrochemical methods. It also compares polymers formed from other Lewis acidic N-pyrrole-boranes with *N*–pyrrolyl–bis(pentafluorophenyl) borane in terms of capacitance and stability.

Chapter 5 focuses on fabrication of a new supercapacitor/ hybrid battery which is made for the first time from anthraquinone as a negative electrode and poly**1** as positive electrode. In addition, it describes the electrochemical behaviors of supercapacitor/hybrid battery of AQ-poly**1** using different electrochemical techniques including cyclic voltammetry,

electrochemical impedance spectroscopy (EIS), electrochemical quartz crystal microbalance (EQCM), and charge-discharge techniques. Also, measurement of specific capacitance and stability were done in this chapter by different methods, including cyclic voltammetry and galvanostatic (charge-discharge) methods. Finally, after studying the electrochemical behaviors of the new hybrid battery/ supercapacitor, we applied devices of the new hybrid battery/supercapacitor successfully.

Chapter 6 describes the investigation of hybrid polyoxometalate-polypyrrole films in which the polyoxometalates are covalently linked to the pyrrole monomers. These were electrosynthesised on the surface of both glassy carbon electrodes and FTO glass. X-ray photoelectron spectroscopy (XPS) and energy- dispersive x-ray (EDX)elemental analyses were done which indicate that polyoxometalate loading is higher than in conventional noncovalent inclusion films. Also, the covalent attachment can prevent loss of polyoxometalates on initial reduction cycles. In this work, we applied different electrochemical methods including cyclic voltammetry, electrochemical impedance spectroscopy and galvanostatic charge-discharge measurements.

Chapter 7 is the conclusion of the work and future research suggestions. Also, appendices including list of publications, presentations, and posters that presented at conferences. Finally, awards gained during the PhD are presented.

Introduction

Overview

Since the revolution of using lithium-ion batteries in devices, researchers are still concerned by toxicity, metal leaching and safety. Lithium ion batteries (LiIBs) contain heavy metals such as Mn, Ni, Cu and Co which affect the environment.[1] One of the problems for lithium-ion batteries is that overcharging can lead to thermal runaway and then, explosion or fire.[2] Therefore, this research aims to avoid this problem by using redox molecular materials instead of metals by developing new electrode materials for use in supercapacitor/hybrid batteries. The goal of developing this kind of supercapacitor is to be safer, faster, rechargeable, more environmentally friendly and cheaper than metal based systems. Also, using potentially flexible electrodes opens use in wearable and flexible future devices. In this research, the goal is to try to discover stable materials with high capacitance that can be used in supercapacitors/hybrid batteries. Therefore, the characterization of materials is carried out by electrochemical techniques such as cyclic voltammetry, electrochemical impedance spectroscopy (EIS) and electrochemical quartz crystal microbalance (EQCM). After that, the data is analysed to find out the stability of the material for long cycle life, the capacitance and specific capacitance. Finally, after the successful test of the supercapacitor, it is applied in devices. The following pages will introduce polypyrrole, N-pyrrolyl borane, anthraquinone and polyoxometalates which can be used as electrode materials for hybrid battery supercapacitor devices. In addition, they will introduce carbon electrode materials that can be used in supercapacitor applications and the method to modify carbon electrode materials.

1.1. Energy storage system

With population growth, increasing energy requirements, and the temporal and geographic variability and diffuse nature of renewable energy supplies,[3] new energy storage materials have become urgently required to enable replacement of fossil fuels. The use of petrol and other fossil fuels, such as diesel, gas, and coal as sources of energy, has become essential to modern life. The burning of fossil fuels leads to increased levels of carbon dioxide in the atmosphere which threaten the environment through climate change. Since December 2015, the level of carbon dioxide has exceeded 400 ppm, an increase of nearly 50% on pre-industrial levels.[4] Transportation in particular is responsible for a huge amount of CO_2 emissions.[5]

Consequently, the worldwide aim is to switch to using clean, renewable energy sources, within the next 30 years.[4] There are three sources of renewable energy that can be used to generate abundant heat energy. These are biomass, geothermal and solar. Of these, solar energy is the best because geothermal sources depend on location and cultivating biomass takes up space needed to grow food and for nature.[6]

Because solar and many other renewable energy sources (wind, tidal, wave) depend on environmental factors that vary (e.g. location and weather) they are unreliable for applications requiring a constant, or predictable supply/demand cycle. This means it is necessary to develop effective energy storage systems, such as batteries and supercapacitors. The Ragone plot in Figure 1.1. shows the specific power and the specific energy for energy storage devices. This shows that batteries have more power density than capacitors whereas capacitors have more energy density than batteries. Supercapacitors are in the middle between capacitors and batteries. Consequently, supercapacitors can combine features in between these two devices in

term of high power and energy densities. Fuel cells have the highest power densities compared to other typical energy storage devices.

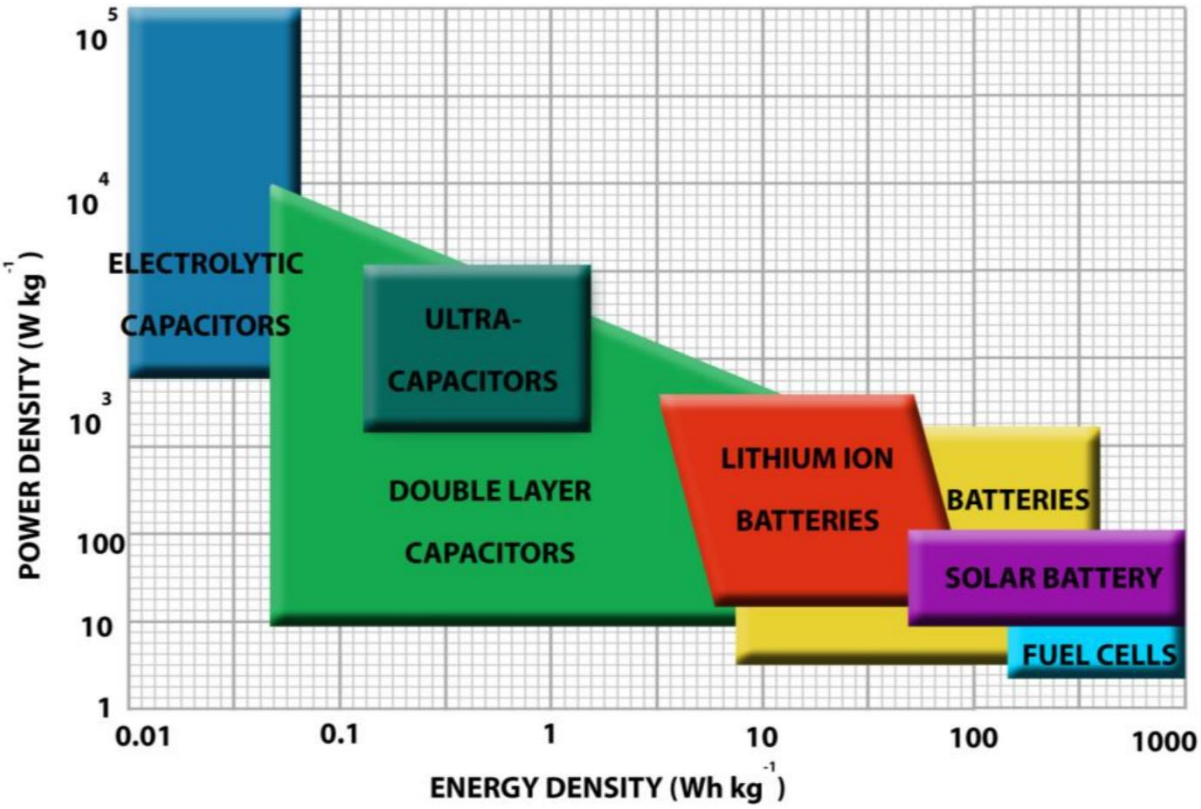

Figure 1.1 Ragone plot for typical common energy storage devices. Reproduced with permission from reference 6.

1.2. Batteries

Batteries are electrochemical devices that can convert chemical energy to electrical energy. This conversion occurs through redox reactions – an oxidation at the anode, and reduction at the cathode – that lead to electrons passing through the external circuit. The electrolyte enables charge to be transferred in the cell between the two electrodes by migration of anions and cations, balancing the movement of electrons.[7] The maximum electrical energy that can be stored and supplied to the anode /cathode electrodes is described by the change in Gibbs energy ΔG (equation 1).[7]

$$\Delta G = -nFE^{\circ} \quad (1)$$

Where F is Faraday constant (96487 C/mol) and n the number of electrons transferred between electrodes, E° is standard electrochemical potential (V).

1.2.1. Battery chemistry types

Batteries can be divided into two types – non-rechargeable **primary batteries** and **secondary (rechargeable) batteries.** Primary batteries are a great source of power for many electric and portable devices. Magnesium (Mg/MnO_2), alkaline ($Zn/alkaline/MnO_2$) and lithium/solid cathode are examples of primary batteries.

Nickel-cadmium batteries (NiCd) can be used in industrial applications due to the fast charge capability although NiCd batteries have some issues including toxicity which affects the environment. Nickel-metal hydride batteries (Ni-MH) that appeared around 1989 have less problems with toxicity than Ni-Cd because (Ni-MH) contains hydrogen which is absorbed in the alloy instead of using cadmium.[8]

Lithium ion batteries were launched commercially in 1991 by Sony.[9] Lithium ion batteries (LIB) consist of carbon (graphite) as a negative electrode and lithium cobalt oxide ($LiCoO_2$ - generally lithium compounds) as a positive electrode.[10] The Lithium/carbon alloys can form by the reaction between lithium and carbon directly.[9] The main advantage in lithium batteries is the voltage range which extends to 3.01 V and the low density of lithium, only 0.54 g/cm^3. The suitable electrolytes for lithium ion batteries are lithium salts, such as bis(trifluoromethane) sulfonimide lithium (LiTFSI) salt which can provide a wide potential window.[11]

Sodium-ion (Na-ion) battery chemistry has gained more attention in the past eight years. Sodium has advantageous characteristics as it is light – the next alkali metal after lithium, and

also inexpensive (because 75% of the earth is covered by salt water which is the main source of sodium). Therefore, a large number of research articles have investigated Na-ion batteries from around 2010 onwards, although Na-ion batteries have some issues including the decomposition of electrolyte at high potential values, leading to degradation of the capacity during the charge-discharge process.[12]

Table 1.1 The main features of rechargeable batteries with their applications.[7]

Rechargeable Batteries	Advantages	Disadvantages	Applications
1.Lead-acid	Inexpensive Popular Low temperature	Low specific energy Toxic	Vehicles And marine
2.Nickel-cadmium batteries	Excellent cycle life of storage	Toxic	Portable tools and equipment
3.Nickel-metal hydride	Higher capacity more than Ni-Cd High energy and power density	Heavy	Hybrid electric vehicles
4.Lithium-ion batteries	High specific energy Long lifetime High power	Expensive Slow recharge times Safety concerns	Portable and consumer electronic and electric equipment

1.3. Supercapacitors

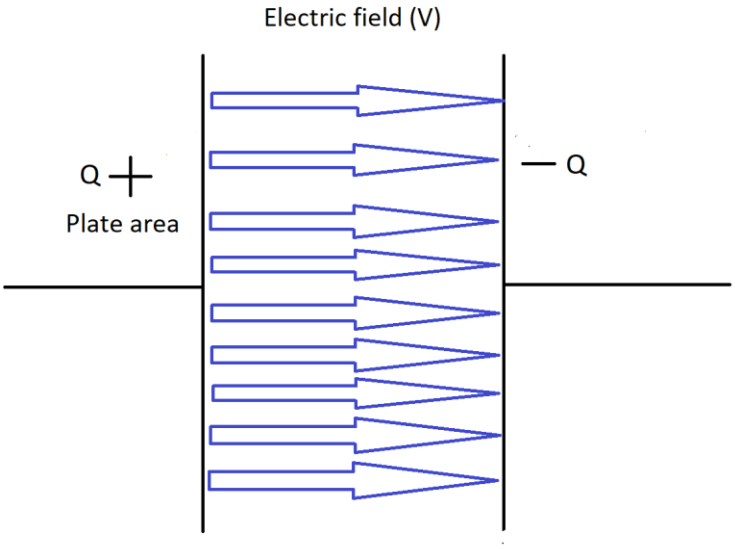

Figure 2.1 Schematic digram of a capacitor.

A capacitor is a device that can store and release electrical charge with a long cycle life.[13] Helmholtz layers which are produced when charge is separated during polarization at the electrode / electrolyte interface can be described by the following equation:

$$C = \varepsilon_{\circ}\varepsilon_{r} A/d \qquad (2)$$

Where $\varepsilon_{\circ}$ is the dielectric constant of the vacuum, ε_{r} is electrolyte dielectric constant, d is thickness of the double layer charge separation distance and A is the electrode surface area.[13]

Supercapacitors contain two electrodes with a non-electrically conductive separator which prevents the two electrodes from making electrical contact (Figure 2.1).[14] Supercapacitors are advanced energy storage devices that provide high capacitance and power density with long cycle life and they can adapt to cope with a variety of operating environments, such as tolerating high humidity and temperatures.[14] According to Figure 2.1 the capacitance is the electric charge that can be stored on the capacitor with the difference in potential between two

parallel plates. The unit of capacitance is the Farad which can be described as charge, coulombs, divided by the difference in voltage between the plates.

$$C = Q/V \qquad (3)$$

Where C is the capacitance, Q is the amount of charge and V the difference in voltage between the plates. The energy stored in a capacitor can calculated by following equation:

$$E = CV^2/2 \qquad (4)$$

Where E is energy stored in capacitor, C is the capacitance and V is the difference in voltage between electrodes.

Figure 2.1 shows a diagram of a capacitor and the electric field between two plates. Q+ and Q- are equivalent charges on the plates. Supercapacitors store more charge than capacitors because they have different structures to capacitors, for example having higher surface area. Also, supercapacitors have higher energy density compared to capacitors and low internal resistance compared to batteries. Therefore, supercapacitors provide higher power densities compared to rechargeable batteries. Supercapacitors are more expensive compared to capacitors.

The first carbon supercapacitor was patented by Becker in 1957, and the first supercapacitor used in a device in 1970. Widespread utilization of supercapacitors was somewhat limited until around 1985. After this time, supercapacitors have become a significant interest in research, especially for hybrid electric vehicles.[15] Another supercapacitor that was developed by Conway is the faradaic supercapacitor or "pseudocapacitor" in the late 1970s.[15-16] Recent research has focused on raising energy density for capacitors and thus, currently, a lot of electronic devices are relying on supercapacitors which provide higher power densities than batteries. The majority of research is interested in supercapacitors because the characteristics of supercapacitors are better in lifetime and power than lithium ion batteries as well as

conventional capacitors. Supercapacitors can store more energy than capacitors, in the same way, supercapacitors can charge and discharge faster than batteries because the electrodes of supercapacitors have a large surface area compared to capacitors and this can hold more charge than capacitors. The lifetime of supercapacitors ranges from 500,000 to 1,000,000 cycles which is in between capacitors (unlimited cycle number) and lithium ion batteries which are limited to around 10000 cycles.[14, 17] Consequently, high power density and long lifetime give supercapacitors the ability to cover the disparity between lithium ion batteries and conventional capacitors.[14] Therefore, supercapacitors with long life time and high power density are very interesting and versatile for applications recently, such as automotive and portable devices.[14] Figure 3.1 represents classifications of supercapacitor which can be divided into three types: electric double layer capacitors, hybrid supercapacitors and pseudocapacitors. According to Figure 3.1, the electrodes in supercapacitors can be pseudocapacitors such as metal oxides and conducting polymers or electric double layer capacitors including carbon nanotubes, graphene, and activated carbon. The electrode of supercapacitors can be also hybrid which is combined between pseudocapacitor and EDLCs.

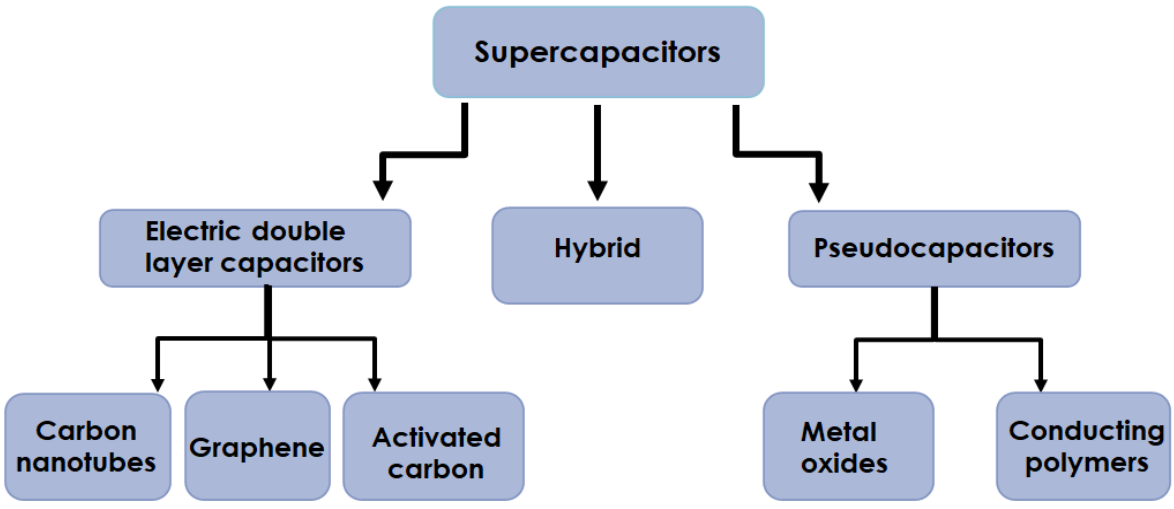

Figure 3.1 Classification of supercapacitors.

1.3.1. Types of Supercapacitors

1.3.1.1. Carbon-carbon (EDLCs) supercapacitor

The theoretical basis for electric double layer capacitors (EDLCs) was first developed by Helmholtz in 1853 and then Backer patented porous carbon material as an electrode to form EDLCs. In 1971, the first commercial supercapacitor was produced by the Nippon electric company.[18]

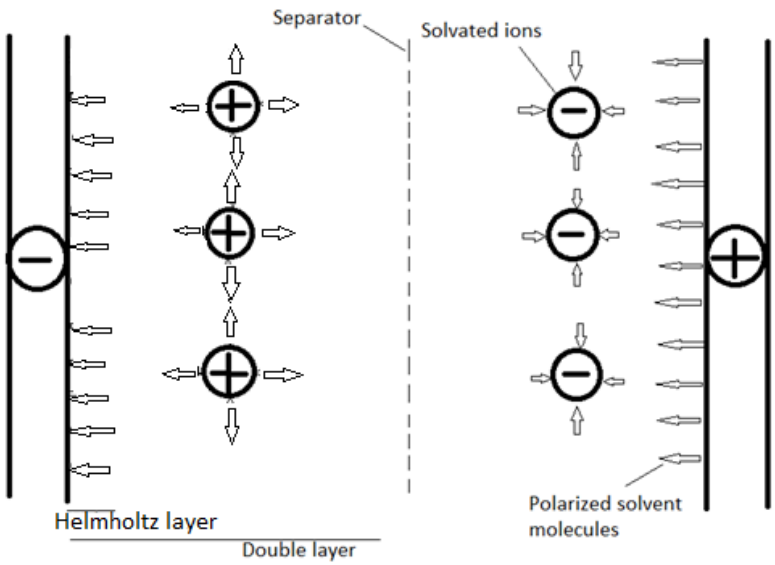

Figure 4.1 Electric double layer capacitor.

Due to the difference in energy storage mechanism, supercapacitors are divided into two types: the first one is electric double-layer capacitors (EDLCs). EDLCs can store energy by capturing the charges at the interface of electrode /electrolyte and releasing them. EDLCs have a long cycle life, more than 100,000 cycles, they can be used in nonaqueous and aqueous electrolyte

but the potential window in nonaqueous media (3V) is wider than aqueous media (1.2V). The storage of charge in EDLCs is by the electrostatic system (double Helmholtz layers) (Figure 4.1).

Therefore, a supercapacitor contains two electrodes which consist of two equivalent capacitors in series and the capacitance can be explained by the following equation

$$1/C = 1/C^{+} + 1/C^{-} \qquad (5)$$

Where C^{+} and C^{-} are the capacitance in Farads of the two electrodes.[19]

1.3.1.2. Pseudocapacitors

The second type of supercapacitor is faradaic supercapacitors which are often called "pseudocapacitors" (figure 5.1). Pseudocapacitors exhibit low power because the movement of ions in the faradaic process is slow.

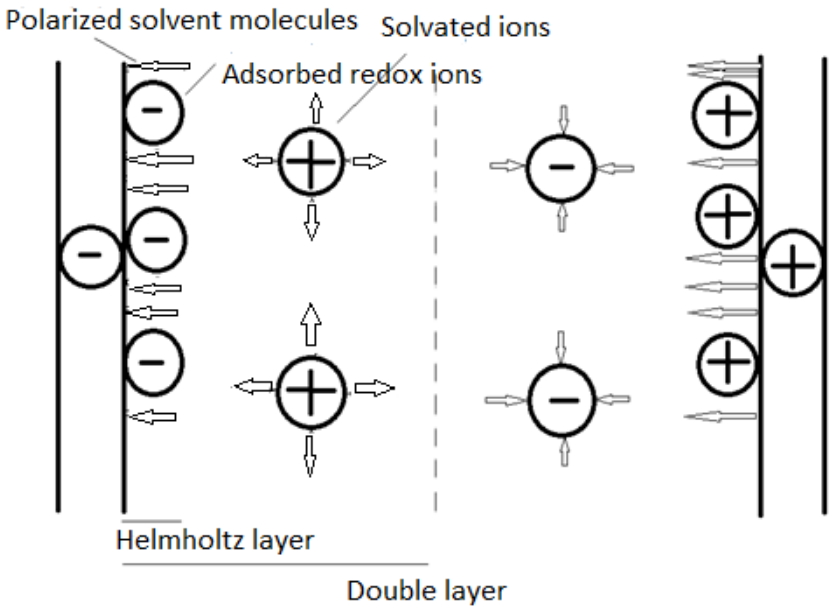

Figure 5.1 Scheme of Pseudocapacitor.

Faradaic pseudocapacitors depend on reversible faradaic redox processes. Faradaic capacitors can provide more capacitance than EDLCs.[20] The faradaic reaction extends the potential window during electrochemical reaction and this enables the material to gain more specific capacitance.[21] There are three kind of electrochemical process used to develop supercapacitors by using faradaic capacitance, the first process is redox reactions occurring in ions from the electrolyte and the second process is adsorption of ions from the electrolyte. Both are surface mechanisms and therefore they depended on the surface area of the electrode. The last process is the doping and undoping of an active conducting polymer material at the electrode.[7] Figure 6.1 shows three different types of faradaic capacitor resulting in three different physical proccesses occuring on the surface. The first type (a), known as underpotential deposition involves adsorption of metal ions as a monolayer. The second type (b) is when ions are reduced electrochemically onto or near the surface with redox faradaic proccesses. The third mechanism (c) occurs when faradaic reaction leads to ions intercalating into the layers of an electrode material without changing its crystallographic phase.[22]

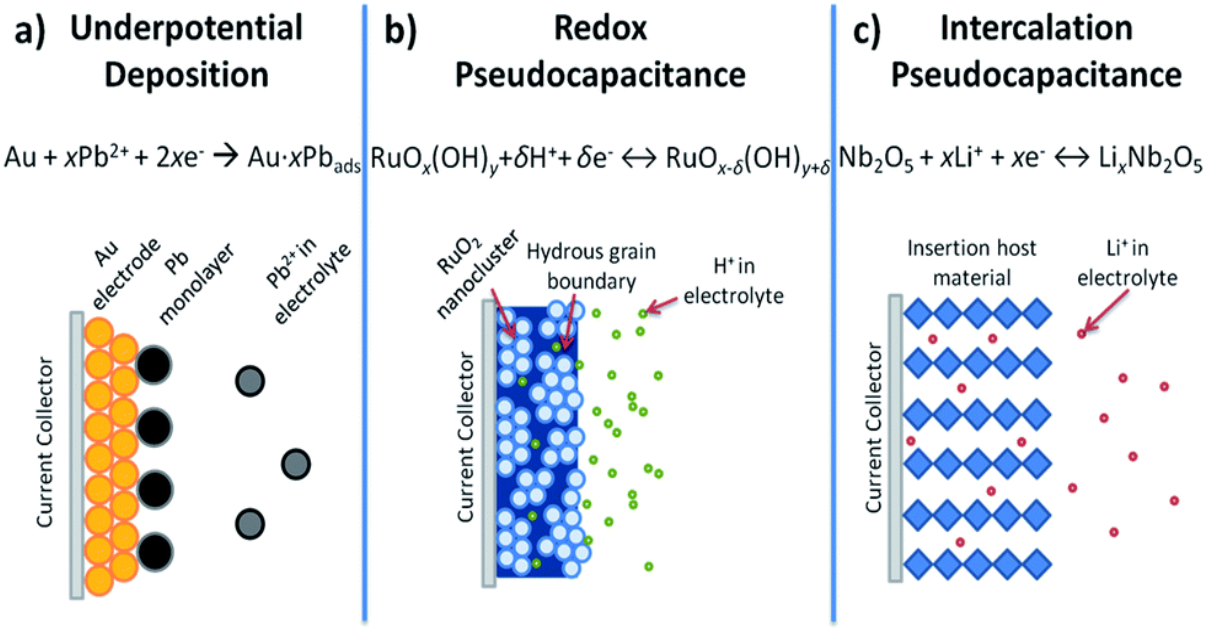

Figure 6.1 Three different types of faradaic capacitor. Figure reproduced with permission from reference 21.

1.4. Batteries and Supercapacitor electrolytes

Electrolytes are an essential component and an important part in supercapacitors which can impact their performance. The electrolyte plays a role in the capacity, cycling, power density and balancing and transferring charge between the electrodes in the cell.[23]

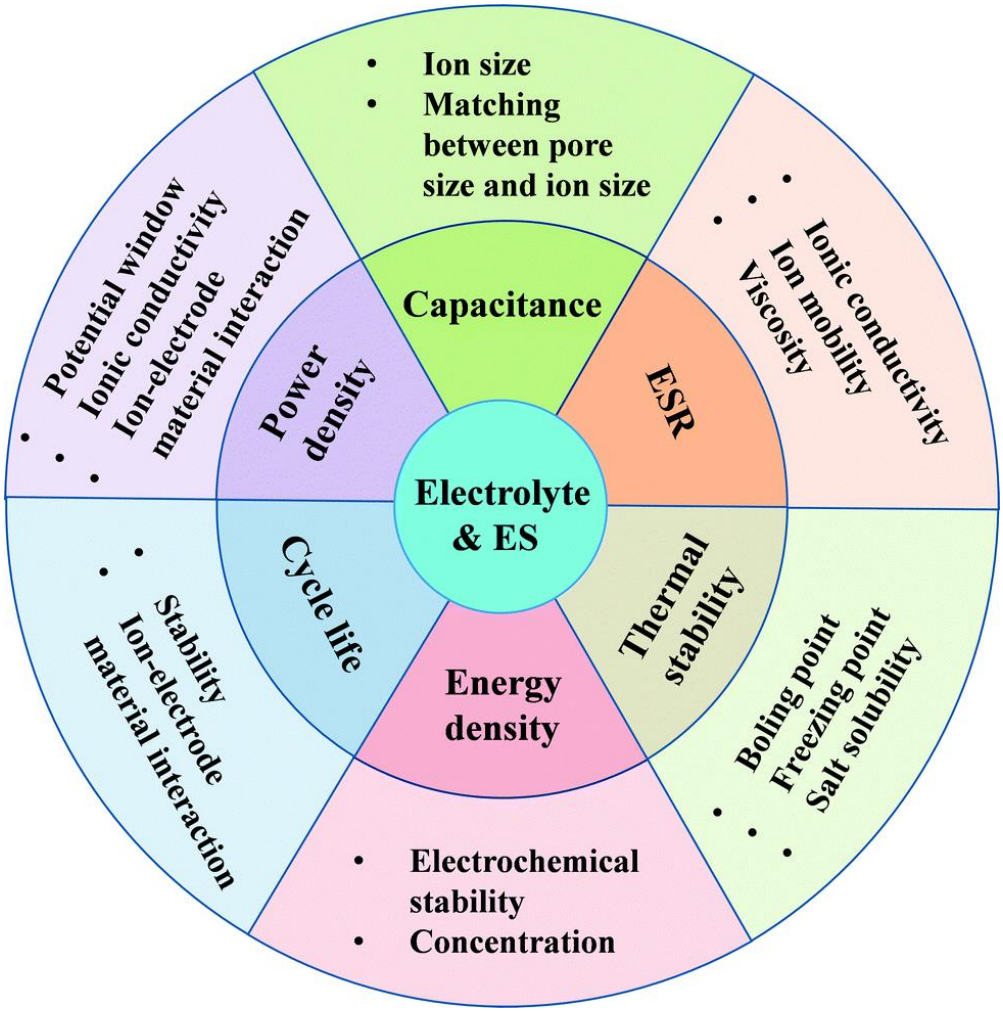

Figure 7.1 Effect of electrolyte on electrical supercapacitor (ES) performance. Figure reproduced with permission from reference 22.

To choose a suitable electrolyte, it should be high in ionic conductivity and have a good potential window stability, be non-reactive with other materials (stable electrochemically), have a high ionic concentration, low resistance and viscosity and be inexpensive. There are three types of electrolytes that can be used in supercapacitors. The first are electrolytes

normally used in aqueous solutions, such as H_2SO_4 or KOH, which can also be used in acetonitrile or propylene carbonate. Their conductivity is approximately 1 S/cm but the main drawback of this type of electrolyte is the potential window cannot exceed 1.23 V (because of the decomposition of water to H_2/O_2 occurs at around 1.2V). The potential window limits the energy stored in the device which means increasing the potential window leads to increases in the energy density of supercapacitors according to the following equation.[19]

$$E = ½ CV^2 \quad (6)$$

The second kind of electrolyte solution is non-aqueous (aprotic, organic), which can have a potential window of up to 3 V. Most devices currently used this kind of electrolyte because the potential window is higher than aqueous electrolytes and they are able to operate in a wide temperature window: -30 to +50 $^{\circ}$C for acetonitrile. The disadvantage of this kind of electrolyte is that they are flammable and present a potential explosion risk due to the high vapour pressure of organic solvents. Acetonitrile is used as a solvent in many commercial supercapacitors. The most positive point of the combination of salt electrolyte with solvent is high conductivity due to low viscosity but the disadvantages are that it is flammable, toxic and volatile which limits the usage in high performance supercapacitors.[8] The last type is ionic liquids (ILs), which are attractive due to their non-volatile, heat-resistant and less flammable nature. The potential windows of ionic liquids are from 3.5 to 4 V. Ionic liquids can be developed with different physicochemical properties and because of this, ionic liquids have been described as designer solvents. The main disadvantage of ionic liquids (IL) electrolytes is their conductivity is low (less than 10 mS cm^{-1}) and also they are less compatible with microporous carbons.[24] Using solid electrolytes in batteries is an excellent choice because they are safer than liquid electrolytes and the temperature window is wider. Many researchers are interested in solid electrolytes which can be used for many applications, such as fuel cell, Li- air batteries and lithium -sulfate as well as solid lithium batteries and sensors. Inorganic oxides and sulfides are

examples of solid-state electrolytes.[25] Figure 7.1 shows some information that describes five characters related to electrolytes and electrochemical supercapacitors (ES). These properties are capacitance, equivalent series resistance (ESR), power density, cycle life, energy density and thermal stability.

1.5. Conducting polymers

Alan Heeger, Alan MacDiarmid, and Hideki Shirakwa were awarded the Nobel prize in 2000 because of the discovery of conducting polymers,[26] which can be synthesized by chemical or electrochemical methods. Conducting polymers, known as conjugated polymers or synthetic metals, are effective in capacitors. This is due to high conductivity and high capacitance. The conjugated polymers are highly π- conjugated sp^2 hybridized polymeric essential chains that in some cases show more electrical conductivity than inorganic materials including semiconductors and metals.[27] [28] The most extensive research to date on conductive polymers has been on polypyrrole, polyaniline, polythiophene and polypyridine, which are considered as archetypes.[29] The conducting polymer can be synthesized from its monomers by electrochemical methods, such as cyclic voltammetry (electropolymerisation), as well as chemical methods, enabling straightforward deposition on an electrode surface. The charge can be stored and released through the redox (reduction/oxidation) processes of the resulting polymer.[30]

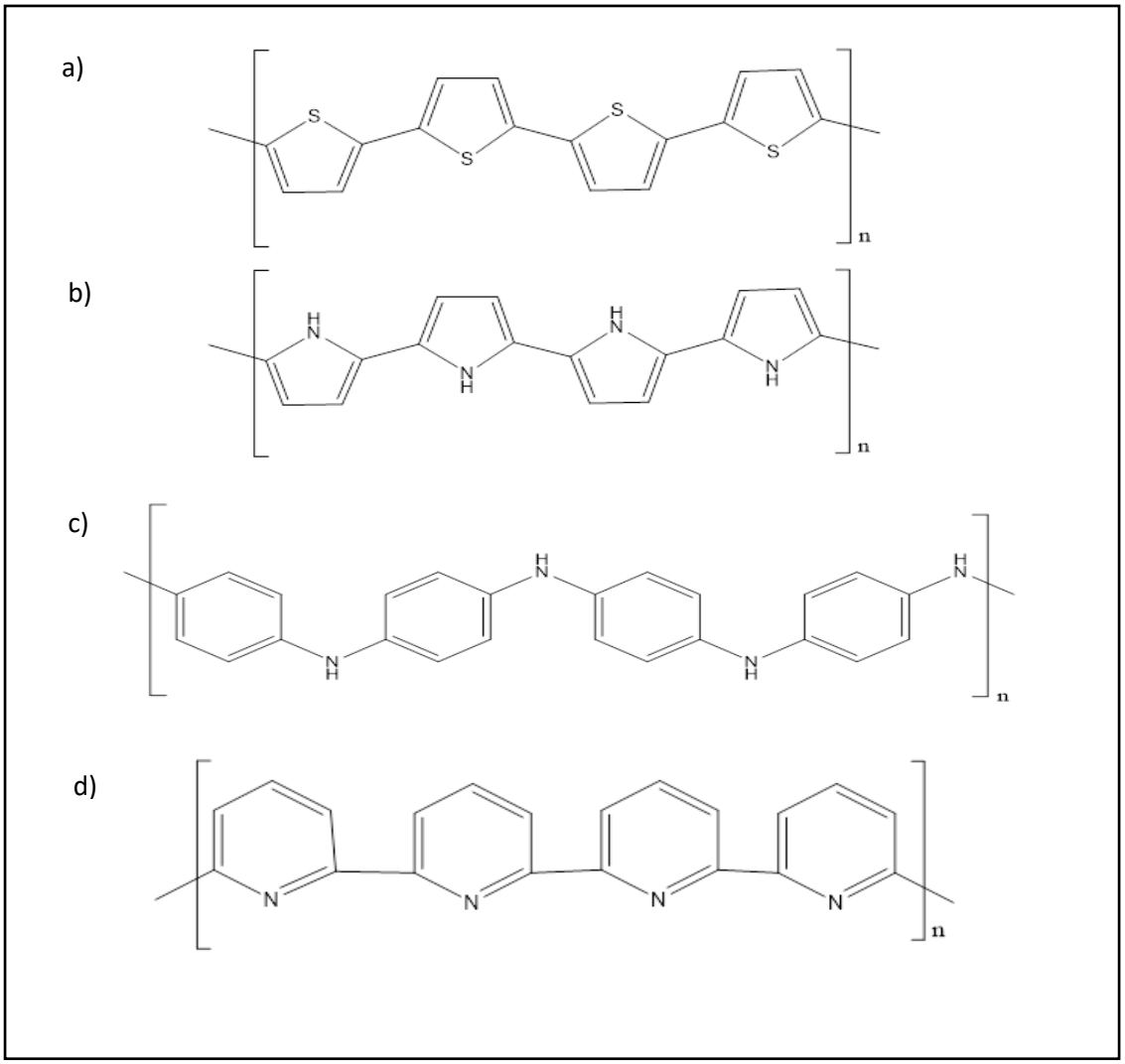

Figure 8.1 a) is polythiophene, (b) polypyrrole, (c)polyaniline, (d) is polypyridine.

The arrangement of bonds (single and double carbon-carbon bonds) in the aromatic rings of the conducting polymer helps to enhance the conductivity of conducting polymers (figure 8.1).

Polypyrrole (PPy) has been used for many applications including sensors, supercapacitors, batteries, and corrosion protection.[31] To synthesise polypyrrole electrochemically, the pyrrole is oxidised sweeping the range between 0 to 1.1 V vs Ag. Electropolymersation of pyrrole has been studied from the time when Diaz et al made polypyrrole film electrochemically.[32] The polymerization of polypyrrole monomers can be broken down into three processes (Figure 9.1).[33] The first process is oxidation of monomers to form radical cations. The second step is deprotonation and dimerization of the radical cations. The third step is chain propagation by continued oxidation and oligomerisation of the cationic monomers.[33]

During the electropolymerisation of polypyrrole, the polymer is partially oxidized to produce film of PPy/ $PPy^{+}BF_4^{-}$ if the electrolyte is for example $[^{n}Bu_4N]BF_4$ ($^{n}Bu_4N^{+}$ = tetra-n-butylammonium).[34] The polymer oxidation needs the inclusion of doping anions to maintain the polymer electroneutrality.[32, 35] When the potential is swept to positive voltage the charge is increased in polypyrrole whereas when the potential is reversed, the charge decreases as the film of polypyrrole is reduced its natural form.

Monomer oxidation

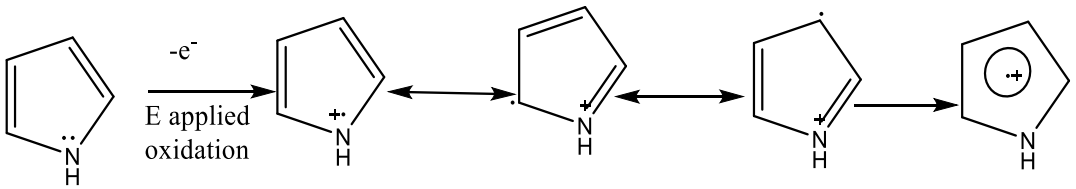

Dimer formation

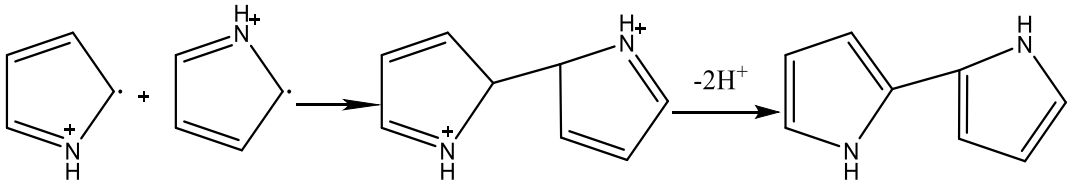

Chain propagation

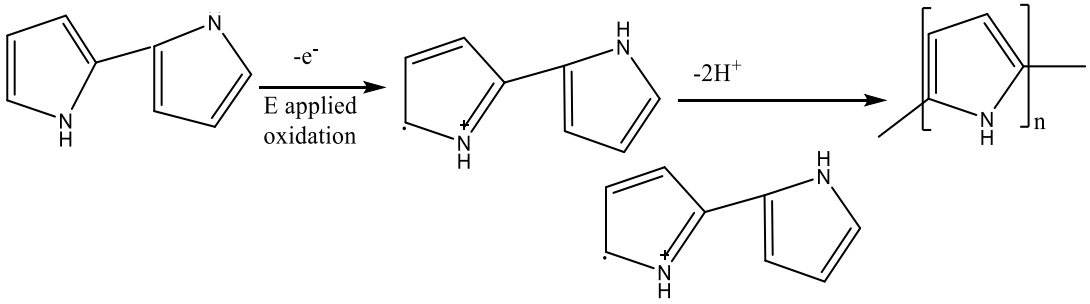

Figure 9.1 Shows mechanism for polymerization of polypyrrole.

In the electropolymerisation process, the oxidation or reduction of the monomers leads to formation of a polymer that is partially oxidized or reduced. This is referred to as p-doping (oxidation) or n-doping (reduction). Generally, the conductivity of the polymer increases when the doping level is increased and the doping /de-doping process depends on the nature of polymer and the movement of anion and cation in solution.[36] The oxidation (doping anions) or reduction (doping cations) depends on the involvement of the anions or cations which are

referred to as dopants. For example, during the oxidation, cations are formed which require anions to compensate the charge.[37]

The level of polypyrrole doping (oxidation) ranges from 20 to 40 % which depends on the concentration of polypyrrole and the conditions of synthesis.[33] The conductivity of polypyrrole is 10-50 S/cm which is higher than some polymers, such as polyaniline (PA/mn Ni) (0.1-5 S/cm).[38] Polypyrrole electrical conductivity can vary a lot, which limits its usage in applications. The conductivity of PPy varies because it depends on the synthesis and also the doped ion.[31]

The combination of polypyrrole with carbon materials helps to enhance the conductivity of polypyrrole. Figure 10.1 shows the polymerization of polypyrrole when polypyrrole doped by anions the polypyrrole become conductive and the conductivity is ranges between 10^{-5}-100 S/cm.[39]

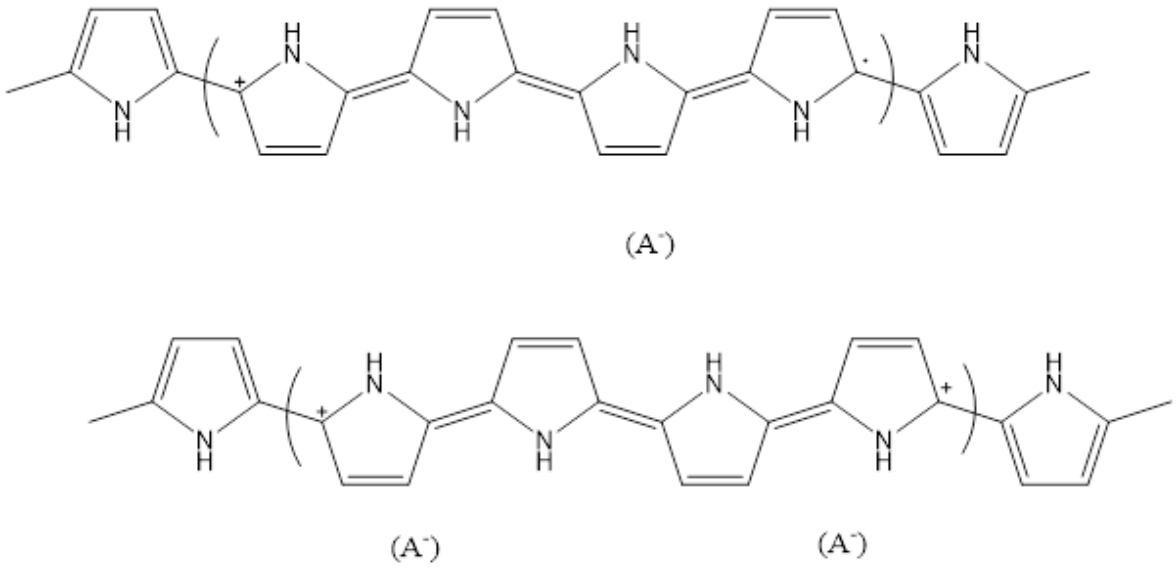

Figure 10.1 Shows structures of polaron and bipolaron where (A-) are dopant anions.

During polypyrrole oxidation the positively charged polymer film of polypyrrole brings in inclusion anions whereas throughout the de-doping (reduction), the anions are forced out.[40] The polypyrrole has a cationic polymer backbone, therefore, the polypyrrole units have positive charge which can compensate the anions used in solution during the redox process.[40] The redox waves of polypyrrole present faradaic capacitance charge storage kinetics during charge -discharge cycles.[41] However, much research has demonstrated that the cycle life stability is limited (poor) due to the structural breakdown during the repeated charge-discharge, which results from ingress and egress of anions during the doping/de-doping process.[42]

Figure 10.1 shows the oxidized states of polypyrrole.[43] The first step involves production of a radical cation (polaron). In the second step polypyrrole is oxidized again, producing a bipolaron or another independent polaron.[44] Bipolarons are responsible for the conductivity of polypyrrole. The cycle life of the conducting polymer is low compared to the combination of conducting polymer and carbon materials because of the effect of doping and n-doping during the electropolymerisation process whereas the combination of conducting polymers with carbon materials have high power because of sorption and desorption of ions.[44-45]

Polypyrrole application in supercapacitor devices is limited because of the deficiency of supercapacitor properties and α, β bonding.[46] Because of the formation of stable radical cations (polaron) is easy, N-substituted pyrrole can polymerize by oxidative polymerization through electrochemical or chemical methods. Therefore, the resulting polymer can also be developed (e.g functionality and solubility).[46] Consequently, the functionalization of polypyrrole can develop the specific properties of polypyrrole.[46] The functionalization of the monomer of pyrrole by functional groups leads to a new polymer and properties including a unique structure, mechanics, conductivity and morphology.[47] N-substituted pyrroles can be made with a redox active group. In previous research, by using 1989 Lian & Dong method, hexacyanoferrate was entrapped in polypyrrole layer. The result of cyclic voltammetry

presented redox waves of $Fe(CN)_6^{4-}$/ $Fe(CN)_6^{3-}$.[48] Also, another study used pyrrole derivatives of the chromophore $[Ru(bpy)3]^{2+}$ where bpy is 2,2-bipyridine, which showed redox couples.[49] Some organometallic complexes with N-substitution of pyrrole that derived from cyclam, porphyrins or polypyridines provides excellent modified electrode kinetics. Some research used 3-substitued pyrrole instead of N-substituted pyrrole which is higher conductivity than N-substituted pyrrole. However, the synthesis of 3-substituted polypyrroles is less straightforward than the synthesis of N-substituted polypyrroles.[50]

1.6. Carbon electrode materials

Carbon is a versatile material that can be used in many areas, such as supercapacitors, water purification and gas separation.[51] Carbon can be found in different types, such as glassy carbon, carbon fibre (which may be woven into cloth) and nano-carbon materials including nanotubes, Buckminster fullerenes, and graphene (Figure 11.1). This variety of carbons helps the engineer to match the exact material to a given application.[19] It has become more attractive because it has many advantages, such as low cost, large potential window, and high electrical conductivity.

The glassy carbon electrode (GCE) is one of the most popular in electrochemistry because GCE is inexpensive, has negligible porosity, excellent electrochemical behavior and a wide potential window.[52] The surface of GCE is homogeneous which allows the electrode to be reused when the electrode is polished.

Carbon fibre can resist corrosion, unlike some other polymer fibers, especially at high temperatures. Carbon fibre is usually used in applications that require lightweight, portability, wearability and strength.[53] It has high porosity, is stable chemically and has excellent electrical conductivity which is important for many applications.[54] The advantages of carbon

fibre enable its use to support composite materials. Carbon fiber has an excellent wear resistance, high specific strength and modulus.[55]

Microporous carbons are the essential materials that can be used to make the electrodes for supercapacitors. The most attractive features of microporous carbons are a large specific surface area which helps to improve the capacitance and also, a high electrical conductivity which is important for power applications.[19]

Graphene has become interesting in supercapacitor applications that are required to be flexible and portable. The redox-active component based on graphene is fixed to the graphitic network by Van der Waals interactions. This helps to keep the characteristics of the double-layer capacitance for graphene which is modified on the electrodes.[56] Graphene has a large surface area and high conductivity which allows electrons to move easily. However, many studies have found that pristine graphene does not make a good electrode material whereas graphene hybrid -which is graphene combined with other materials such as conducting polymers or organic or inorganic materials – has more advantages as an electrode material including high stability and high capacitance compared to pristine graphene. Graphene oxide is another type of graphene which consists of one layer. The graphene oxide is the result of the treatment of graphite during the oxidation reaction[57] Figure 11.1 shows a schematic of structures of different carbons.

Carbon nanotubes have become extensively used in energy storage applications, electrocatalysis and electrochemical analysis due to their large specific surface area, high conductivity and they are chemically and thermally stable.[58] Carbon nanotubes are similar to graphene, carbon nanotubes are one dimensional carbon allotropes which are hollow, and the structures are cylindrical whereas graphene is a 2-dimensional nanostructure which contains oxygen functional groups. Carbon nanotubes have been used for supercapacitor applications

since 1997.[59] Single-walled carbon nanotubes are formed from a single rolled up graphene sheet, multi-walled carbon nanotubes are built from several graphene sheets.[60]

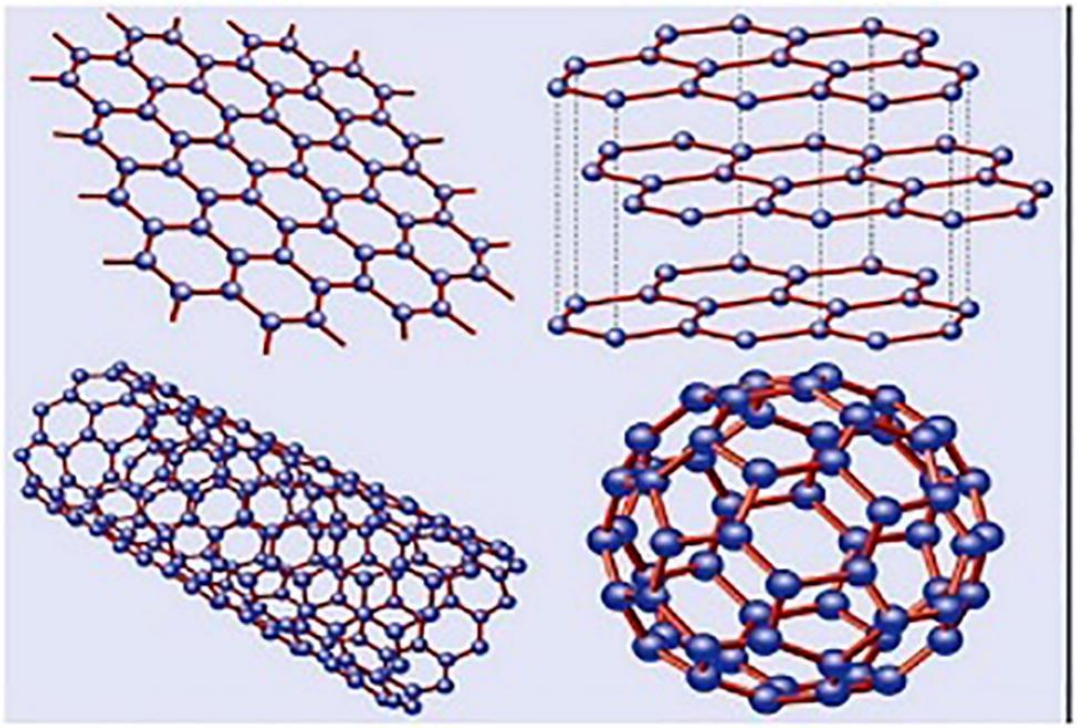

Figure 11.1 Schematic of structures of diffrent carbon. Figure reproduced with permission from reference 60.

1.7. Modification of carbon electrodes using reduction of diazonium salts

Diazonium salts are a group of organic compounds which can share a common functional group $R\text{-}N^{+2}x^{-}$ where R represents organic residue (e.g alkyl or aryl) and X^{-} represents organic or an inorganic counter-anion. The first reaction of diazonium salts was reported in 1858 by Griess when they discovered some reactions related to new class of diazonium salts.[61]

Lots of methods have been used to improve the stability and electrochemical performance of organic electrodes. Polymerization of organic compounds (such as conducting polymers) is an

example of this.[62] Here though, we focus on electrochemical grafting – reactions that enable organic layers to deposit on solid surfaces electrochemically. Electrografting can be used a wide range of materials, for example carbon, metals and their oxides and polymers. Modifying carbon material with an electroactive group is a quick method that can be used to increase capacitance because of the redox wave of the faradaic reaction.[63] Electrografting processes can occur on a number of materials such as carbon, metals, their oxides and polymers.[64] Organic compounds, such as anthraquinone can be attached the surface of carbon electrode by reduction of diazonium salts. The substrate can attach to the surface of the carbon electrode by several methods. The first one is the substrate can attach to the surface of carbon covalently. The second method is physisorption. The substrate adsorbs on the surface of carbon electrode.[53] Redox active organic molecules have been studied for many applications because they are inexpensive, lightweight and can be designed with high precision.[62c] Although the surface modification with such molecules is a common methods in energy storage, there are some disadvantages including lack of control on the grafted layer in structures and also, the nature of diazonium chemically which can be hard to manipulate.[65]

1.8. Quinones

Many applications need suitable energy storage to provide high power. EDLCs have fast and long cycle life (1000 000 times), despite this, the energy density of EDLCs is low which limits their applications. However, EDLCs can be improved by using electrolytes which provide a large potential window or by designing new electrodes. Quinone derivatives have become interesting as electroactive groups in rechargeable lithium-ion batteries because of their

properties, such as high redox potential vs lithium.[66] Therefore, quinone derivatives can develop the energy density of materials.[66] Anthraquinone has two redox waves (Scheme 1) which can store energy and have a more negative potential window compared to other quinones in organic solutions. Anthraquinone electrochemically shows different behavior depending on the media (electrolyte and solvent). First, producing a semiquinone radical anion which is unstable. The second step produces the quinone dianion. Figure 12.1 shows the redox chemistry of the anthraquinone radical anion and dianion and Figure 13.1 summarises the aqueous electrochemistry of anthraquinone.

Anthraquinone has become attractive for many researchers because of the fast redox behaviour, low cost and high faradaic capacity.[67] In many examples, anthraquinone was synthesised by the Diels-Alder reaction.[68] Anthraquinones and their derivatives have the fast reaction behaviours needed in organic cathodic materials, but the redox potentials of anthraquinone and its derivatives are less than the potential of conventional inorganic electrode materials.[69] The modification of carbon material with anthraquinone will combine two capacities - electric double layer capacity and faradaic capacity from the reduction of the organic compound. This helps to enhance the capacity of the material. Anthraquinone derivatives have become extensively important and studied in many fields including biochemistry, pharmacology and electrochemistry.[70] The anthraquinone derivatives can be used in anticancer drugs, in textile industries, rechargeable batteries and supercapacitor applications.[66, 70-71] For example, Campbell *et al* developed anthraquinone modified graphene macro assemblies as hybrid battery/ supercapacitor which increased energy storage capacity 3 fold (23Wh/kg).[72] Anthraquinone can be used to modify carbon fibre as the negative electrode throughout the charging and ruthenium oxide as the positive electrode in supercapacitors.[73] Anthaquinone and 1,2-dihydroxybenzene modified carbon fabric electrodes were studied as an asymmetric supercapacitor using 1M H_2SO_4 as electrolyte resulting in the energy density doubling

compared to a symmetric supercapacitor with two unmodified carbon fibre electrodes.[74] Anthraquinone with porous carbon nanotubes can improve supercapacitor application and enhance the specific capacitance of supercapacitors.[75] Recently,1,5-diamino-4,8-dihydroxyanthraquinone was modified by a nitrogen doped graphene aerogel which can increase energy density of supercapacitors. The modification occurred by formation of covalent bonds and the existence of intermolecular hydrogen bonds of 1,5-diamino-4,8-dihydroxyanthraquinone, which provided good stability and reversibilty during the charge-dischage process.[76] Also the sodium anthraquione-2-sulfonate composite graphene hydrogels for supercapacitor electrodes provide high specific capacitance 387.43 F/g at 1 A/g and excellent cycle stability of 91.11% after 10000 cycles at 10 A/g.[77]

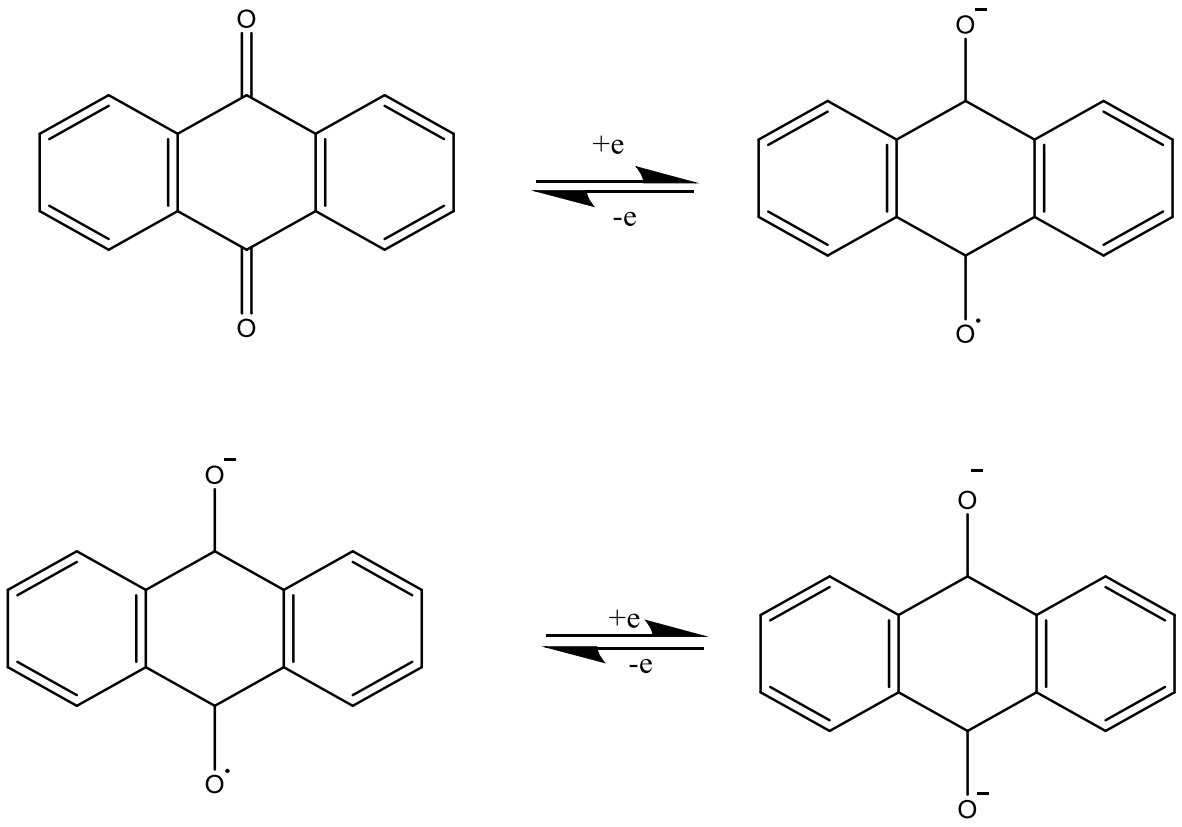

Figure 12.1 Redox reactions of the anthraquinone radical anion and dianion.

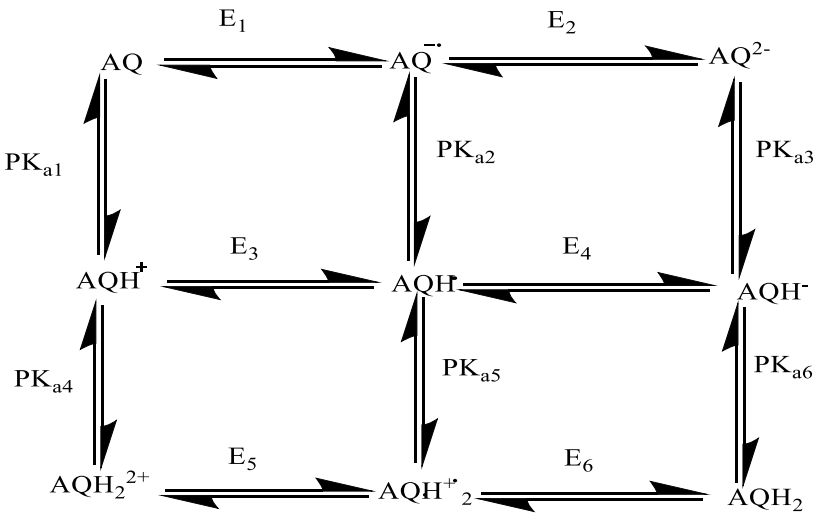

Figure 13.1 Scheme of squares showing the redox chemistry of anthraquinone in aqueous media.

1.9. Polyoxometalates (POMs)

Polyoxometalates are a class of metal oxide cluster anions predominantly based on molybdenum, tungsten or vanadium addenda atoms. Also, polyoxometalates can contain heteroatoms including silicon, oxygen and phosphorus.[78] POMs have dynamic structures that range from several angstroms, to nanometers in scale and have an unmatched range of physical and chemical properties. Broadly, they divide into three classes – isopolyanions based only on Mo, W or V addenda atoms, for example the $[M_6O_{19}]^{n-}$ Lindqvist structures; heterpolyanions such as the Keggin $[XM_{12}O_{40}]^{n-}$ and Wells-Dawson-types $[X_2M_{18}O_{62}]^{n-}$, where X can be many

different main group or transition elements; and giant, partially reduced clusters such as $[Mo_{132}O_{372}(CH_3CO_2)_{30}(H_2O)_{72}]^{42-}$.[79]

Polyoxometalates are inexpensive as faradaic supercapacitors and have fast electrochemical redox reactions. The variety of structures and scales of POMs lead to extensive research starting in the beginning of the 1990s.[80] Polyoxometalates are known to store up to 24 electrons, because of this POMs are called electron sponges in some research (figure 14.1).[81]

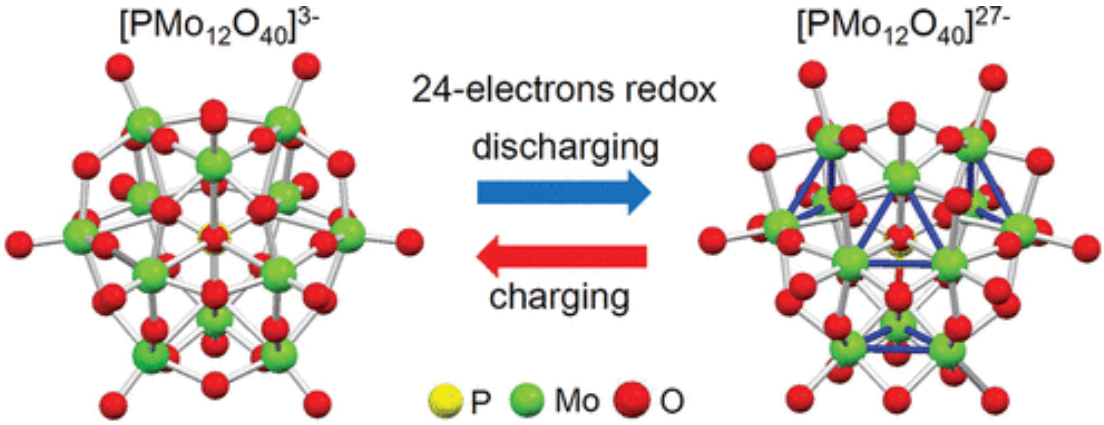

Figure 14.1 Shows the reduction of $[PMo_{12}O_{40}]^{3-}$ to form $[PMo_{12}O_{40}]^{27-}$ throughout the discharge proccess. Figure was reproduced with premission from reference 80.

POMs have excellent stability and can transfer electrons electrochemically with no change in structures.[82] Polyoxomelates have various properties and many applications due to their redox waves, ionic charge, photochemical response and conductivity.[83] Polyoxometalates can be used for many application including supercapacitors, lithium batteries as cathodic material and sensors, corrosion resistant coatings.[83] More detail on polyoxometalates is provided in Chapter 6.

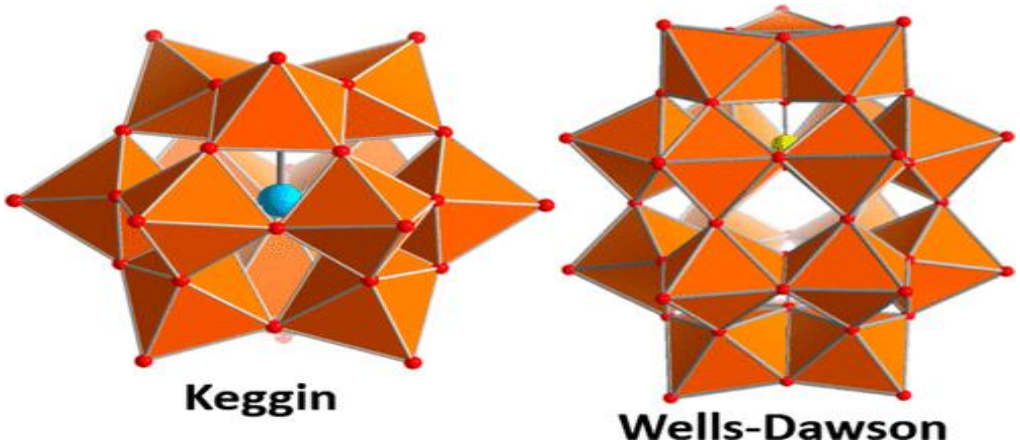

Figure 15.1 Shows Keggin and Wells-Dawson structures. Figure was reproduced with permission from reference[82].

1.10. References

[1] J. Yu, Q. Tan, J. Li, *Journal of Cleaner Production* **2020**, *255*, 120269.
[2] J. Wen, Y. Yu, C. Chen, *Materials express* **2012**, *2*, 197-212.
[3] G. Heal,*The Economics of Renewable Energy* **2009**.DOI 10.3386/w15081.
[4] J. Winsberg, T. Hagemann, T. Janoschka, M. D. Hager, U. S. Schubert, *Angewandte Chemie International Edition* **2017**, *56*, 686-711.
[5] X. Yu, N. S. Sandhu, Z. Yang, M. Zheng, *Applied Energy* **2020**, *271*, 115169.
[6] aE. Kabir, P. Kumar, S. Kumar, A. A. Adelodun, K.-H. Kim, *Renewable and Sustainable Energy Reviews* **2018**, *82*, 894-900; bA. Demirbaş, *Energy conversion and Management* **2001**, *42*, 1357-1378.
[7] T. B. Reddy, *Linden's handbook of batteries, Vol. 4*, Mcgraw-hill New York, **2011**.
[8] N. Kularatna, *Energy storage devices for electronic systems: rechargeable batteries and supercapacitors*, Academic Press, **2014**.
[9] Y. Nishi, *Journal of Power Sources* **2001**, *100*, 101-106.
[10] A. Jansen, A. Kahaian, K. Kepler, P. Nelson, K. Amine, D. Dees, D. Vissers, M. Thackeray, *Journal of Power Sources* **1999**, *81*, 902-905.
[11] Y. Cheng, S. Lu, R. Zheng, D. Zhang, H. Zhang, *Applied Surface Science* **2019**, *485*, 119-127.
[12] K. Kubota, S. Komaba, *Journal of The Electrochemical Society* **2015**, *162*, A2538.
[13] P. Simon, Y. Gogotsi, *Nature materials* **2020**, *19*, 1151-1163.
[14] J. Yang, Y. Liu, S. Liu, L. Li, C. Zhang, T. Liu, *Materials Chemistry Frontiers* **2017**, *1*, 251-268.
[15] F. Liu, Q. Q. Li, S. H. Zhang, C. Ma, Q. Z. Ren, X. Y. Tao, J. P. Cheng, X. B. Zhang, in *Advanced Materials Research, Vol. 507*, Trans Tech Publ, **2012**, pp. 48-51.
[16] R. Kötz, M. Carlen, *Electrochimica Acta* **2000**, *45*, 2483-2498.
[17] aL. Dagousset, G. Pognon, G. T. Nguyen, F. Vidal, S. Jus, P.-H. Aubert, *Journal of Power Sources* **2017**, *359*, 242-249; bS. Wang, W. Quan, Z. Zhu, Y. Yang, Q. Liu, Y. Ren, X. Zhang, R. Xu, Y. Hong, Z. Zhang, *Nature communications* **2017**, *8*, 1-8; cV. Dragunov, D. Ostertak, K. Pelmenev, R. Sinitskiy, E. Dragunova, *Sensors and Actuators A: Physical* **2021**, *318*, 112501.
[18] aK. Ueno, H. Shimotani, H. Yuan, J. Ye, M. Kawasaki, Y. Iwasa, *Journal of the Physical Society of Japan* **2014**, *83*, 032001; bM. Endo, T. Takeda, Y. Kim, K. Koshiba, K. Ishii, *Carbon letters* **2001**, *1*, 117-128.
[19] F. Béguin, V. Presser, A. Balducci, E. Frackowiak, *Advanced Materials* **2014**, *26*, 2219-2251.
[20] Q. Wei, Y. Jiang, X. Qian, L. Zhang, Q. Li, S. Tan, K. Zhao, W. Yang, Q. An, J. Guo, *Iscience* **2018**, *6*, 212-221.
[21] S. Yang, X. Wu, C. Chen, H. Dong, W. Hu, X. Wang, *Chemical Communications* **2012**, *48*, 2773-2775.
[22] V. Augustyn, P. Simon, B. Dunn, *Energy & Environmental Science* **2014**, *7*, 1597-1614.
[23] B. Pal, S. Yang, S. Ramesh, V. Thangadurai, R. Jose, *Nanoscale Advances* **2019**, *1*, 3807-3835.
[24] A. González, E. Goikolea, J. A. Barrena, R. Mysyk, *Renewable and Sustainable Energy Reviews* **2016**, *58*, 1189-1206.
[25] M. V. Reddy, C. M. Julien, A. Mauger, K. Zaghib, *Nanomaterials* **2020**, *10*, 1606.
[26] S. C. Rasmussen, in *100+ Years of Plastics. Leo Baekeland and Beyond*, ACS Publications, **2011**, pp. 147-163.

[27] M. Vangari, T. Pryor, L. Jiang, *Journal of Energy Engineering* **2013**, *139*, 72-79.
[28] J. Hazarika, A. Kumar, *The Journal of Physical Chemistry B* **2017**, *121*, 6926-6933.
[29] A. Borenstein, O. Hanna, R. Attias, S. Luski, T. Brousse, D. Aurbach, *Journal of Materials Chemistry A* **2017**, *5*, 12653-12672.
[30] T. O. Magu, A. U. Agobi, L. HITLER, P. M. Dass, *Journal of Chemical Reviews* **2019**, *1*, 19-34.
[31] J. Zhong, S. Gao, G. Xue, B. Wang, *Macromolecules* **2015**, *48*, 1592-1597.
[32] J. Ghilane, P. Hapiot, A. J. Bard, *Analytical Chemistry* **2006**, *78*, 6868-6872.
[33] A. M. Bryan, L. M. Santino, Y. Lu, S. Acharya, J. M. D'Arcy, *Chemistry of Materials* **2016**, *28*, 5989-5998.
[34] A. F. Diaz, J. I. Castillo, J. Logan, W.-Y. Lee, *Journal of Electroanalytical Chemistry and Interfacial Electrochemistry* **1981**, *129*, 115-132.
[35] A. Diaz, J. Bargon, *TA Skotheim Ed* **1986**, *1*, 82-100.
[36] R. John, G. Wallace, *Journal of Electroanalytical Chemistry* **1993**, *354*, 145-160.
[37] aA. M. Christie, S. J. Lilley, E. Staunton, Y. G. Andreev, P. G. Bruce, *Nature* **2005**, *433*, 50-53; bH. Ullah, A.-u.-H. A. Shah, S. Bilal, K. Ayub, *The Journal of Physical Chemistry C* **2014**, *118*, 17819-17830; cW. W. Chiu, J. Travaš-Sejdić, R. P. Cooney, G. A. Bowmaker, *Synthetic Metals* **2005**, *155*, 80-88; dD. Ateh, H. Navsaria, P. Vadgama, *Journal of the Royal Society Interface* **2006**, *3*, 741-752.
[38] M. A. A. M. Abdah, N. H. N. Azman, S. Kulandaivalu, Y. Sulaiman, *Materials & Design* **2020**, *186*, 108199.
[39] E. Håkansson, T. Lin, H. Wang, A. Kaynak, *Synthetic Metals* **2006**, *156*, 1194-1202.
[40] R. K. Sharma, A. Rastogi, S. Desu, *Electrochimica Acta* **2008**, *53*, 7690-7695.
[41] X. Liu, L. Zang, C. Liang, Q. Liu, Y. Deng, C. Yang, J. Qiu, *Synthetic Metals* **2021**, *271*, 116654.
[42] Y. Huang, J. Tao, W. Meng, M. Zhu, Y. Huang, Y. Fu, Y. Gao, C. Zhi, *Nano Energy* **2015**, *11*, 518-525.
[43] J. L. Bredas, G. B. Street, *Accounts of Chemical Research* **1985**, *18*, 309-315.
[44] G. A. Snook, P. Kao, A. S. Best, *Journal of Power Sources* **2011**, *196*, 1-12.
[45] M. E. Abdelhamid, G. A. Snook, *Encyclopedia of Polymer Science and Technology* **2002**, 1-20.
[46] S. Ahmad, S. S. Gursoy, S. Kazim, A. Uygun, *Solar Energy Materials and Solar Cells* **2012**, *99*, 95-100.
[47] D. A. Walker, C. D'Silva, *Electrochimica Acta* **2014**, *116*, 175-182.
[48] W. Schuhmann, R. Lammert, M. Hämmerle, H.-L. Schmidt, *Biosensors and Bioelectronics* **1991**, *6*, 689-697.
[49] A. J. Downard, N. A. Surridege, T. J. Meyer, S. Cosnier, A. Deronzier, J.-C. Moutet, *Journal of Electroanalytical Chemistry and Interfacial Electrochemistry* **1988**, *246*, 321-335.
[50] H. KorriáYoussoufi, *Journal of the Chemical Society, Chemical Communications* **1993**, 1550-1552.
[51] M.-M. Titirici, R. J. White, N. Brun, V. L. Budarin, D. S. Su, F. del Monte, J. H. Clark, M. J. MacLachlan, *Chemical Society Reviews* **2015**, *44*, 250-290.
[52] J. Wang, Ü. A. Kirgöz, J.-W. Mo, J. Lu, A. N. Kawde, A. Muck, *Electrochemistry Communications* **2001**, *3*, 203-208.
[53] C. G. Heald, G. G. Wildgoose, L. Jiang, T. G. Jones, R. G. Compton, *ChemPhysChem* **2004**, *5*, 1794-1799.
[54] R. Devi, K. Tapadia, T. Maharana, *Heliyon* **2020**, *6*, e03122.
[55] S.-S. Yao, F.-L. Jin, K. Y. Rhee, D. Hui, S.-J. Park, *Composites Part B: Engineering* **2018**, *142*, 241-250.

[56] C. Zhou, T. Gao, Q. Liu, Y. Wang, D. Xiao, *Electrochimica Acta* **2020**, 135628.
[57] A. T. Lawal, *Biosensors and Bioelectronics* **2019**, *141*, 111384.
[58] K. Li, H. Li, M. Li, C. Li, L. Su, L. Qian, B. Yang, *Composites Science and Technology* **2019**, *175*, 92-99.
[59] S. Z. Hussain, M. Ihrar, S. B. Hussain, W. C. Oh, K. Ullah, *SN Applied Sciences* **2020**, *2*, 1-23.
[60] M. V. Kiamahalleh, S. H. S. Zein, G. Najafpour, S. A. SATA, S. Buniran, *Nano* **2012**, *7*, 1230002.
[61] B. D. Assresahegn, T. Brousse, D. Bélanger, *Carbon* **2015**, *92*, 362-381.
[62] aB. Li, J. Zhao, Z. Zhang, C. Zhao, P. Sun, P. Bai, J. Yang, Z. Zhou, Y. Xu, *Advanced Functional Materials* **2019**, *29*, 1807137; bJ. Yang, Y. Shi, P. Sun, P. Xiong, Y. Xu, *ACS Applied Materials & Interfaces* **2019**, *11*, 42305-42312; cA. Jaffe, A. Saldivar Valdes, H. I. Karunadasa, *Chemistry of Materials* **2015**, *27*, 3568-3571.
[63] K. Jurewicz, S. Delpeux, V. Bertagna, F. Beguin, E. Frackowiak, *Chemical Physics Letters* **2001**, *347*, 36-40.
[64] D. Belanger, J. Pinson, *Chemical Society Reviews* **2011**, *40*, 3995-4048.
[65] M. Deschanels, F. Favier, O. Fontaine, S. Le Vot, *Electrochimica Acta* **2020**, *361*, 137027.
[66] S. B. Sertkol, B. Esat, A. A. Momchilov, M. B. Yılmaz, M. Sertkol, *Carbon* **2017**, *116*, 154-166.
[67] Y. Yang, K. He, P. Yan, D. Wang, X. Wu, X. Zhao, Z. Huang, C. Zhang, D. He, *Electrochimica Acta* **2014**, *138*, 481-485.
[68] aD. Hansen Jr, R. Pappo, R. Garland, *The Journal of Organic Chemistry* **1988**, *53*, 4244-4253; bM. A. Castro, J. M. M. del Corral, M. Gordaliza, P. A. García, A. M. Gamito, S. A. Gualberto, R. Batista, A. San Feliciano, *Synthesis* **2005**, *2005*, 3202-3208.
[69] Z. Wang, A. Li, L. Gou, J. Ren, G. Zhai, *RSC advances* **2016**, *6*, 89827-89835.
[70] M. Shamsipur, A. Siroueinejad, B. Hemmateenejad, A. Abbaspour, H. Sharghi, K. Alizadeh, S. Arshadi, *Journal of Electroanalytical Chemistry* **2007**, *600*, 345-358.
[71] L. Gao, S. Gan, H. Li, D. Han, F. Li, Y. Bao, L. Niu, *Nanotechnology* **2017**, *28*, 275602.
[72] P. Campbell, M. Merrill, B. Wood, E. Montalvo, M. Worsley, T. Baumann, J. Biener, *Journal of Materials Chemistry A* **2014**, *2*, 17764-17770.
[73] Z. Algharaibeh, X. Liu, P. G. Pickup, *Journal of Power Sources* **2009**, *187*, 640-643.
[74] Z. Algharaibeh, P. G. Pickup, *Electrochemistry Communications* **2011**, *13*, 147-149.
[75] aX. Chen, H. Wang, H. Yi, X. Wang, X. Yan, Z. Guo, *The Journal of Physical Chemistry C* **2014**, *118*, 8262-8270; bG. Ma, F. Hua, K. Sun, E. Feng, Z. Zhang, H. Peng, Z. Lei, *Ionics* **2018**, *24*, 549-561.
[76] L. Yang, K. Zhuo, X. Xu, Z. Zhang, Q. Du, G. Bai, J. Wang, *Electrochimica Acta* **2021**, *393*, 139057.
[77] C. Zhu, W. Zhang, G. Li, C. Li, X. Qin, *Journal of Alloys and Compounds* **2021**, *862*, 158472.
[78] T. Ueda, *ChemElectroChem* **2018**, *5*, 823-838.
[79] S. Liu, Z. Tang, *Nano Today* **2010**, *5*, 267-281.
[80] D. L. Long, R. Tsunashima, L. Cronin, *Angewandte Chemie International Edition* **2010**, *49*, 1736-1758.
[81] H. Wang, S. Hamanaka, Y. Nishimoto, S. Irle, T. Yokoyama, H. Yoshikawa, K. Awaga, *Journal of the American Chemical Society* **2012**, *134*, 4918-4924.
[82] M. Samaniyan, M. Mirzaei, R. Khajavian, H. Eshtiagh-Hosseini, C. Streb, *ACS catalysis* **2019**, *9*, 10174-10191.
[83] D. E. Katsoulis, *Chemical Reviews* **1998**, *98*, 359-388.

Chapter 2

Electrochemistry

Electrochemistry is an essential field of chemistry to study electron kinetics between electrodes and electroactive species. There are many examples related to the importance of electrochemistry. For example, fuel cells and supercapacitors, electrochemical synthesis of useful chemicals, electrochemical devices for solar energy conversion, and electrochemical sensors.[1] To analyze electrochemical reactions, a three electrode system is typically used which applies a specific potential between electrodes in the cell. The first electrode is a working electrode such as carbon, platinum, mercury or gold, which is the electrode where the procedure of interest occurs – and the second electrode is a reference electrode, such as a saturated calomel electrode (SCE) or silver quasi-reference electrode. The third electrode is a counter electrode, such as a Pt electrode.[2] The benefit of using the counter electrode is to avoid current passing through the reference electrode and make the measurement of potential accurate.

Figure 2.1(a) shows an electrochemical cell with two electrode configurations.

$$\text{Potential difference (E)} = (Q_M\text{-}Qs)_{\text{working electrode}} + IR\text{-}(Q_M\text{-}Qs)_{\text{Reference electrode}} \quad (7)$$

Where the IR term is the Ohmic drop which is the electric resistance in solution between the working electrode and reference electrode. Q_M is the potential of metal electrode and Qs is the potential of solution and the charge separation will be Q_M-Qs. Therefore, changes in E can cause unknown alterations in IR and thus change $(Q_M\text{-}Q_s)_{\text{working}}$. Therefore, the change in potential at the working electrode would not be controlled.[2]

a)

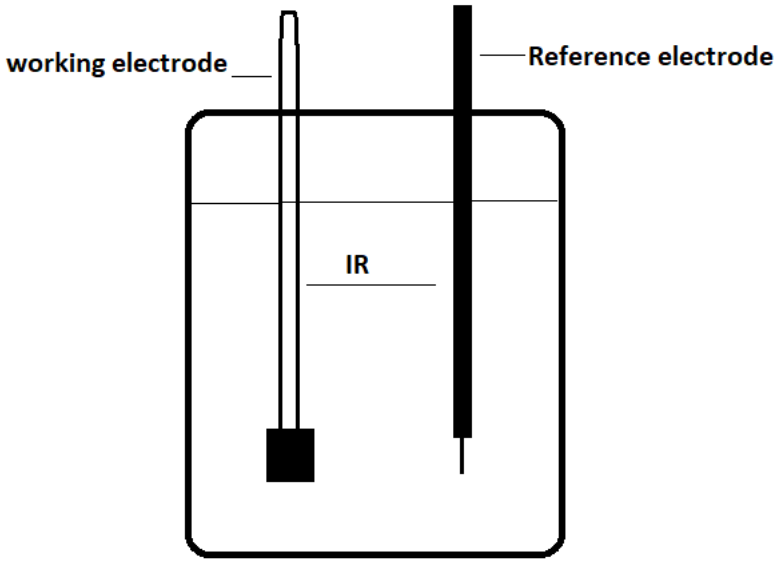

b)

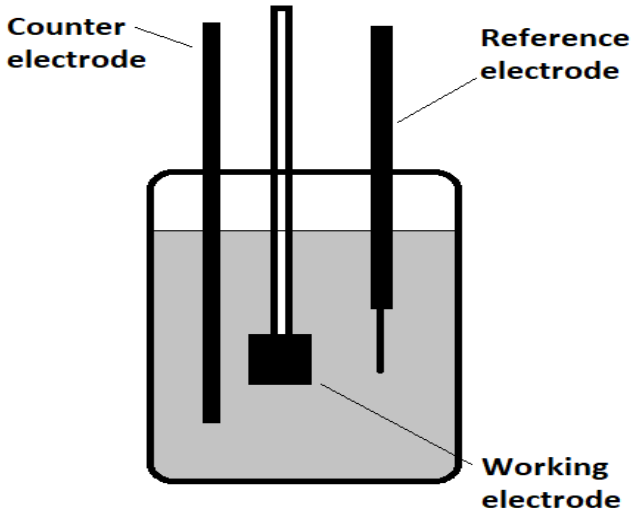

Figure 2.1 a) Electrochemical cell with two electrode configuration. **b)** Electrochemical cell with three electrode configuration.

In the three-electrode system (figure2.1 b), the potential of the working electrode is controlled vs the reference, and no current flows between the working and reference electrodes, while the counter electrode completes the circuit with the working electrode. So, if the working electrode is oxidising the substrate (acting as the anode) the counter electrode will be reducing it and vice versa.[3] The potential difference between working and counter electrodes is not controlled and can become very high as the counter electrode may need to oxidise or reduce solvent/electrolyte to drive the process at the working electrode. Also, the third electrode plays role to make sure that reference electrode is not affected by Ohmic IR drop and the potential of the reference electrode will be stable.[2, 4]

2.1. Electrochemical techniques

2.1.1. Cyclic voltammetry

Cyclic voltammetry is the most commonly used technique in electrochemistry. The current is recorded as a function of the applied potential and used to characterize the electrochemistry that happens at the interface between the electrode and the electrolyte solution. Figure 2.2a shows a reversible cyclic voltammogram of ferrocene. It is an example to show the redox wave where E_{pa} is the oxidative peak potential and E_{pc} is the reductive peak potential. Electroactive species can show a range of behaviours ranging from reversible to irreversible. In cyclic voltammetry, the applied potential is swept from initial potential, E_1, to a final potential, E_2 and back again to E_1, (Figure 2.2b).

In reversible cyclic voltammetry, as the potential increases, oxidation starts and the current increases as the driving force for electron transfer increases. Then, when most of chemical species is oxidized (around the electrode) the current drops because depletion of substrate near the electrode means that fresh substrate has to diffuse to the electrode. As the potential is swept back in the opposite direction, the reduction peak appears, and the current will be in the opposite direction to reduce the species. For irreversible processes, which occur if there is a slow electron transfer or a chemical reaction that follows electron transfer, reaction may be in one direction and the peak current of reduction will be absent, or a large separation may be observed between the oxidation and reduction peaks.

$$E_{1/2} = E^0 = (E_{pc} + E_{pa})/2 \qquad (8)$$

Where E^0 is the standard reduction potential

The peak current increases by increasing the scan rate. The Randles-Sevcik equation (equation number 9) can explain this relationship, at rapid scan rates the diffusion layer is small and then provide large current whereas at slow scan rate, the diffusion layer is large which means the diffusion of analyte to the surface of electrode is slow that leads to small current.[2]

$$Ip = 2.69x10^5 nFAC^* D^{1/2} \upsilon^{1/2} \qquad (9)$$

Where I_p = peak current (A), n = number of electrons, F = Faraday constant (96485 C mol^{-1}), A = Area (cm^2), C* = Bulk [A] ($mol.cm^{-3}$), D_x = Diffusion coefficient (cm^2s^{-1}), υ = scan rate (Vs^{-1}).[5] For a reversible one electron process (corresponding to fast electron transfer behaviour), this becomes:

$$Ip = 2.69x10^5 A D^{1/2} [A]_{bulk} \upsilon^{1/2} \qquad (10)$$

And for an irreversible one electron process (slow electron transfer):

$$Ip = 2.69x10^5 \sqrt{\alpha} D^{1/2} [A]_{bulk} A \upsilon^{1/2} \qquad (11)$$

Where α is the transfer coefficient ($0< \alpha <1$).

During irreversible processes, the electron transfer is hindered. The main difference between a reversible and irreversible is the potential separation between the current peaks ΔE_{pp} which can be described by following equation:

$$\Delta E_{pp} = |E_p \text{ (anodic)} - E_p\text{(cathodic)}| \qquad (12)$$

Where E_p (anodic) and E_p (cathodic) are the peaks potential of oxidation and reduction and the separation for a fully reversible process of one electron is 59 mV.[2,6]

a)

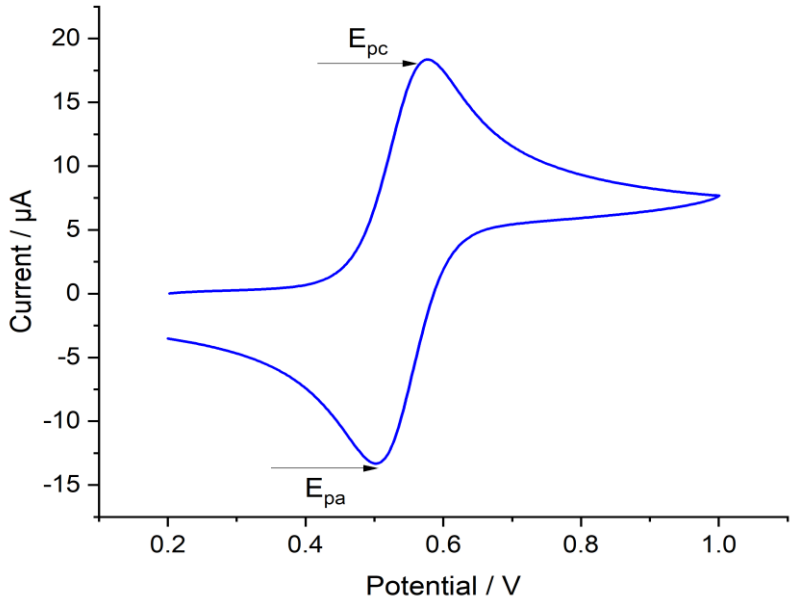

b)

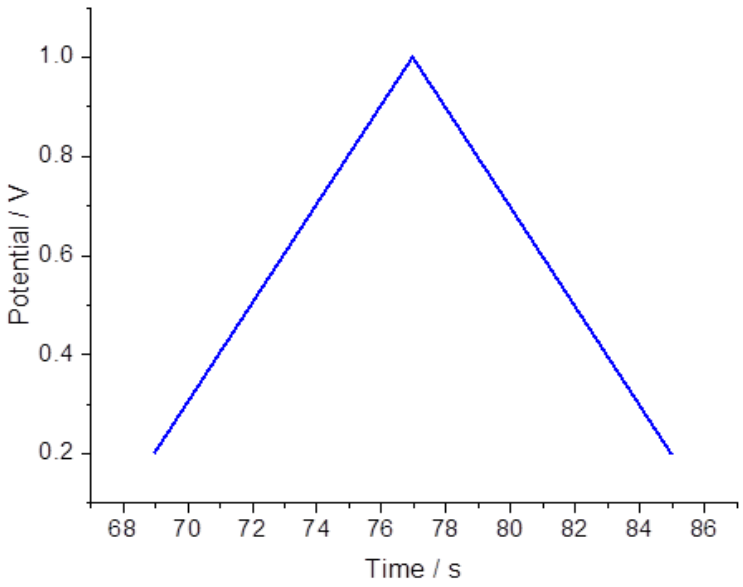

Figure 2.2(a) Typical cyclic voltammogram, E_{pc} and E_{pa} are reduction and oxidation peak potentials of ferrocene in 0.1 M of $[^{n}Bu_4N]PF_6$ with acetonitrile at 100 mV/s. **(b)** Typical cyclic voltammetry, potential vs time.

2.1.2 Adsorbed voltammetry:

Species can be adsorbed onto electrodes during electrochemical processes, or before conducting electrochemical experiments, and this changes their behaviour. Also, adsorption can be used for the determination of traces of metal ions.[7] During the adsorption process, a thin layer of the electroactive species sticks onto the electrode surface reducing or eliminating diffusion. There are two situations. First, in ideal reversible kinetics, the redox peak currents are identical in both scan directions and occur at the same potential, which means $\Delta E_p = 0$. The second situation is an irreversible process, where the forward and backward peaks will be shifted and separated which means $Ep_c < Ep_a$. In the second situation an overpotential needs to be applied to drive the reaction, separating the forward and reverse peaks. Transfer of electroactive species from the bulk of solution to electrode can happen by adsorption during solution experiments. When adsorption and diffusion occur at the same time, electrochemical results are complicated.[8]

$$Ox_{(solution)} \longleftrightarrow Ox_{(adsorbed)}$$

$$Ox_{(adsorbed)} + e^- \longleftrightarrow Red_{(adsorbed)}$$

$$Red_{(solution)} \longleftrightarrow Red_{(adsorbed)}$$

This shows a reversible electron transfer which is complicated by adsorption processes which are in equilibrium with diffusion for the oxidised and reduced states.[9]

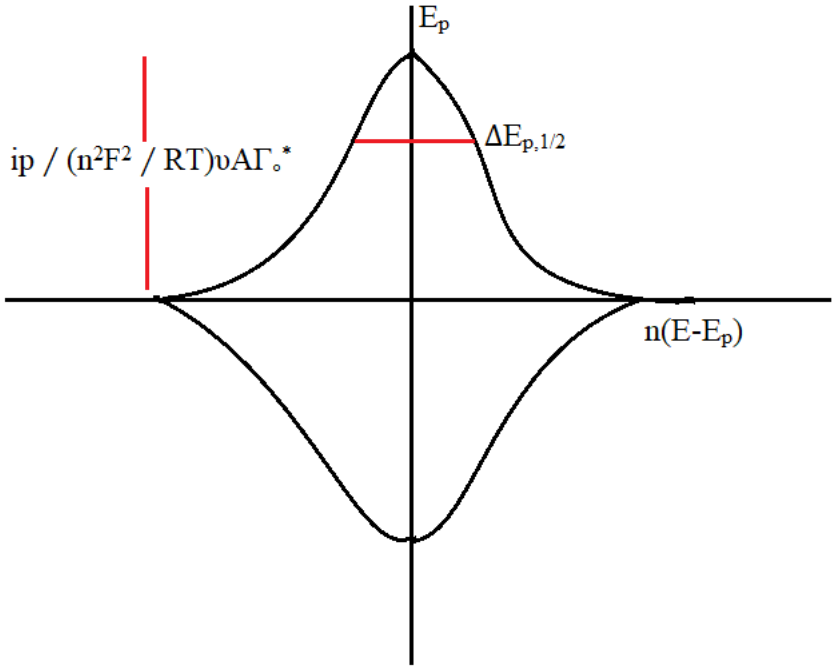

Figure 3.2. Shows example of reversible adsorption voltammetry.

If the chemical species A and B are redox reactants adsorbed on the electrode surface

$$A(ads) + e^- \longleftrightarrow B(ads)$$

The amount of chemical species A and B on the electrode can be quantified by the surface coverage Γ with the unit mol cm^{-2}.

$$\Gamma_{total} = \Gamma_A(t) + \Gamma_B(t) \qquad (13)$$

Where Γ_{total} is coverage, $\Gamma_A(t)$ is the coverage of chemical species A and $\Gamma_B(t)$ is the coverage of chemical species.

Figure 3.2 represents adsorption cyclic voltammogram. The peak current can be described as following equation

$$Ip = (n^2F^2/4RT)\,\upsilon A\Gamma_{Total} \qquad (14)$$

In addition, Ip is proportional to the scan rate which is different to the situation with solution phase voltammetry were I_p is proportional to the square root of the scan rate. Furthermore, the width of the peak at half height is

$$3.53\ RT/F = 90.6\ mV \quad \text{at } 25\ ^\circ C \qquad (15)$$

And the potential of the forward and backward peaks are symmetrical with no diffusion process. In the case when the forward scan is integrated

$$\int I dt = FA\Gamma_{Total} \qquad (16)$$

The total coverage can be measured from the area under the cyclic voltammogram for each peak

$$\Gamma_A = b_A[A]\ ,\ \Gamma_B = b_B[B] \qquad (17)$$

Where b_A and b_B are the adsorption coefficients which are the standard Gibbs energies of adsorption A and B.

$$\Gamma_A = \exp(-\Delta G^\circ_A/RT) \qquad (18)$$

$$\Gamma B = \exp(-\Delta G^\circ_B/RT) \qquad (19)$$

And the potential of the adsorbed species A and B will be as following equation

$$E^\circ_f(A/B)(ads) = E^\circ_f(A/B)(aq) - RT/Fln(b_A/b_B) \qquad (20)$$

2.1.3. Chronoamperometry

Chronoamperometry is the electrochemical technique which can measure current in a certain time with applied specific potential. The difference between chronoamperometry compared with cyclic voltammetry is the potential of working electrode is fixed at a certain voltage for specified periods of time during the experiment.

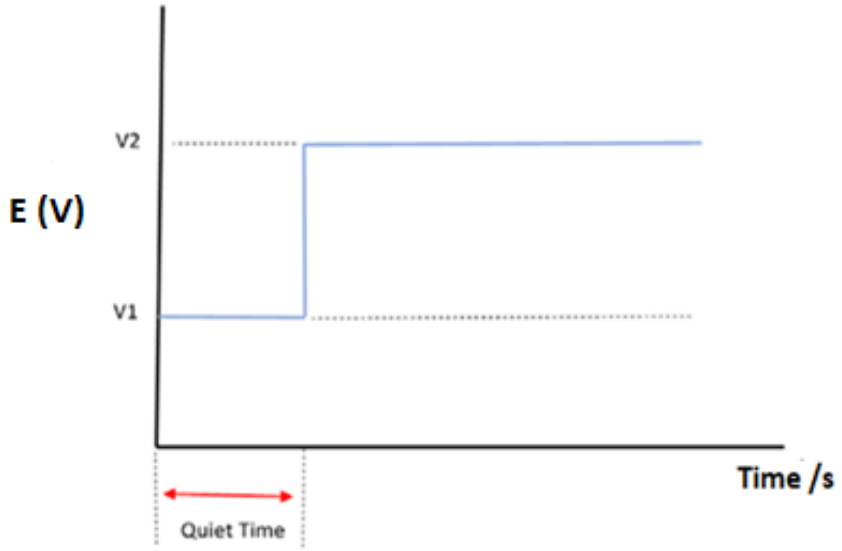

Figure 4.2 Potential over time in a chronoamperometry experiment.

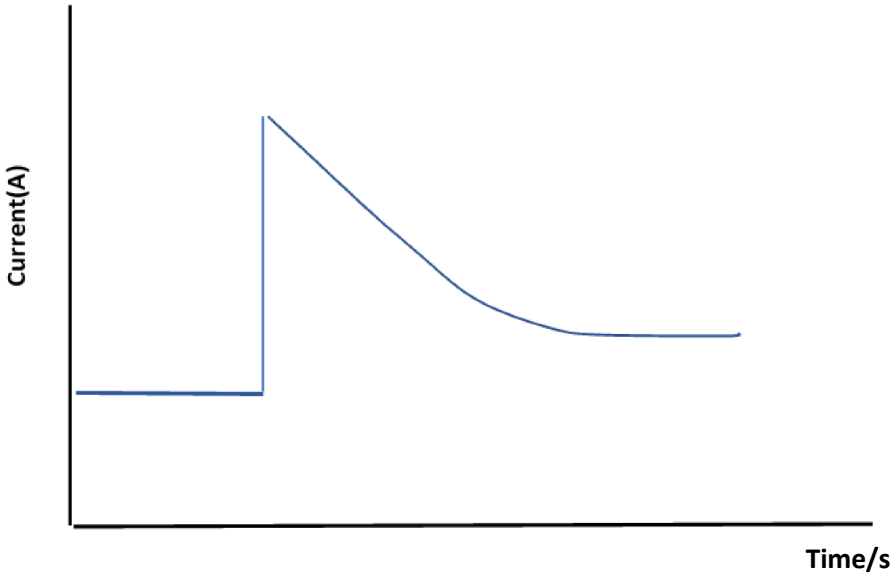

Figure 5.2 Typical chronoamperometry curve of an electrochemical analyte.

When the experiment starts the potential is held at V_1 until the end of the quiet time. Then, the potential is stepped up or down to V_2, where the substrate can be oxidized or reduced.

The Cottrell equation explains the rate of the Faradaic component of the current which is related to the electron transfer reduction/oxidation reaction. The redox decays at a macro disc electrode are very slow and the Cottrell equation is described below:

$$i = \frac{nFAc * \sqrt{D}}{\sqrt{\pi t}} \qquad (21)$$

Where *i* is the current passed, n is the number of electrons passed through reduction/oxidation conditions, *A* is the area of electrode (cm^2), *c** is the analyte concentration, *D* is the diffusion coefficient ($cm^2\ s^{-1}$) and *t* is time (s). The Faradaic current is controlled by the rate of the electrochemical reaction. Figure 4.2 shows V_1 which is the initial potential value with no

current in this point. V_2 is the final potential which causes electron transfer reaction. For macroelectrodes, such as GCE, the diffusion can limit the current until it becomes zero. Figure 5.2 represents the relationship between current and time during chronoamperometry. The spike shows the current from the substrate starting to react when the required potential V_1 is achieved and drop in current as the diffusion layer is established. After that, the current drops down gradually versus time because of the consumption of substrate.[11]

2.1.4. Capacitance and charging current in electrochemical experiments:

When the electrochemical circuit is charged and the current is constant the following equation will apply

$$E = E_R + Ec = iRs + q/C_d \quad (22)$$

where $q = \int idt$ and the current is constant.

$$E = i(Rs + t/C_d) \quad (23)$$

And therefore the potential will increase linearly with time as shown in figure 6.2.

When the capacitor is uncharged which means (q = 0 and t = 0)

$$q = EC_d[1 - e^{-t/RsCd}] \quad (24)$$

For charging the double layer capacitance the current falls to 37% at $t = \tau$.

Where τ is the transition time.

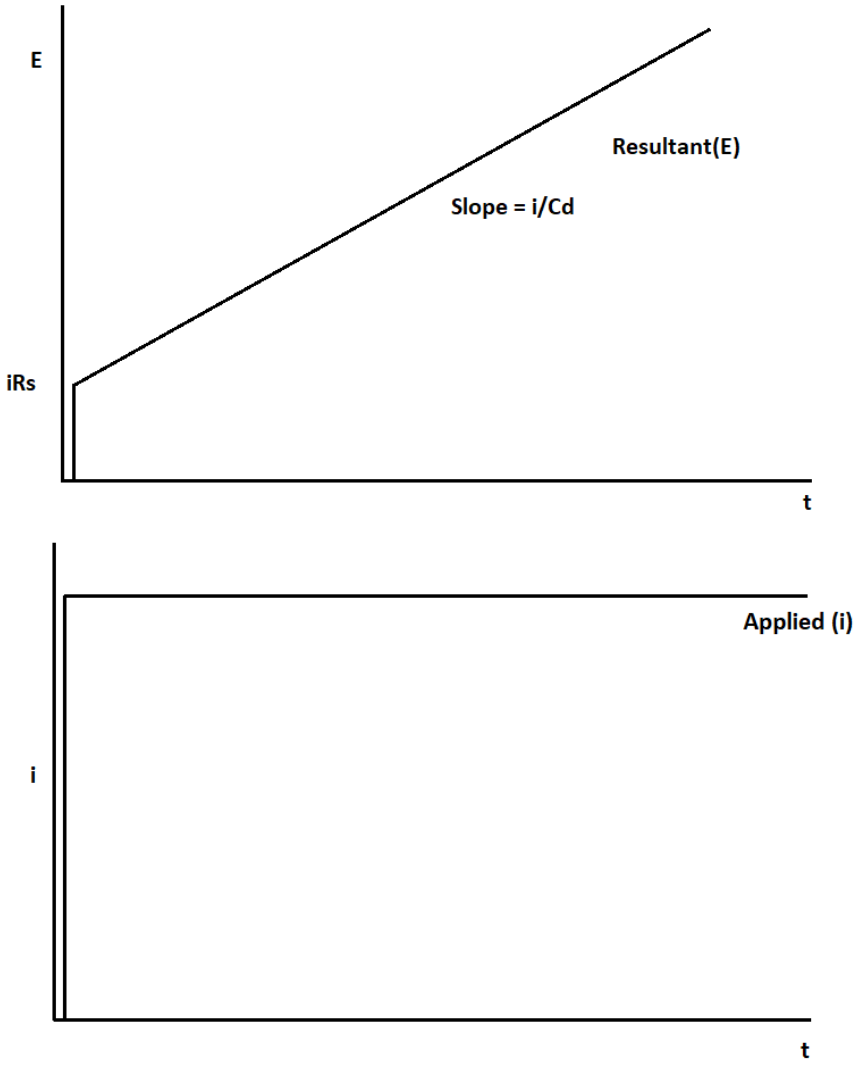

Figure 6.2 Potential-time kinetics resulting from a current step measurement.

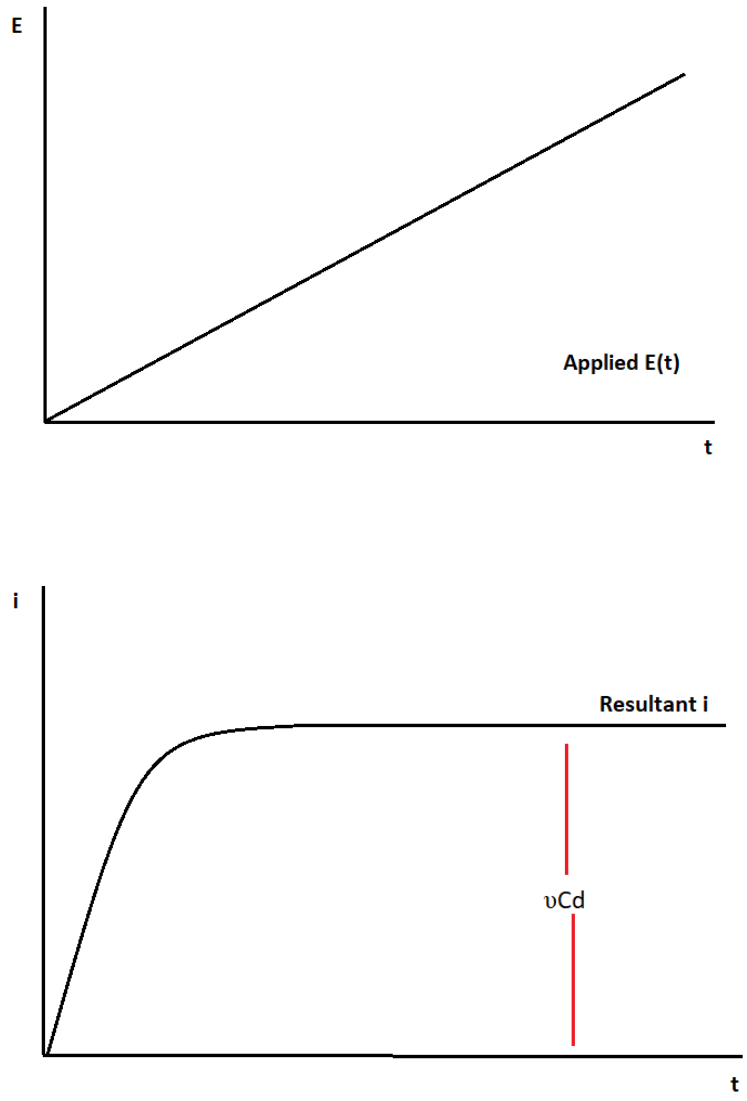

Figure 7.2 Current-time kinetics resulting from a linear voltage sweep applied to circuit.

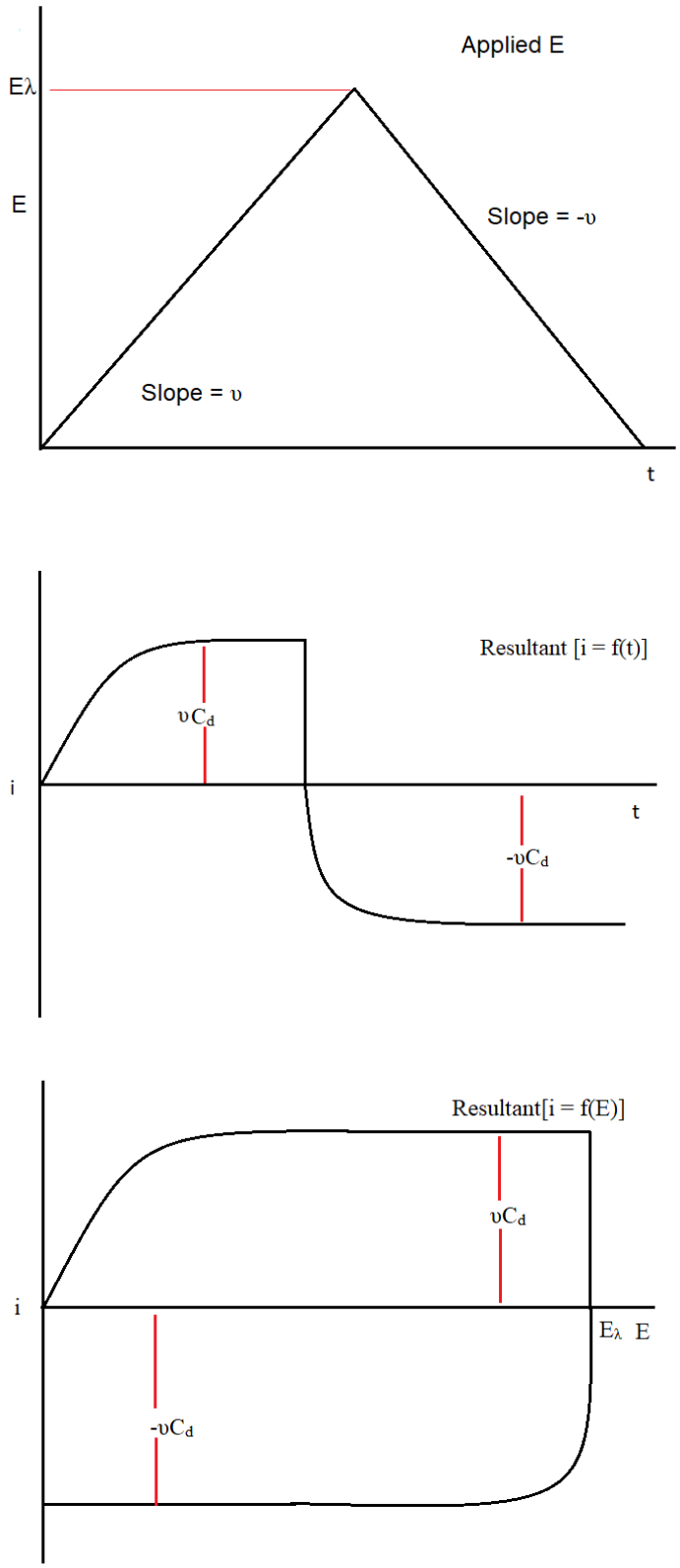

Figure 8.2 Current-time and current-potential plots which result from a cyclic linear potential sweep applied to RC circuit.

Figure 7.2 (a) describes a linear potential sweep which means potential increases with time linearly. When the potential is applied to the electrochemical circuit, the equation number 14 will be applied again and therefore

$$\upsilon t = Rs(dq/dt)+q/C_d \quad (25)$$

if q = 0 at t = 0

$$i = \upsilon C_d[1-\exp(-t/RsC_d)] \quad (26)$$

Then, the current increases from zero and gets a steady state value υC_d which can be seen in figure 7.2 (b). Therefore, the steady state current is used to evalute the double layer capacitance C_d. Figure 8.2 represents current -time and current potential resulting from a cyclic linear potential sweep which applied to the circuit.[12]

2.1.5. Galvanostatic (charge-discharge)

Galvanostatic measurement is an electrochemical technique which can measure the capacitance of active material, stability, and capacitance retention.

The specific capacitance can be calculated from galvanostatic (charge-discharge) data by using the following equation.

$$Cs = I\, dt/(m)\, dE \quad (27)$$

Where *I* is the current (A), *m* is the mass of active material (g). Figure 9.2 is an example charge -discharge cycle of an active material through galvanostatic methods.

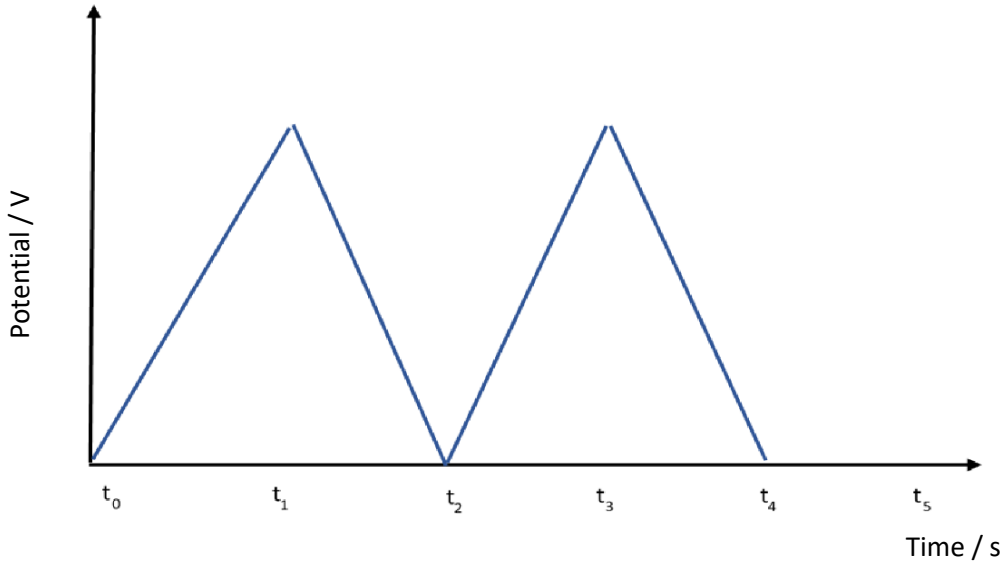

Figure 9.2 Galvanostatic (charge-discharge) cycle.

2.1.6. Electrochemical quartz crystal Microbalance (EQCM)

Electrochemical Quartz Crystal Microbalance (EQCM) is a powerful frequency control tool that can be used to deposit polymer materials on an electrode surface and monitor the changes of mass by the change in frequency that occurs on a quartz crystal oscillator. The data obtained consist of a cyclic voltammogram showing the oxidation / reduction cycles, and the change in frequency over time indicating deposition of mass on the electrode surface. The crystal is connected to two wire electrodes so that a film can be deposited on a working electrode which is usually gold or carbon according to figure 10.2 (a and b). Sauerbrey invented EQCM in 1959.[13] EQCM has been used to investigate polymer films. It also used in pharmaceutical industry to monitor the binding of proteins in drugs.

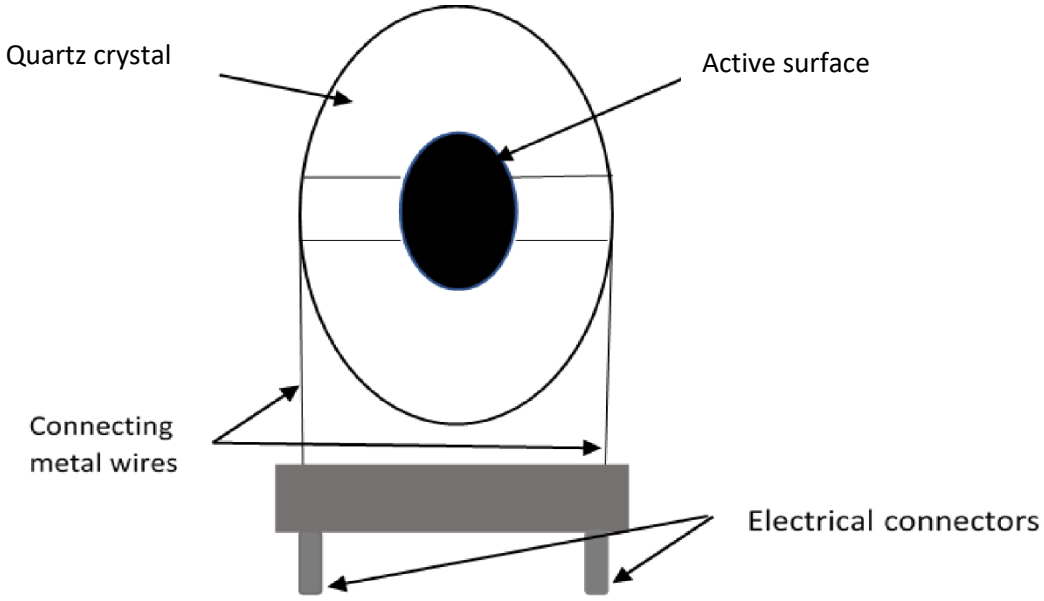

Figure 10.2 a) Quartz crystal electrode.

Figure 10.2 b) Photograph of a quartz crystal electrode.

The Sauerbrey equation is the relationship between the frequency change and the mass changes during the experiment, described by the following equation.

$$\Delta f = -C_f \cdot \frac{\Delta m}{A} \qquad (28)$$

Where Δf is the change in frequency (Hz), Cf is the sensitivity factor of the crystal (0.0815 Hz ng^{-1} cm^{-2}, Δm is the mass change per unit (ng cm^{-2}) and the negative sign means increasing the mass of polymer leads to a decrease in the frequency.[14]

2.1.7. Electrochemical impedance spectroscopy (EIS)

Electrochemical impedance spectroscopy is an advanced technique used to examine the electrochemical behaviours of active materials under non-equilibrium conditions and to analyse the behaviour of supercapacitor electrodes and describe charge transfer resistance and ion diffusion processes. This method is based on applying a small voltage to the electrochemical cell at various frequencies which help to not distribute the equilibrium state throughout the experiment. It is an alternating current technique, this prevents the system reaching equilibrium current because of the variation in voltage with frequency.[15] Recently, many researchers are interested in using impedance measurements. As an example of this, corrosion rates, biosensors, supercapacitors, fuel cells, batteries and organic coatings permittivity are all applications of EIS.[16]

Electrochemical impedance spectroscopy is a technique to measure the impedance electrochemically over a wide range of frequency. In EIS method, an alternating current excitation is applied to the experiment with a wide range of frequencies to measure the impedance. Figure 11.2 represents the sinusoidal waveform response in linear system which can be described by equation number 29. According to figure 11.2, there is constant time shift between potential and current waves which is named phase angle shift (Q). To keep the linear kinetics in the electrochemical impedance spectroscopy system, a small amplitude AC potential (5-10 mV) is usually applied.

$$E_{(t)} = E_{\circ} \sin\omega t \qquad (29)$$

Also $I = dQ/dt = \omega C E_{\circ} \cos\omega t$ (30)

Where $E(t)$ is the potential at time, E_0 is the amplitude of the signal, ω is the radial frequency, t is the time, I is the current, Q is the charge on capacitor C.

Therefore, the current is out of phase with the potential by 90 degrees in an ideal capacitor.

This can be explained by

$$Zc = j/\omega C \quad (31)$$

Where $j = \sqrt{-1}$ which is the imaginary unit.

$$I_t = I_{\circ}\sin(\omega t + Q) \quad (32)$$

Where is I_t is the single response of instantaneous current at the maximum amplitude.[17]

The current and potential are out of phase. [18]

The total impedance can be shown by

$$Z = ReZ_2 + ImZ_2 \quad (33)$$

Where Re is the real part of the impedance. *Im* is the imaginary part which shifts the phase and magnitude.[18a, 19]

$$|Z| = \sqrt{ReZ_2 ImZ_2} \quad (34)$$

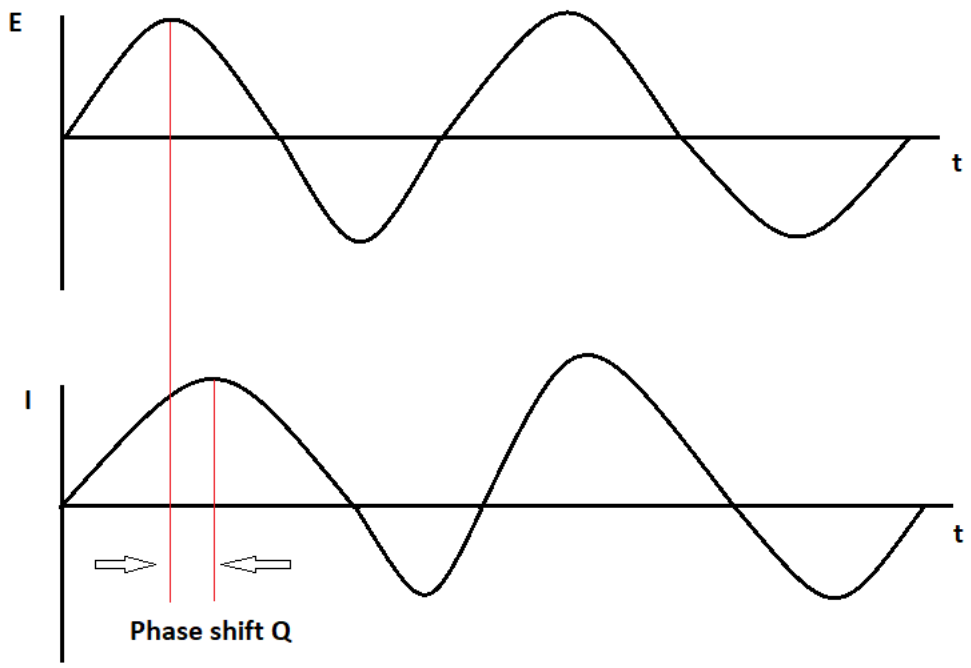

Figure 11.2 shows sinusoidal waveform response in linear system. It shows phase shift angle which used to explain the reactions at the interfaces electrochemically.

EIS results are shown in a Nyquist plot and a Bode plot. Nyquist plots display imaginary impedance (reactance) versus the real impedance (resistance) whereas the Bode plot indicates the relationship between the impedance and log of frequency, in this technique electrochemical circuits can be characterised by the Randles equivalent circuit. Universal circuit is another electrochemical circuit that can be used for carbon materials.[20] Figure 12.2 shows examples of universal and Randles circuits.

The universal circuit is usually used for carbon-based supercapacitors which can be applied for porous electrodes. Universal circuit can help to give a suitable resistance and capacitance values.[20] The Randles circuit is generally used as a simple circuit for electrochemical impedance spectroscopy to explain the behaviour electrochemically. The simplest Randles

circuit consists of solution resistance (R_s) and double layer capacitor (C_{dl}). Randles circuits can be connected in parallel or series.

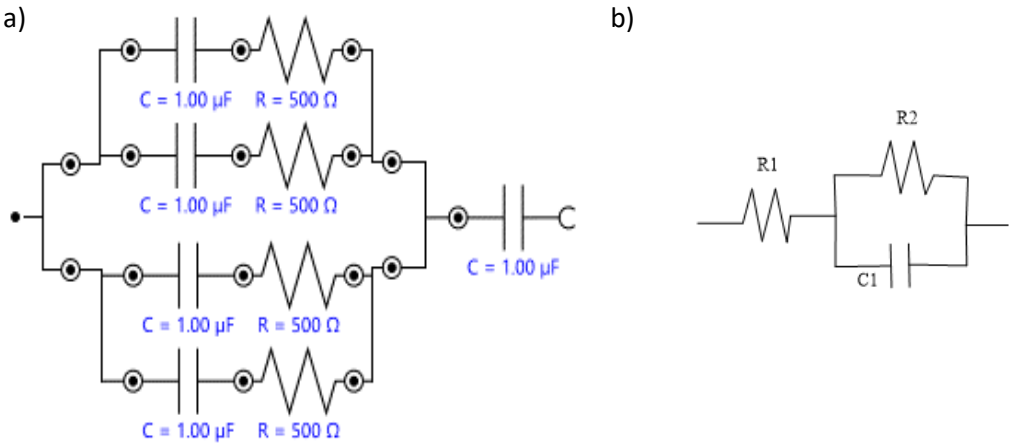

Figure 12.2 Example of universal circuit (a) and Randles circuit (b).

The counter electrode, such as platinum (wire or mesh) is usually used to measure and allow the current flow through the cell. In three electrode experiments, a reference electrode is used to maintain a well-defined and constant potential difference. In this thesis, all the impedance measurements presented were performed with a three-electrode set up.

EIS is a useful technique to investigate the kinetics of doping processes and ion diffusion into the polymer.[3]

2.1.7.1. Nyquist plots

The Nyquist plot shows the relationship between the imaginary impedance component and the real impedance at each excitation frequency. Figure 13.2 a) shows the semicircle of Nyquist plot and represents the maximum capacitance at the peak of the semicircle on the imaginary axis. Figure 13.2 b) represents an example of Randles circuit were R_1 is solution resistance, C_1 and R_2 are the capacitance and resistance of double layer capacitor respectively.

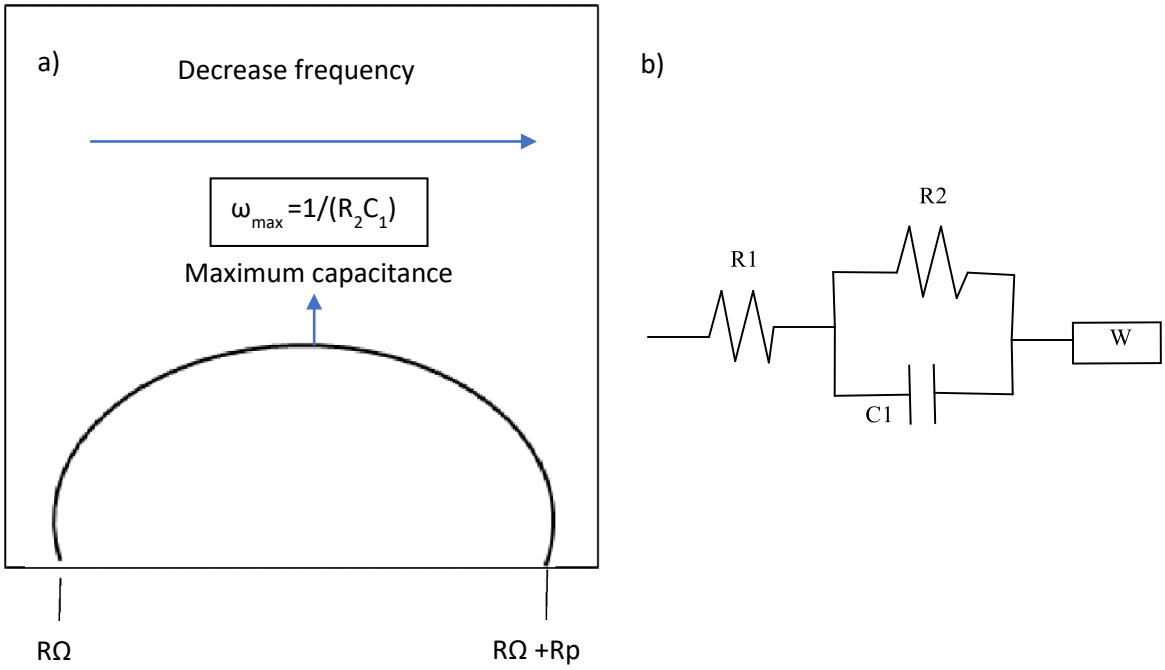

Figure 13.2 a) Shows Nyquist plot of a simple electrochemical impedance system.[3]

b) Electrical circuit which corresponding to the Nyquist plot.

2.1.7.2. The Bode and phase plots

The Bode plot is the relationship between absolute impedance and the change in frequencies which can be seen in figure 14.2 in the same way, the phase plot presents the relationship between the phase angle versus the change in frequency. An example phase plot is presented in figure 15.2.

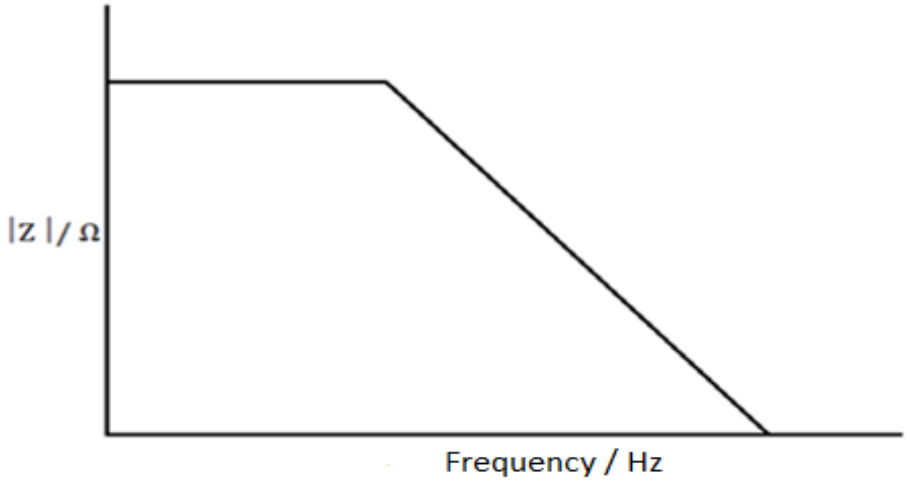

Figure 14.2 Example of Bode plot showing the association between $|Z|$ and frequency.

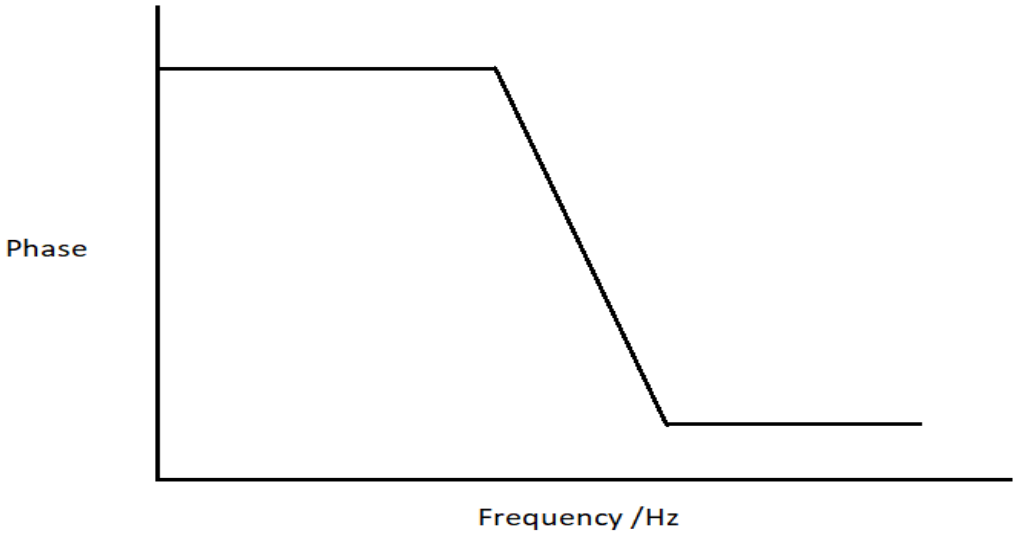

Figure 15.2 Example of a Phase plot showing the association between phase and frequency.

2.1.8. Impedance components

After measurement of electrochemical cell impedance components such as resistance of solution (R_Ω), capacitor of EDLCs (C_{dl}), resistance of EDLCs (R_{ct}) and Warburg impedance (W) are effective way to mimic the experiment behaviour and model the electrode. In addition, it is important to understand the current response of an electrochemical cell. There are many components to model the electrical circuit physically, such as capacitors, resistors, inductors. This research will explain specifically the component that used to model hybrid battery/supercapacitor application only which is capacitors, resistance, and Warburg impedance.

2.1.8.1. Capacitor

Capacitors are two electrodes separated by non-conductive material which enable charge to be stored. Capacitors are described by equation 35.

$$I = \frac{C\,dV}{dt} \qquad (35)$$

2.1.8.2. Resistance

There are some essential resistances that can be found in any type of supercapacitor, both electric double layer capacitors (EDLCs) or Faradaic capacitors, which are the resistance of the solution and the resistance of the capacitor. The resistor can be described by following equation.

$$R = \frac{V}{i} \qquad (36)$$

2.1.8.3. Warburg component (W)

This component is usually used to define the diffusion of electrolyte. For most electrochemical experiments, the reaction rate is limited by how fast a species can diffuse to the electrode surface. Warburg impedance is the component that can be used to model the ion diffusion process.

ω max, seen in the high frequency domain in the Nyquist plot, is calculated with the following equation.

$$\omega \text{ max} = 1/(R.C) \qquad (37)$$

Where $\omega\ max$ is the maximum capacitance which is usually chosen after fitting data in the high frequency domain (semicircle) in the Nyquist plot. R is the resistance and C is the capacitor value.

Modeling supercapacitors helps to estimate the performance of supercapacitors, and this leads to lower cost and shortens the time to fabricate supercapacitors. As an example of these models are the intelligent model, electrical double layer model, porous electrode model and equivalent circuit model.[21] In this work, we focused on the equivalent circuit model, which is an essential model to analyze Nyquist, Bode and phase plots for the impedance of hybrid battery supercapacitor device.

Experimental section

All synthetic experiments were performed under dry nitrogen or argon using schlenk line techniques. Anhydrous solvents were dried by refluxing the solvent and collected by distillation. The solvents were degassed by using nitrogen gas.

2.2. Materials

All chemicals were purchased from Sigma Aldrich (Gillingham, UK). Carbon fibre and the chemicals were used without any further purification. Glassy carbon electrodes were polished using 3µm then 1µm polycrystalline diamond suspensions, followed by 0.3 µm alumina. The counter electrode was platinum (Pt) and the reference electrode silver (Ag) in a three electrode experiment. Synthesis of anthraquione-2-diazonium chloride -was done by using Milner method-[22]. $[^{n}Bu_4N][B(C_6F_5)_4]$ electrolyte ($BarF_{20}$), N-pyrrolyl borane and polyoxometalates where synthesised by members of Wildgoose or Fielden groups using published methods.[23] [24]

2.3. Instruments

Scanning electron microscope (SEM)	Jeol JSM5900LV SEM-EDS.
Elemental analysis	Carlo Erba Flash 2000 Elemental Analyser.
Transmission Electron Microscope (TEM)	Philips CM200 FEGTEM fitted with a Gatan SC200 Orius CCD camera and an Oxford Instruments 80 mm^2 EDX SDD running Aztec software.
XPS	VG ESC Alab 250 with a monochromated Al Kα source.
UV-Vis spectroscopy	Agilent Cary 60 UV-vis spectrophotometer.
FT-IR spectroscopy	Perkin Elmer FT-IR spectrum BX and Bruker FT-IR XSA spectrometers.

2.4. Assembly of hybrid battery/supercapacitor

Fibre supercapacitors were assembled from modified carbon fabric electrodes with a non-conductive separator between them. The electrolytes used were organic solutions of $[^{n}Bu_4N][B(C_6F_5)_4]$ ($BarF_{20}$),$[^{n}Bu_4N]BF_4$, and $[^{n}Bu_4N]PF_6$. These two fabric electrodes are sealed. Figure 16.2 shows the structure of Fabric supercapacitor.

Figure 16.2 Fabric supercapacitor with separator between them.

2.5. References

[1] P. Alotto, M. Guarnieri, F. Moro, *Renewable and Sustainable Energy Reviews* **2014**, *29*, 325-335.
[2] R. G. Compton, C. E. Banks, *Understanding voltammetry*, *World Scientific*, **2018**.
[3] T. B. Reddy, *Linden's handbook of batteries, Vol. 4*, Mcgraw-hill New York, **2011**.
[4] N. Elgrishi, K. J. Rountree, B. D. McCarthy, E. S. Rountree, T. T. Eisenhart, J. L. Dempsey, *Journal of Chemical Education* **2018**, *95*, 197-206.
[5] K. Ngamchuea, S. Eloul, K. Tschulik, R. G. Compton, *Journal of Solid State Electrochemistry* **2014**, *18*, 3251-3257.
[6] G. Instruments, *G. Instruments, Complex impedance in Corrosion* **2007**, 1-30.
[7] M. Lovrić, Š. Komorsky-Lovric, *Journal of Electroanalytical Chemistry and Interfacial Electrochemistry* **1988**, *248*, 239-253.
[8] K. Brainina, E. Neyman, *Electroanalytical Stripping Methods, Vol. 185*, John Wiley & Sons, **1994**.
[9] P. Zanello, C. Nervi, F. F. De Biani, *Inorganic electrochemistry: theory, practice and application*, *Royal Society of Chemistry*, **2019**.
[10] H. Shayani-jam, *Monatshefte für Chemie-Chemical Monthly* **2019**, *150*, 183-192.
[11] F. Cottrell, *Z. phys. Chem* **1903**, *42*, 385-431.
[12] A. J. Bard, L. R. Faulkner, H. S. White, *Electrochemical methods: fundamentals and applications*, John Wiley & Sons, **2022**.
[13] L. M. Furtado, H. Su, M. Thompson, D. P. Mack, G. L. Hayward, *Analytical Chemistry* **1999**, *71*, 1167-1175.
[14] Q. Zhang, M. D. Levi, Y. Chai, X. Zhang, D. Xiao, Q. Dou, P. Ma, H. Ji, X. Yan, *Small Methods* **2019**, *3*, 1900246.
[15] S.-I. Pyun, H.-C. Shin, J.-W. Lee, J.-Y. Go, *Electrochemistry of insertion materials for hydrogen and lithium*, *Springer Science & Business Media*, **2012**.
[16] aM. Grossi, B. Riccò, *Journal of Sensors and Sensor Systems* **2017**, *6*, 303-325; bT. J. Freeborn, B. Maundy, A. S. Elwakil, *Materials for Renewable and Sustainable Energy* **2015**, *4*, 1-7; cS. M. Lukic, J. Cao, R. C. Bansal, F. Rodriguez, A. Emadi, *IEEE Transactions on Industrial Electronics* **2008**, *55*, 2258-2267.
[17] H. H. Hernández, A. M. R. Reynoso, J. C. T. González, C. O. G. Morán, J. G. M. Hernández, A. M. Ruiz, J. M. Hernández, R. O. Cruz, *Electrochemical Impedance Spectroscopy* **2020**, 137-144.
[18] aK. S. Cole, R. H. Cole, *The Journal of Chemical Physics* **1941**, *9*, 341-351; bJ. T. Irvine, D. C. Sinclair, A. R. West, *Advanced Materials* **1990**, *2*, 132-138; cY. Yuan, S. Adeloju, G. Wallace, *European PolymerJournal* **1999**, *35*, 1761-1772.
[19] B. E. Conway, *Electrochemical supercapacitors: scientific fundamentals and technological applications*, *Springer Science & Business Media*, **2013**.
[20] S. Fletcher, V. J. Black, I. Kirkpatrick, *Journal of Solid State Electrochemistry* **2014**, *18*, 1377-1387.
[21] R. Niu, H. Yang, in *2011 IEEE International Conference on Robotics and Automation*, IEEE, **2011**, pp. 1-4.
[22] S. Ernst, L. Aldous, R. G. Compton, *Chemical Physics Letters* **2011**, *511*, 461-465.
[23] E. J. Lawrence, V. S. Oganesyan, G. G. Wildgoose, A. E. Ashley, *Dalton Transactions* **2013**, *42*, 782-789.
[24] E. Lawrence, PhD thesis, University of East Anglia **2015**.

Chapter 3

Modification of carbon electrodes using anthraquinone with lithium ions for a hybrid battery /supercapacitor

3.Aim

In this chapter we develop hybrid battery /supercapacitors based on anthraquinone/lithium for use in hybrid-diffusional battery devices. The investigation was carried out by electrochemical methods including cyclic voltammetry, electrochemical impedance spectroscopy (EIS), galvanostatic (charge-discharge technique) and electrochemical quartz crystal microbalance (EQCM).

3.1. Introduction

The initial development of lithium ion batteries occurred between 1970 and 1990.[1] They are now used in many electronic devices, such as laptops and cell phones, solar and electric vehicles because of many positive points including high columbic efficiency, high energy density, and low self-discharge.[2] Although automotive LiBs have some issues due to the large serial parallel numbers, and expense, LiBs still have excellent capacity.[3] Figure 1.3 shows a typical lithium-ion battery.[4]

These days, carbon materials which contain oxygen functional groups can be used as cathodic electrodes for lithium-ion batteries. The reaction between the oxygen functional groups of carbon materials and lithium ions is important for lithium storage and the electrode cycle life.[5] The main cathodic materials used in commercial lithium ion batteries are inorganic metal oxides, such as lithium cobalt oxide and lithium nickel manganese cobalt oxide.[6] However, using metal oxides as cathodes for the LiB gives rise to high energy costs in production and

recycling, and also threatens the environment through mining.[6b] By comparison, using molecular redox materials instead of redox active metals is inexpensive, non-toxic and environmentally friendly. Graphite is already commonly used as an anodic material in lithium ion batteries because of some advantages, such as low cost, excellent cycle life and its structure which leads to intercalated lithium ion through the layers.[7] Therefore, in this work, we developed a new cathode by modification of carbon electrode with anthraquinone. Anthraquinone as mentioned in chapter 1 has become interesting to enhance the capacity of materials because the combination of anthraquinone with carbon material for example will combine two kinds of capacitance (electric double layer capacitance and faradaic capacitance). The combination of anthraquinone with lithium was studied by different electrochemical methods. The hybrid battery /supercapacitor combines high capacitance with excellent life cycle stability.

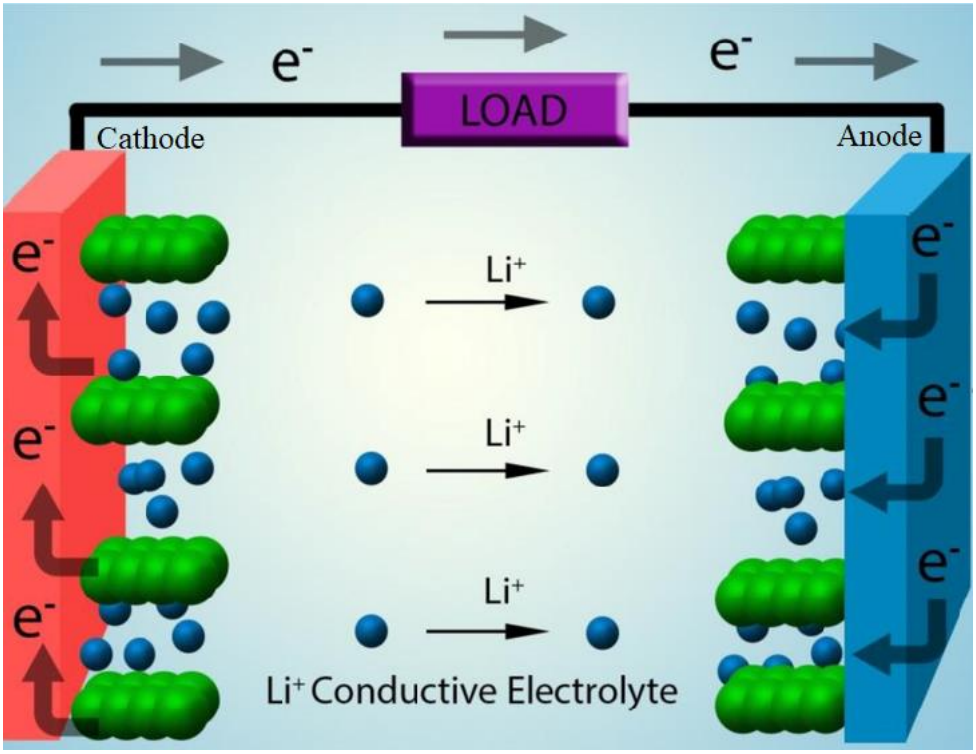

Figure 1.3 A typical lithium-ion battery, Figure reproduced with permission from reference [4].

3.2. Experimental section

Anthraquinone-2-diazonium chloride was synthesized following the Milner method.[8] All chemicals were purchased from Sigma Aldrich (Gillingham, UK). Carbon fibre (Plain weave) (CF) and the chemicals were used without any further purification. Glassy Carbon electrodes were polished using polycrystalline Diamond suspension 3µm and 1µm respectively, and subsequently by alumina 0.3 µm. The counter electrode was platinum (Pt) and silver (Ag) was used as a reference electrode. The experiments were performed using a GC electrode or CF electrode immersed in dry solvent (acetonitrile with 0.05 M of $[^{n}Bu_4N]PF_6$ electrolyte and 2 mmol of anthraquinone-2-diazonium chloride). Acetonitrile was dried by reflux over CaH_2 and collected by distillation. The electrolyte tetrabutylammonium hexafluorophosphate ($[^{n}Bu_4N]PF_6$) was used as purchased for all experiments. The modification of the working electrode was performed under nitrogen and Schlenk line by using chronoamperometry or multicycle voltammetric scans.

3.3. Results and Discussion

3.3.1. Electrochemical characterisation of anthraquinone in solution

Figure 2.3 shows anthraquinone's electrochemical behaviour at different scan rates. According to figure 2.3, two redox waves of anthraquinone are seen at low scan rate and at high scan rate.

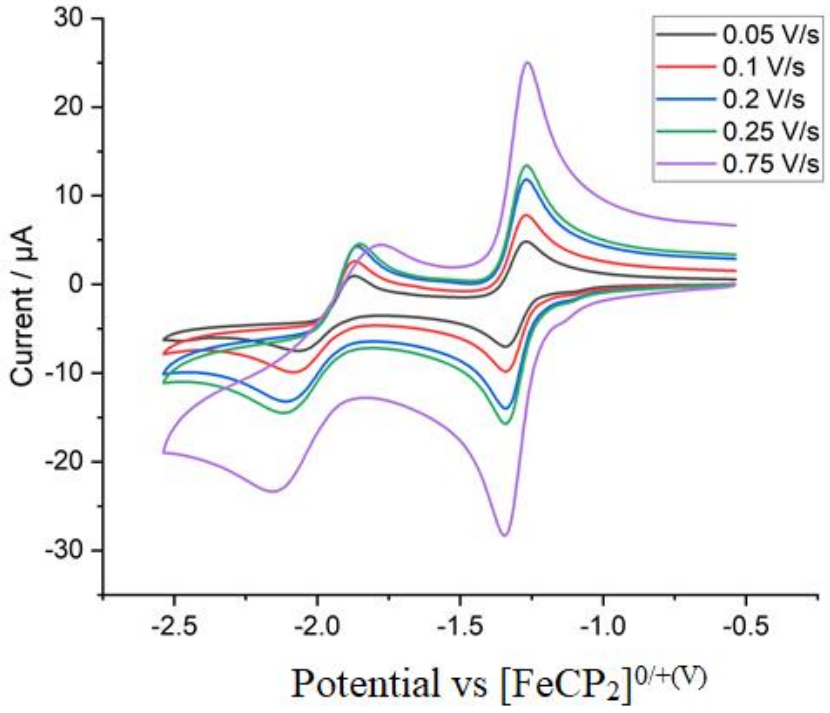

Figure 2.3 Anthraquinone in 0.05 M $[^{n}Bu_4N]PF_6$,CH_3CN at different scan rates (0.05, 0.1, 0.2,0.25 ,0.75 V/s).

3.3.2. Variable Scan Rate Cyclic Voltammetry (VSR-CV) of Anthraquinone with Lithium

Figure 3.3 shows the typical redox waves of anthraquinone affected by addition of lithium ions that leads to change the shape of the oxidative wave and disappearance of the second reduction wave. The oxidative peak increased after each addition of lithium ions.

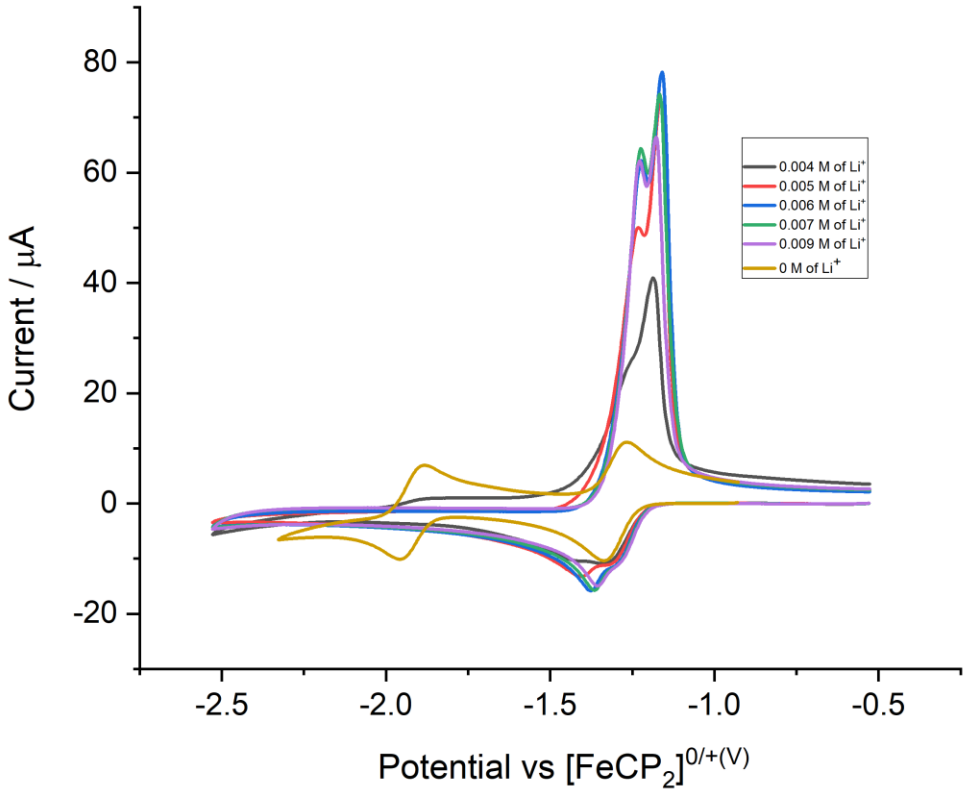

Figure 3.3 The effect of lithium ions on the redox waves of anthraquinone at 100 mV/s using 0.05 M of $[^{n}Bu_4N]PF_6$,CH_3CN as supporting electrolyte, at various Li^+ concentration (0 M, 0.004M, 0.005M, 0.006M, 0.007M, 0.009 M)

To explain figure 3.3, ion pairing of the anthraquinone radical anion with Li^+ shifts the second reduction to more positive potential (*ca.* -1.3 V instead of -1.9 V). This gives the sharp peak after the initial wave that stays in more or less the same place. This likely results from ion pairing or coordination of AQ^- with Li^+, similar to the protonation described in chapter 1 figure 13.1. Some of the ion paired material deposits on the cathode and continues getting reduced

(producing the extra current between -1.5 and -1.8 V compared to no Li). The sharp positive peak on re-oxidation (*ca.* -1.25 V) results from de-insertion of Li^+ as the deposited AQ^{2-} on the electrode surface is reoxidised.[9]

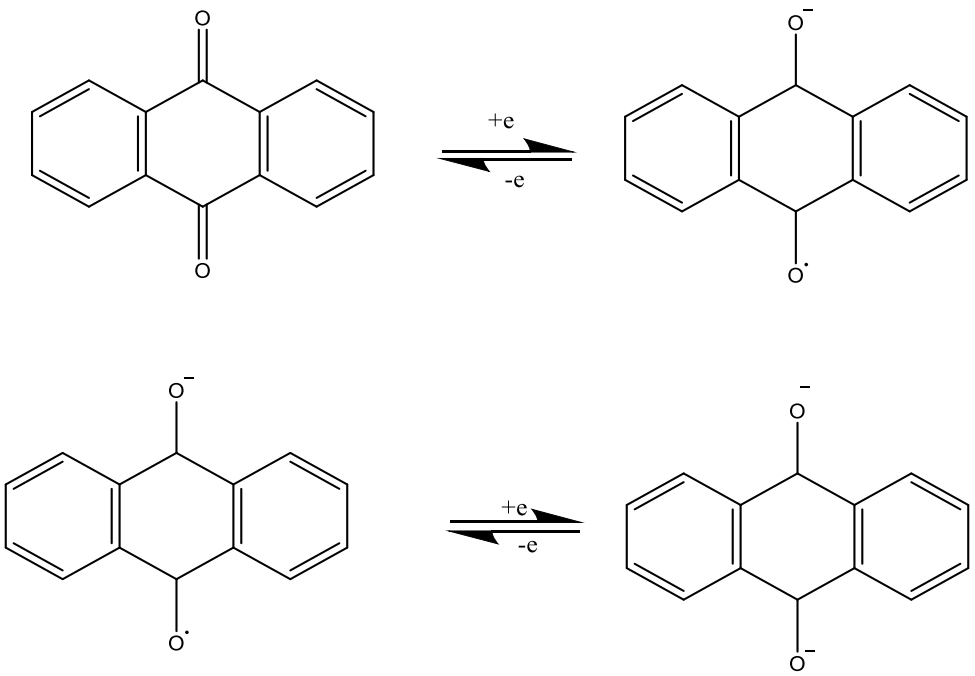

Figure 4.3 Redox of anthraquinone showed radical anions and dianion of AQ.

Figure 4.3 shows the redox processes of the anthraquinone radical anion and dianion. According to Figure 4.3, the reduction mechanism of anthraquinone has two steps which therefore generate two redox waves. The first step appears reversible on the timescale of a typical cyclic voltammetry scan, but produces the semiquinone radical anion which is unstable over longer periods of time. This is the first process observed at $E_{1/2}$ = -0.7 V. The second step at $E_{1/2}$ = -1.4 V produces the quinone dianion.

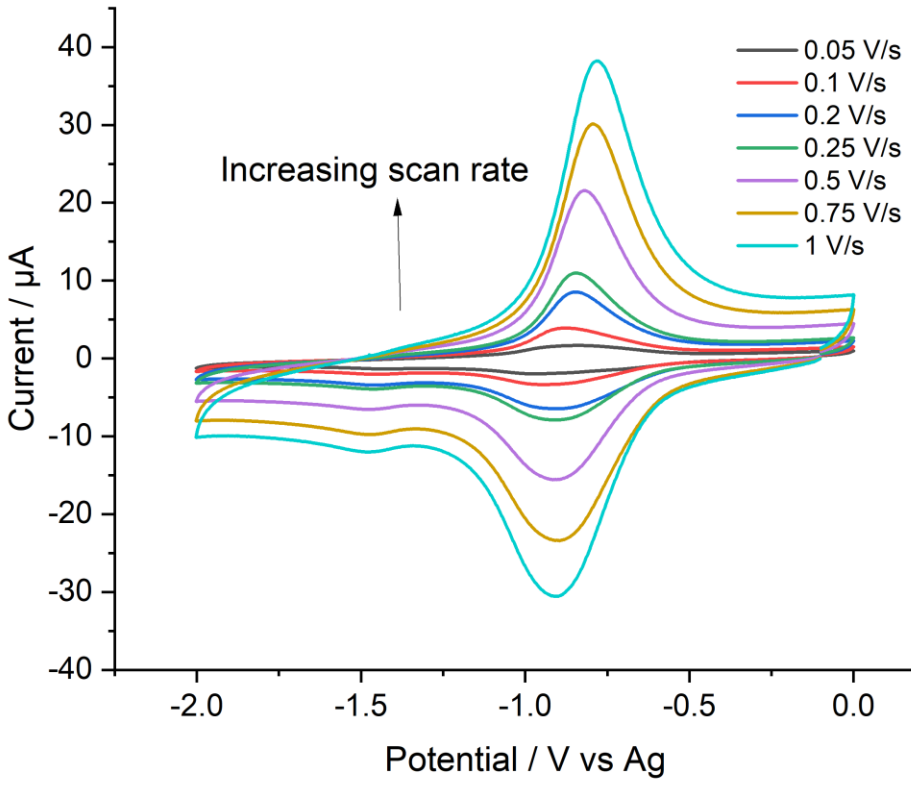

Figure 5.3 Cyclic voltammetry of anthraquinone modified on the surface of GCE using 0.05M of $[^{n}Bu_4N]PF_6$ in CH_3CN at (0.05, 0.1, 0.2, 0.25, 0.5, 0.75,1 V/s), it is not IR compensated.

Figure 5.3 shows cyclic voltammetry of anthraquinone modified GCE at various scan rates from 0.05 V to 1 V/s with 0.05 M $[^{n}Bu_4N]PF_6$ in CH_3CN. At 0.1 V/s the redox wave of anthraquinone appears very clearly whereas at 0.05 V/s it almost disappears,[10] and the shape of the redox peak changes with scan rate, similar to observations in other studies.[11] The separation of the forward and reverse redox peaks between -0.75 and -1.0 V is very small (ΔE = 15 mV, IR uncompensated), suggesting a surface confined process (ideal ΔE = 0 mV). The main peak is broad (for example at 0.1 V/s the width at half height is 0.35 V and at 0.25 V/s it is 0.3 V) too wide for an ideal 1 electron or 2 electron process, suggesting that there could be a range of different surface attached AQ states (for example some covalently bound, and some

physisorbed) rather than a perfect monolayer and also that the second reduction process could start to appear under the main peak. The continued reduction current and weak peak beyond -1.25 V is similar to the observations in the presence of Li^+ where material deposits on the electrode, and implies the second reduction process is spread over a wide potential range. Also, Figure 2.3 shows that in the solution voltammetry, the peak separation of the second reduction of AQ changes a lot with increased scan rate, suggesting a relatively slow electron transfer that may change with chemical attachment to electrode.

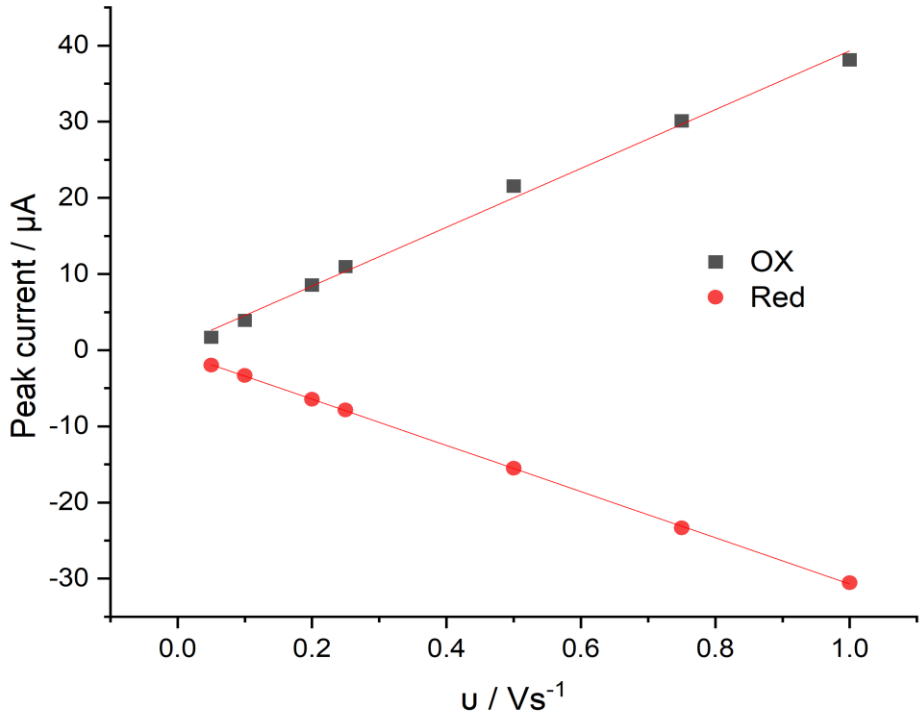

Figure 6.3 Peak current vs. scan rate for the reduction/oxidation of anthraquinone.The peak currents are linearly dependent on scan rate.

The dependence of the peak current vs the scan rate for the reductive and oxidative processes of the AQ modified electrode, based on the data from Figure 5.3, are shown in Figure 6.3. The

linear dependence on scan rate, rather than square root of scan rate, confirms that this is a surface confined process.

3.3.3. Modification of anthraquinone

Figure 7.3 a) shows the reduction of anthraquinone-2-diazonium chloride in a multicycle voltammetric scan. 20 cycles were used to deposit anthraquinone on the surface of the carbon electrode. It can be seen that the capacitance of the anthraquinone functionalised electrode increases with the number of cycles. The current peak of diazonium ion reduction can be seen at about -1.6 V for the glassy carbon electrode with 0.05 M of $[^{n}Bu_4N]PF_6$ in acetonitrile electrolyte. This is constent to research by Marko Kullapere *et al.* when they grafted anthraquione on glassy carbon electrode using in situ generated 9,10-anthraquinone-2-diazonium cations in 0.1 M of tetrabutylammonium tetrafluoroborate in acetonitrile. They found the peak current of the reduction of diazonium ions at 0.28 V and 0.17 V.[10] Figure 7.3 b) shows 20 cycles of the redox waves of anthraquione with 0.1 M of $[^{n}Bu_4N]PF_6$ in acetonitrile at 100 mV/s. Figure 8.3 shows the reduction of anthraquinone-2- diazonium chloride to modify a glassy carbon electrode.

a)

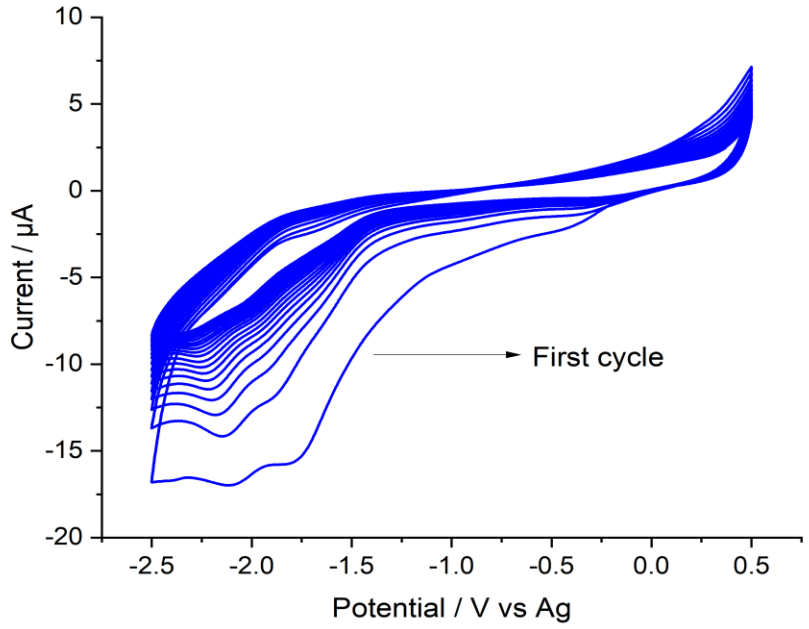

b)

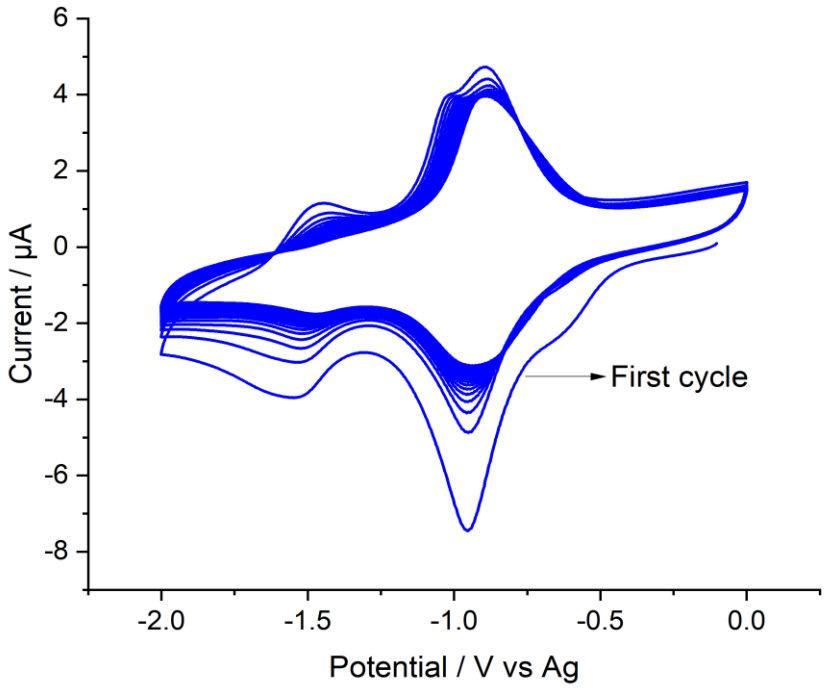

Figure 7.3 a) Reduction of anthraquinone-2-diazonium chloride by cyclic voltammetry with $[^{n}Bu_4N]PF_6$ in acetonitrile at 100 mV/s. **Figure 7.3 b)** 20 Cycles of the redox waves of anthraquinone with $[^{n}Bu_4N]PF_6$ in acetonitrile at 100 mV/s**.**

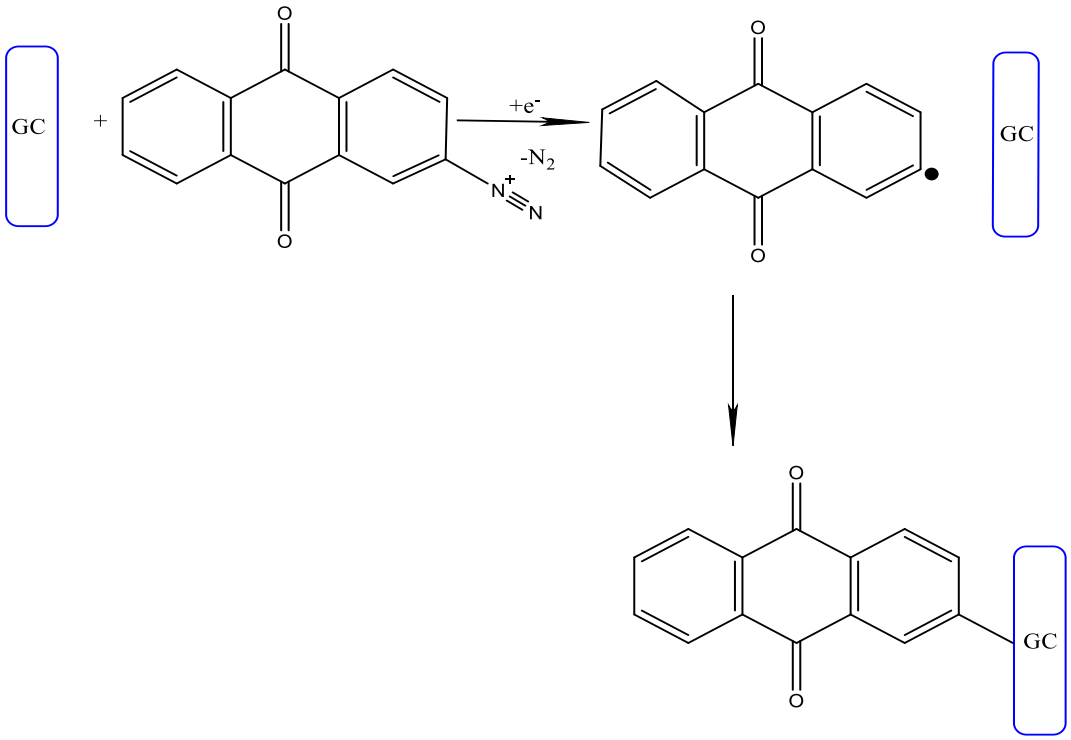

Figure 8.3 The reduction of anthraquinone-2- diazonium chloride to modify a glassy carbon electrode.

Figure 7.3 a) shows the reduction of anthraquinone-2-diazonium chloride in a multicycle voltammetric scan. 20 cycles were used to deposit anthraquinone on the surface of the carbon electrode. It can be seen that the capacitance of the anthraquinone functionalised electrode increases with the number of cycles. The current peak of diazonium ion reduction can be seen at about -1.6 V for the glassy carbon electrode with 0.05 M of $[^{n}Bu_4N]PF_6$ in acetonitrile electrolyte. This is constent to research by Marko Kullapere *et al.* when they grafted anthraquione on glassy carbon electrode using in situ generated 9,10-anthraquinone-2-diazonium cations in 0.1 M of tetrabutylammonium tetrafluoroborate in acetonitrile. They found the peak current of the reduction of diazonium ions at 0.28 V and 0.17 V.[10]

Figure 7.3 b) shows 20 redox cycles of the anthraquinone film. The experiment was recorded in acetonitrile with $[^{n}Bu_4N]PF_6$ and 20 cycles run to make sure anthraquinone layers are stable. According to figure 7.3 b) the electrografting of anthraquinone occurred which means anthraquinone reacted with the surface of glassy carbon electrode and formed a strong bond on the surface of carbon electrode. As a result, monolayers of anthraquinone can be covalently grafted on the carbon electrode. This strategy is called chemisorption.[12] Figure 8.3 shows the mechanism of the reduction of anthraquinone -2-diazonium chloride which can modify glassy carbon electrode. Therefore, anthraquinone can enhance the properites of carbon electrode because of faradaic contribution to the double layer capacitance.[13]

3.3.4. Titration of AQ-Li

The surface-immobilized anthraquinone was titrated with Li^+ and cyclic voltammograms measured over a voltage range from -2 to 1.5 V (Figure 9.3). The first CV shows the adsorbed anthraquinone (synthesized in Figure 7.3) with no Li^+, and redox processes between -1.0 and -2.0 V. Then, after adding Lithium ions and running the cyclic voltammetry again the redox process were shifted to more positive potential (+0.3 to -0.8 V). After each CV, EIS was applied.

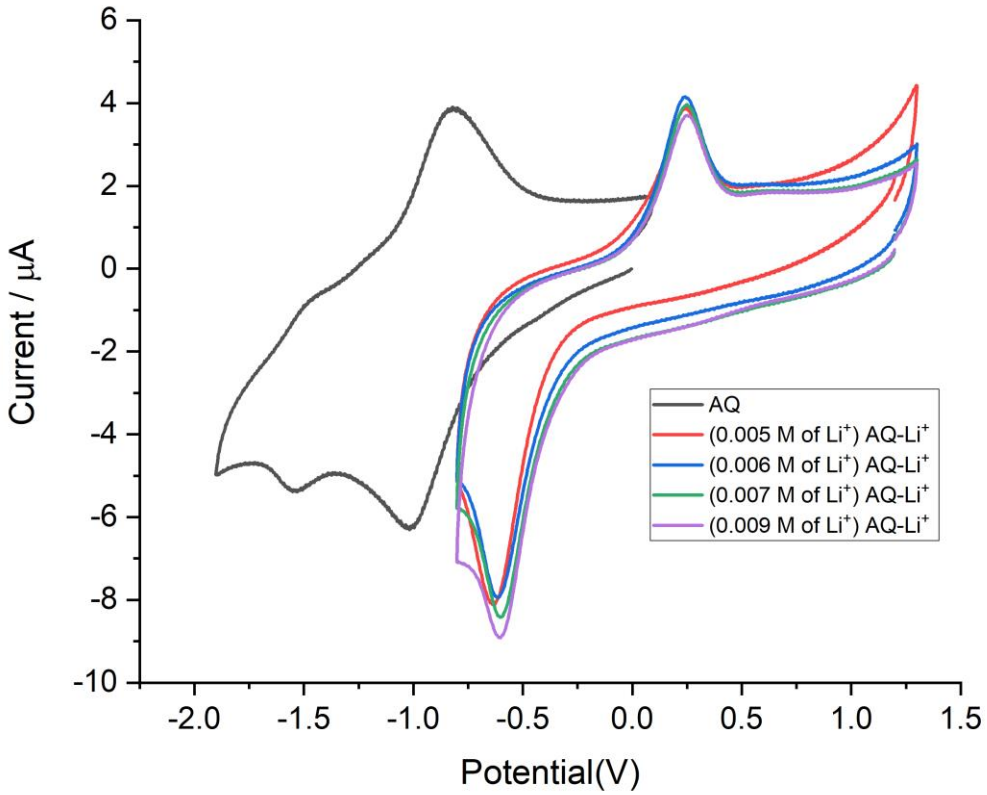

Figure 9.3 Shows redox behaviour of surface-adsorbed anthraquinone at negative potential, (at 100 mV/s, with 0.05 M of $[^nBu_4N]PF_6$, CH_3CN) and the effect of lithium ions which shifted the redox potential to more positive values.

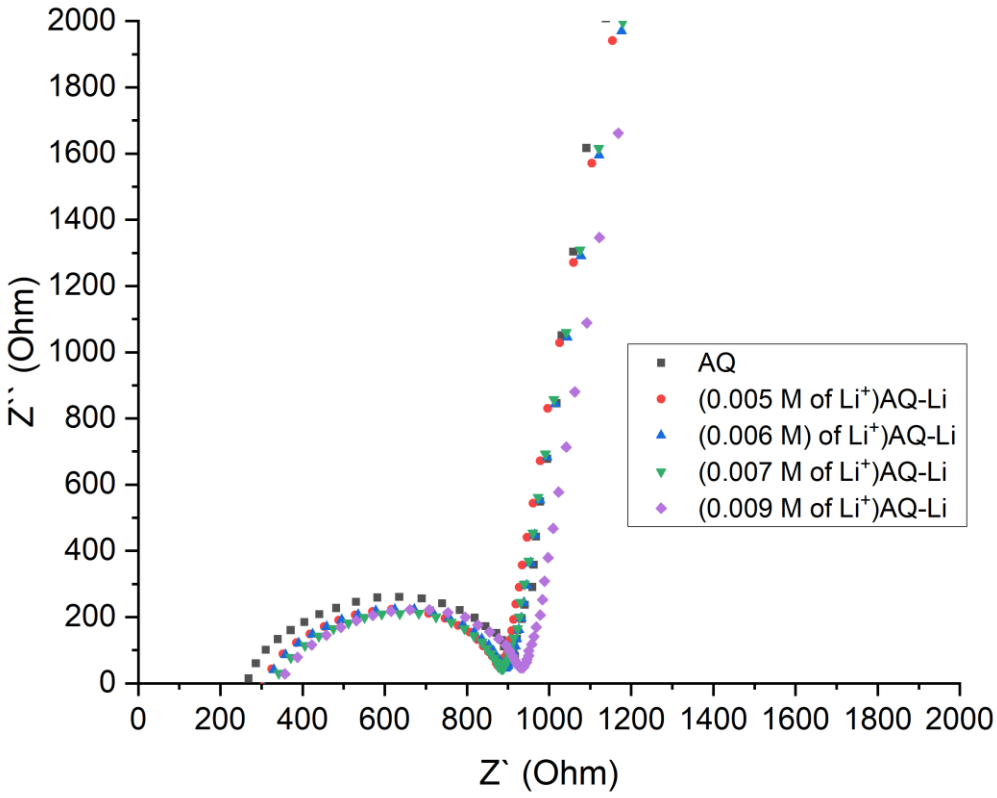

Figure 10.3 Nyquist plot of anthraquinone-modified electrode in presence and absence of Li^+ at of Li^+ (0.005M), (0.006M), (0.0.007M) and (0.009M).

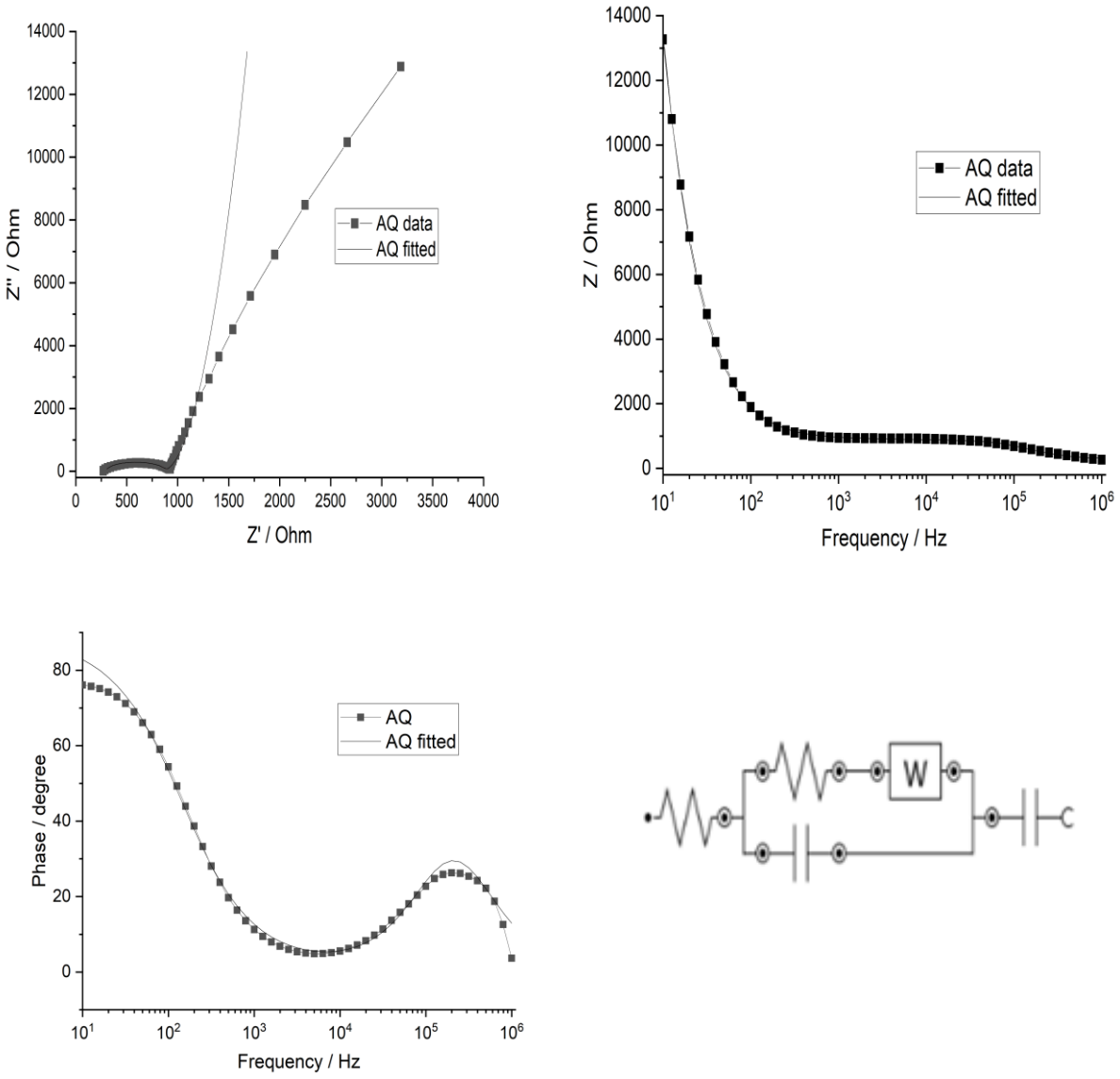

Figure 11.3 EIS of anthraquinone, 0.05M of $[^{n}Bu_4N]PF_6$, CH_3CN.

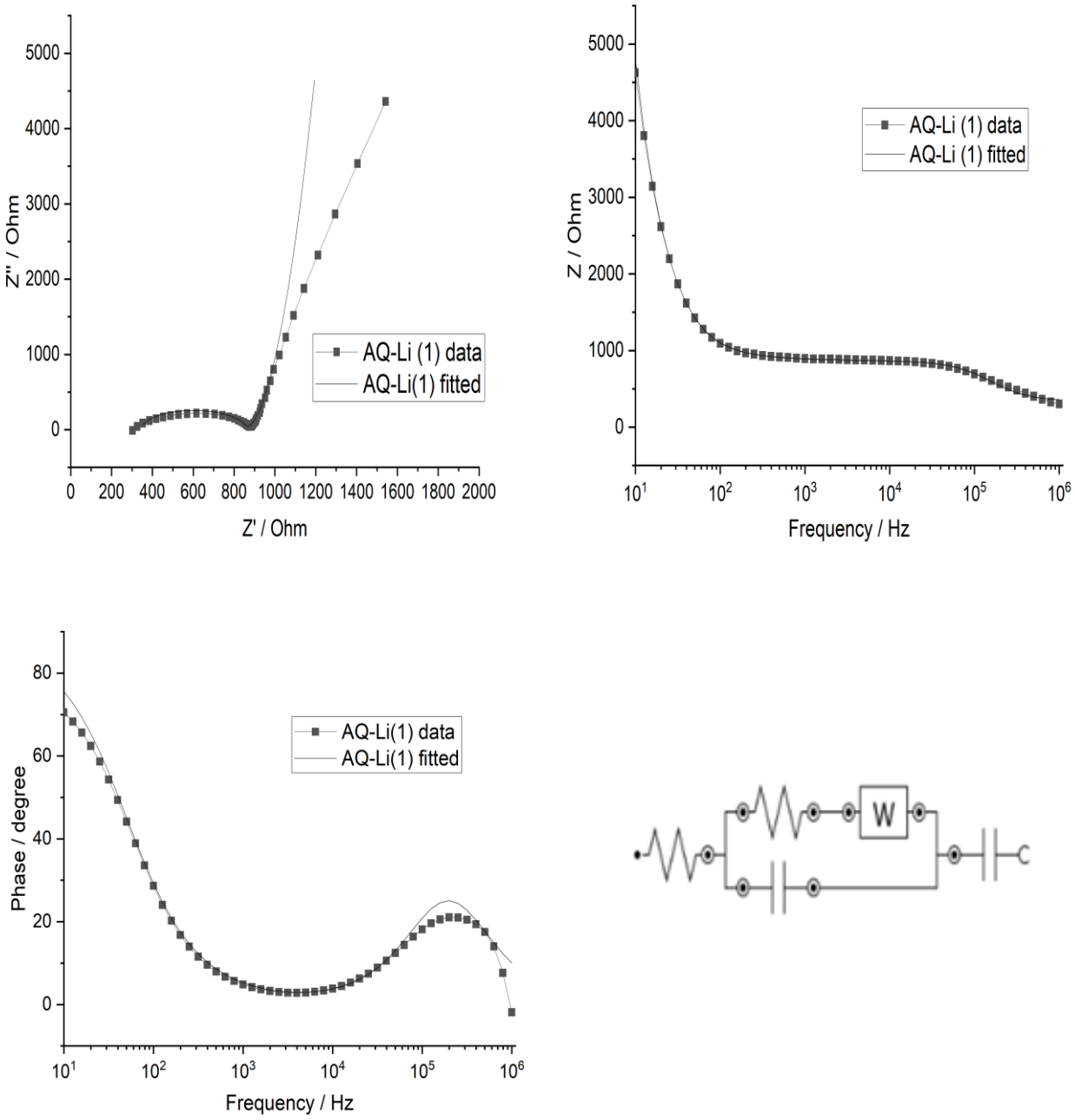

Figure 12.3 EIS of AQ-Li^+, addition of (0.007 M) Li^+, 0.05M of $[^nBu_4N]PF_6$, CH_3CN.

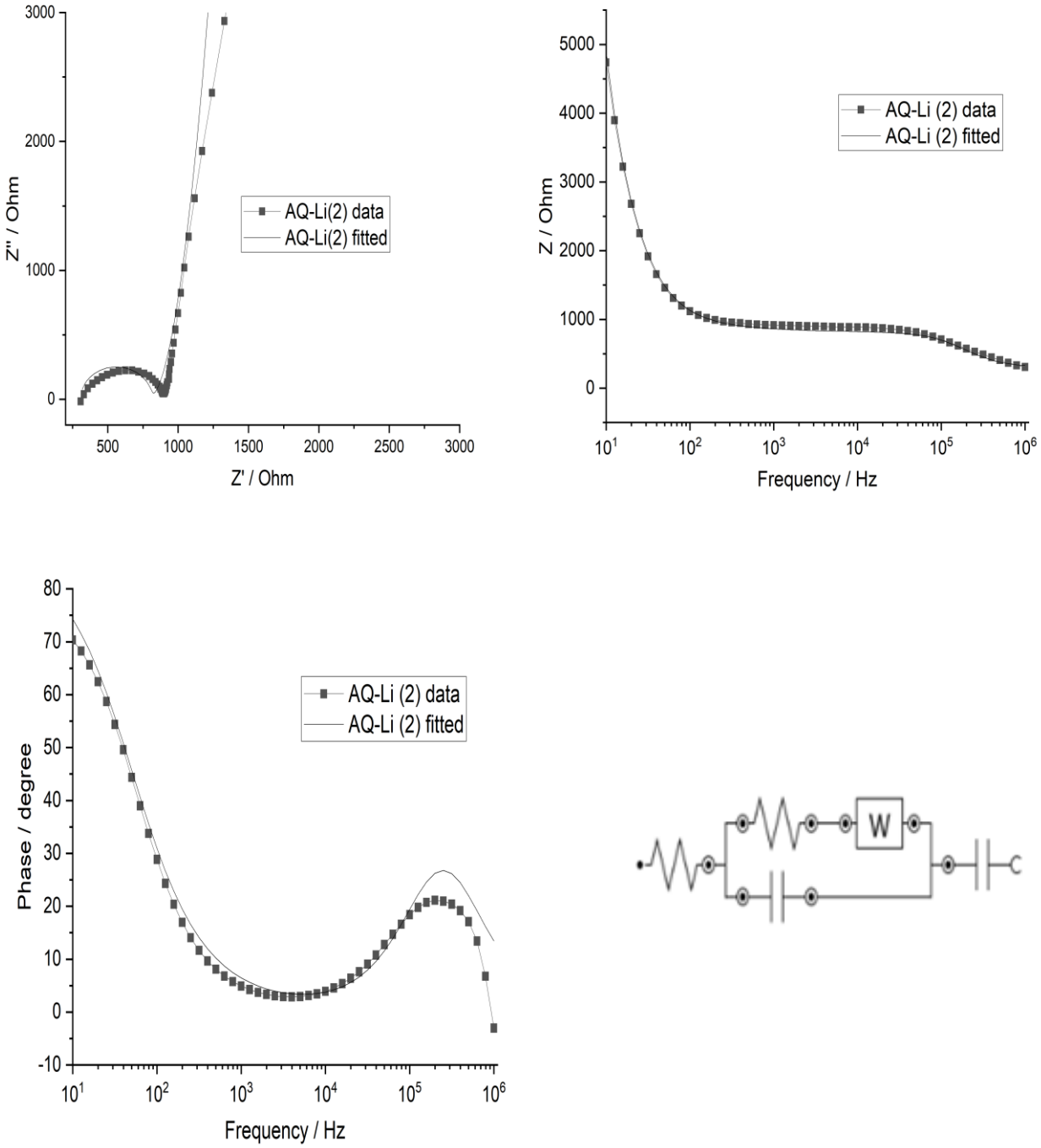

Figure 13.3 EIS of AQ-Li^+, after addition of (0.006 M) Li^+, 0.05 M $[^nBu_4N]PF_6$, CH_3CN.

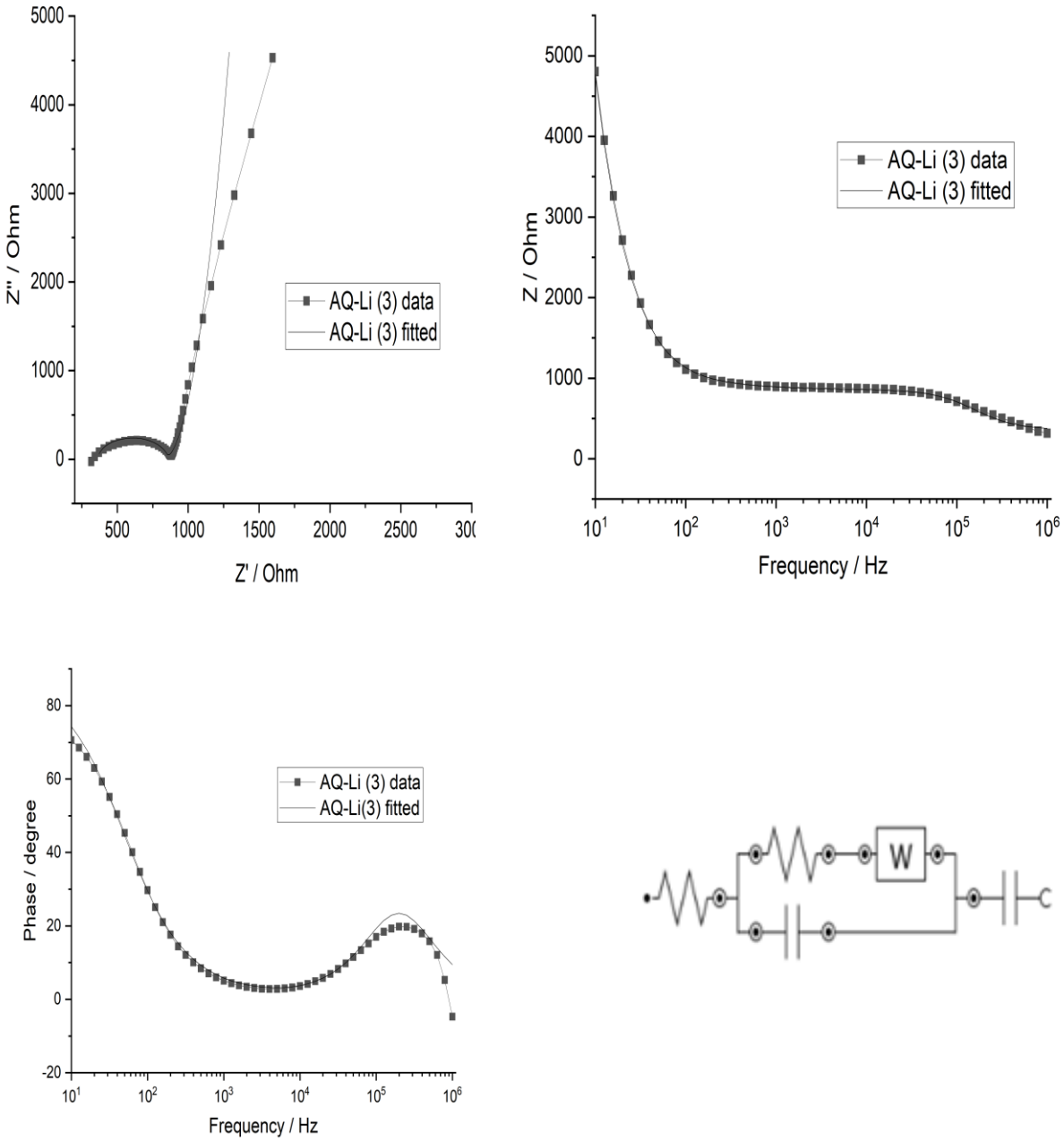

Figure 14.3 EIS of AQ-Li^+, with 0.005 M Li^+, 0.05M of $[^nBu_4N]PF_6$, CH_3CN.

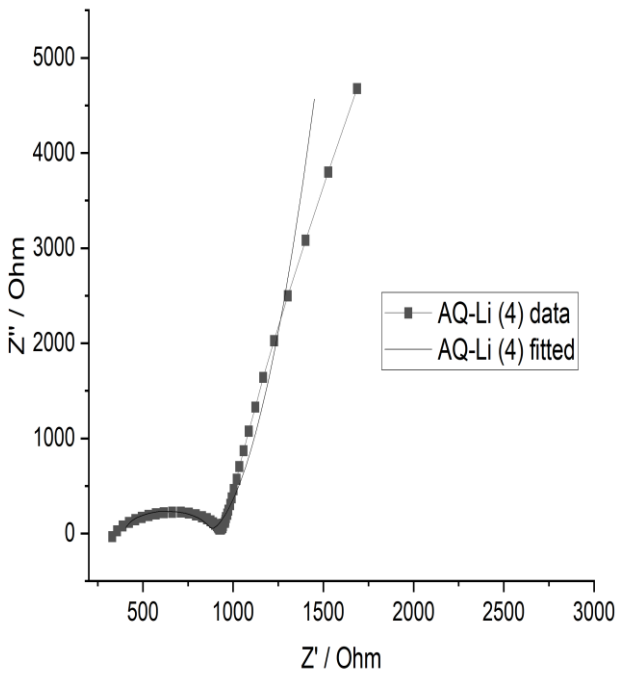

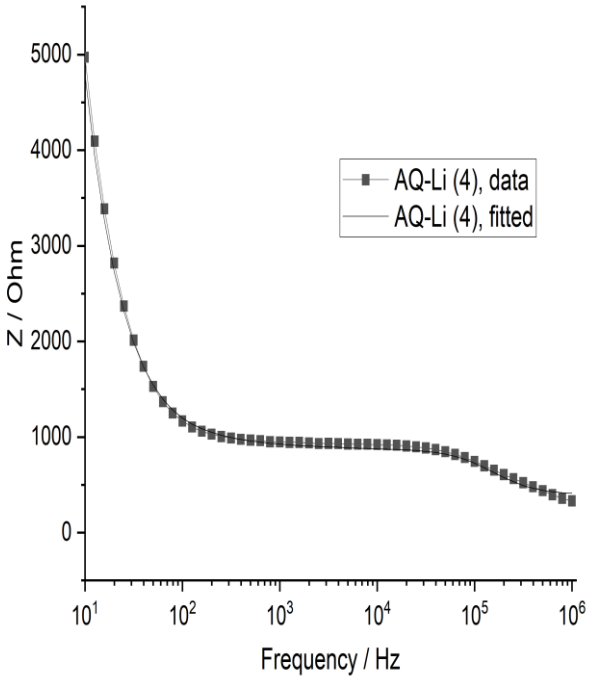

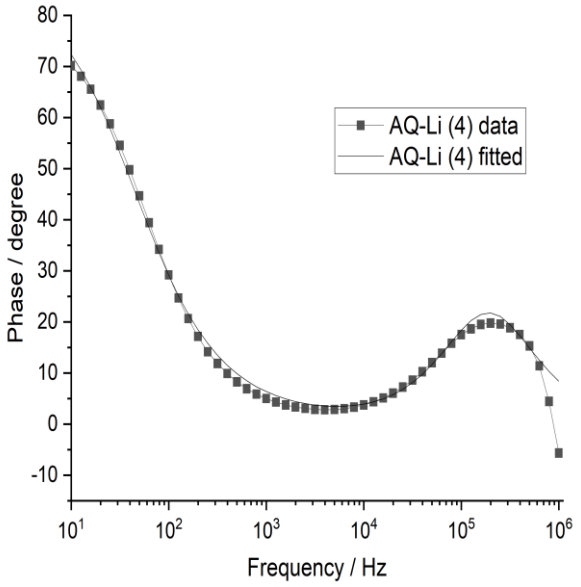

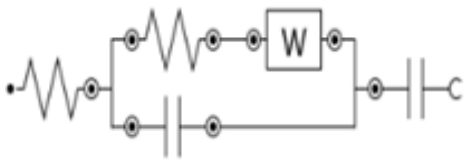

Figure 15.3 EIS of AQ-Li^+, after addition of 0.004 M Li^+, 0.05 M of $[^nBu_4N]PF_6$, CH_3CN.

Table 3.1 Electrode behaviour (AQ and AQ-Li^+) calculated from the electrochemical circuit fit of the experimental EIS data using Autolab Nova 1.11.

Sample	R1/Ohm	R2/Ohm	C1/F	Y0	C2/F
AQ	297	570	2.24×10^{-9}	109	1.27×10^{-6}
(0.007 M of Li^+) AQ-Li^+	346	507	2.491×0^{-9}	206	3.70×10^{-6}
(0.006 M of Li^+) AQ-Li^+	307	500	2.04×10^{-9}	173	3.80×10^{-6}
(0.005 M of Li^+) AQ-Li^+	365	478	2.51×10^{-9}	200	3.84×10^{-6}
(0.004 M of Li^+) AQ-Li^+	398	465	2.61×10^{-9}	152	4.00×10^{-6}

Figure 9.3 shows the impact of lithium on the redox waves of anthraquinone by electrochemical titration at different additions of lithium with 0.05 M $[^nBu_4N]PF_6$ electrolyte in acetonitrile using cyclic voltammetry. The typical redox waves of anthraquinone shifted to more positive values and increased the redox peak of anthraquinone with each addition of lithium ions. This is consistent with research by the Compton group.[9] Figure 10.3 presents electrochemical impedance spectroscopy of the anthraquinone–modified electrode in the presence and absence of lithium ions (Nyquist plot). Adding lithium results in increased capacitance. According to figure 10.3, from Nyquist plot, the diameter of the semicircle corresponds to the size of charge transfer resistance. The diameter of the semicircle in the Nyquist plot for AQ (figure 10.3) was bigger than AQ-Li, which means the addition of lithium improved the electrolyte and the reaction between AQ and Li. Consequently, the diameter of the semicircle for AQ-Li was much lower for each addition of Li which means the reaction between AQ and Li increased.

Figure 12.3,13.3,14.3 and 15.3 show the fitting data of the 0.007 M, 0.006 M, 0.005 M and 0.004 M addition of lithium ion on anthraquinone modified glassy carbon (figure11.3). Table 3.1 shows R_1 which is the resistance of solution, R_2 and C_1 represent the resistance and capacitance of double layers, C_2 shows the Faradaic capacitance. According to Table 3.1, the value of solution resistance is similar which is expected. In addition, the double layer capacitance value is similar. The value of the resistance of the double layer becomes slightly lower per every addition of lithium. Finally, the value of C_2 which is the Faradaic capacitance is slightly increased and this is explains why the semicircle from Nyquist plot becomes smaller by each addition of Lithium. The Bode plot in all cases, represents the relationship between impedance and frequency. From Phase plot, in all cases, the value of phase is from 79° to 70° which is close to an ideal capacitance (90).

3.3.5. Electrochemical quartz crystal microbalance (EQCM)

Electrochemical quartz crystal microbalance experiments were applied using electrochemical cell connected by a quartz crystal oscillator to the potentiostat. The cyclic voltammogram was run while monitoring changes in frequency. The CV potential was swept from -1.4 to 0.1 V for anthraquinone-2-diazonium chloride deposition, and -1.1 to 1.2 V for the cyclic voltammogram after adding Li^+.

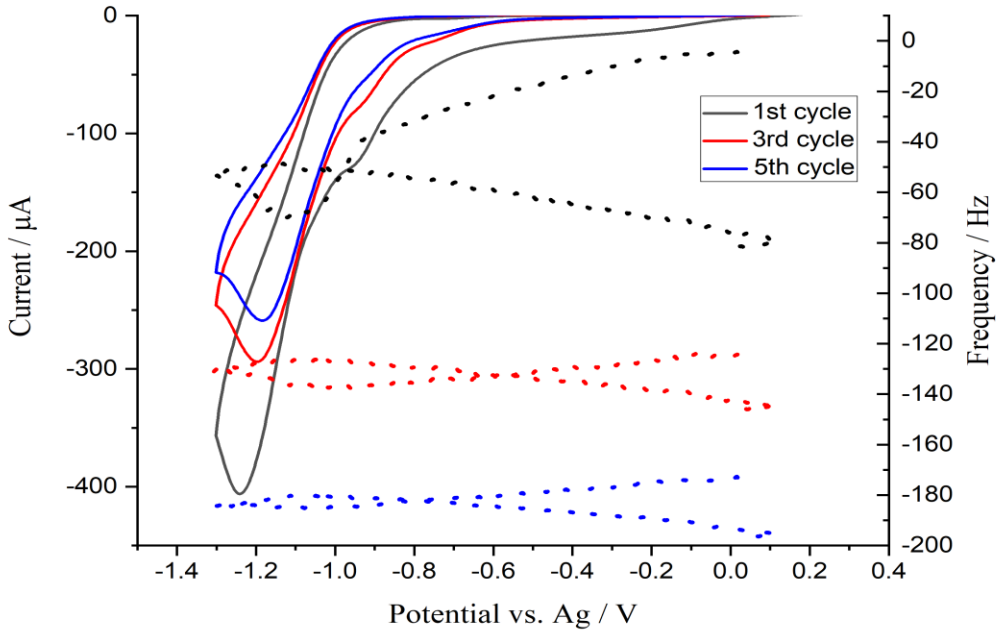

Figure 16.3 Cyclic voltammogram (100 mV/s) of anthraquinone-2-diazonium chloride deposition showing the EQCM frequency change on each cycle.

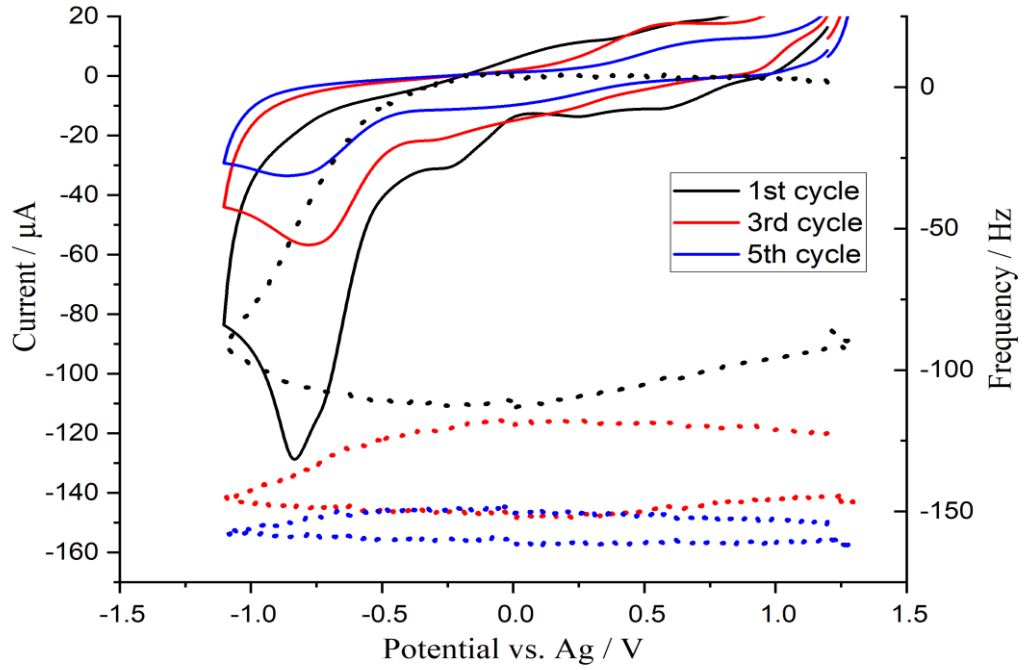

Figure 17.3 Cyclic voltammogram (100 mV/s) of anthraquinone after adding lithium (0.3 M).

Electrochemical quartz crystal microbalance (EQCM) was recorded using anthraquinone-2-diazonium chloride (2 mmol) in acetonitrile with 0.05M of $[^{n}Bu_4N]PF_6$. Figure 16.3 shows the cyclic voltammogram of anthraquinone-2-diazonium chloride and frequency change during deposition of anthraquinone on the surface of carbon coated quartz crystal electrode. Figure 17.3 shows the cyclic voltammogram and frequency change of the AQ functionalised electrode in the presence of lithium. According to figure 17.3, the frequency changed from -200 to -150 and consequently changed in the mass which deposited on the surface electrode.

$$AQ + 2e^- + 2Li^+ \longleftrightarrow AQLi_2$$

According to figure 16.3 and 17.3, the frequency decreases in each cycle, which indicate increased mass because of AQ film deposition in 16.3 and inclusion of Li^+ ions in 17.3. The change in frequency calculated according to the Sauerbrey equation which is mentioned in chapter 2 equation number 28.

3.3.6. Galvanostatic charge-discharge measurements

Figure 18.3(a) shows galvanostatic charge-discharge of a carbon fibre-carbon fibre (CF:CF) supercapacitor. It shows a potential range of 0.8 to -0.8 V because the blank carbon fibre only has electric double layer capacitance.

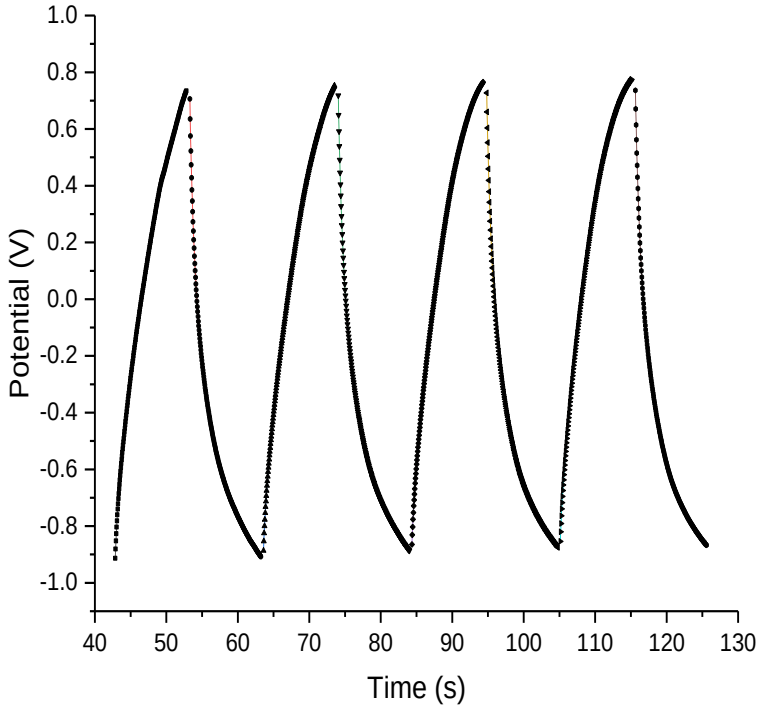

Figure 18.3 Charge-discharge (galvanostatic) of a carbon fibre symmetric supercapacitor.

a)

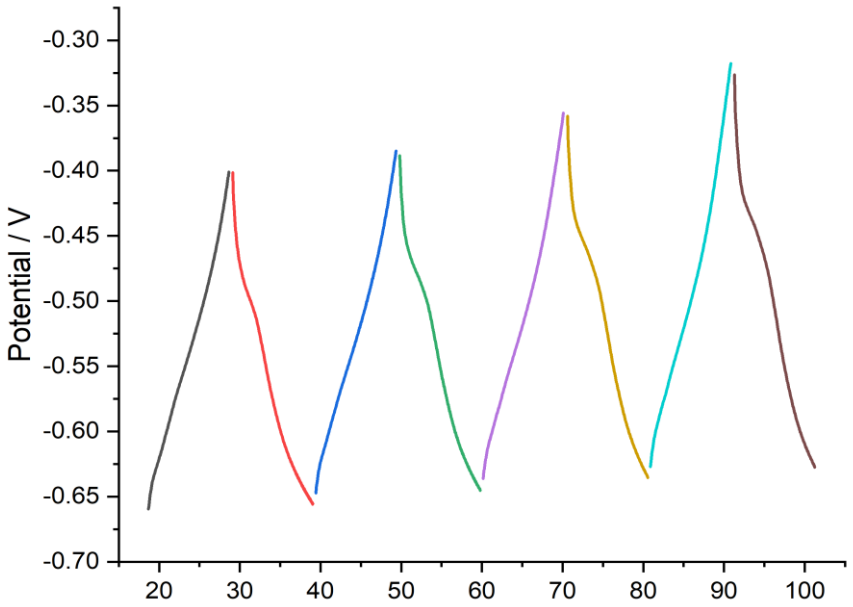

b)

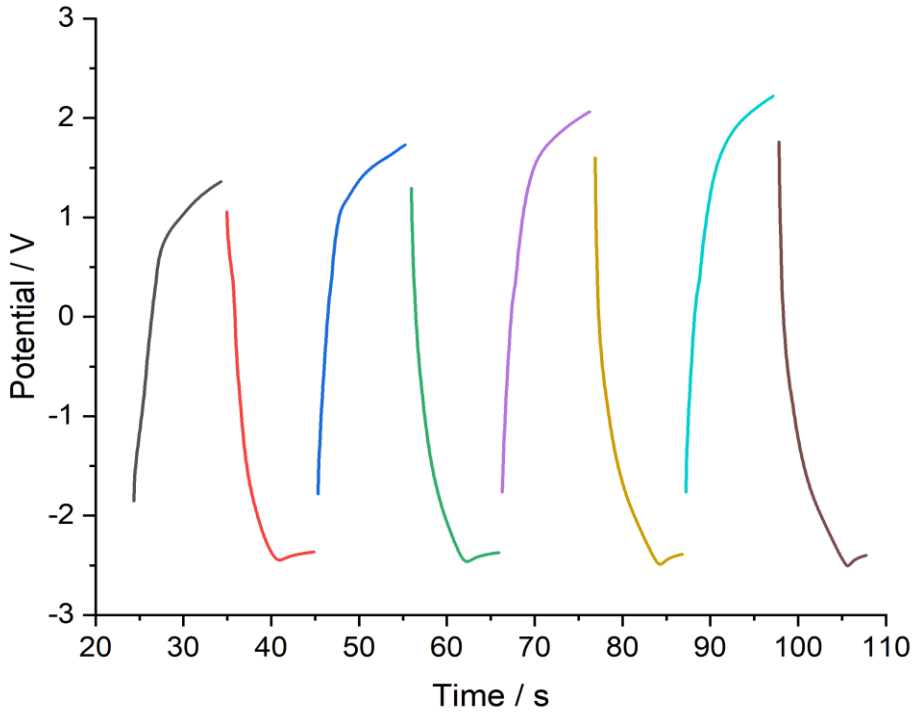

Figure 19.3 a) Charge-discharge of anthraquinone-carbon fibre asymmetric supercapacitor.

b) Charge-discharge of anthraquinone-lithium asymmetric hybrid-battery/supercapacitor.

Figure 19.3(a) presents the anthraquinone-carbon fibre (AQ:CF) supercapacitor charge – discharge that shows a potential range from 1.1 to -1.15 V which is higher than CF:CF supercapacitor. This is because AQ:CF is combines both electric double layer charging and faradaic redox charging which increases the capacitance. Figure 19.3 (b) shows the excellent electrochemical behaviour of anthraquinone-lithium hybrid battery /supercapacitor (AQ:Li), with further increased voltage range. It shows stable charge-discharge behaviour (Figure 20.3). This means it is durable and stable with a long lifetime. The specific capacitance was calculated according to equation number 27 (Chapter 2).

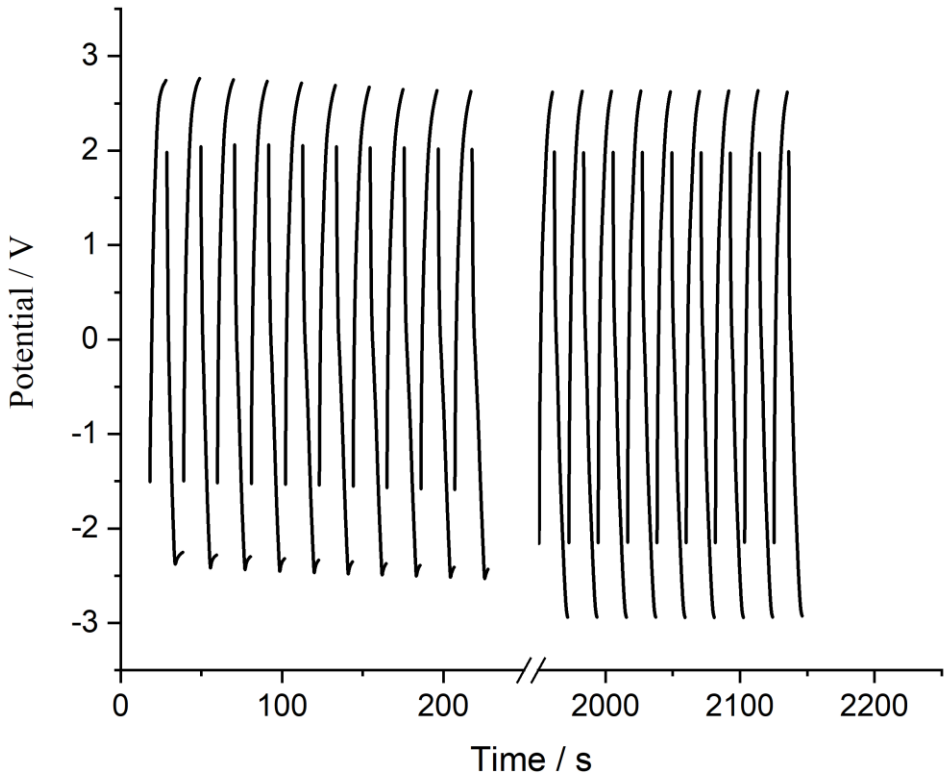

Figure 20.3 Shows 100 cycles of AQ-Li charge-discharge with 0.05 M of Both $[^{n}Bu_4N]PF_6$ and 0.03 M $Li[CLO_4]$ in acetonitrile.

Figure 20.3 represents a charge-discharge (galvanostatic) of AQ-Li of the first ten and the last ten of 100 cycles. The experiment runs using the maximum constant current with 0.05 M of [^{n}Bu$_4$N]PF$_6$ and 0.03 M of Li[ClO$_4$] (which was optimised by testing at 0.01, 0.02 and 0.03 M) in acetonitrile. As a result, it shows good electrochemical behaviour for the first 100 cycles.

3.3.7. Capacitance and specific capacitance of AQ-CF and AQ-Li measurements

Capacitance of anthraquinone-carbon (GCE) and anthraquoione lithium (AQ-Li) were indicated from cyclic voltammetry measurements using the following equation

$$C_s = \frac{\int i(E)\, dE}{2 \cdot m \cdot v \cdot \Delta E} \qquad (38)$$

where $\int i(E)dE$ is the area of the cyclic voltammogram, m is the mass of the polymer film (g), v is the voltage scan rate (Vs^{-1}) and ΔE is the potential range. The capacitance of AQ was indicated from CV which is 4.092 $\times 10^{-6}$ F where the capacitance after adding Li was 4.8 $\times 10^{-6}$ F. Therefore, the specific capacitance of AQ and AQ-Li can be seen in table number 3.2.

Table 3.2 Shows the specific capacitance (from CV at 100 mV/s) of AQ and AQ-Li on GCE.

Sample	F/g
AQ	19.20
AQ-Li	24.15

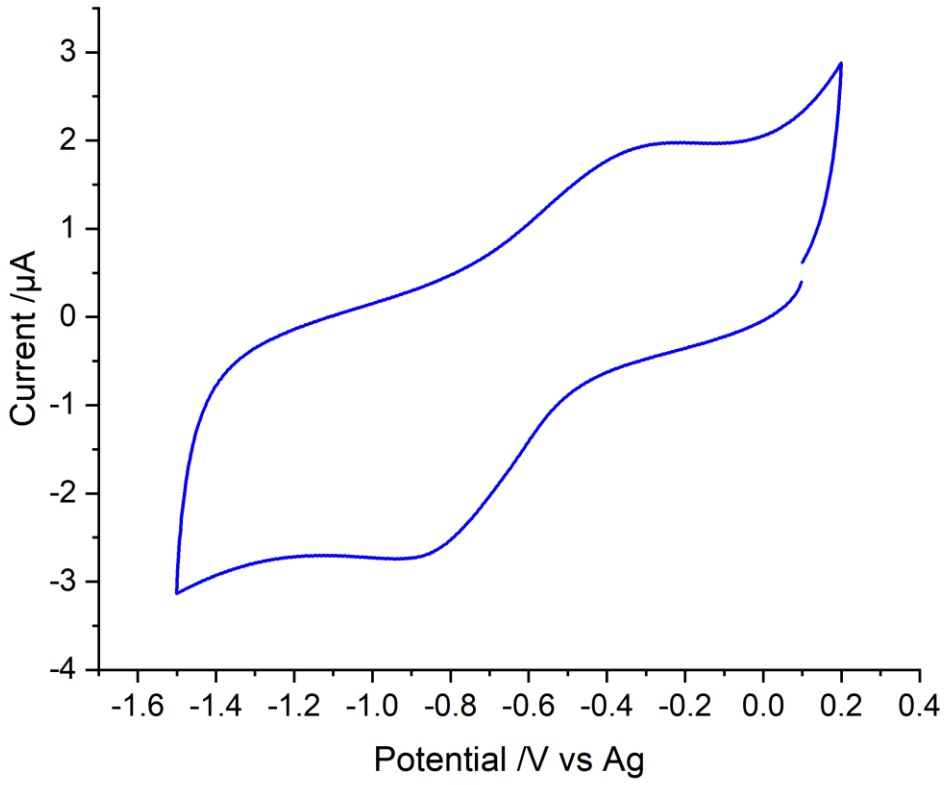

Figure 21.3 CV of AQ at 100 mV/s with 0.05 M of [^{n}Bu$_4$N]PF$_6$ after adding Li^+.

Galvanostatic charge-discharge were carried out using carbon fiber 1cm^2 with 0.05 M of [^{n}Bu$_4$N]PF$_6$ in acetonitrile. From galvanostatic charge discharge, the capacitance of supercapacitor of AQ-CF was 21 F/g whereas the capacitance of AQ-Li was 59 F/g (Table 3.3). The specific capacitance of Galvanostatic charge-discharge measurement are different from those obtained by CV, particularly for the AQ-Li system where the GCD value is nearly three times higher. Possibly, this is due to the working electrode for CV being a glassy carbon electrode, while carbon fibre was used as a working electrode for GCD measurement, so surface area and porosity would be different. Also, cyclic voltammetry and galvanostatic charge-discharge measurement are different techniques, in particular charge-discharge measurements are better able to reveal capacitance from slower processes than cyclic voltammetry.

Table 3.3 Shows specific capacitance (from GCD) of AQ-CF and AQ-Li.

Sample	F/g
AQ-CF	21.3
AQ-Li	59

3.4. Summary

The combination of anthraquinone with lithium was studied by different electrochemical methods including galvanostatic (charge-discharge), electrochemical impedance spectroscopy and cyclic voltammetry. The hybrid battery /supercapacitor combines high capacitance with excellent life cycle stability. The anthraquinone/lithium system shows (from GCD) specific capacitance of 59 F/g compared to 21.3F/g using carbon fibre 1 cm^2 for a symmetric anthraquinone -carbon fibre (AQ-CF) supercapacitor.

3.5. References

[1] M. V. Reddy, A. Mauger, C. M. Julien, A. Paolella, K. Zaghib, *Materials* **2020**, *13*, 1884.

[2] R. Sneha, K. Vinayaka, K. Rana, in *2020 IEEE International Conference on Power Systems Technology (POWERCON)*, IEEE, **2020**, pp. 1-6.

[3] L. Lu, X. Han, J. Li, J. Hua, M. Ouyang, *Journal of Power Sources* **2013**, *226*, 272-288.

[4] S. Holmberg, A. Perebikovsky, L. Kulinsky, M. Madou, *Micromachines* **2014**, *5*, 171-203.

[5] Y. Qin, J. Li, X. Jin, S. Jiao, Y. Chen, W. Cai, R. Cao, *Ceramics International* **2020**, *46*, 15379-15384.

[6] aE. Mossali, N. Picone, L. Gentilini, O. Rodrìguez, J. M. Pérez, M. Colledani, *Journal of Environmental Management* **2020**, *264*, 110500; bJ. Yang, Z. Wang, Y. Shi, P. Sun, Y. Xu, *ACS Applied Materials & Interfaces* **2020**, *12*, 7179-7185.

[7] aS. Goriparti, E. Miele, F. De Angelis, E. Di Fabrizio, R. P. Zaccaria, C. Capiglia, *Journal of Power Sources* **2014**, *257*, 421-443; bE. Gavilán-Arriazu, J. Hümöller, O. Pinto, B. L. de Mishima, E. Leiva, O. Oviedo, *Physical Chemistry Chemical Physics* **2020**, *22*, 16174-16183.

[8] S. Ernst, L. Aldous, R. G. Compton, *Chemical Physics Letters* **2011**, *511*, 461-465.

[9] A. J. Wain, G. G. Wildgoose, C. G. Heald, L. Jiang, T. G. Jones, R. G. Compton, *The Journal of Physical Chemistry B* **2005**, *109*, 3971-3978.

[10] M. Kullapere, J.-M. Seinberg, U. Mäeorg, G. Maia, D. J. Schiffrin, K. Tammeveski, *Electrochimica Acta* **2009**, *54*, 1961-1969.

[11] A. Subrata, R. D. Webster, *Electrochemical Science Advances* **2022**, *2*, e2100084.

[12] C. G. Heald, G. G. Wildgoose, L. Jiang, T. G. Jones, R. G. Compton, *ChemPhysChem* **2004**, *5*, 1794-1799.

[13] M. Weissmann, O. Crosnier, T. Brousse, D. Bélanger, *Electrochimica Acta* **2012**, *82*, 250-256.

Chapter 4

Lewis Acid Modified Conducting Polymer Materials for Electrochemical Energy Storage

4. Aim

This chapter studies the electropolymerisation of the N–pyrrolyl–bis(pentafluorophenyl) borane monomer and compares the resulting material with the known conducting polymer poly(pyrrole) by using different electrochemical methods. It also compares polymers formed from other Lewis acidic N-pyrrole-boranes with *N*–pyrrolyl–bis(pentafluorophenyl) borane in terms of capacitance and stability.

4.1. Introduction

Polypyrrole (PPy) is one of the important conducting polymers, that can be used in many applications including energy storage, electromagnetic shielding and corrosion protection.[1] Pyrroles are N-heterocycles and are electron rich aromatics due to participation of the nitrogen lone pair in the π-system. PPy can be synthesized chemically or electrochemically by oxidizing pyrrole. Although PPy has lots of advantages - including excellent specific conductivity and stability- it also has some limitations, such as rigidity and lack of processability.[2] These restrict the applicability of PPy for use in coatings and other materials. To improve on these limitations, pyrrole derivatives with modified properties are being explored for many applications.[3] Pyrrole derivatives are present in many natural products, such as vitamin B_{12}, and can also be used in material and surface science, which has led to increased efforts to find synthetic methods, such as Paal-Knorr and Hantzsch.[4]

Pyrroles and their derivatives are one of the P-doped polymers that can be used as organic cathodic materials for rechargeable batteries and supercapacitors. The reason for using PPy as

a cathode material is because of its high specific energy, stability, and high theoretical capacity. Despite these advantages, PPy suffers from low practical capacity because of the doping process.[5]

Previous work in the Wildgoose research group focused on the synthesis and electrochemical properties of borane Lewis acids, and their applications in electrochemical frustrated Lewis pairs for energy applications.[6] This work was expanded into investigating the effect of borane Lewis acid groups on pyrroles, resulting in synthesis of the N-pyrrolyl boranes **1** to **3** (Figure 4.1). The change in the electron donating ability of the aromatic ring can be seen in the reduced B-N bond length bond, and also by the more positive oxidative peak potential during cyclic voltammetry. Figure 4.2 shows the coupled electron density can delocalizes into the vacant *P*z orbital in the borane.

Linking Lewis acid groups to the pyrrole increases the stability of both pyrrole and borane. This is because the organic ring can contribute electrons to the vacant orbitals on the Lewis acidic compound. In research published in 2002 by Douglade and Fabre, they polymerized the monomer tris-(pyrrolyl)borane with the Lewis acid bonded to the pyrrole nitrogen centre.[7] During the electropolymerisation, the potential for oxidation is higher and the potential for borane reduction is lower. Fabre reported the synthesis and electropolymerisation of *tris*(N–pyrrolyl) borane, $B(NC_4H_4)_3$, finding that the resulting polymer films were non-conducting, N-derivatisation with Lewis acids can be expected to influence both polypyrrole structure through the steric bulk of the borane, and electronic properties due to donor-acceptor interactions between the pyrrole-N and vacant p-orbital on boron.[7] Therefore, the borane can improve porosity, electronic conductivity, ion diffusion and better supercapacitor performance.[8]

Therefore, all Lewis acidic N-pyrrole-boranes were already available to investigate and characterize electrochemically to do this research (figure 4.1).

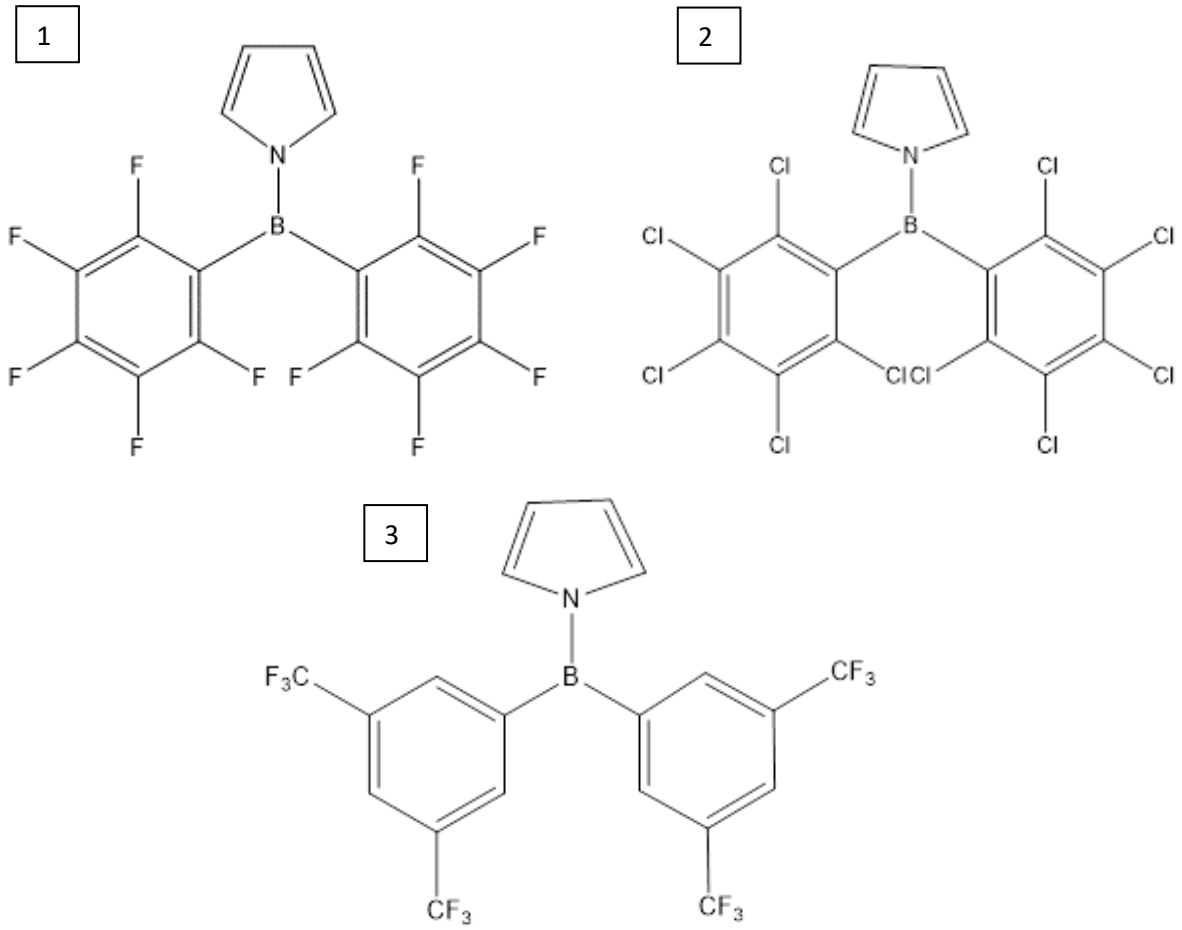

Figure 4.1 The structures of N–pyrrolyl boranes: $(NC_4H_4)B(C_6F_5)_2$ **1**; $(NC_4H_4)B(C_6Cl_5)_2$ **2**; $(NC_4H_4)B\{3\text{-}5\text{-}(CF_3)C_6H_3\}_2$ **3**.

Figure 4.1 shows the structures of the three N–pyrrolyl boranes used in this work. All pyrrolyl boranes are affected by steric bulk and electronic effects.[9] This means the large aromatic ring groups on the boron centre in N-pyrrolyl boranes may lead to an increase in the pore size between chains compared to the polypyrrole chain which is more close to each other. Consequently, the steric bulk of the aromatic groups on the boron can increase the pore size between the chains.[10]

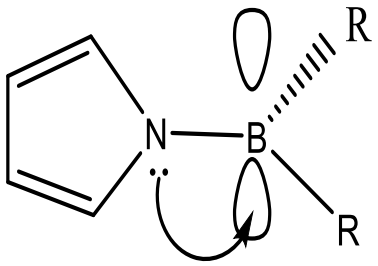

Figure 4.2 Electrons delocalized into vacant Pz orbitals.

In this research, preliminary investigation by the Wildgoose group indicated that the pyrrolyl boranes could be electropolymerized and indicated increased capacitance for Poly**1** compared to PPy.[11] In this chapter, we fully investigate the charge storage capabilities of LAMPS based on poly**1** to poly**3** by using cyclic voltammetry, electrochemical impedance spectroscopy (EIS), electrochemical quartz crystal microscopy (EQCM) and galvanostatic (charge-discharge) techniques. We discuss how the steric and electronic influence of the borane can improve the properties. This work is about the electrochemical properties of the monomers and films and also the ability of the films to store charge (supercapacitors).

4.2. Experimental section

4.2.1. Polymersation and characterization of Lewis acidic N-pyrrole-boranes

Each of three *N*–pyrrolyl–bis(pentachlorophenyl)boranes was polymerised and the polymer characterised by cyclic voltammetry, EQCM and galvanostatic (charge-discharge). Electrochemical impedance spectroscopy (EIS) was used to compare and investigate them on carbon electrode.

The specific capacitance of poly**1**, poly**2** and poly**3** were tested in blank solution of 0.1 M $BarF_{20}$ with DCM using a three-electrode system.

All electrochemical techniques were used to investigate Lewis acidic N-pyrrole-boranes on the carbon electrode using three electrode system. The counter electrode was platinum. The reference electrode was silver wire electrode. The carbon electrode was polished by alumina 0. 3µm. The working electrode immersed in dry solvent (acetonitrile or DCM) with 0.1 M of $[^{n}Bu_4N][B(C_6F_5)_4]$ electrolyte.

4.3. Results and discussion

4.3.1. Electrochemical characterization and electropolymerisation of *N*–pyrrolyl–boranes

Figure 4.3 a) and b) show capacitance increasing with each cycle resulting in increased current during polymerisation of both PPy and Poly**1**. This capacitance increase is seen in increased current for Poly**1** between 0 and 0.6 V whereas PPy (Figure 4.3 a) showed an increase in the range between – 0.1 to 0.4 V vs Ag. This shows that PPy and Poly1 adsorbed onto the surface successfully. The potential needed to electropolymerize pyrrole is smaller than for the borane derivative which means the N lone pair can delocalize into the empty *P*z orbital in borane, but this makes the borane derivatives hard to oxidise, which means a higher positive potential is needed to initiate electropolymerisation.

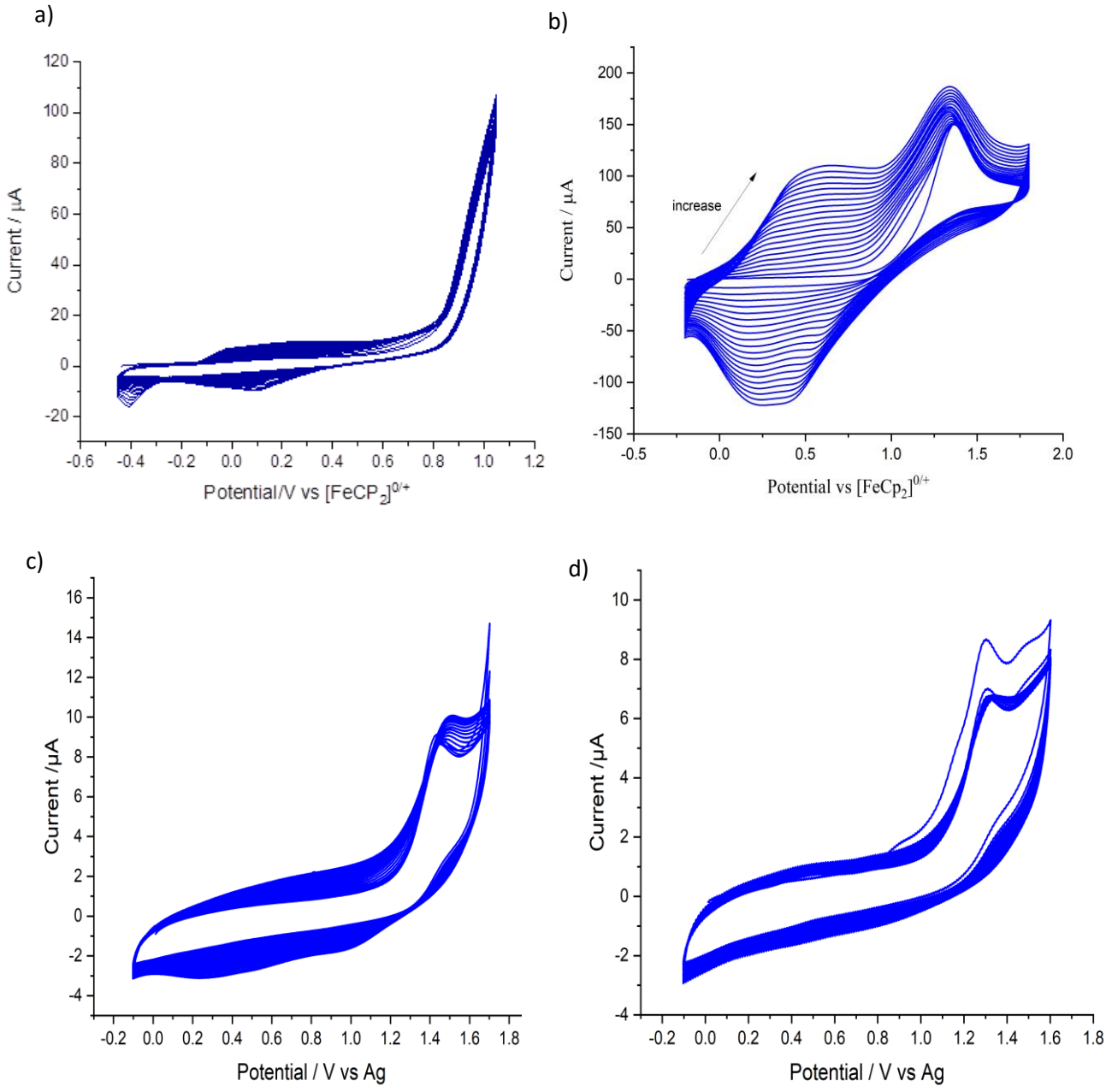

Figure 4.3 a) 20 cycles polymerization of pyrrole in 0.1 M[^{n}Bu$_4$N][B(C$_6$F$_5$)$_4$] and CH$_2$Cl$_2$ at 100 mV/s. **b)** 20 cycles polymerisation of 0.01(NC$_4$H$_4$)B(C$_6$F$_5$)$_2$(poly**1**) in 0.1 M[^{n}Bu$_4$N][B(C$_6$F$_5$)$_4$] and CH$_2$Cl$_2$ at 100 mV/s. **c)** Polymerisation of poly**2** with [^{n}Bu$_4$N]PF$_6$ in CH$_3$CN, 20 cycles. **d)** Polymerisation of poly**3** vs Ag, 20 cycles with 0.1 M of BarF$_{20}$ in DCM at 100 mV/s.

Figure 4.3(c) and (d) show electropolymerisation of poly**2** and poly**3**. The potential was applied from -0.1 V to 1.8 V for poly**2** and poly**3**. At 1.5 V the oxidation of poly**2** occurred and then the potential was reduced to the starting potential -0.1 V. At 1.4 V the oxidation of poly**3** occurred and therefore the potential was reduced to the starting potential -0.1 V. The capacitance of material (poly**3**) increased from 0 V to 1 V whereas the capacitance of poly**2** increased from 0 V to 1.2 V.

To compare the oxidation of pyrrole with other monomers in the same conditions (0.1 M of $BarF_{20}$ in DCM). All monomers are shifted to more positive potentials which can be seen in the table 4.1.

Table 4.1 Represents oxidation/reduction of pyrrole/polymerization.

Compounds	**Ep(OX)/V pyrrole/polymerisation**
Poly**1**	+1.21
Poly**2**	+1.5
Poly**3**	+1.4
PPy	+1.09

4.3.2. Electrochemical quartz crystal microbalance measurements (EQCM)

EQCM measurements were carried out to investigate the polymer growth and mass deposited. EQCM measured with a three electrode system where a glass carbon substrate was the working electrode, Pt was the counter electrode and silver was the reference electrode. The changes of mass at the working electrode are monitored by the change in frequency which occurs on a quartz crystal oscillator.

4.3.2.1. EQCM of polypyrrole

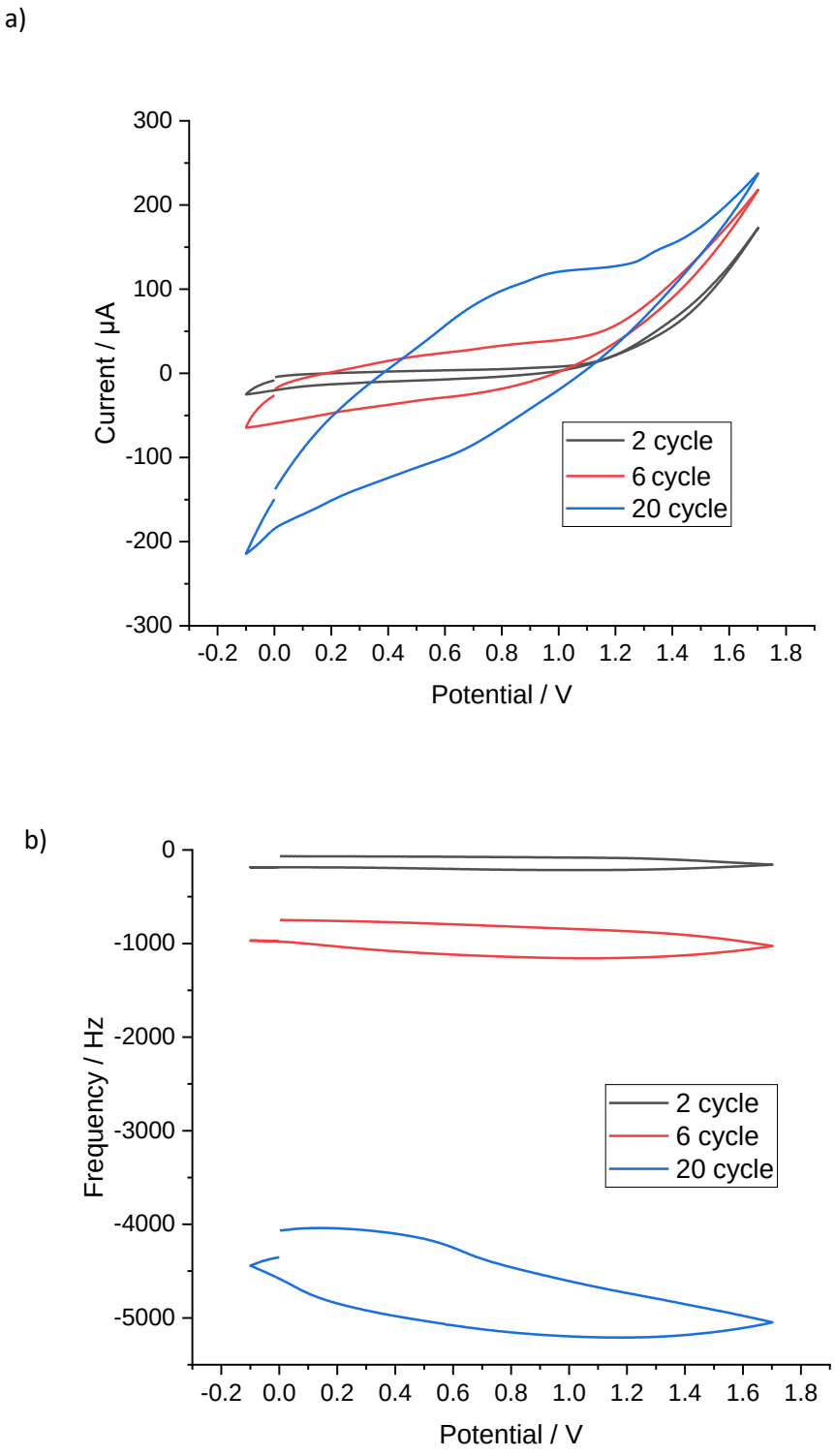

Figure 4.4 EQCM of 20 cycles of PPy, 0.1 M of $BarF_{20}$ in DCM at 100 mV/s.

4.3.2.2. EQCM of Poly1

a)

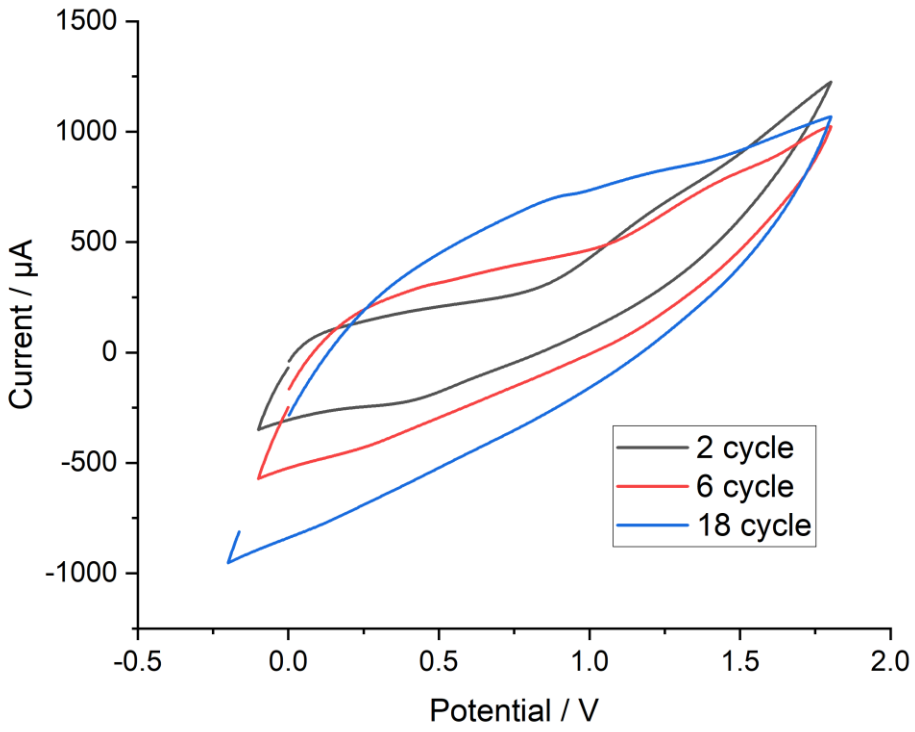

b)

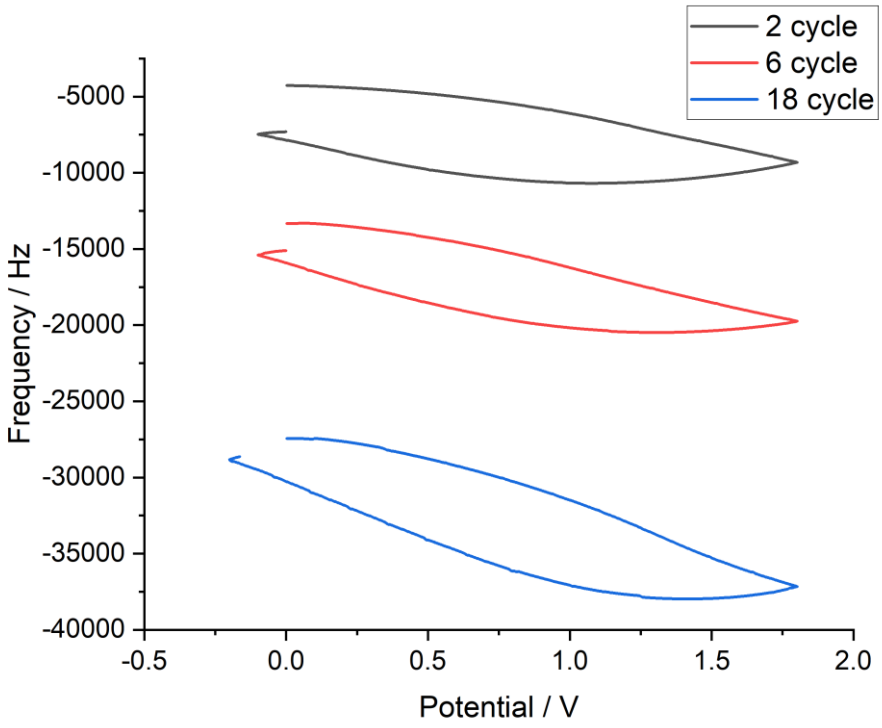

Figure 4.5 EQCM of 18 cycles of 0.01 M of poly**1**, 0.1 M of $BarF_{20}$ in DCM at 100 mV/s.

4.3.2.3. EQCM of poly(2)

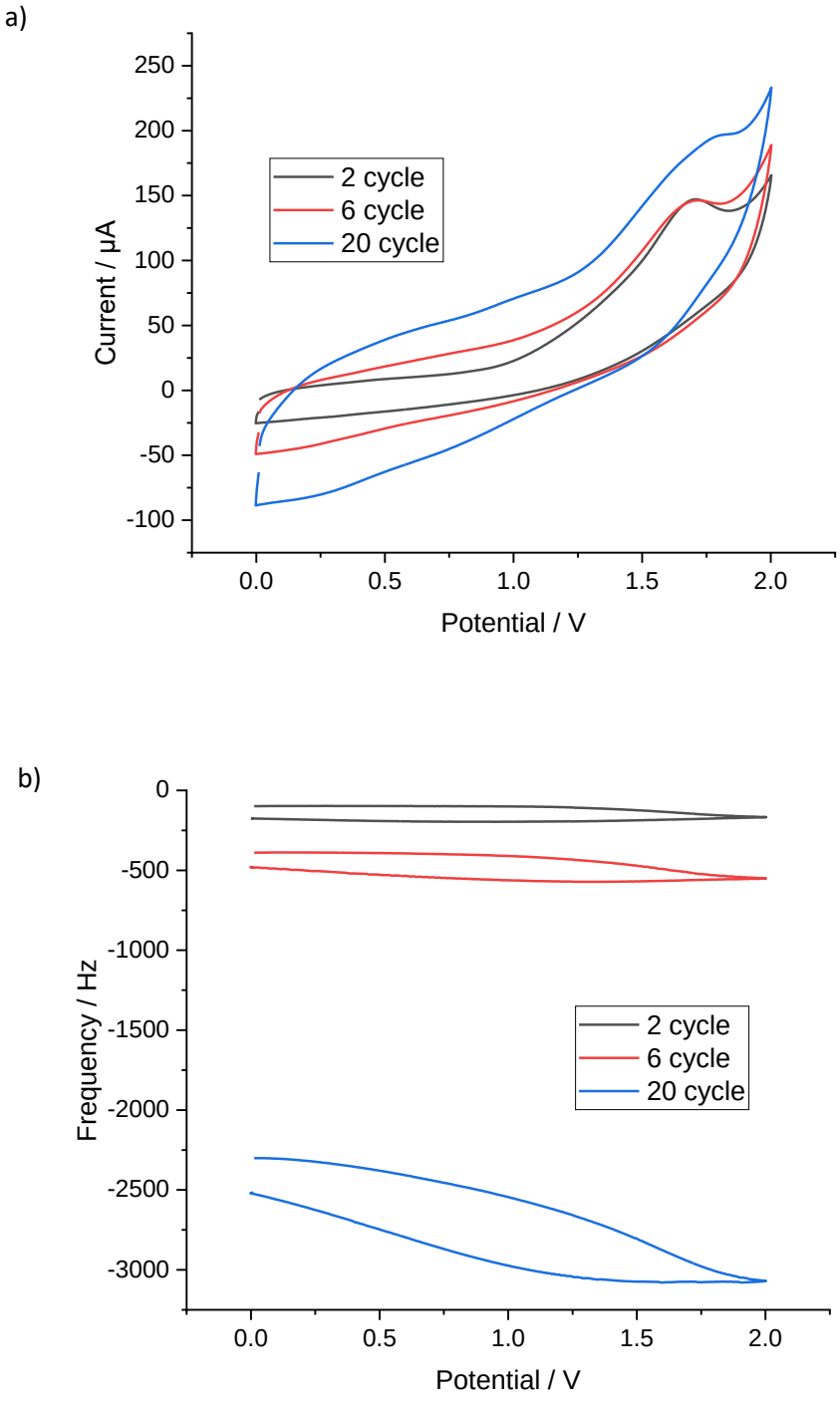

Figure 4.6 a) 20 Cyclic voltammogram of poly **2**. **b)** The corresponding plots of frequency change during the first 6 polymerisation cycles of poly**2** by EQCM measurements, 0.1 M of $BarF_{20}$ in DCM at 100 mV/s.

Figure 4.4 represents electrochemical quartz crystal microbalance (EQCM) of conventional polypyrrole using 0.1 M of $BarF_{20}$ in dichloromethane. Figure 4.4 (a) shows the cyclic voltamogram to deposit polypyrrole film on the surface of carbon electrode whereas, figure 4.4 (b) shows the frequency vs potential during EQCM of conventional polypyrrole. The frequency change for polypyrrole is smaller, indicating that less material is deposited.

EQCM of poly**2** is shown in figure 4.6 a) and b). The potential was swept from 0 to 2V, and the frequency grew steadily indicating deposition of poly**2**.

Figure 4.7 (a) represents EQCM of poly**3** by using cyclic voltammetry with frequency ranged from 10 to 10^6 Hz. The potential was swept from 0V to 1.8V. Figure 4.7 (b) shows the frequency vs potential during deposited of poly**3**.

SEM was carried out for poly**1**, PPy and poly**2**. All polymers were the glassy carbon electrodes (GCE) using 200 polymerisation cycles for each of them with three electrode system. The investigation shows that the poly**1** film is substantially (7 or 8 ×) thicker than poly**2** and PPy (Figures 4.8 to 4.10). This is consistent with the higher mass deposited for poly**1**.

4.3.2.4. EQCM of poly3

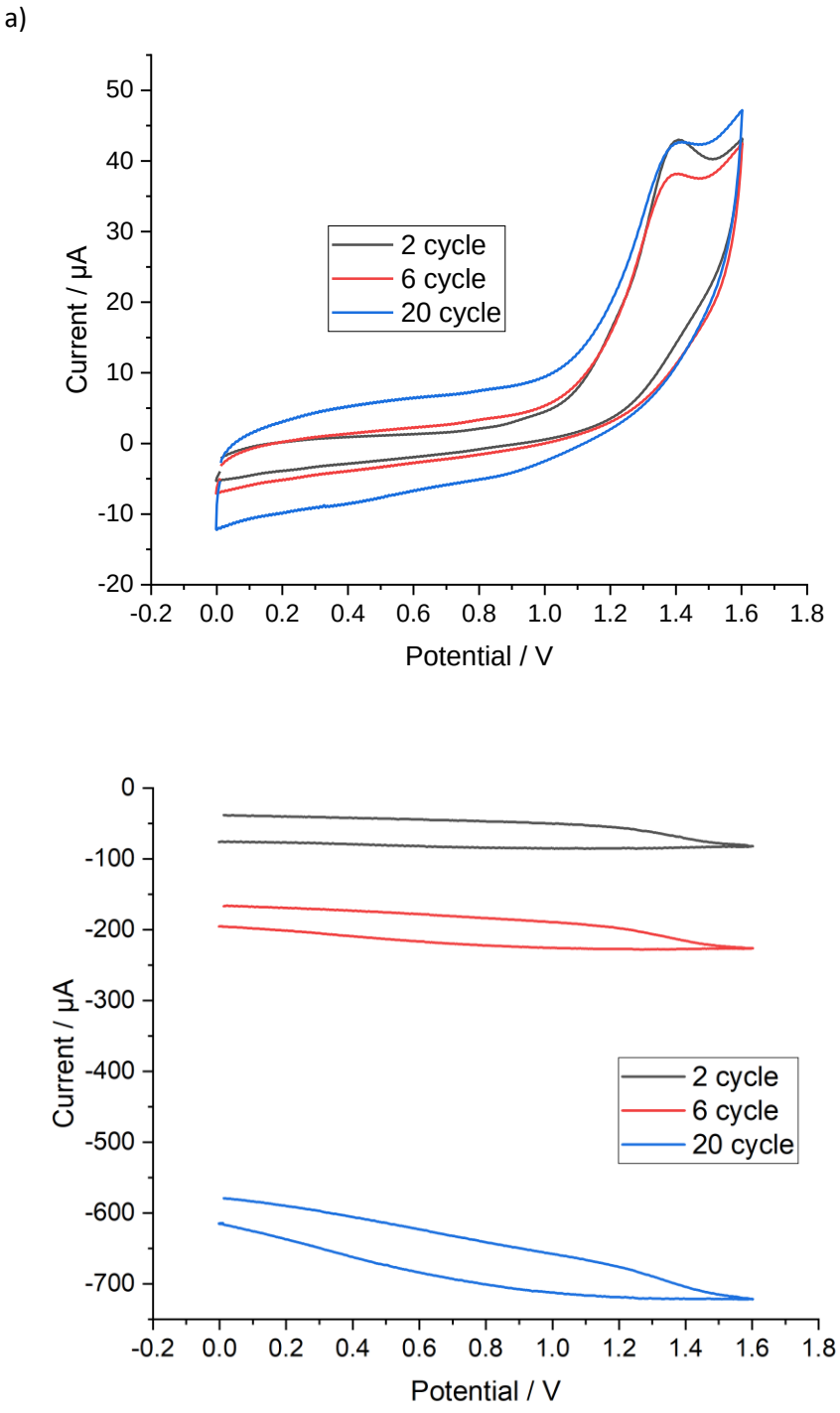

Figure 4.7 Cyclic Voltammetry of poly**3** at 100 mV/s. The corresponding plots of mass added during the first 6 polymerisation cycles of poly**3** by EQCM measurements, 0.1 M of $BarF_{20}$ in DCM

4.3.3. SEM of polypyrrole and poly1

To investigate the morphology of poly**1** compared to polypyrrole, samples were prepared by a 200 cycle electrodeposition of the polymer onto a glassy carbon electrode. The glassy carbon electrode was sealed in epoxy and cut into a cross section by the UEA technical team before imaging. The film thickness can be seen visually in the SEM images, and also using EDX elemental maps which distinguish the films by showing elements (F) which are only associated with the PPy-borane derivative or counter anion. The 200 cycle film for Poly**1** is about 7 or 8 times thicker than the PPy film, consistent with increased mass deposition observed by EQCM.

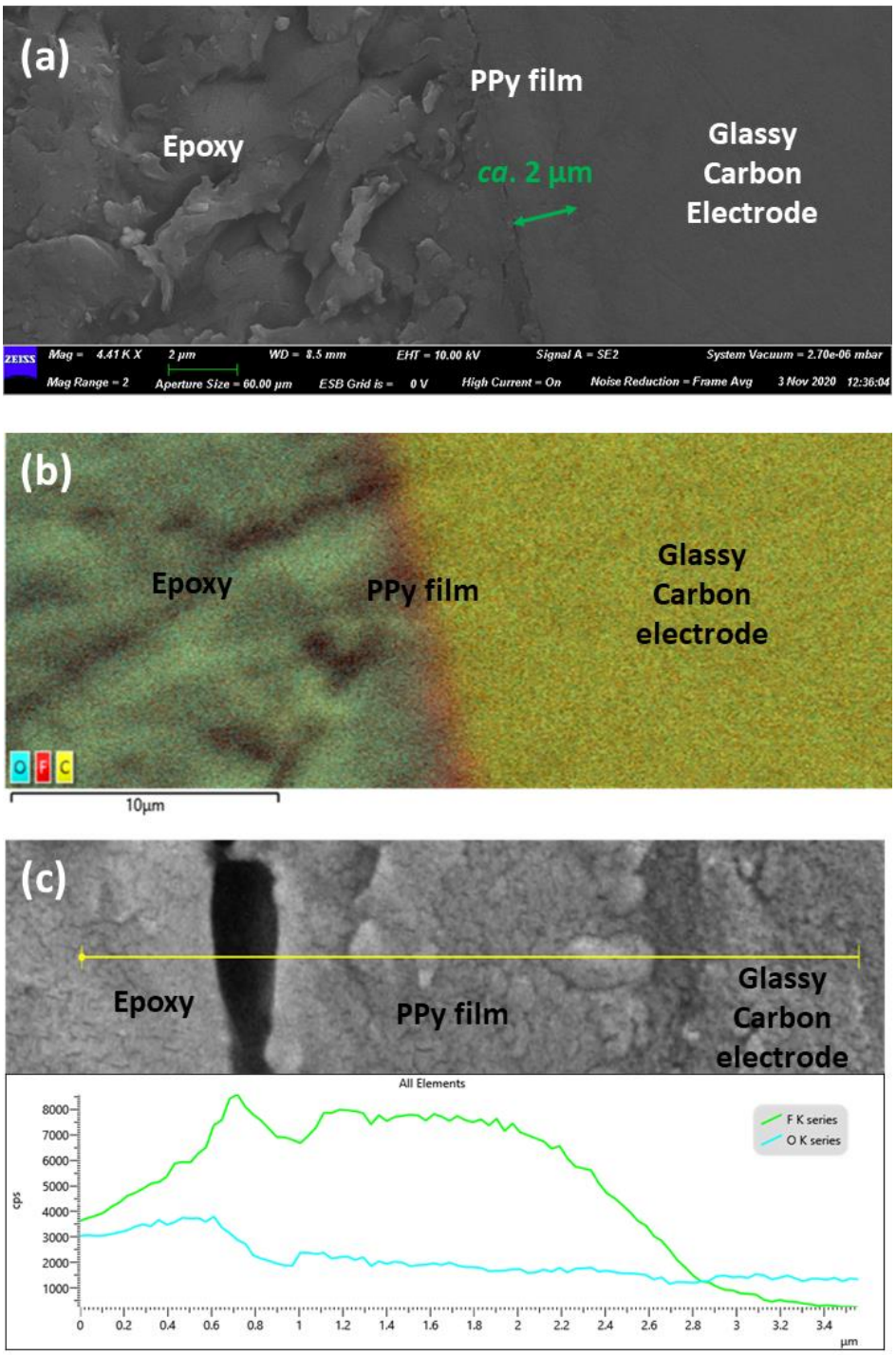

Figure 4.8 SEM cross section of a 200 cycle PPy film with $BArF_{15}$ anion. (**a**) Image showing ca 2 µm thick film between epoxy and glassy carbon electrode. (**b**) EDX elemental map (O blue, C yellow, F red) with presence of F indicating the PPy film. (**c**) F and O signal across the section indicating presence of the film.

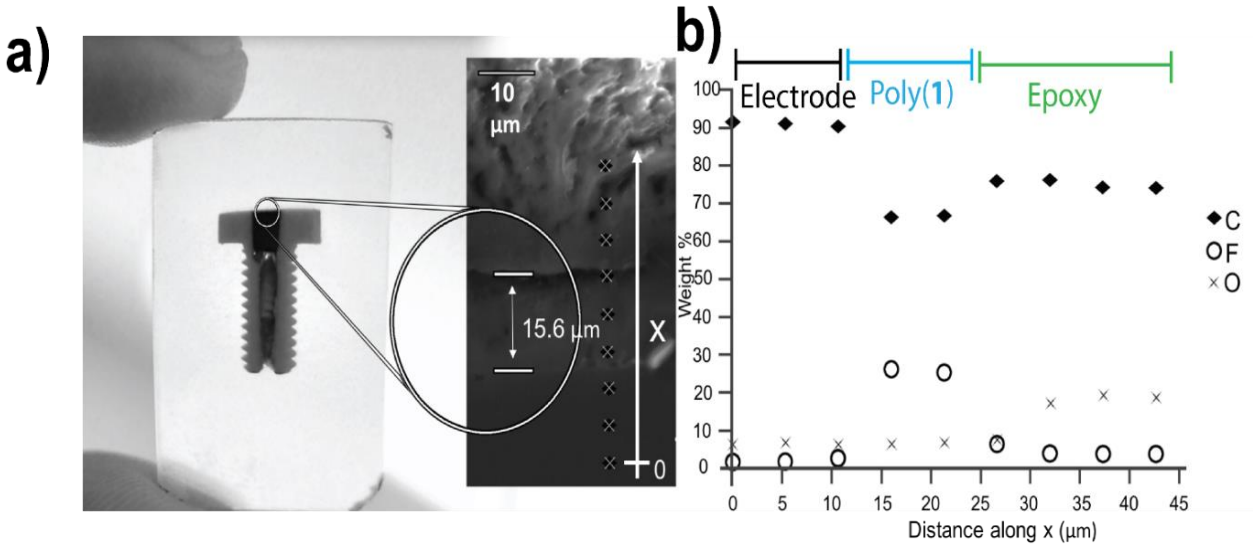

Figure 4.9 a) SEM image of poly**1**, **b)** EDX which is the consistent with analysis through a 15.6 µm thick (200 cycle) layer of poly**1**. The poly**1** film was on a GC electrode which presents the relative atomic % of C, O, and F. Obtained from James Courtney, Wildgoose group.

4.3.4. SEM of poly 2

A poly**2** film was prepared on a glassy carbon electrode using 200 polymerisation cycles, and cross-sectioned in the same way as the Poly**1** and PPy films. According to figure 4.10 the SEM of poly**2** shows a film around 2 to 3 μm thick which is less than poly**1** (15 μm), and similar to PPy. This can be seen through the EDX maps which show increased concentration of Cl and F. The decreased thickness relative to poly**1** is consistent with a lower mass and the lower frequency change observed in EQCM measurements. Comparing poly**2** with polypyrrole, the thickness of the films is similar but the frequency change is smaller, consistent with around 50% of the mass. This may suggest that the poly**2** film is less dense which would be expected for all of the boranes but it is not seen in the poly**1** result. However, such interpretation must be treated with caution as the EQCM experiments were done in different experiments to the depositions for SEM measurements. Any drift in the potential of the Ag pseudo reference lead to different extents of deposition of film, particularly considering the very different areas of the EQCM substrate (0.504 cm^2) and glassy carbon voltammetry electrode (0.07 cm^2).

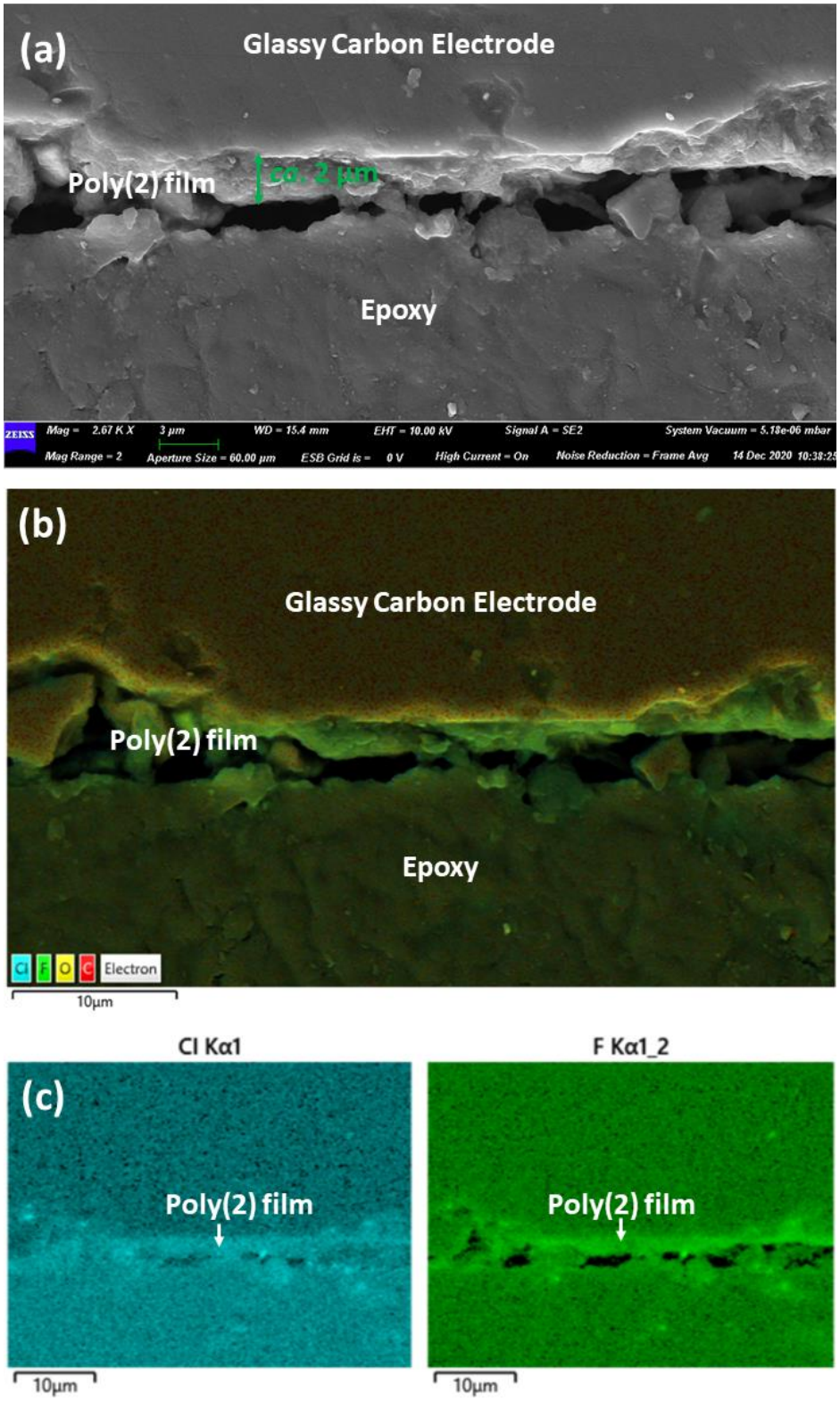

Figure 4.10 SEM cross section of a 200 cycle Poly(**2**) film with $BArF_{15}$ anion. (**a**) Image showing fragmented, ca 2 µm thick film between epoxy and glassy carbon electrode. (**b**) EDX elemental map (Cl blue, F green, O yellow, C red) with presence of F and Cl indicating the Poly(**2**) film. (**c**) Cl and F elemental maps whith increased concentration indicating presence of the film.

4.3.5. Cyclic voltammetry of films

To investgate the charge storage properties of poly**1**, a film of poly**1** was studied in dichloromethane (DCM) as electrolyte using [$^{n}Bu_4N$][$B(C_6F_5)_4$] and [$^{n}Bu_4N$][BF_4] at scan rate 100 mV/s According to figure 4.11, when poly**1** was compared with PPy by cyclic voltammetry, the capacitance of a 20 cycle poly**1** film was 8 times higher. This indicates that the Poly**1** film is storing more charge per unit area, but the higher mass deposited per cycle means that specific capacitance is likely similar to PPy.

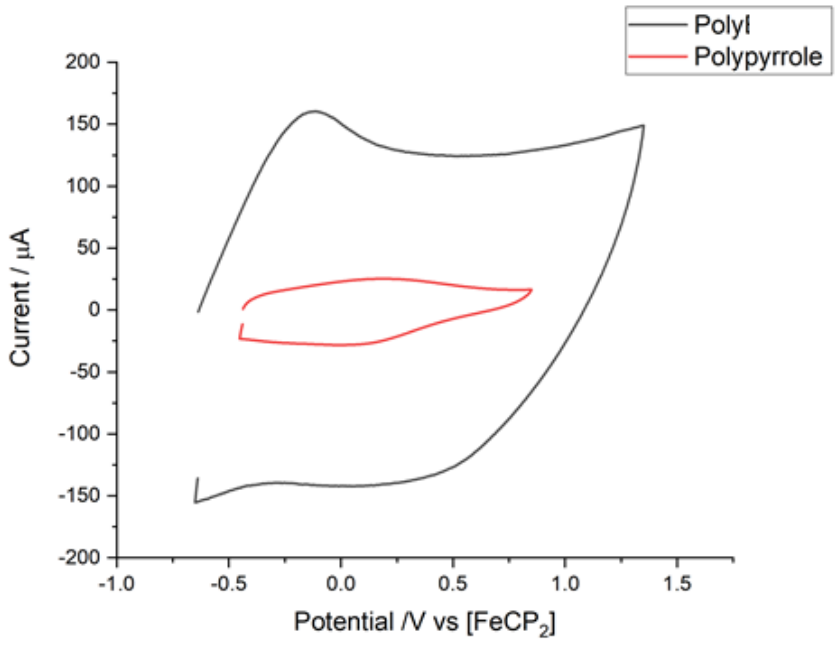

Figure 4.11 20 cycle film, comparison between polypyrrole and poly**1** in capacitance, 0.1 M of $BarF_{20}$ in DCM at 100 mV/s.

Table 4.2 Specific capacitance values obtained from cyclic voltammograms of poly**1**, poly**2** and poly**3** films on **GC** electrodes (20 polymerisation cycles), recorded at 10 and 100 mV/s scan rates in DCM.

	Specific capacitance (F/g)		
Sample	poly**1**	poly**2**	poly**3**
10 mV/s	50	11	39
100 mV/s	41	9	21.2

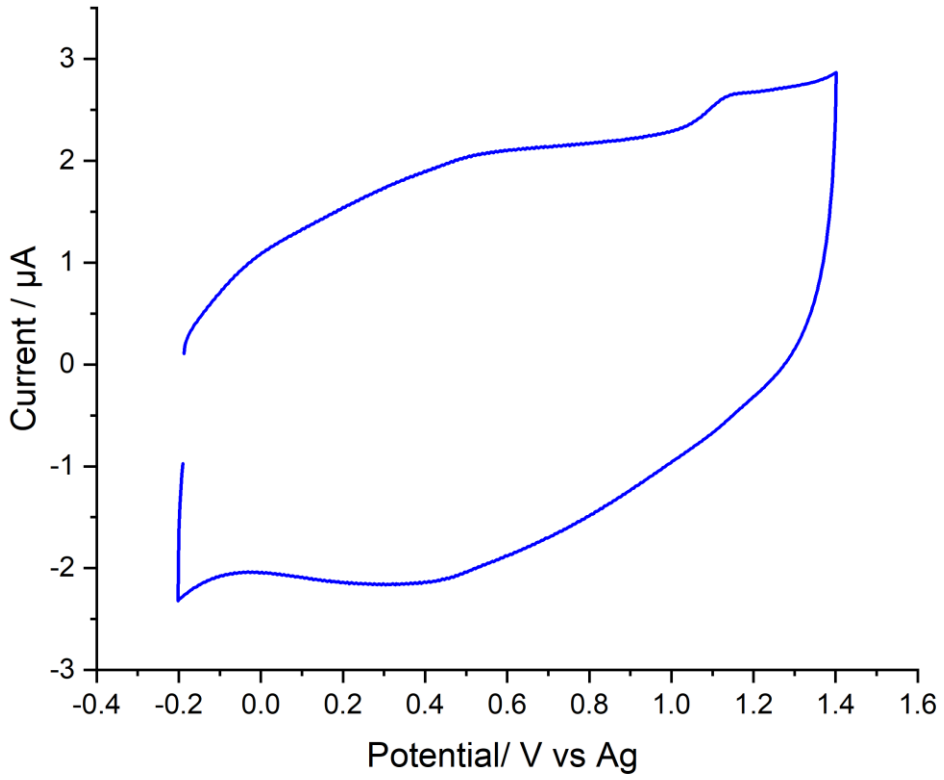

Figure 4.12 CV of a 20 cycle film of poly**2** in 0.1 M $BarF_{20}$ in DCM at 100 mV/s.

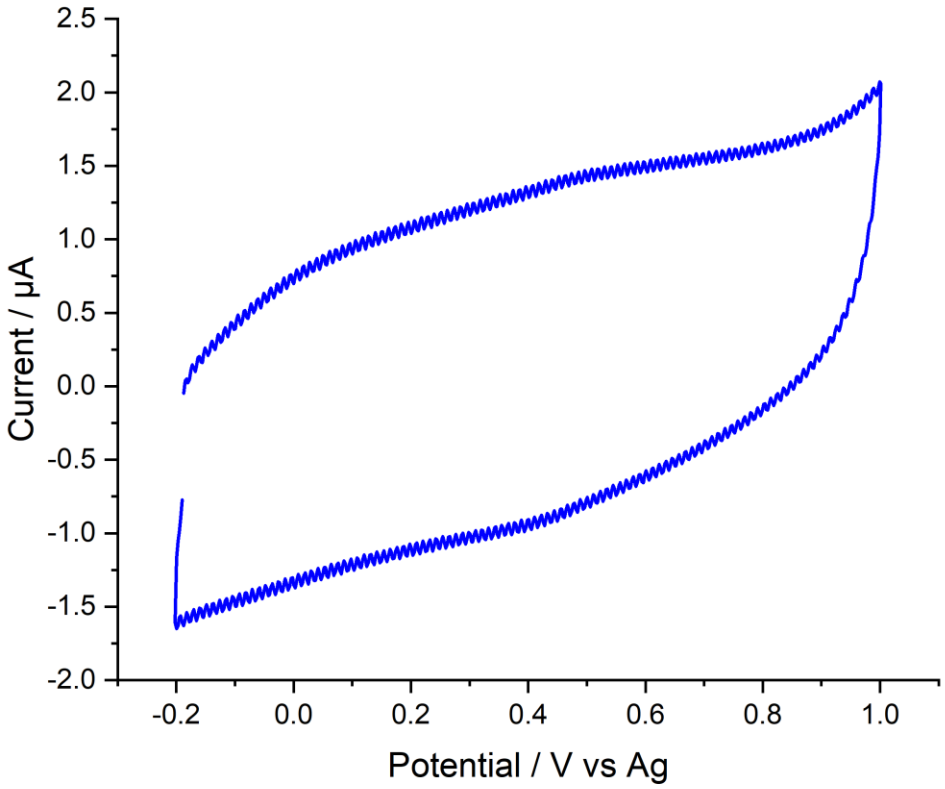

Figure 4.13 CV of a 20cycle film of poly**3** in 0.1 M $BarF_{20}$ in DCM at 100 mV/s.

Figure 4.12 is the cyclic voltammogram of poly**2** after 20 electrodeposition cycles, at a scan rate of 100 mV/s. Figure 4.13 shows the cyclic voltammetry of poly**3**, also after 20 electropolymerisation cycles at the same scan rate. The specific capacitance of poly**1**, poly**2** and poly**3** were calculated according to equation number 21 and shown in table 4.2, using EQCM data to estimate the mass deposited. The specific capacitance of poly**1** was 50 F/g at 10 mV/s and 41 F/g at 100 mV/s which are higher than specific capacitance of poly**2** and poly**3** according to table 4.2. The specific capacitance of PPy at 100 mV/s calculated from CV is 79 F/g.

4.3.6. Galvanostatic (charge-discharge) measurements

4.3.6.1. Galvanostatic (charge-discharge) measurement of Poly1

Galvanostatic (charge-discharge) measurements were carried out by modifying the electrode with Poly**1**, inserting the electrode in blank electrolyte solution and running for 6000 cycles.

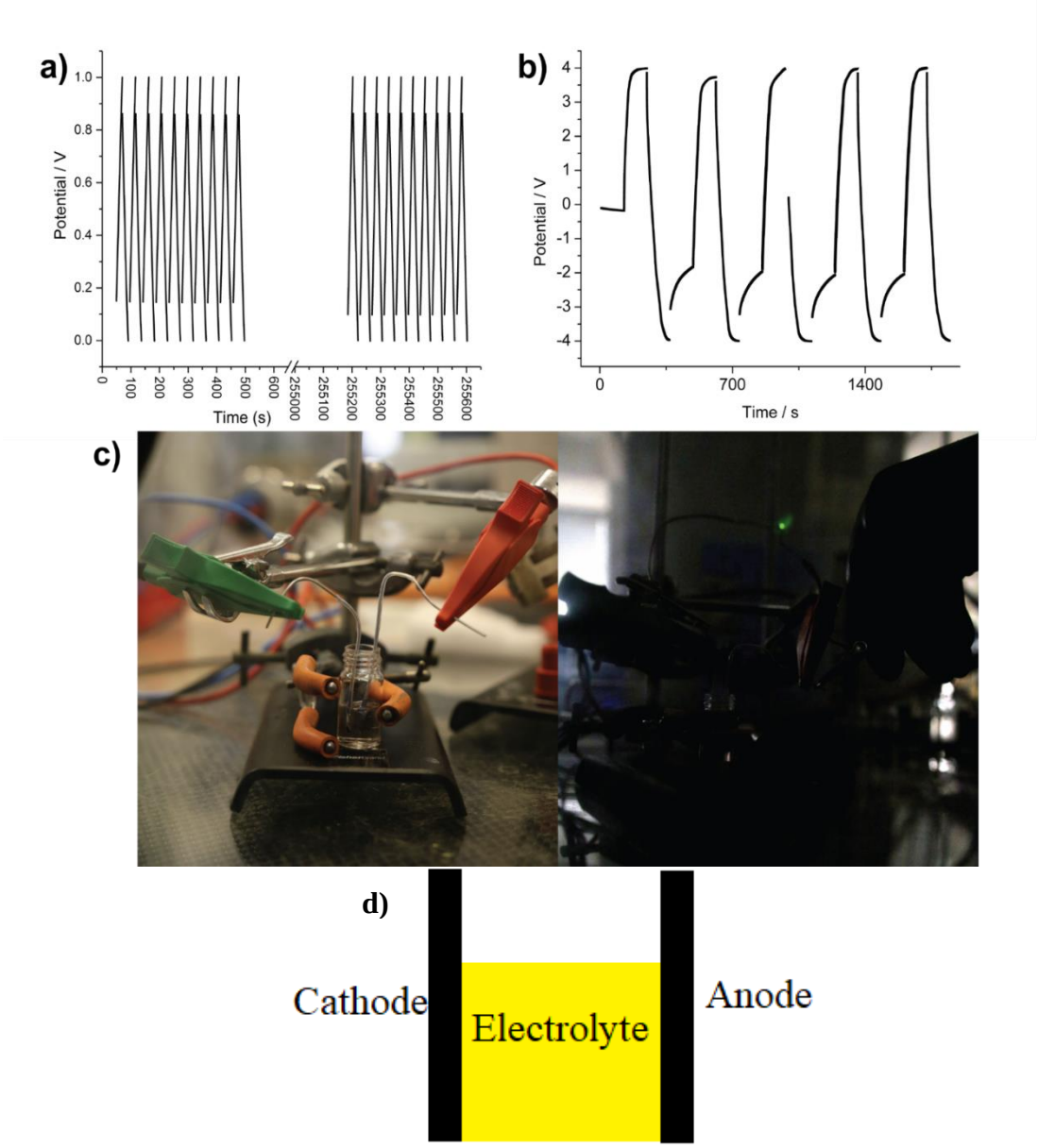

Figure 4.14 a) The first ten and last ten cycles of a series of 6000 galvanostatic charge–discharge cycles recorded for a poly(**1**) modified **GC** electrode immersed in DCM containing 0.1 M $[^{n}Bu_4N][B(C_6F_5)_4]$ at 1 A/g over a 0–1 V range; **b)** Repeated galvanostatic charge–discharge cycles recorded for a symmetric poly(**1**):poly(**1**)–modified **CC** supercapacitor in DCM containing 0.1 M $[^{n}Bu_4N][B(C_6F_5)_4]$ at 20 A/g; **c)** images of the symmetric poly(**1**):poly(**1**)–modified **CC** supercapacitor assembly in b) during charging (left) and discharging (right) to illuminate a green LED connected across the capacitor device terminals. The data is obtained from James Courtney, Wildgoose group. (**d**) Shows an example of electrochemical cell that applied on Poly**1.**

4.3.6.2. Galvanostatic (charge-discharge) measurements of poly2 and poly3

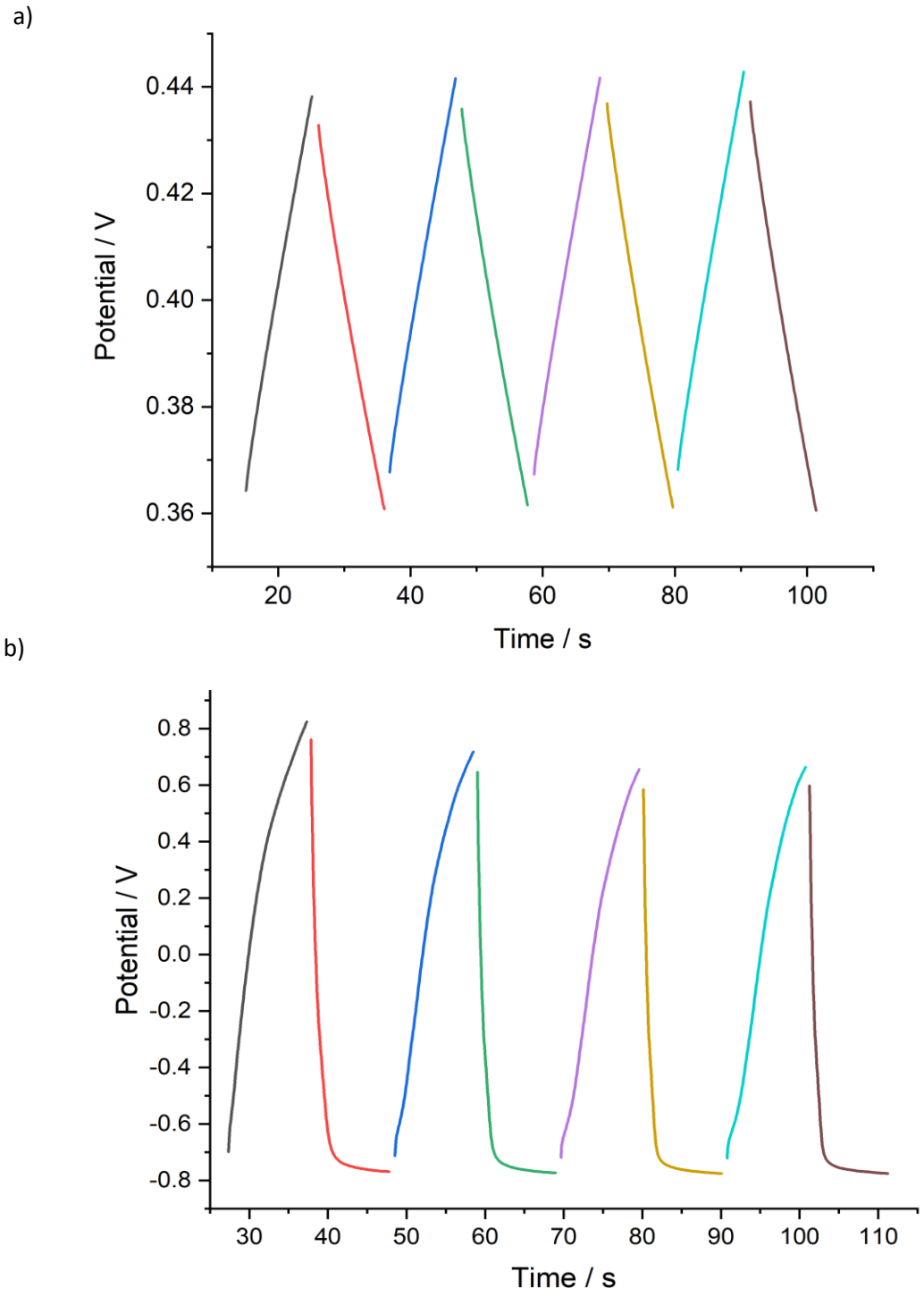

Figure 4.15 a) Charge-dischage of, poly**2**, b) charge-discharge of poly**3** with 0.1 M of $BarF_{20}$ in DCM.

Figure 4.14 shows galvanostatic charge discharge of poly**1**. The charge-discharge was repeated for 6000 charge–discharge cycles. As can be seen from Figure 4.14 the resulting charge–discharge curves are stable over 6000 repetitive cycles, with no signs of voltage instability of the poly**1** material or other degradation in performance.

Figure 4.15 (a) shows the first charge-discharge of Poly**2** which was repeated for 2000 cycles. Figure 4.15 (b) represents charge-discharge of poly**3** that repeated 2000 cycles.

For all three polymers, the average specific capacitance recorded for GCE electrode under these conditions can be estimated from the slope of the galvanostatic discharge curve according to equation (27) in chapter 2.

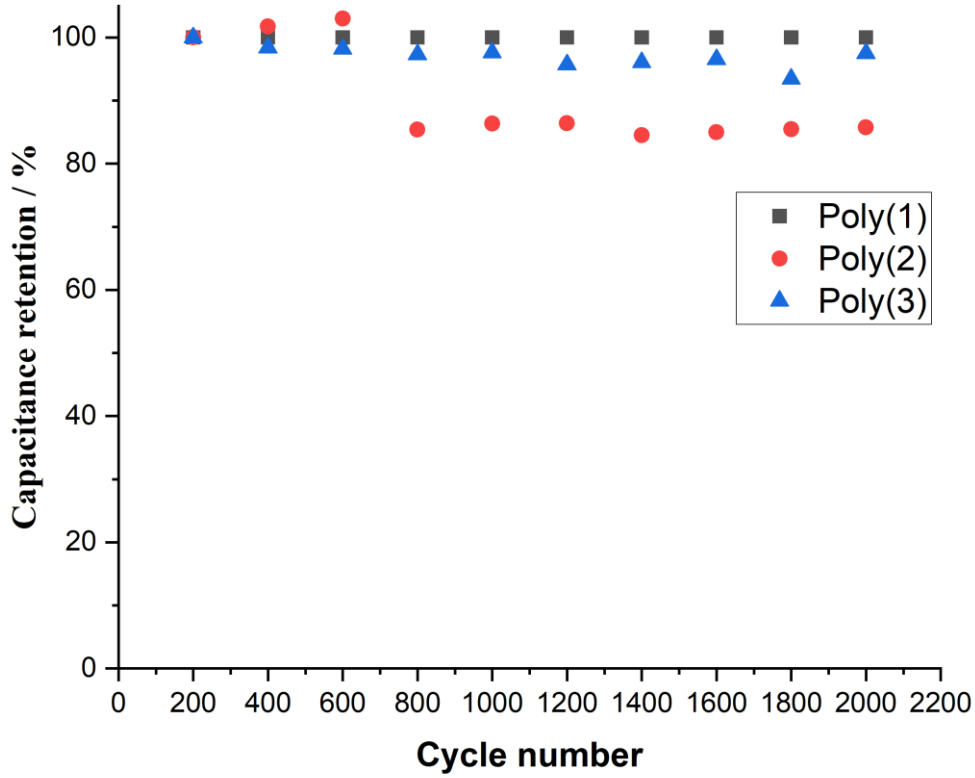

Figure 4.16 Capacitance retention of poly**1**, poly**2** and poly**3** are 2000 cycles in 0.1M of $BarF_{20}$ in DCM.

Table 4.3 Specific capacitance of poly**1**,poly**2** and poly**3**

Sample	F/g
Poly**1**	90.4
Poly**2**	19
Poly**3**	48.1

Table 4.3 shows the specific capacitance of poly**1**, poly**2** and poly**3** from GCD that was calculated according to equation number 27 (chapter 2) by dividing capacitance which calculated from GCD of each material by the mass of material. It is likely that GCD gives higher values because it reveals capacitance from slower processes that the CV timescale does

not pick up. This is also seen to some extent in the difference between capacitance measured at 10 mV/s and 100 mV/s in the CV. According to table 4.3, poly**1** shows high specific capacitance (90.4 F/g) compared to poly**2** (19 F/g) and poly**3** 48.1 F/g. in the same way, the specific capacitance of poly**1** that calculated from cyclic voltammetry was 41 F/g which is higher than poly**2** (9 F/g) and poly**3** (21.2 F/g). The values for poly**1** are significantly lower than those obtained by Courtney and Wildgoose, the reasons for this are subject to further investigation that is beyond the scope of this thesis.[11]

Poly**1**, poly**2** and poly**3** all have high molecular weights for their monomers. These are 411.00 (**1**), 575.55 (**2**) and 503.09 g/mol for (**3**) vs only 67.09 g/mol for pyrrole. Supposing a similar doping level (0.33 per monomer) and using the same voltage range as poly(pyrrole) allows theoretical maximum capacitance to be approximated of 100 F/g for poly**1**, 72 F/g for poly**2** and 83 F/g for poly**3,** while poly(pyrrole) has a theoretical maximum capacitance of over 600 F/g.[12] In the literature, and in our CV measurement, the typical specific capacitance of polypyrrole is in the range between 40 to 100 F/g, [13] in other words, no more than 1/6 of the theoretical maximum. For poly**1**, we obtain 50 F/g by CV 90 F/g by GCD), much closer to the theoretical maximum of 100 F/g. This shows that, considering molecular weight, Poly**1** is performing better than the other borane derivatives and PPy and getting unusually close to its supposed theoretical maximum capacitance – potentially suggesting different charge storage mechanisms to PPy.

4.3.7. Electrochemical impedance spectroscopy measurements (EIS)

EIS is a powerful technique to study kinetics and investigate poly**1**, poly**2** and poly**3** on the surface of carbon electrodes. This was carried out using a three electrode system at with a blank solution with a frequency range from 10 to 10^6 Hz. The electrochemical impedance spectroscopy was carried out in capacitive region to get the comprehensive details about poly**1**, poly**2** and poly**3** properties. Figures 4.17, 4.18 and 4.19 show the results and the electrochemical circuit fit used to fit the results. For all cases, Nyquist plot shows two parts, a semicircle which represents the highest frequency area that corresponds to the charge transfer resistance. The second part is the straight line which represents the low frequency, and it shows the ion (electrolyte) charging during charge-discharge process. The Bode plot shows the relationship between the frequency and impedance *z*. According to figure 4.17(b), it is clear that poly**1** has less impedance than conventional PPy and this means higher capacitance can be expected for poly**1** than PPy.

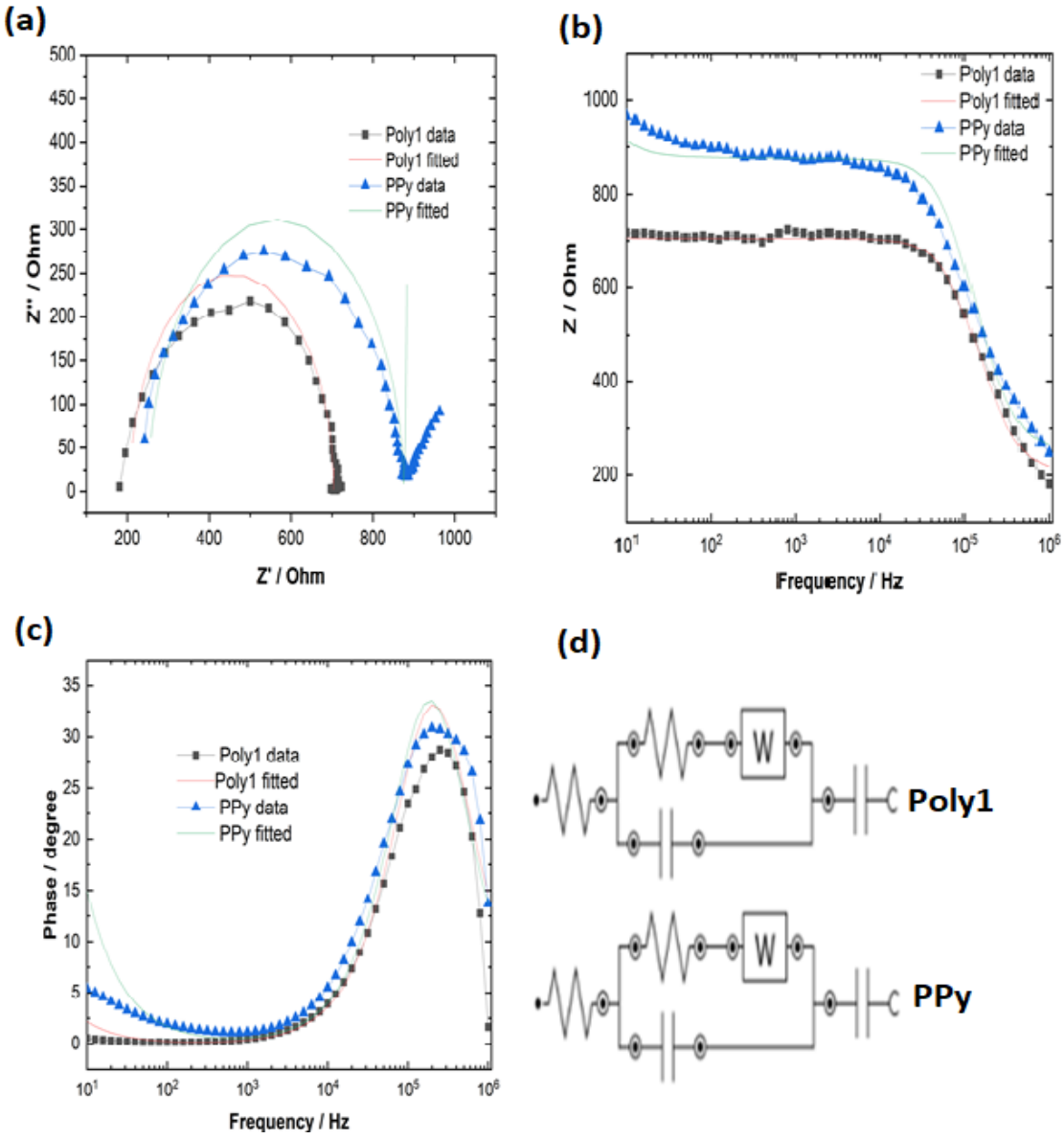

Figure 4.17 Poly**1** and PPy with 0.1 M of [^{n}Bu$_4$N]BF$_4$ in CH$_3$CN.

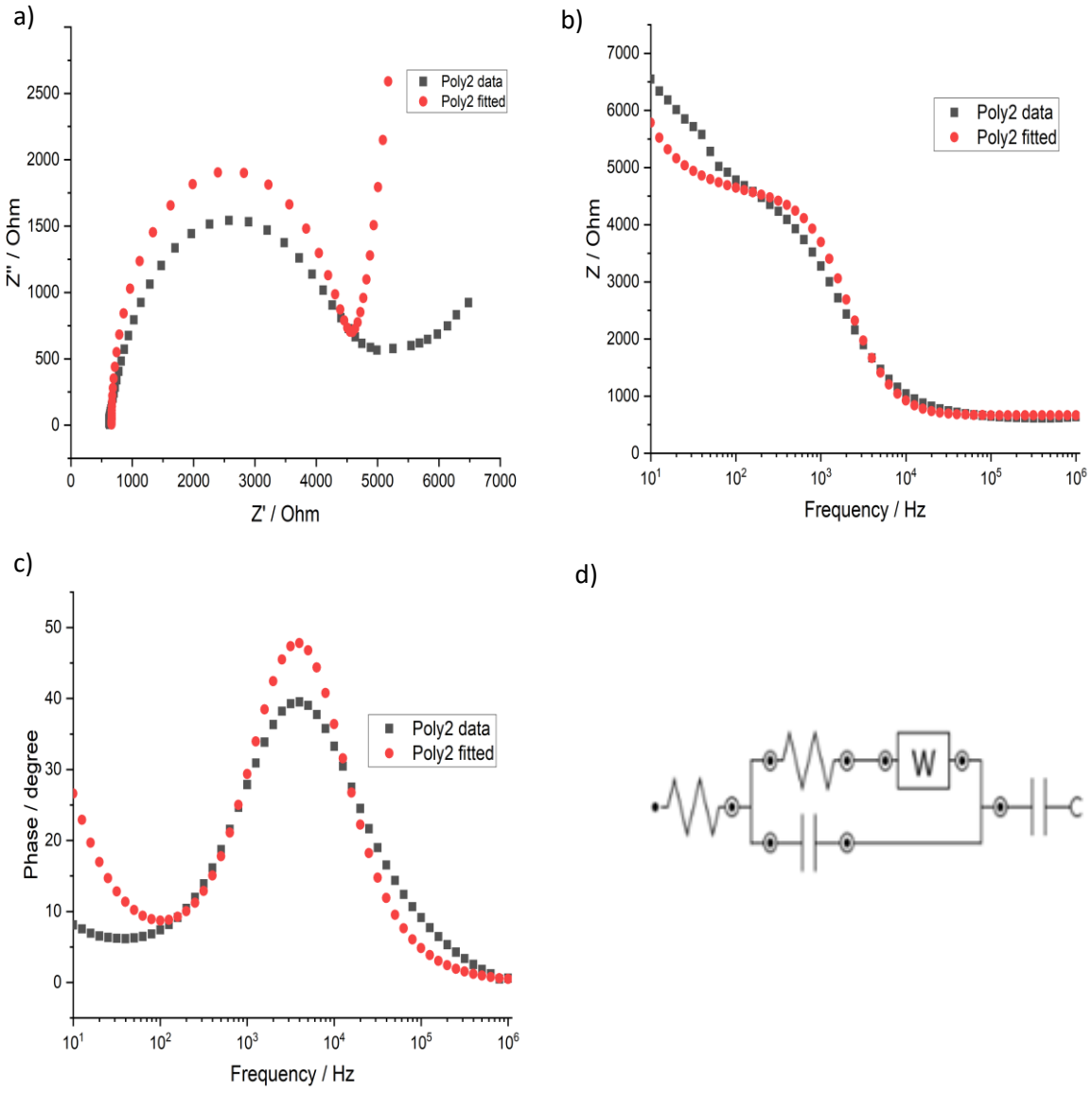

Figure 4.18 a) Nyquist, b) Bode, c) Phase plot of poly**2** in 0.1 M of $BarF_{20}$ in DCM with three electrode system.

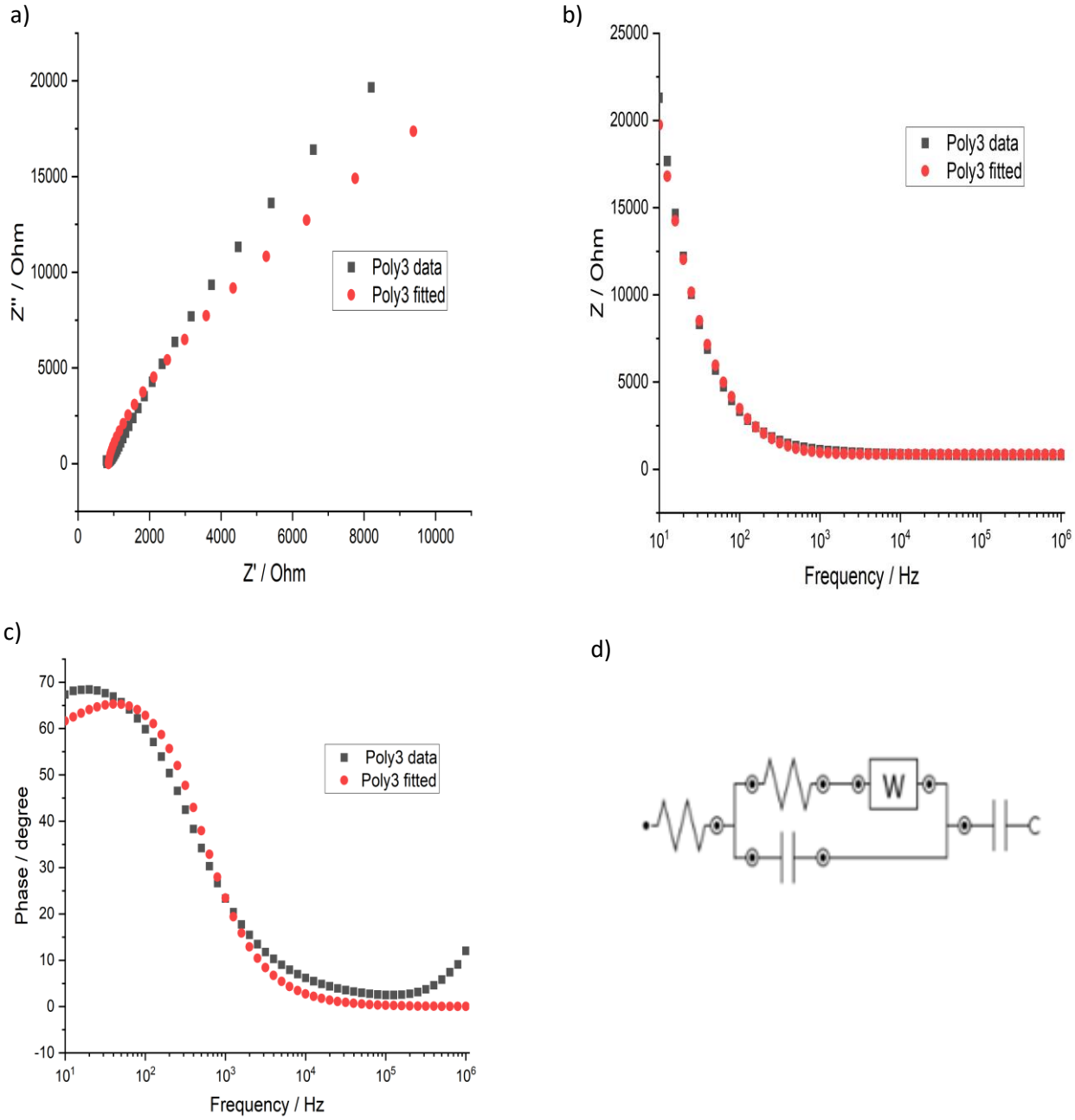

Figure 4.19 Poly**3** with 0.1 M of $[^{n}Bu_4N]BF_4$ in DCM.

Table 4.4 Electrode behaviour (Poly**1**, PPy, Poly**2**, Poly**3**) calculated from the electrochemical circuit fit of the experimental EIS data.

Sample	Rs(Ω)	R1(Ω)	C1(F)	C2(F)	Y∘(μMho)
Poly**1**	206.19	498	2.82×10^{-9}	6×10^{-4}	209
PPy	251.56	622.79	2.521×10^{-9}	7×10^{-5}	10.4
Poly**2**	663.81	3735.7	2.8421×10^{-8}	9×10^{-6}	113
Poly**3**	855.57	6.7×10^{-5}	3.7451×10^{-7}	9.9×10^{-5}	4.13

Table 4.4 shows the results calculated from the electrochemical circuit fit of the electrochemical impedance spectroscopy experiments data for all materials (poly**1**, PPy, poly**2** and poly**3**. *R*s is the resistance of solution, according to table 4.4 poly**1** has less resistance compared to other materials. C_1 and R_1 are the electric double layer capacitance and resistance. According to table 4.4 the capacitance of electric double layer is different for poly**2** and poly**3** to poly**1** and PPy which all carried out in the same condition of electrolyte and solvent. C_2 represent the capacitance of material and according to Table 4.4, poly**1** shows highest capacitance compared to other materials – consistent with other measurements.

4.3.8. Spectroelectrochemistry of polypyrrole and poly1

Spectroelectrochemical measurements were carried out because formation of charge carriers (polarons and bipolarons) in polypyrroles can be observed in the UV-visible spectra. Because Poly**1**, compared to PPy, appears to get much closer to its theoretical maximum specific capacitance, we used spectroelectrochemistry to observe bipolaron formation and see if the spectra suggested any electronic differences.

a)

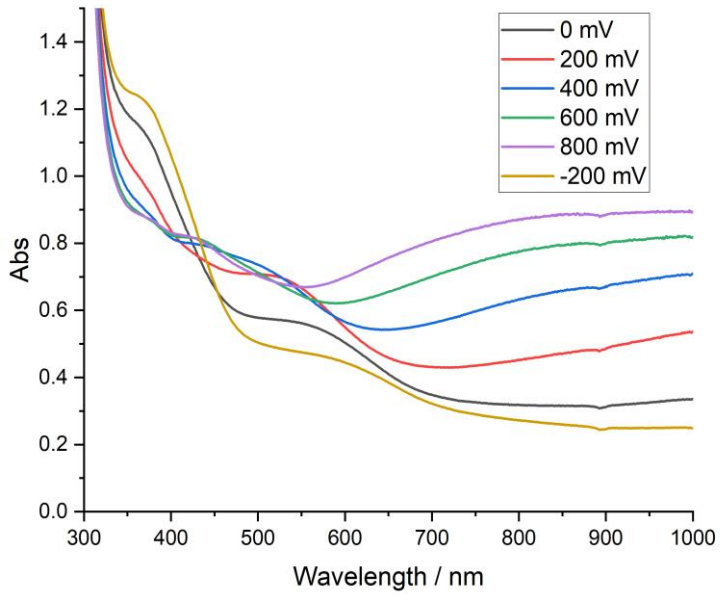

b)

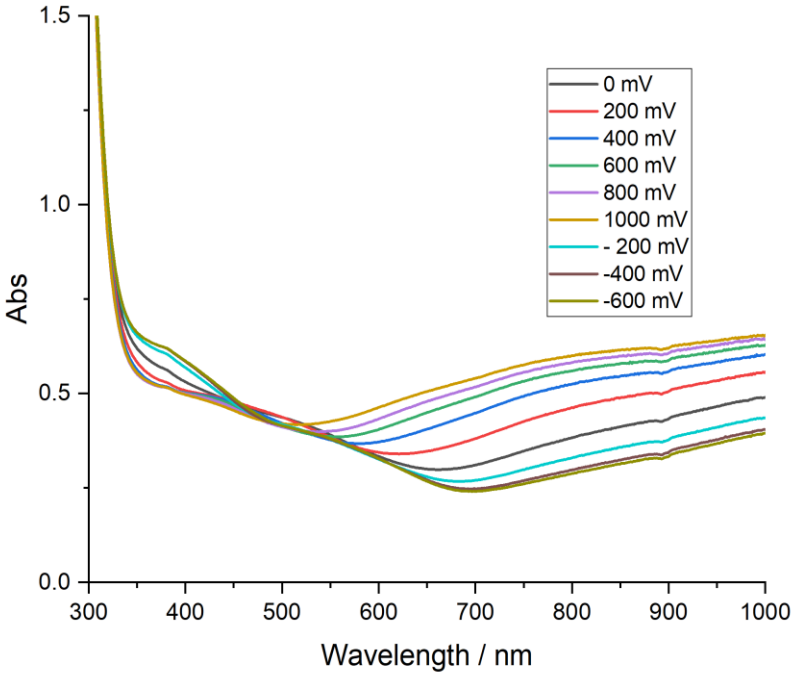

Figure 4.20 Poly**1** (a) and Polypyrrole (b) with 0.1M of $^{n}Bu_4ClO_4$ in CH_3CN. Potentials are vs solid state Ag / AgCl reference.

Films for spectro-electrochemistry were prepared on conductive fluorine tin oxide (FTO) glass using by cyclic voltammetry with 10 cycles. Then, the film tested by spectroelectrochemistry using blank solution of 0.1 $TBAClO_4$ in acetonitrile. Spectroelectrochemistry of poly**1** and PPy exhibit similar spectra for oxidized films of poly**1** and PPy. Both figures 4.20 a and b show a broad absorption at wavelengths above 600 nm. This indicates formation of the bipolarons which relate to conductivity and charge storage for both poly**1** and PPy. The PPy spectrum curves up towards a maximum beyond 1000 nm. This is consistent with literature showing an absorption maximum of around 1200 nm (1.0 eV) for oxidized PPy,[14] but poly**1** appears to reach a flat maximum between 800 and 900 nm. Therefore, the difference implies an electronic influence of the borane groups on the chain of PPy and bipolarons, or transitions emerging within the borane groups as positive charge is delocalised onto them. In addition, more evidence for the influence of the borane groups is seen in the greater increase in low energy absorption for poly**1** compared to PPy. Deposition of the film is not perfectly uniform, and the masses deposited on FTO are unknown, but the similar absorbances at 500 nm (where there are no absorptions from the borane) suggest that a similar amount of PPy backbone is seen in both measurements. Therefore, the greater increase in low energy absorption for poly**1** indicates more charge carriers form and storage of more charge per formula unit.

Generally, the borane group in poly**1** (and poly**2**/**3**) may facilitate improved performance through two mechanisms. First, the bulky $B(Ar)_2$ unit may lead to a more porous, less dense structure as has been shown for inclusion of bulky anions.[15] The bulk provides and prevents collapse of ion channels leading to improved charge transport and stability, and gives greater accessibility of all of the polymer for oxidation and increased contribution from double-layer charging through the porous polymer

matrix. Some evidence is seen for this in the lower resistances found in impedance fits, and in the lower density for poly**2** (though not poly**1**) suggested by the combination of SEM and EQCM results. The second mechanism is suggested by the spectroelectrochemistry through the different oxidised spectrum (different peak) indicating electronic interaction between borane and pyrrole in poly**1**. Lone pair donation from F^- could stabilise positive charge and enable its delocalisation onto the borane. This likely happens in poly**1** but not poly**2** because F lone pairs interact better with the aromatic system than Cl lone pairs. This may be enabling the borane in poly**1** to stabilise a higher level of oxidation on the pyrrole.[16] Thus, when poly**1** is oxidised, a large amount of the electron density may be removed from the borane unit which increases the accessible charge per monomer to result in a higher theoretical maximum capacitance C_{Th} than would be assumed based on underivatized PPy.

NOTE IN PROOF: Since this thesis was examined fresh EQCM data has been obtained for Poly**1** indicating a much lower frequency change (and thus lower mass deposited) per cycle than presented above. However, determination of capacitance by CV at 100 mV/s directly on the EQCM substrate, giving certainty in mass, produced a very similar specific capacitance value (45 F/g) to that presented above which was obtained by measuring capacitance on a voltammetry electrode and *estimating* the mass based on the old (high mass) EQCM results. The new data are not presented here for the sake of consistency in approach: it has not been possible to perform the same measurements on poly**2** and poly**3**. The new EQCM data, combined with the existing SEM, could imply a lower density for the poly**1** film than PPy, as also suggested for poly**2**. However, this work has raised questions about the reliability of both the EQCM measurements, and the comparability of depositions carried out on EQCM substrates and voltammetry electrodes when there is a near eight-fold difference in area. Such issues are most likely

behind the very high (300 F/g) specific capacitance value reported for poly**1** by Courtney and Wildgoose in their patent:[11] having measured the capacitance directly on a known mass of poly**1**, we can be confident that its specific capacitance lies within the range of 40 – 90 F/g presented here.

4.4. Summary

Poly**1** poly**2** and poly**3** were characterised using a variety of electrochemical and other techniques. The specific capacitance of poly**1** was found to be of the order of 50 to 90 F/g, an excellent value considering its high molecular weight, possibly resulting from stabilisation of increased positive charge by the borane. Poly**1** also demonstrated a much wider stable operating voltage window when used in a symmetric supercapacitor device of ± 4 V and exhibited a more stable charge storage performance over 6000 charge–discharge cycles. The comparison of poly**1**, poly**2** and poly**3** shows that the specific capacitance of poly**1** is the highest. Poly**2** has the lowest specific capacitance, which is acceptable considering its high molecular weight and reduced ability of the chlorine groups to stabilise positive charge.

4.5 References

[1] K. Jüttner, C. Ehrenbeck, *Journal of Solid State Electrochemistry* **1998**, *2*, 60-66.
[2] E. S. Lee, J. H. Park, G. G. Wallace, Y. H. Bae, *Polymer International* **2004**, *53*, 400-405.
[3] W. Khan, T. Marew, N. Kumar, *Biomedical Materials* **2006**, *1*, 235.
[4] Y. Wang, C. Zhang, S. Li, L. Liu, *European Journal of Organic Chemistry* **2021**, *2021*, 3837-3849.
[5] C. Su, L. Wang, L. Xu, C. Zhang, *Electrochimica Acta* **2013**, *104*, 302-307.
[6] E. J. Lawrence, V. S. Oganesyan, G. G. Wildgoose, A. E. Ashley, *Dalton Transactions* **2013**, *42*, 782-789.
[7] G. Douglade, B. Fabre, *Synthetic Metals* **2002**, *129*, 309-314.
[8] L. Zhang, G. Xia, Z. Guo, X. Li, D. Sun, X. Yu, *International Journal of Hydrogen Energy* **2016**, *41*, 14252-14260.
[9] aJ. R. Lawson, R. L. Melen, *Inorganic chemistry* **2017**, *56*, 8627-8643; bN. L Guernion, W. Hayes, *Current Organic Chemistry* **2004**, *8*, 637-651.
[10] E.-L. Kupila, J. Kankare, *Synthetic Metals* **1995**, *74*, 241-249.
[11] G. G. Wildgoose, A. E. Ashley, J. M. Courtney, E. J. Lawrence, *PCT Int. Appl* **2019**, WO 2019012271.
[12] N. Mermilliod, J. Tanguy, F. Petiot, *Journal of the Electrochemical Society* **1986**, *133*, 1073.
[13] aG. Garcia-Belmonte, J. Bisquert, *Electrochimica Acta* **2002**, *47*, 4263-4272; bC. Xu, J. Sun, L. Gao, *Journal of Materials Chemistry* **2011**, *21*, 11253-11258; cD. Zhang, X. Zhang, Y. Chen, P. Yu, C. Wang, Y. Ma, *Journal of Power Sources* **2011**, *196*, 5990-5996.
[14] J. Bredas, J. Scott, K. Yakushi, G. Street, *Physical Review B* **1984**, *30*, 1023.
[15] M. D. Ingram, H. Staesche, K. Ryder, *Journal of Power Sources* **2004**, *129*, 107-112.
[16] A. E. Ashley, T. J. Herrington, G. G. Wildgoose, H. Zaher, A. L. Thompson, N. H. Rees, T. Krämer, D. O'Hare, *Journal of the American Chemical Society* **2011**, *133*, 14727-14740.

Chapter 5

Developing New electrode Material for Hybrid-Battery / supercapacitor application

5. Aim

The aim of the work in this chapter is to fabricate a new supercapacitor/ hybrid battery from anthraquinone as the negative electrode and the polypyrrole borane poly**1** as the positive electrode. In addition, the electrochemical behaviors of the AQ-poly**1** supercapacitor/hybrid battery are studied using different electrochemical techniques including cyclic voltammetry, electrochemical impedance spectroscopy (EIS), electrochemical quartz crystal microbalance (EQCM), and charge-discharge techniques. Also, measurement of specific capacitance was carried out by different methods including cyclic voltammetry and galvanostatic (charge-discharge) methods. Finally, after studying the electrochemical behaviors of the new hybrid battery/ supercapacitor, we applied device of the new hybrid battery/supercapacitor device to light LEDs successfully.

5.1. Introduction

Supercapacitors are the most demanding energy storage system currently comparable with the conventional lithium-ion batteries. This is because of their high power densities and their long cycle life stability.[124] Electrode materials are one of the keys to improve the performance of supercapacitors. The behaviour of Faradaic capacitance is controlled by redox reactions and ion diffusion.[125] Quinones as organic compounds have been used in many applications to store energy due to their fast redox (electrochemical) behaviour, good chemical durability and high capacitance.[126] For example, they have been used in aqueous flow batteries instead of vanadium.[127] It has been reported that anthraquinone is an effective way to increase

capacitance and store energy. For example, Wu *et al* reported that 2-aminoanthraquinone modified self-assembled graphene hydrogels increase specific capacitance of to 258 F/g at 0.3 A/g compared to unmodified graphene hydrogels 193 F/g.[128] Pickup *et al* used a supercapacitor of anthraquinone modified carbon fibre electrode with unmodified carbon fibre and Nafion as separator with 1 M sulfuric acid. As a result, the average capacitance was 40% and the energy density 56 to 86% higher than unmodified carbon fibre material.[129] Juanli Liu *et al* reported that modification of carbon cloth by oxidation with 1,5-diaminoanthraquinone and reduction of hydrazine provides high specific capacitance (921 mF/cm^2) at 1.0 mA/cm^2 and the capacitance remained 116% after 20000 cycles in 1.0 M H_2SO_4.[130] Recent research by Lei Xu *et al* examined a supercapacitor of 1,4,5,8-tetrahydroxy-anthraquinone/graphene which exhibits specific capacitance of 259 F/g at 1 A/g and retained 97.9% capacitance after 10000 cycles at 20 A/g.[131] Chen *et al* used anthraquinone with hierarchical porous carbon nanotubes which showed higher specific capacitance (710 F/g) at mass ratio of 7/5 compared with unmodified HPCNT (304 F/g) at 1 A/g .[74a] Campbell *et al* developed hybrid battery /supercapacitor of anthraquinone modified graphene macro-assemblies, which increased electrical energy storage capacity more than untreated graphene macro-assemblies 2.9 times.[71] Zhang *et al*, used 1,5-diaminoanthraquinone molecules on graphene material and the composite exhibit high specific capacitance (277 f/g) at 5 mV/s compare with the pristine DAA and RGO which are 7.5 F/g and 63.3 F/g respectively.[132] In all of these examples anthraquinone enhances reversible energy storage capacity, because the phenolic rings can add and extract two protons and two electrons to store energy.[133] This means anthraquinone has two electron reduction/oxidation Faradaic reactions that help to store two charges compared to many transition metal salts that can only store one electron.[134]

According to chapter 4 poly**1** has high specific capacitance and stability compared to other N-pyrrolyl-bis(pentachlorophenyl)boranes. Therefore, in this chapter for first time we fabricated a new hybrid battery/supercapacitor of AQ-poly**1** and studied the behaviors and specific capacitance, stability, and charge-discharge by using electrochemical methods. The combination of both (AQ-poly**1**) gives an excellent storage system, with fast charge-discharge with long cycle life and significantly increased specific capacitance compared to (AQ-CF) supercapacitor.

5.2. Experimental section

5.2.1. Electrochemical characterisation methods

Cyclic voltammetry experiments were performed in acetonitrile or DCM with supporting electrolyte $[^{n}Bu_4N]BF_4$ at a scan rate of 100 mV/s.

Galvanostatic charge-discharge experiments were measured by charging a supercapacitor at the maximum constant current and discharging at constant current throughout specific voltages.

Electrochemical impedance spectroscopy (EIS) measurements were performed at 0.01 V with Ag wire reference with a frequency range from 10 to 10^6 Hz that represents an evaluation of charge transfer resistance and electrolyte diffusion in both the anthraquinone and poly**1**(polyBarF_{10}) electrodes. For the supercapacitor of both materials (anthraquinone -poly**1**) the potential was set up at the capacitive potential of poly**1**. All EIS measurements were performed using three electrodes whereas asymmetric hybrid -Battery /supercapacitor used two electrodes, consisting of an anthraquinone film modified on carbon fibre as a cathode electrode and poly**1** modified on carbon fibre as the anode electrode. Experimental data were fitted using

the Randles equivalent circuit. All electrochemical measurements were performed using the Autolab PGSTAT302N potentiostat/galvanostat module (Metrohm).

5.3. Results and discussion

5.3.1. Cyclic voltammetry

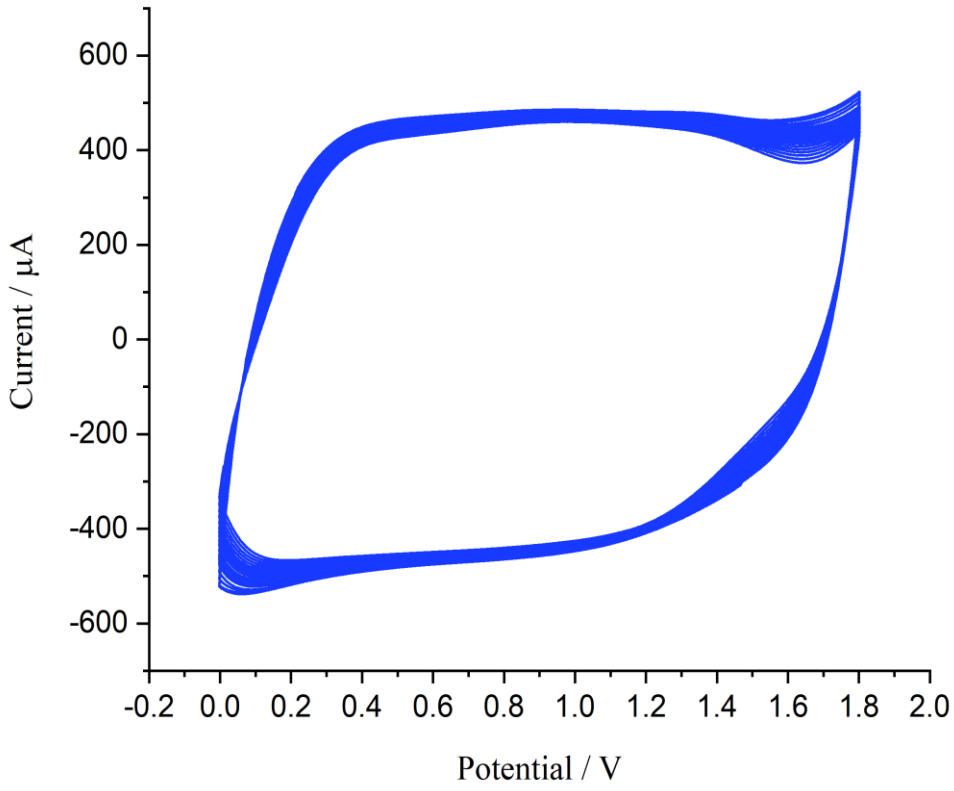

Figure 1.5 20 Cyclic voltametry of GCE modified with $(NC_4H_4)B(C_6F_5)_2$ in 0.1 M $[^nBu_4N][BF_4]$ and CH_3CN at 100 mV/s.

Figure 1.5 shows the stability of poly**1** in $[^nBu_4N][BF_4]$ with acetonitrile by using 20 deposition cycles. The potential window is wider than conventional polymers which is around 0 to 1.8 V compared with polypyrrole which is usually from 0 to 1 V. The cyclic voltammetry of poly**1** gives a near-rectangular shape, indicating near ideal capacitive behaviour, with high

capacitance indicated by the high charging and discharging currents. Poly**1** was tested in different electrolytes, but using $(NC_4H_4)B(C_6F_5)_2$ in 0.1 M $[^nBu_4N][BF_4]$ and CH_3CN provides the highest capacitance and this can be used as an anode to fabricate hybrid battery/supercapacitor.

5.3.2. Electrochemical Impedance spectroscopy (EIS)

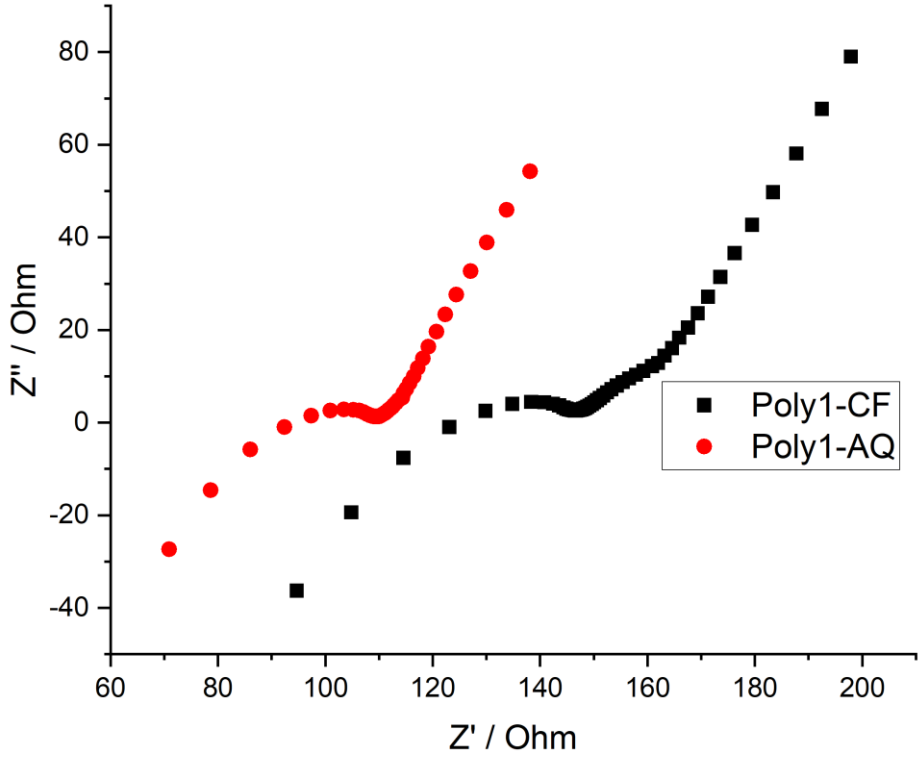

Figure 2.5 Nyquist plot of hybrid battry/supercapacitor of poly **1**-AQ. B) Nyquist plot of supercapacitor of poly**1**- CF.

Figure 2.5 shows the Nyquist plots of both Poly**1**-CF and Poly**1**-AQ. It can be seen that the semicircle of poly**1**-CF is larger than poly**1**-AQ, indicating higher resistance. Estimating from figure 2.5, the diameter of the poly**1**-AQ semicircle gives a resistance of *ca*. 40 Ohm whereas for poly**1**-CF it is close to 80 Ohm. Also, the straight line part for poly**1**-CF extends further into the low frequency domain, which may be linked to Warburg diffusion, while the shorter

straight line for poly**1**-AQ tends to indicate faster reaction, due to the absence of low frequency data associated with slower processes.

5.3.2.1. EIS of poly1- carbon fibre (poly1-CF)

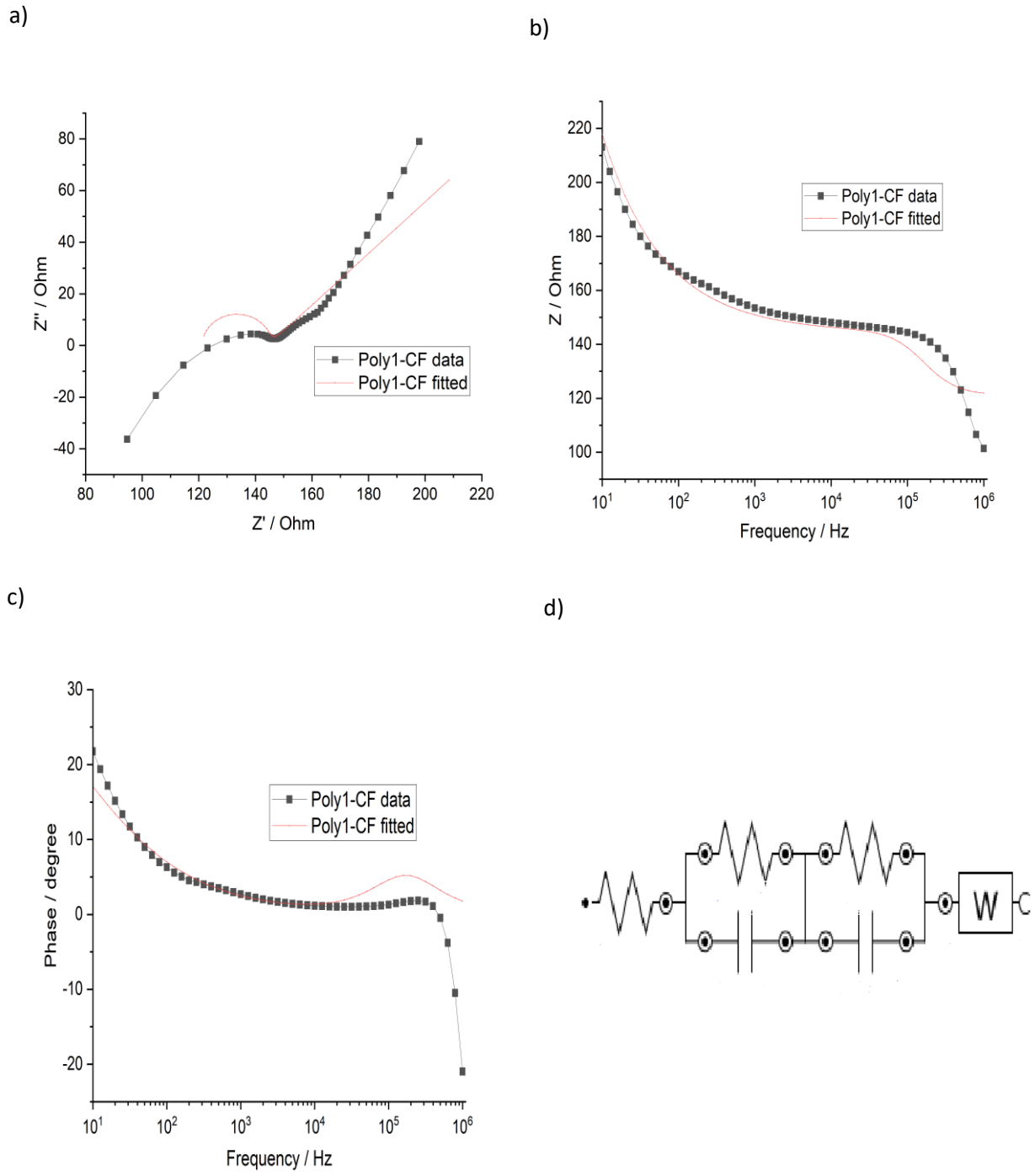

Figure 3.5 EIS of poly**1**-CF of hybrid battery / supercapacitor: a) Nyquist plot, b) Bode plot, c) Phase plot and d) Fitting circuit of poly**1**-CF.

5.3.2.2. EIS of poly1-anthraquinone(poly1-AQ)

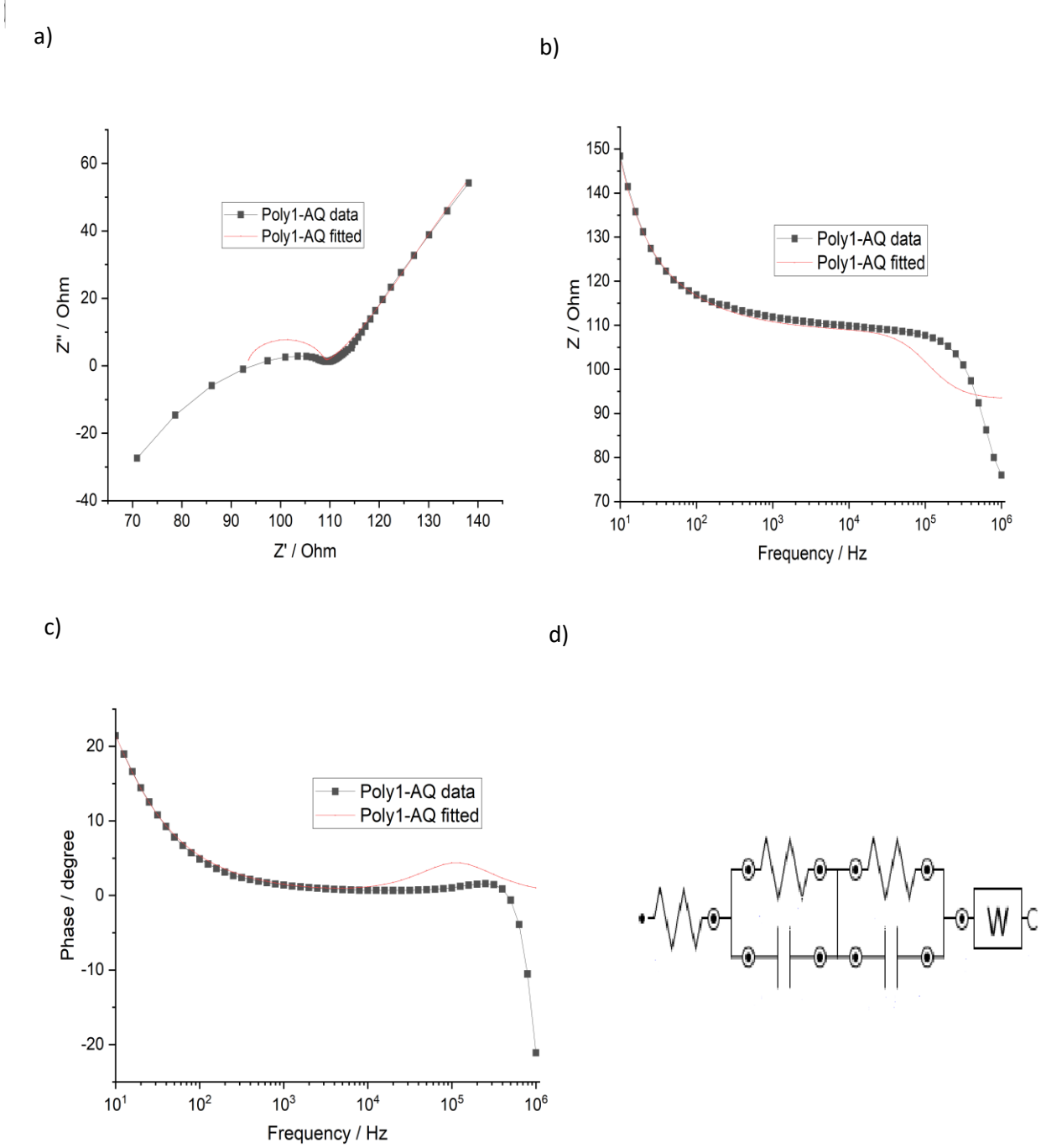

Figure 4.5 EIS of supercapacitor/hybrid battery of poly**1**-AQ: a) Nyquist plot, b) Bode plot, c) Phase plot, d) Fitting circuit of poly**1**-AQ.

Figures 3.5 and 4.5 represent electrochemical impedance measurement of poly**1**-CF and poly**1**-AQ respectively. The Nyquist plots (a) curves were fitted using modified equivalent electrical circuit models that shown in figure 4.5(d) which is two parallel RC circuit with a Warburg component. This model describes the supercapacitor which means R_1 and C_1 represent the resistance and capacitance of the electric double layer (EDL) whereas R_2 and C_2 describe the resistance and capacitance of the conducting polymer and R_s is the resistance of solution. According to figure 4.5 (a) the semicircle of poly**1**-AQ at high frequencies corresponds to charge transfer kinetics and the straight-line part corresponds to ion diffusion at low frequencies which is limited compared to the straight part of poly**1**-CF. A possible explanation for this is that AQ provides a reversible faradaic store of electrons at the cathode. This will improve performance as oxidation of poly**1** will reduce AQ at the cathode, while without AQ (just carbon fibre) a limited double layer can charge and then poly**1** can only be charged further by reduction of solvent which will be slow. The same goes in the opposite direction: electrons stored in AQ can reduce poly**1**, without this the electrons can only be provided by oxidising solvent which is slow. According to the Bode plots (figure 3.5b and 4.5b) of both poly**1**-CF and poly**1**-AQ, there is also evidence that the decreased resistance of poly**1**-AQ leads to increased capacitance in poly**1**-AQ of hybrid battery/ supercapacitor.

5.4. Galvanostatic (charge-discharge) of hybrid battery/supercapacitor of AQ-poly1

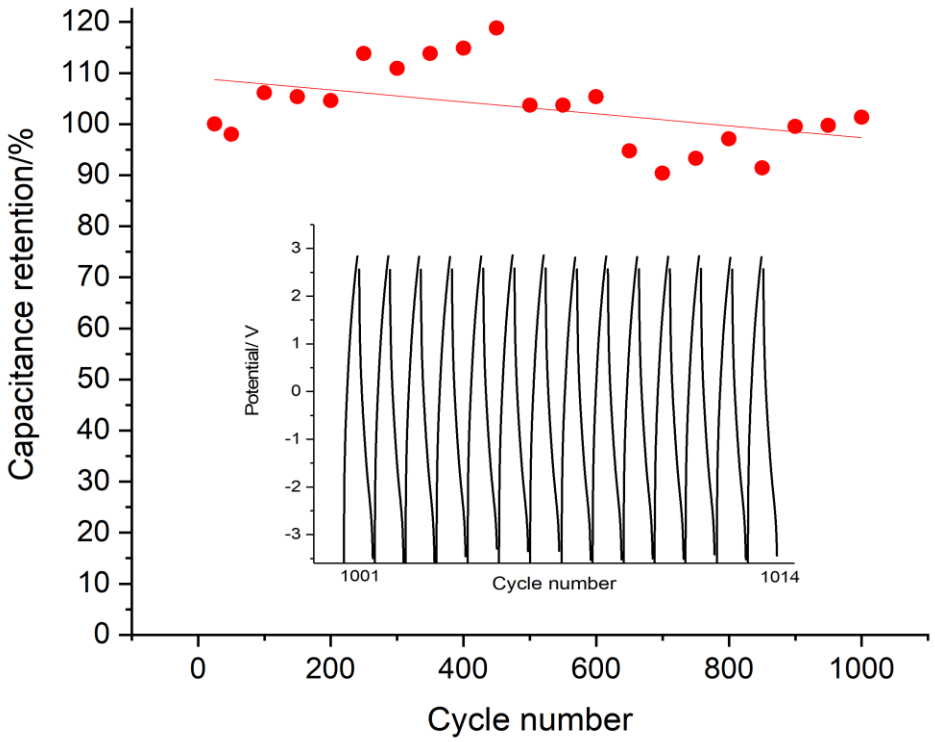

Figure 5.5 Capacitance retention of AQ-poly1 for the first 1000 cycles were performed under nitrogen using cyclic voltammetry (20 cycles) in 0.1 M tetrabutylammonium tetrakis(pentafluorophenyl) borate in dichloromethane at 100 mV/s.

Figure 5.5 shows the capacitance retention of AQ-poly**1** for the first 1000 cycles. The stability of capacitance is excellent the capacitance remained 90% after 1000 cycle which suggests a long cycle life. The specific capacitance of hybrid battery/ supercapacitor was calculated according to equation number 27 which mentioned in chapter 2.[135]

The capacitance for each electrode was calculated from discharge process according to following equation

$$C = 1/dv/dt \qquad (39)$$

5.5. Specific capacitance of hybrid battery/supercapacitor of AQ-poly1

The specific capacitance of poly**1**-AQ was calculated according to equation number 27, chapter 2. For the hybrid battery supercapacitor, the result was 142 F/g which is an excellent value compared to the specific capacitance of AQ-Li in chapter 3 (59 F/g). The result was consistent with research by K. Brousse *et. al*.[126] which modified carbide derived carbon (CDC) thin film electrodes with anthraquinone by using chronoamperometry technique, in 0.1 M NEt_4BF_4/CAN solution of anthraquinone diazonium derivatives. The capacitance of anthraquinone on CDC electrode gives larger double layer than pristine CDC film with capacitance of 44 mF/cm^2, 39% of capacitance remained after 500 cycles with 44 mF/cm^2.[126]

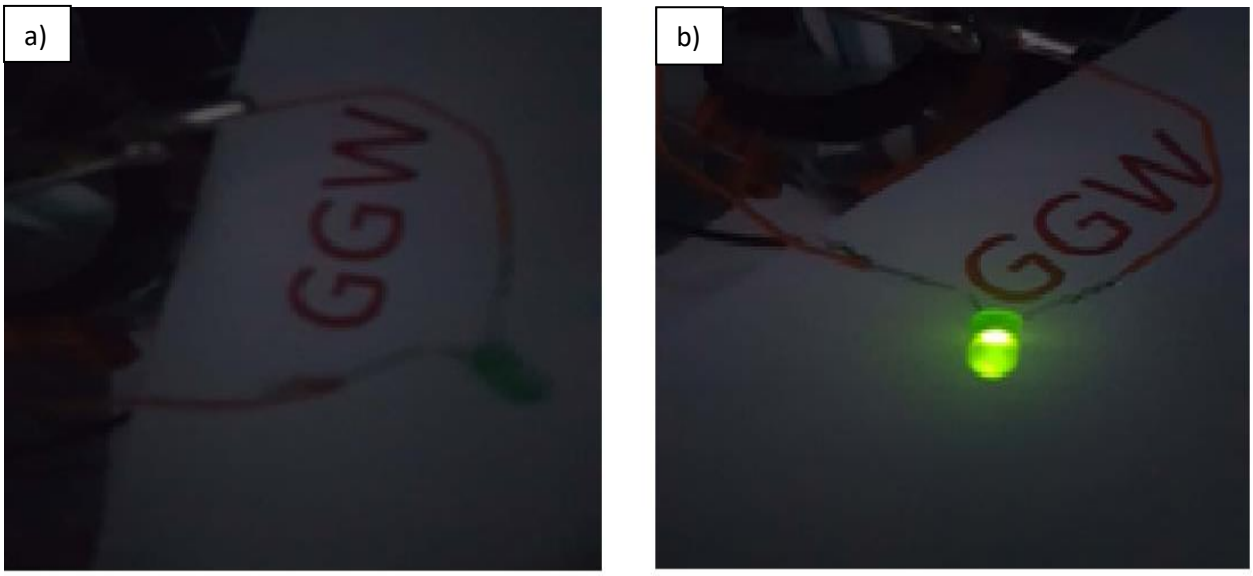

Figure 6.5 Shows a picture of an LED on and off during a galvanostatic experiment **a)** is the hybrid battery/supercapacitor during charging time, **b)** is during discharge time.

Figure 6.5 shows a picture of an LED on and off during a galvanostatic experiment. The hybrid battery /supercapacitor made from two parallel carbon fibre electrodes, the negative electrode was modified by anthraquinone, and the positive electrode was poly**1**.

5.6. Summary

Both AQ-Li and Poly**1** electrodes have been studied by cyclic voltammetry, galvanostatic (charge-discharge), electrochemical impedance spectroscopy (EIS). As a result, the combination of both hybrid electrodes in a supercapacitor achieved a high specific capacitance (142 F/g) and high capacitance retention (90% over 1000 cycles), indicating promise for the materials in energy storage.

5.7. References

[1] P. K. Adusei, S. Gbordzoe, S. N. Kanakaraj, Y.-Y. Hsieh, N. T. Alvarez, Y. Fang, K. Johnson, C. McConnell, V. Shanov, *Journal of Energy Chemistry* **2020**, *40*, 120-131.

[2] M. Yang, J. Xu, L. Zhang, Y. Shi, J. Xie, F. Lei, L. Fan, *Materials Letters* **2021**, 130095.

[3] K. Brousse, C. Martin, A. Brisse, C. Lethien, P. Simon, P.-L. Taberna, T. Brousse, *Electrochimica Acta* **2017**, *246*, 391-398.

[4] M. R. Gerhardt, L. Tong, R. Gómez-Bombarelli, Q. Chen, M. P. Marshak, C. J. Galvin, A. Aspuru-Guzik, R. G. Gordon, M. J. Aziz, *Advanced Energy Materials* **2017**, *7*, 1601488.

[5] Q. Wu, Y. Sun, H. Bai, G. Shi, *Physical Chemistry Chemical Physics* **2011**, *13*, 11193-11198.

[6] K. Kalinathan, D. P. DesRoches, X. Liu, P. G. Pickup, *Journal of Power Sources* **2008**, *181*, 182-185.

[7] J. Liu, Q. Wang, P. Liu, *Colloids and Surfaces A: Physicochemical and Engineering Aspects* **2020**, *588*, 124388.

[8] L. Xu, R. Shi, H. Li, C. Han, M. Wu, C.-P. Wong, F. Kang, B. Li, *Carbon* **2018**, *127*, 459-468.

[9] X. Chen, H. Wang, H. Yi, X. Wang, X. Yan, Z. Guo, *The Journal of Physical Chemistry C* **2014**, *118*, 8262-8270.

[10] P. Campbell, M. Merrill, B. Wood, E. Montalvo, M. Worsley, T. Baumann, J. Biener, *Journal of Materials Chemistry A* **2014**, *2*, 17764-17770.

[11] J. Ren, X. Zhao, J. Zhang, Q. Zhang, *International Journal of Electrochemical Science* **2016**, *11*, 2550-2559.

[12] S. Ryu, E. Kim, J. Yoo, *Electrochimica Acta* **2021**, *370*, 137809.

[13] T. J. Carney, S. J. Collins, J. S. Moore, F. R. Brushett, *Chemistry of Materials* **2017**, *29*, 4801-4810.

[14] T. Chen, L. Dai, *Journal of Materials Chemistry A* **2014**, *2*, 10756-10775.

Chapter 6

Covalently-Linked Polyoxometalate-Polypyrrole Hybrids: Electropolymer Materials with Dual Mode Enhanced Capacitive Energy Storage

6.Aim

This chapter investigates the electropolymerisation of pyrroles covalently derivatised with polyoxometalates, and the properties of the resulting hybrid electropolymer materials. These materials were originally synthesised and characterised by Ahmed Al-Yasari (Fielden group), showing by X-ray photoelectron spectroscopy (XPS) and energy- dispersive x-ray (EDX) elemental analyses that the polyoxometalate loading is higher than for conventional noncovalent inclusion films, and that the covalent attachment can prevent loss of polyoxometalates on initial reduction cycles. In this work, the electrosynthesis and basic electrochemical characterization have been repeated and different electrochemical methods applied including cyclic voltammetry, electrochemical impedance spectroscopy and galvanostatic charge-discharge measurements to assess the capacitive performance of the films. The polyoxometalates improve specific capacitance by both introducing an additional Faradaic charge storage mechanism and modifying the properties of the polypyrrole itself.

6.1. Introduction

Polyoxometalates (POMs) are polyatomic ions which contain three or more atoms. The transition metals are linked together to form closed 3-dimensional frameworks by shared oxygen atoms between them. POMs have structures that range from several angstrom to > 5 nm in size,[78] and their structural diversity gives rise to an unmatched range of physical and chemical properties.[79] They are inexpensive, have fast electrochemical redox reactions and

they are based on earth abundant metals (V, Mo, W). The variety of structures and scales of POMs has led to extensive research since the beginning of the 1990s.[79]

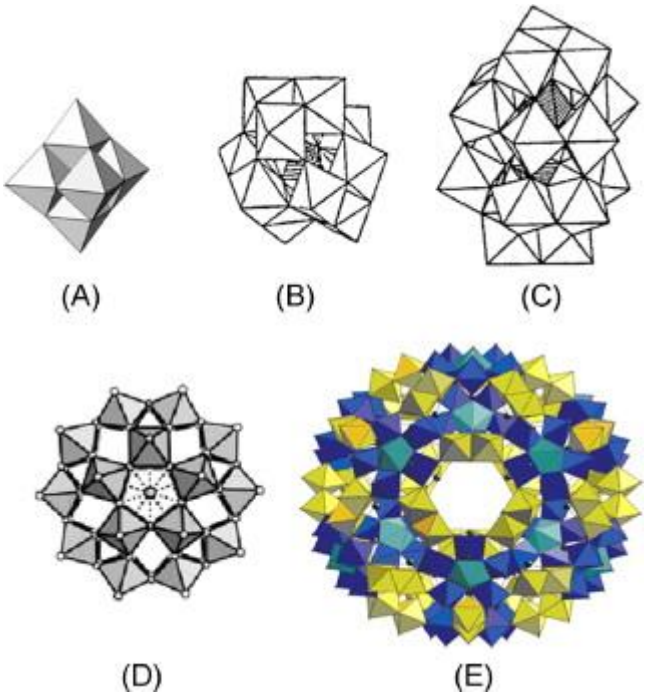

Figure 1.6 Typical structures of polyoxometalates, (A) is $[Mo_6O_{19}]^{n-}$, (B) is Keggin-type $[XM_{12}O_{40}]^{3-/4-}$, (C) Well-Dawson type $[X_2M_{18}O_{62}]$, (D) is Preyssler-type$[MP_5W_{30}O_{110}]^{14/12-}$, (E) Keplerate $[Mo_{132}O_{372}(CH_3COO)_{30}(H_2O)_{72}]^{42-}$. Figure was reproduced with premission from reference [78]

Polyoxometalates have become interesting materials for many researchers because of the stability of multielectron redox waves and structural diversity and chemical versatility which are suitable to store energy. Polyoxometalates have a large capacity for charge storage because they can accept many electrons. This has led to them being called in some literature electron reservoirs or sponges, for example, the Keggin anion can store up to 24 electrons.[137] This is can be adapted for specific demands at the molecular level. As an example of this, by inclusion of almost any heterometal[138] or connection of organic moieties.[139] [140] Combined with their facility for fast electron transfer, this can make them an excellent basis for energy storage

system, such as supercapacitors and batteries.[141] They can be used in rechargeable batteries as a cathode material. As an example of this, $[PMo_{12}O_{40}]^{3-}$ and $[PW_{12}O_{40}]^{3-}$ were successfully used as cathode material for lithium ion batteries.[142] However, application of polyoxometalates has been limited because of the low conductivity and high solubility of their solids, which are salts.[143] Therefore, polyoxometalates can be made more conductive by combining them with conductive compounds, such as conductive polymers with complimentary electronic and optical properties, to form hybrid materials.[144] The combination of POMs with conductive polymers can improve the charge storage and enhance the properties in composite materials. This can be achieved by adding other functional compounds, such as metal oxides or nanoparticles to supercapacitor materials.

Polyoxometalates have three general types which are heteropolyanions, isopolyanions and giant nanosized polymolybdate clusters.[78] Heteropolyanions contain one type of transition metal named addenda atom, and small proportion of other type atoms named heteroatoms. Mo, V and W are example of addenda atom where nonmetals and transition metals are example of the small type of heteroatoms. The most common structures represent of heteropolyanions are the Keggin and Dawson structures.[78] Isopolyanions consist of one type of high-valent group 5 or group 6 transition metals ions, for example the Lindqvist structure ($[Mo_6O_{19}]^{2-}$). Lindqvist type POMs are easy to synthesis and stable chemically and thermally.[78]

Giant nanosized polyoxomolybdate clusters is the third type of polyoxometalates, this class of polyoxometalates was described when Muller *et al.* reported in 1995 that a solution consisting of $\{Mo_{17}\}$-type-based species might be reduced and acidified more to yield a mixed-valence wheel-shaped cluster.[78, 145] An example giant polyoxomolybdate is $[Mo_{132}O_{372}(CH_3COO)_{30}(H_2O)_{72}]^{42-}$, (E) in Figure 1.6.

Because polyoxometalate clusters are soluble molecular species, they do not naturally form films. However, there are some methods to form polyoxometalate-based nanostructured thin films. There are two ways to incorporate POMs into the polymer matrix (e.g polypyrrole, polyaniline, polythiophene). The first is simple inclusion, for example a film of polymer is first deposited on the substrate by electropolymerisation or spin-coating techniques. After that, it is soaked in the solution which consist of POMs because this help to its passive diffusion into the polymer matrix.[78]

The second approach is covalent derivatization with polyoxometalates. This is very interesting because the covalent approach gives some advantages including enhancement of the stability of hybrid materials and improved communication between the POM and conjugated parts of the hybrid.[78, 146] Covalent attachment is less explored and completely new in polypyrroles.

Organoimido polyoxometalates are a class of polyoxmetalate derivatives described for the first time by Kang and Zubieta.[147] There is a lot of research related to organoimido derivatives because of their ease of synthesis and the strong electronic communication between POM and organic,[139] the vast majority focused on the hexamolybdate Lindqvist anion.[148]

6.2. Experimental section

All chemicals that used were purchased from Sigma-Aldrich (Gillingham, UK). The solvent was acetonitrile (CH_3CN) which was dried by reflux over calcium hydride (CaH_2). The electrolyte was tetra-n-butylammonium tetrafluoroborate ($[^nBu_4N]BF_4$). Monomer **1** ($[^nBu_4]_2[Mo_6O_{18}NC_6H_4NC_4H_4]$) and monomer **2** ($[^nBu_4]_2[Mo_6O_{18}NC_6H_4CCC_6H_4NC_4H_4]$) were synthesized by other members of the Fielden group.

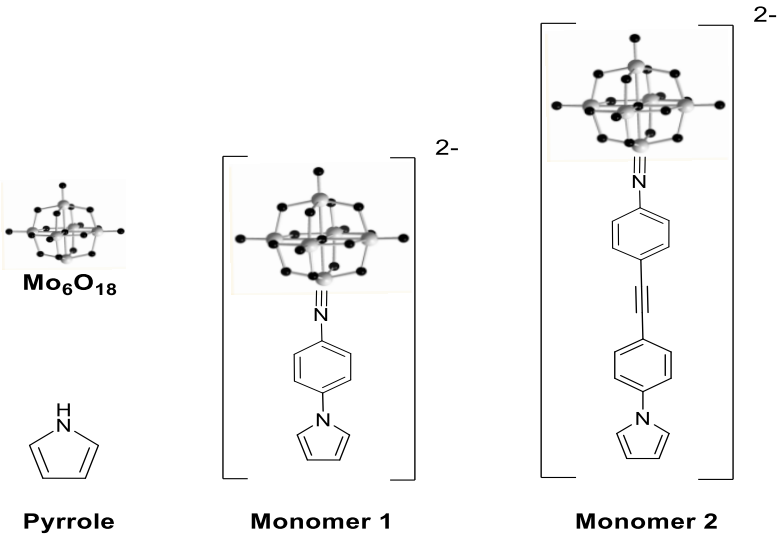

Figure 2.6 Scheme of pyrrole and organoimido-hexamolybdate anion based monomer**1** and **2**

All electrochemical measurements were performed by using an Autolab PGSTAT302N potentiostat/galvanostat module (Metrohm) with three electrode configurations. The working electrode was glassy carbon (GCE) electrode which was polished by using polycrystalline Diamond suspension 3µm and 1µm respectively and then alumina 0.3µm. The counter electrode was platinum (Pt) and silver (Ag) or Ag/AgCl as a reference electrode. The ferrocene (II/III) couple (Fc/Fc^{+}) is at 0.43 V versus Ag/AgCl. The experiments were performed under nitrogen. Cyclic voltammetry measurements were carried out using a three electrode system. Electrodeposition experiments were performed by cyclic voltammetry at potential range from -0.2 to 1.8 V by using glassy carbon (GCE), fluorine tin oxide (FTO) glass and Pt electrodes immersed in dry acetonitrile with 0.1 M $[Bu_4N][BF_4]$ electrolyte, 7×10^{-4} M POM derivative monomer 1 or 2, and 3×10^{-4} M pyrrole.

Electrochemical quartz crystal microbalance (EQCM) experiments were performed by using a carbon-coated 6 MHz quartz AT-cut crystal electrode (ø = 6.0 mm) immersed in dry

acetonitrile with 0.1 M [$^{n}Bu_4N$][BF_4] electrolyte, with three electrode system, and 7 ^{x} 10^{-4} M POM derivative monomer 1 or 2, and 3 ^{x} 10^{-4} M pyrrole.

Electrochemical impedance spectroscopy (EIS) experiments were carried out by using -0.9 to 1.5 V potentials at current range 1 mA with a frequency range from 10 to 10^6 Hz, to evaluate the charge transfer resistance and electrolyte diffusion of 10 deposition-cycles co-polymer films on glassy carbon electrode. The electrolyte was dry acetonitrile (CH_3CN) with 0.1 M [$^{n}Bu_4N$][BF_4] and the reference electrode was Ag wire.

Galvanostatic (charge-discharge) measurements were carried out on glassy carbon electrodes modified by using cyclic voltammetry (10 deposition cycle films of PPy, PPy-1 and PPy-2) and the potential was from 2 to -2 V against an Ag wire pseudo reference electrode. The electrolyte was 0.1 M [$^{n}Bu_4N$][BF_4] in dry acetonitrile (CH_3CN).

SEM, TEM and XPS experiments were performed by Ahmed Al-Yasari using high-resolution TEM at the Leeds EPSRC National Nanoscience Facility (LENNF). Sample preparation involved the use of FEI Nova200 dual beam SEM/FIB fitted with a Kleindiek micromanipulator and operated at 30 keV (5 keV for final cleaning) with beam currents between 5 and 0.1 nA, technique for cross-section TEM (for both film thickness determination and bulk morphological studies). By taking advantage of the combination of FIB with an SEM, it was possible to have high-resolution images for the surface of the polymer films. SEM images and EDX analysis were also measured at UEA using Philips CM200 FEGTEM fitted with a Gatan SC200 Orius CCD camera and an Oxford Instruments 80 mm2 EDX SDD running AZtec software.[149]

6.3. Results and discussion

6.3.1. Cyclic voltammetry

According to figure 3.6, the cyclic voltammetry of monomer **1** shows the same behaviour as $[Mo_6O_{19}]^{2-}$ in a reductive sweep but the potential is shifted around 180 mV more negative by the electron-donating organoimido group. The $E_{1/2}$ is approximately around -0.5 V vs Ag/AgCl for both monomer **1** and **2**, which shows similar behaviour. An oxidative scan of these monomers up to 1.8 V shows an irreversible oxidative behaviour with a peak at 1.4 V which is related to the pyrrole units (according to figure 5.6) but in the same way there is no sign of electropolymerisation and the oxidations resulted in poor and broad peak currents without deposition of films on the surface of electrode. This is because polymerization of N-substituted pyrroles is impeded by steric hindrance (presence of the sterically demanding phenyl ring and the (Mo_6) cluster), and there is a possibility of a weak interaction between the radical cation of the monomer and the negatively charge cluster which is $[Mo_6O_{18}NAr]^{-2}$.[149, 151]

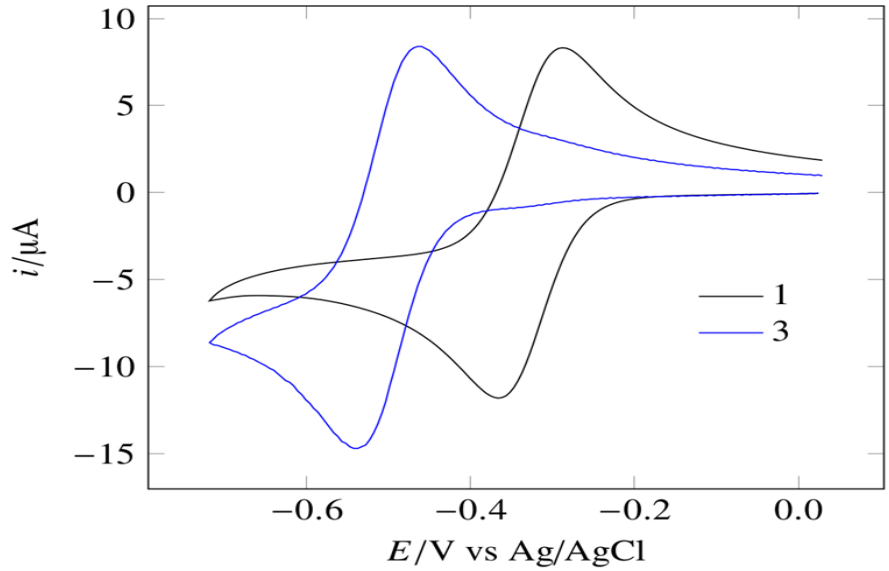

Figure 3.6 Cyclic voltammogram of $[Mo_6O_{19}]^{2-}$ (black trace) and monomer1 (blue trace) in 0.1 M $[^nBu_4N]BF_4$/MeCN at 25 °C vs Ag/AgCl at scan rate 100 mV/s.[150]

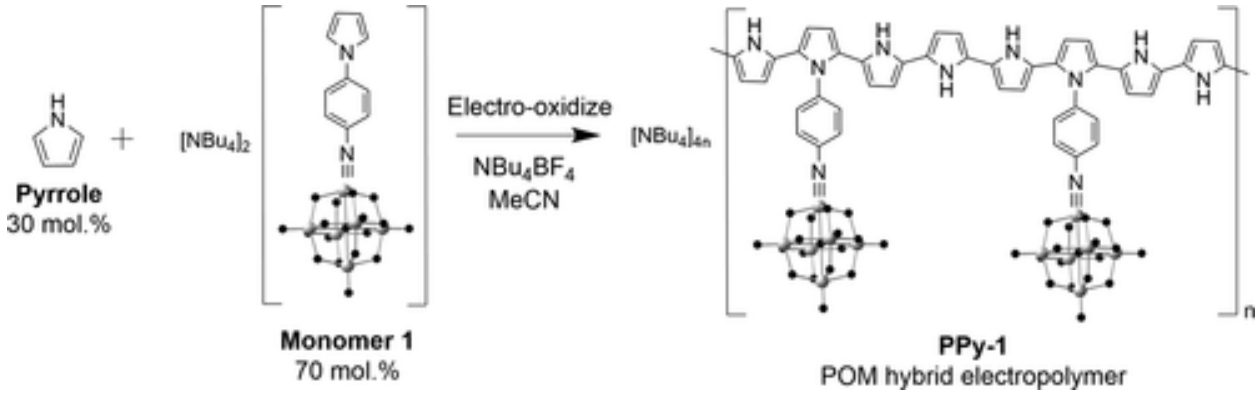

Figure 4.6 Scheme of Electropolymerization of Monomer **1** to produce PPy-**1**.

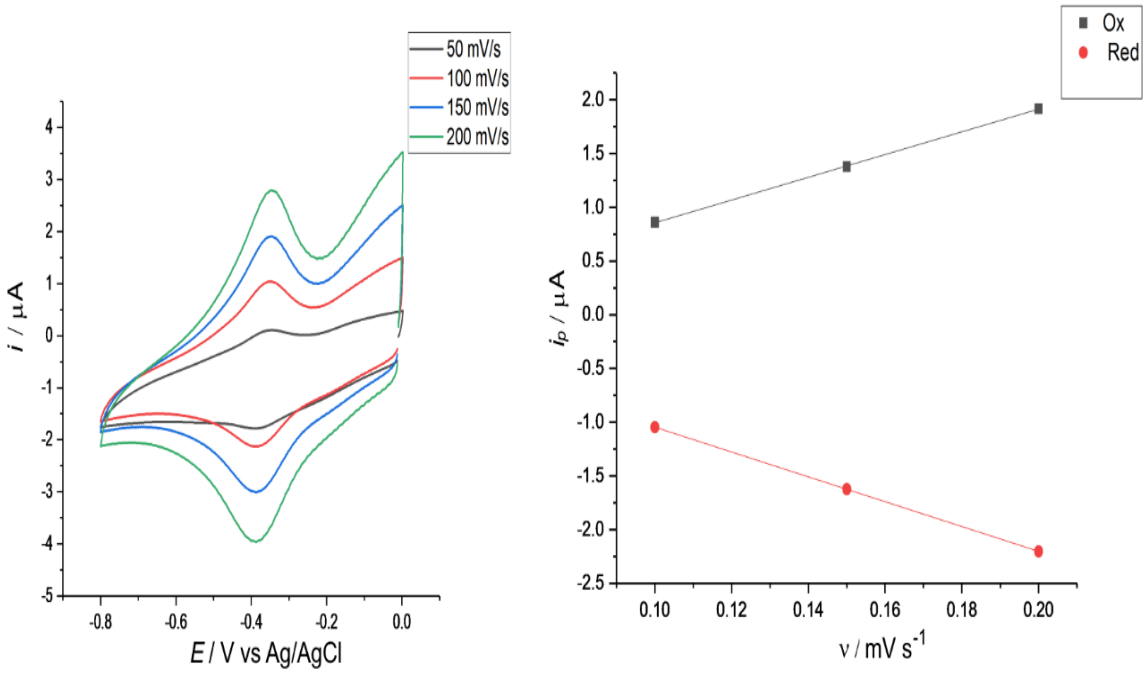

Figure 5.6 a) Background-corrected CVs of PPy-**1** co-polymer film recorded vs Fc/Fc^{+} at various scan rates vs Ag/AgCl, and b) A plot of current peak I_{pc} vs the scan rates (ν) for reduction of PPy-**1** co-polymer film. Electrolyte is 0.1 M $[^{n}Bu_4N][BF_4]$ in CH_3CN at 25 °C, scan rate 100 mV/s, working electrode GC of 7 mm^2 surface area.

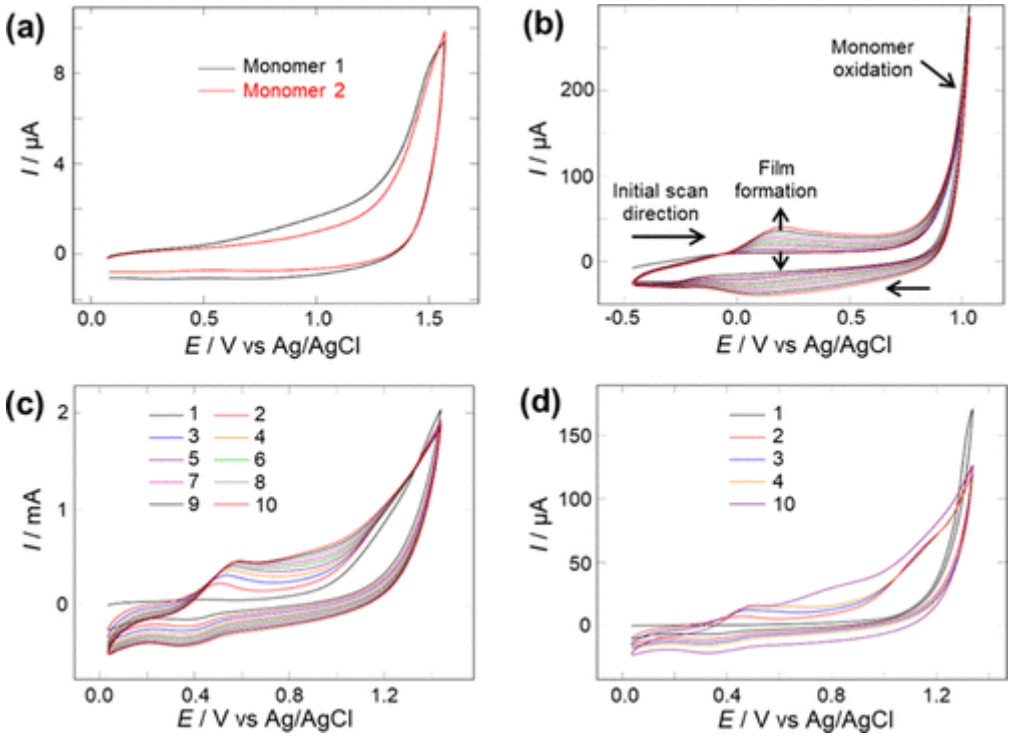

Figure 6.6 a) Shows cyclic voltammetry of monomer **1** (Black line) and monomer **2** (red line), 70: 30 pyrrole to form PPy-**1** and PPy-**2**. b) PPy modified by electropolymerisation on the Pt surface, c) Coelectropolymerization of monomer 1 70:30 pyrrole on FTO to form PPy-**1**; and d) Coelectropolymerization of monomer 2 70:30 pyrrole to form PPy-**2** on FTO. All measurements were carried out by using 0.1 M $[^{n}Bu_4N]BF_4$ in CH_3CN with an aqueous Ag/AgCl as reference electrode at 100 mV/s.[150]

Figure 6.6 (a) and Figure 6.6 (b) represent the copolymerization of pyrrole. The pyrrole is mixed with desired monomer. Therefore, the result is the derivative monomers would coelectropolymerize with underivatized pyrrole at up to 70 mol% of monomers **1** and **2** to form corresponding copolymers **PPy-1** and **PPy-2** according to Figure 6.6 c, d and Figure 7.6. The peak oxidation potentials observed in synthesis of **PPy-1** and **PPy-2** are positively shifted (by ca. 0.4 V) compared to that for underivatized polypyrrole (**PPy**). This change in potential implies the involvement of monomer **1** and **2** in the polymerisation reactions and thus formation of polymer chains with a distribution of the derivatized and underivatized pyrrole units. It is also consistent with the literature, where functionalization of pyrrole, especially at the N-

position, may introduce electronic effects that shift the oxidation potential of the monomer.[151b, 152]

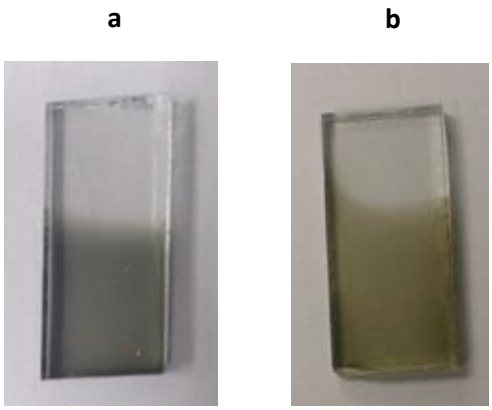

Figure 7.6 FTO electrodes modified with: (a) co-polymer PPy-**1**, and (b) co-polymer PPy-**2**. The colours are exhibited by the reduced states of PPy-**1** and PPy-**2** polymeric films.[150]

6.3.2. Electrochemical quartz crystal microbalance (EQCM)

Figure 8.6 a, b and c show the EQCM of PPy, PPy-**1** and PPy-**2**. The mass of the deposited film was calculated according to the Sauerbrey equation (chapter 2, equation number 28).

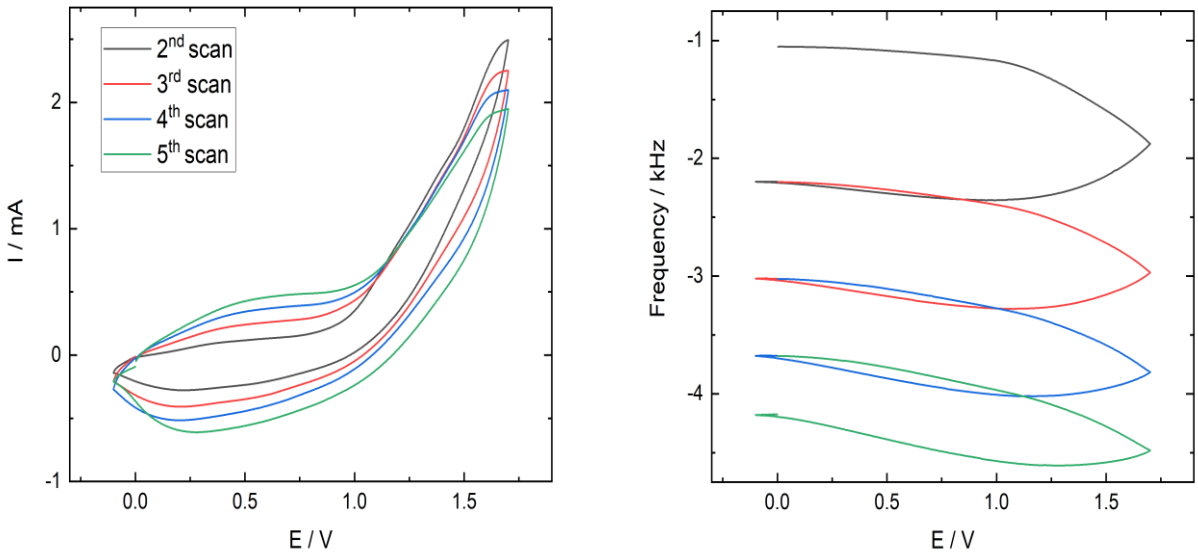

Figure 8.6 a) PPy in acetonitrile with 0.1 M [^{n}Bu$_4$N]BF$_4$ at 100 mV/s.

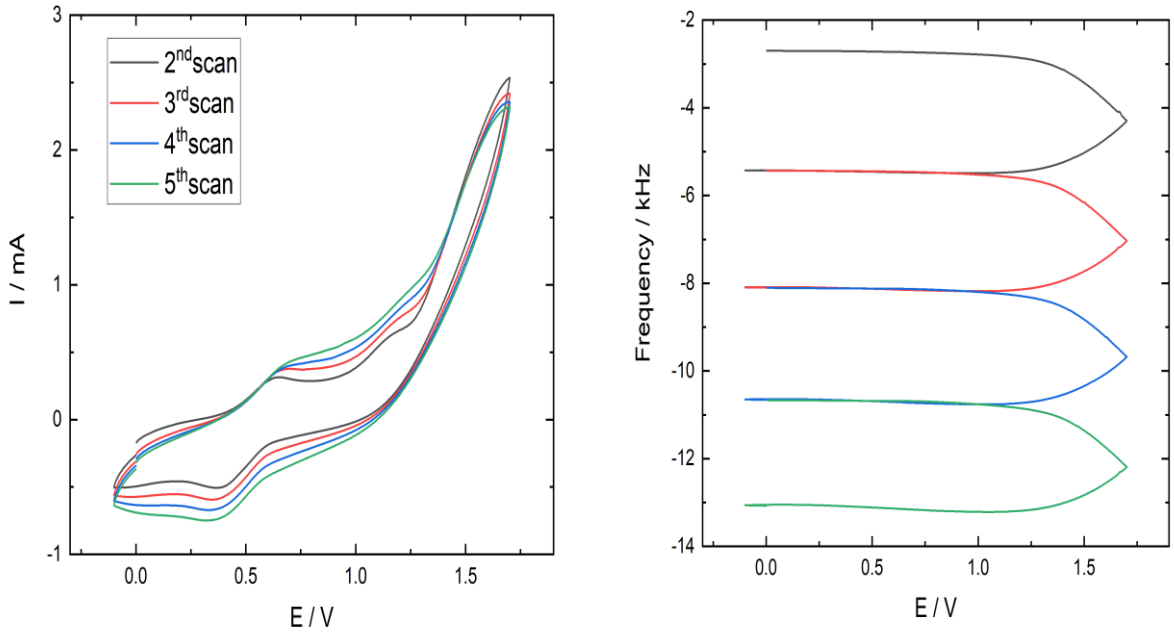

Figure 8.6 b) PPy-**1** in acetonitrile with 0.1 M [^{n}Bu$_4$N]BF$_4$ at 100 mV/s.

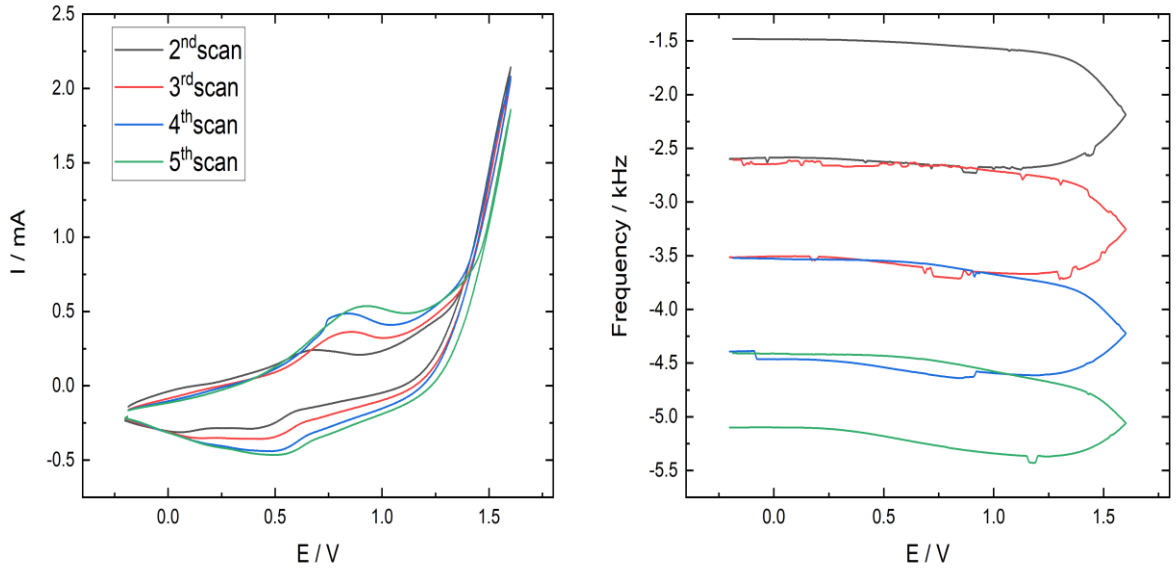

Figure 8.6 c) PPy-**2** in acetonitrile with 0.1 M [^{n}Bu$_4$N]BF$_4$ at 100 mV/s.

For each EQCM experiment, a frequency decrease is observed in each cycle in the potential range from -0.2 to 1.6 V, which indicates increased mass due to film deposition on the surface of working electrode. According to figure 8.6 a,b and c, although PPy-**1** (2.08×10^{-6} g average per cycle on 0.07 cm^2) deposits more mass than PPy (1.04×10^{-6} g average per cycle), consistent with the high formula weight of monomer 1, PPy-**2** shows less deposited mass (0.86×10^{-6} g average per cycle) compared to either of the other materials. This is consistent with the increased steric bulk provided by the longer π-bridge in monomer **2** impeding the process of polymerisation and deposition[151a, 153] which can lead to slower[154] and therefore more ordered[119] polymer chain growth.

6.3.3. Electron microscopy

The surface morphology of the electrogenerated films on FTO glass electrodes, at different film thicknesses, were analysed by using scanning electron microscopy (SEM) and high-resolution transmission electron microscopy (TEM) using cross-section analysis. The morphology of PPy-**1** and PPy-**2** copolymers is uneven but other N-substituted pyrroles have been found to present a more even morphology.[120] This implies a higher surface area. This suggests potential for higher performance for these POM-derivatized materials because of improved charge transport between the film and the electrolyte.

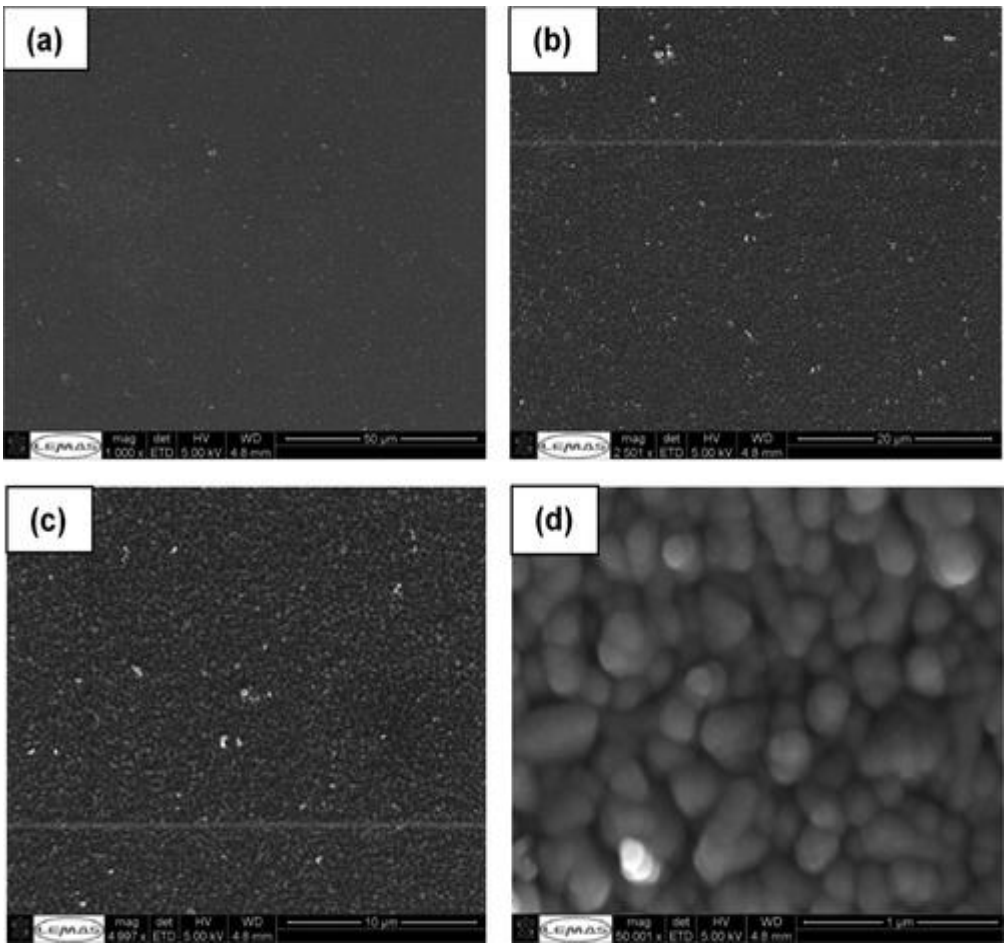

Figure 9.6 SEM imges of **PPy-2** copolymer modified on FTO electrode, 10 cycles, at 50 µm(a), 20µm(c), and 1µm(d) resolutions.[150]

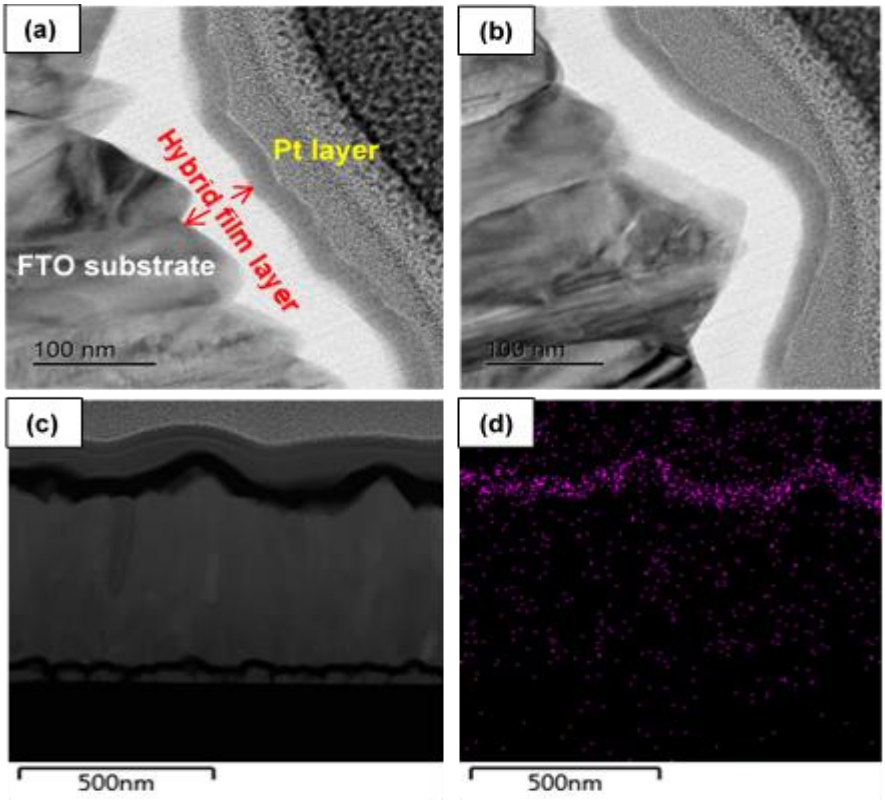

Figure 10.6 TEM cross-sectional view images of PPy-**2**, the film made on FTO (10 cycles) with thickness of 60 nm. A) 100 nm layer of the deposited film, b) 100 nm of the deposited film topography. C) it represents at 500 nm cross-sectional and d) it represents Mo map -which is the violet-coloured- of the deposited polymeric film.[150]

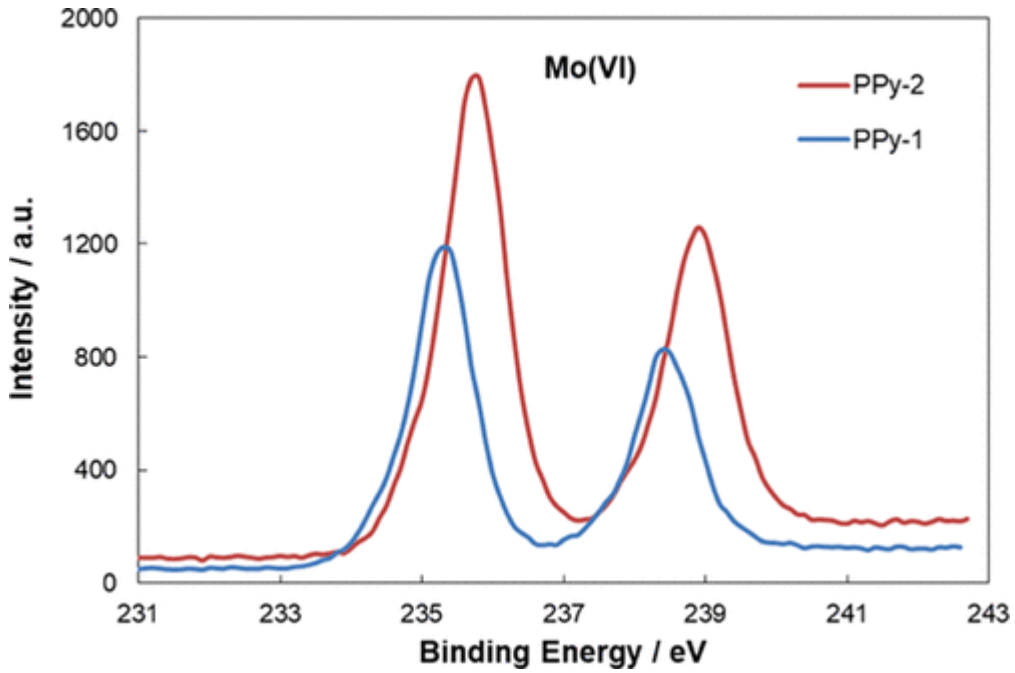

Figure 11.6 XPS spectrum of the Mo 3d core levels for PPy-**1** (blue) and PPy-**2** copolymers (red) of 20-deposition-cycle film thickness. The data were calibrated with the carbon signal at 288 eV.[150]

Table 6.1 XPS Surface Elemental Analysis.[150]

	Elemental Abundance [atomic %]						
Material, thickness	C1s	F1s	Mo3d	N1s	Na1s	O1s	S2p
PPy-1, 20 cycles	69.16	-	6.96	5.23	0.34	17.25	1.05
PPy-2, 10 cycles	75.76	-	4.70	4.63	-	14.00	0.92
PPy-2, 20 cycles	75.49	-	5.00	5.16	0.01	14.17	0.17
PPy-2, 30 cycles	72.34	-	5.90	4.19	0.00	17.27	0.31
PPy, 20 cycles	73.36	0.38	0.22	8.93	0.25	14.44	2.43

Figure 9.6 represents the SEM images of PPy-**2** of 10-cycle film thickness. According to figure 9.6, in the high-magnification image, the amorphous nature with densely packed surfaces based on spherical particles can be observed, with no phase-separated domains. Figure 10.6 shows TEM images which indicate that the topography of the films is similar to the FTO substrate. Film thicknesses were between 60 and 120 nm depending on the number of deposition cycles, and also elemental mapping shows that Mo is present through the entire thickness of the film. This confirms that there is no phase separation.[149]

6.3.4. Electrochemical impedance spectroscopy of PPy, PPy-PPy1 and PPy-PPy2

Electrochemical impedance spectroscopy (EIS) was carried out in the conductive / capacitive potential region of the polypyrroles to get comprehensive information about the properties of capacitors based on the PPy component. The result is shown in Figure 12.6.

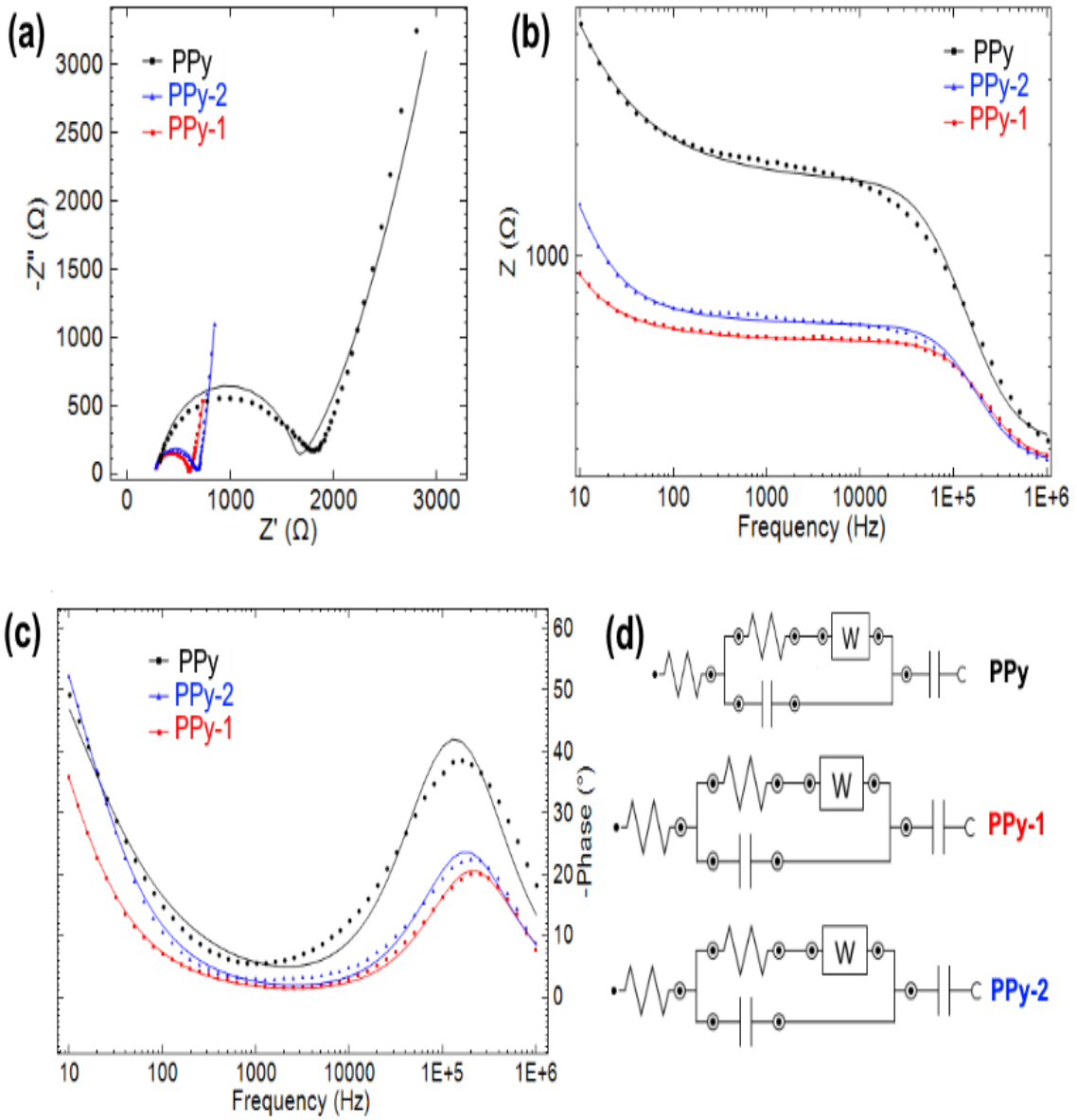

Figure 12.6 Nyquist plot, b) Bode plot, c) phase plot and d) electrochemical circuit fit of 10 -cycle deposited films of PPy at 0.9 V and PPy-**1** and PPy-**2** at 0.6 V vs Ag/Ag^{+} with 1 mA current. Points are experimental data, and lines are data fitted.

The Nyquist plots includes three parts, a semicircle in the at high frequency region corresponds to the charge transfer resistance. The second part is a transition region that possible is related to Warburg impedance (W) within the film. The final part is the straight-line (C) part at low frequency which corresponds to the ion (electrolyte) charging during the charge/discharge process.

According to Figure 12.6, the semi-circles of PPy-**1** and PPy-**2** in the high frequency region much are smaller than the PPy electrode, indicating a much lower apparent charge transfer resistance (R_{ct}). As the POMs cannot be participating in Faradaic reactions at the potential used for the measurement (+0.6 V), this is likely due to a more open structure with a higher surface area for charge transfer between film and electrolyte.[123, 155] [123]. In the low-frequency domains, both PPy-**1** and PPy-**2** show similar behaviour. The Bode and Phase angle plots (Figure 12.6 (b/c) show that at low frequencies (10 Hz), the phase angle of PPy-**2** is 53°, is higher than PPy (50°) or PPy-**1** (36°). This indicates that PPy-**2** has the most ideal capacitive performance. At higher frequencies, the phase angles of PPy-**1** and PPy-**2** fall to 19° and 22° respectively. This is (in part) due to Warburg impedance and arises from the porous structure of the film. The difference to PPy may be linked to inclusion of NBu_4^+ cations, rather than BF_4^- anions in the film – NBu_4^+ is large and upon oxidation there may be processes ejecting it from the film, as well as taking in the smaller BF_4^- anions. Figure 12.6 (d) shows the electrochemical circuit fit where R_s is the solution resistance. R_1 and C_1 are the resistance and capacitance of the double layer capacitor and C_2 is capacitance of the pseudocapacitor, resulting from the film.

Table 6.2 Electrode behaviour (PPy, PPy-**1** and PPy-**2**) calculated from the electrochemical circuit fit of the experimental EIS data.

Sample	**Rs [Ω]**	**R_1[Ω]**	**C_1[F]**	**C_2[F]**
PPy	316	1280	$2.06^{x}10^{-9}$	$8.85^{x}10^{-6}$
PPy-**1**	282	308	$3.55^{x}10^{-9}$	$41.6^{x}10^{-6}$
PPy-**2**	278	375	$3.68^{x}10^{-9}$	$17.9^{x}10^{-6}$

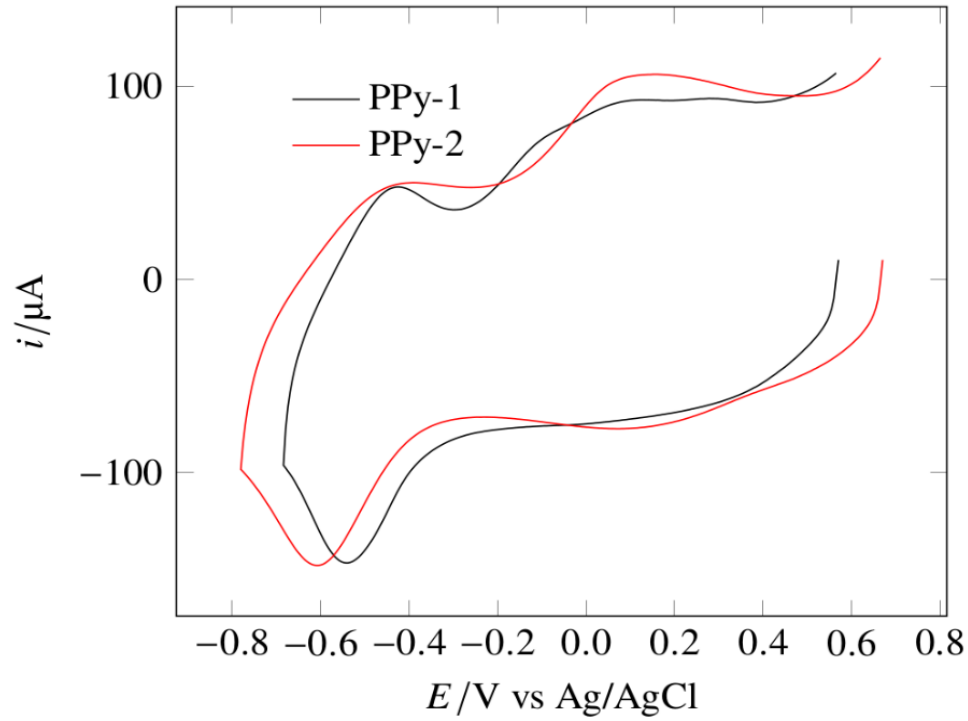

Figure 13.6 CVs of PPy-**1** (black trace) and PPy-**2** (red trace) of 10 cycles film thickness on FTO electrode in 0.1 M [$^{n}Bu_4N$]BF_4/CH_3CN at 25 °C vs Ag/AgCl at scan rate 250 mV/s.[150]

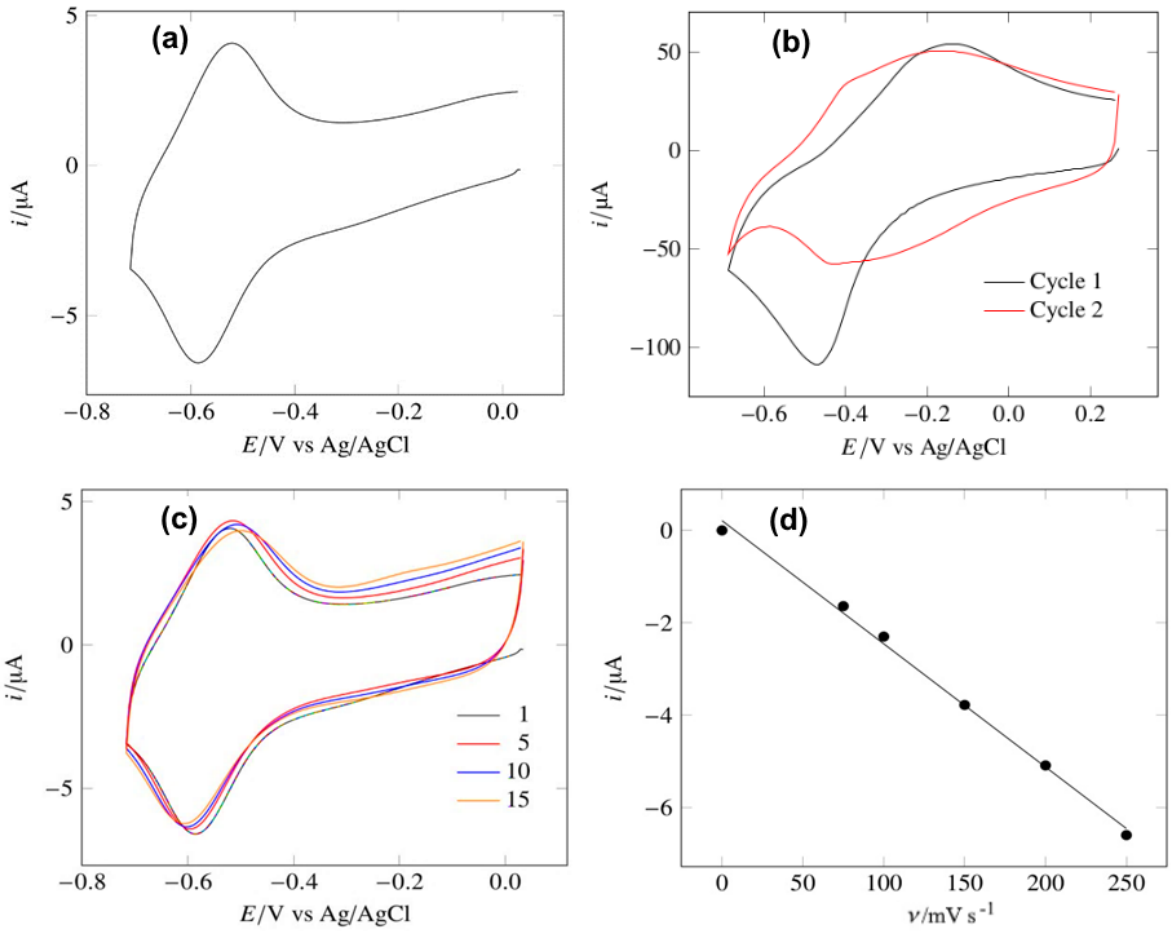

Figure 14.6 (a) CV showing the {Mo_6} redox wave in PPy-**1**. (b) CVs of an {Mo_6}-PPy inclusion film showing the loss of POM after the first redox cycle. (c) Consecutive cyclic voltammograms of a PPy-**1** film showing minimal changes from redox cycle 1 to 15. (d) A plot of current peak I_{pc} vs the scan rates (ν) for reduction of polypyrrole-3 co-polymer film. Conditions: electrolyte 0.1 M [^{n}Bu$_4$N]BF$_4$ in MeCN, scan rate 100 mV/s, working electrode 0.07 cm^2 GC, Ag/AgCl as reference electrode.

6.3.5. Specific Capacitances obtained from Cyclic Voltammetry

The specific charge and discharge capacitances related to the polypyrrole and {Mo_6}[149] anions at a potential range between 0.7 to -0.8 V, were calculated -according to figure 13.6- by integrating the current density of the CV curve in the oxidation wave for polypyrrole and in the

reduction wave for the {Mo_6} anions, respectively. Compared to un-derivatized polypyrrole (PPy) measured under the same system, films with covalently connected {Mo_6} anions show a significant increase in capacitance as shown in table 6.3: to 22 F/g for PPy-**1** and 34 F/g for PPy-**2**. This corresponds to a specific capacitance increase of *ca.* two times vs PPy for PPy-**1**, and 3 times for PPy-**2**, roughly in line with that seen for non-covalent inclusion of $[Mo_6O_{19}]^{2-}$ in PPy (2 times).[37] Nevertheless, the large loading of polyoxometalate in these films also contributes a significant Faradaic-capacitance. This was assessed in the same way as the PPy contribution. The POM contributes around 50% of the capacitance of the polypyrrole film, to give totals of 33.5 F/g for PPy-**1** and 52 F/g for PPy-**2** and therefore an enhancement *vs* PPy of 3 to 5^x. This POM contribution is approximately consistent with the ratio of POMs to pyrrole units estimated by XPS, considering that each POM stores one electron on reduction, and each pyrrole 0.33 positive charges on oxidation. Overall, the results show that the modification of PPy with hexamolybdate {Mo_6} anions via covalent linkage gives access to composites with enhanced capacitive charge storage that can be attributed both to steric bulk that improves the structure (surface area/porosity) of the film, and a direct faradaic contribution from the POM electron acceptor.[149]

Table 6.3 Specific capacitance of PPy, PPy-**1**, and PPy-**2** obtained from CV analysis at 250 mV/s.

Specific Capacitance [F/g]			
Sample	Polypyrrole^{oxi}	POM^{red}	Total
PPy	11.5	-	11.5
PPy-**1**	22	11.5	33.5
Ppy-**2**	34	19	53

6.3.6. Galvanostatic charge-discharge (GCD) Analysis of Capacitance and Stability

The electrochemical cycle performance of PPy-**1** and PPy-**2** was used to assess the capacitance and electrochemical stability of PPy-**1** and PPy-**2**, through galvanostatic (charge-discharge) measurements over 1200 cycles. The specific capacitance was calculated according to equation number 27, chapter 2.

Figure 15.6 represents the galvanostatic charge-discharge curves of PPy, PPy-**1** and PPy-**2** which have nearly symmetrical charge-discharge curves. This indicates good capacitive behaviour. The shapes for PPy-**1** and PPy-**2** extend to negative voltages, consistent with involvement of the POM in the process, and the time per charge/discharge cycle is shorter than for PPy, at around 21 seconds vs 36 seconds. This indicates better charge transport in the POM derivatised films. The specific capacitances (Table 6.4) show the same trend as those calculated by cyclic voltammetry, with PPy-**1** and PPy-**2** showing excellent agreement with the total POM + polypyrrole capacitance calculated from the cyclic voltammetry.

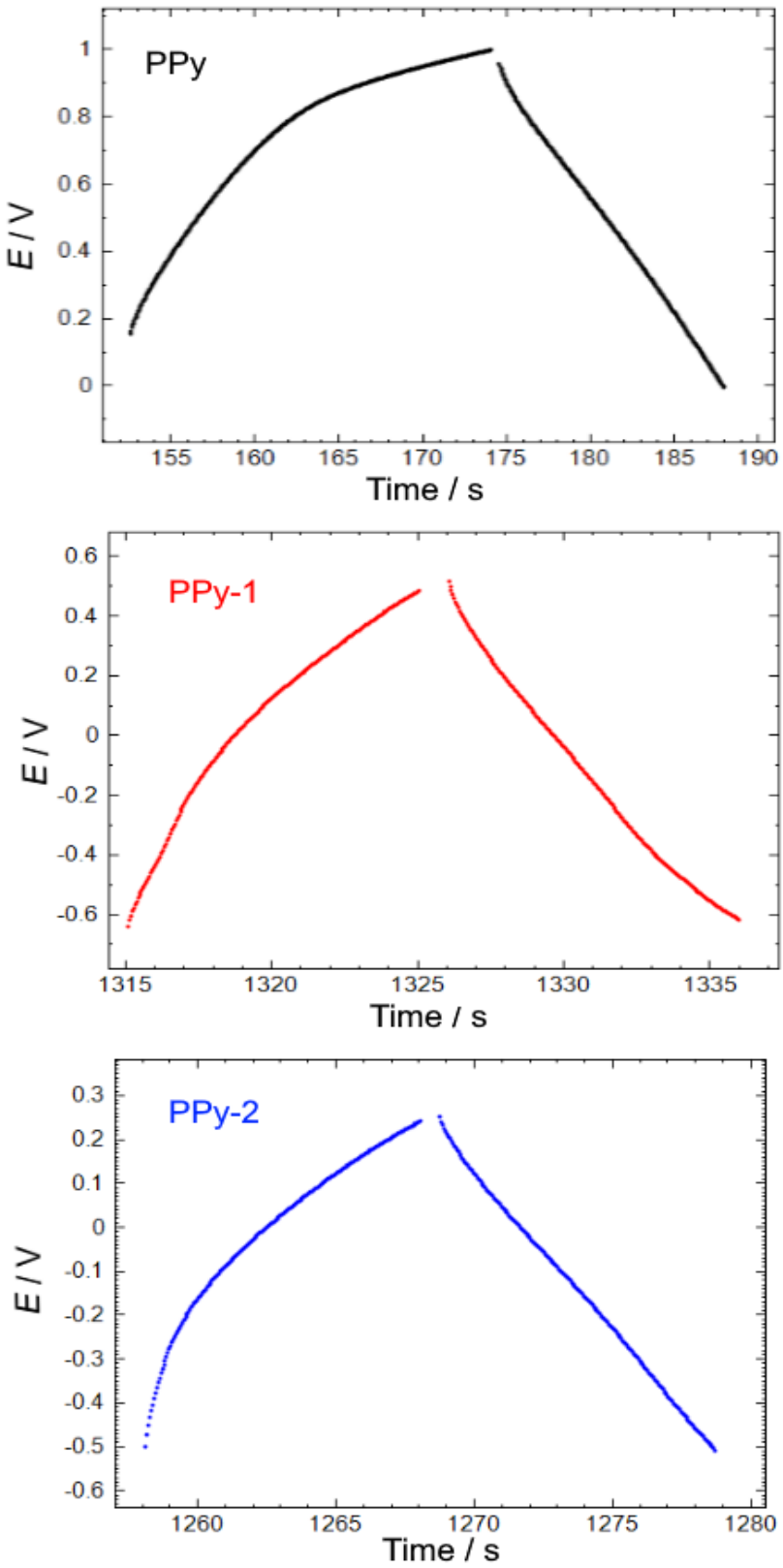

Figure 15.6 Galvanostatic charge-discharge curves for 10 cycle PPy, PPy-**1** and PPy-**2** films on GC electrodes. Electrolyte: 0.1 M [^{n}Bu$_4$N]BF$_4$/MeCN at 25 °C vs Ag wire reference.

Table 6.4 Specific capacitance of PPy, PPy-**1**, and PPy-**2** obtained from GCD analysis.

Sample	**Specific Capacitance [F/g]**
PPy	19
PPy-1	35
PPy-2	54

Interestingly, PPy-**2** shows higher cyclic stability compared with PPy-**1**. Figure 16.6 represents the capacitance retention of both co-polymers where PPy-**1** exhibits 81% and PPy-**2** 95% capacitance retention over 1200 cycles. Consequently, although the multi-cycle stability of PPy-**1** is comparable to that shown for non-covalent inclusion of $[Mo_6O_{19}]^{2-}$, PPy-**2** demonstrates the potential of covalent linkage to improve the stability of POM-polymer composite systems. The improved performance of PPy-**2** compared to PPy-**1** in both stability and specific capacitance is consistent with the length of spacer which is between pyrrole-N and POM forcing larger ion channels, increasing active surface area and reducing disruption of the film by ion migration.[149]

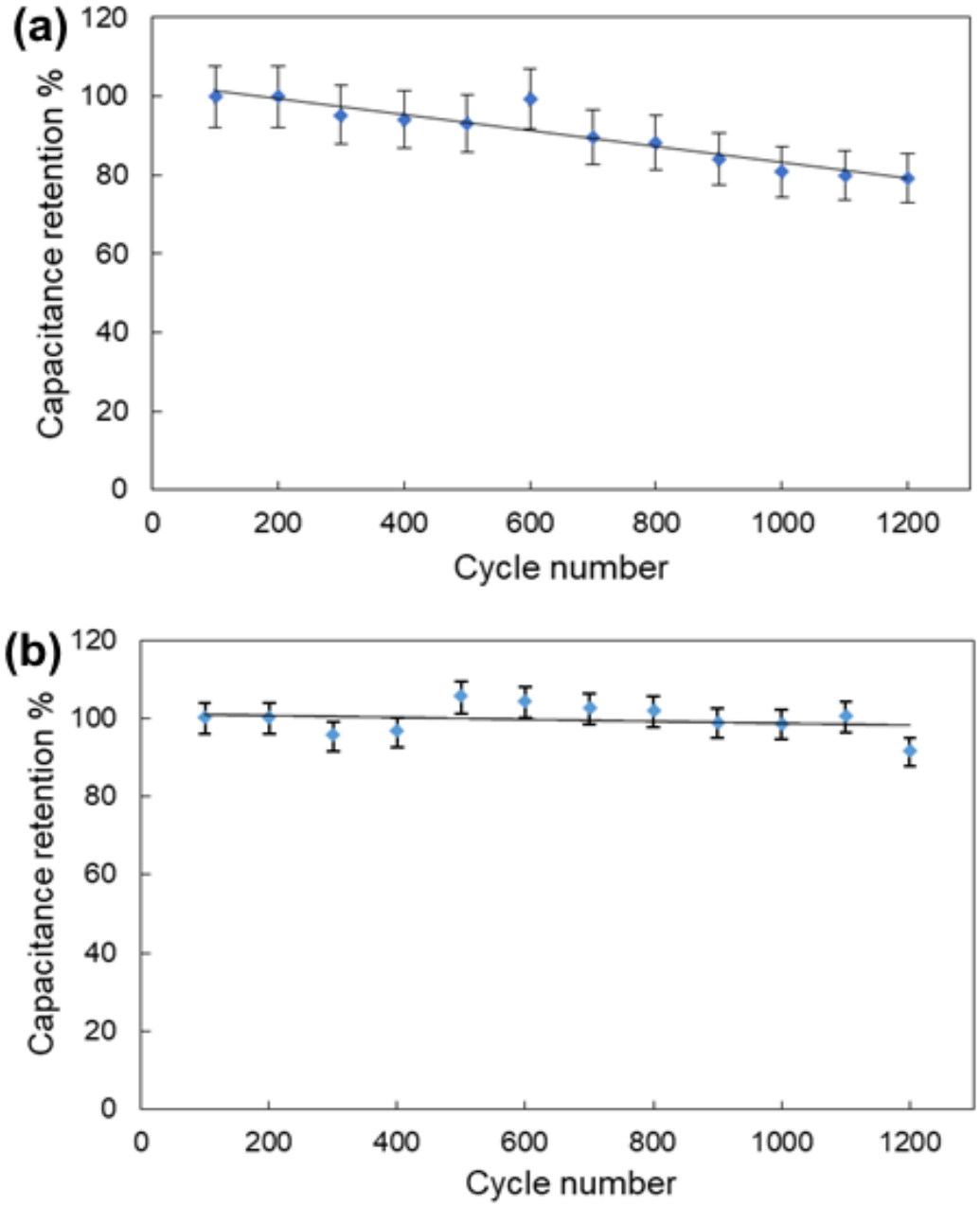

Figure 16.6 Capacitance retention % of (a) PPy-**1** and (b) PPy-**2** of 10 cycles-deposited film thickness on GC electrodes for the first 1200 cycles. Electrolyte: 0.1 M [$^{n}Bu_4N$]BF_4/CH_3CN at 25 °C vs Ag wire reference.

6.4. Summary

In this chapter, polypyrroles with covalently linked Lindqvist polyoxometalates were successfully prepared by electropolymerisation. These films are the first covalent POM-PPy hybrids, and the first demonstration of electropolymerisation of a POM-derivatised monomer. This is opens new possibilities for construction of POM hybrid materials. The covalent linkage gives access to far higher loadings of POM than obtained in non-covalent inclusion films, prevents loss of POM in early reduction cycles, and increasing its length increases both the specific capacitance and stability of the film to cycling – such that 95% capacitance retention over 1200 cycles is achieved for the longer diphenylacetylene spacer. The POM enhances specific capacitance both by modifying the polypyrrole itself, and reduced charge transfer resistance implying that a more open structure results from the steric bulk of the POMs, and by a direct faradaic contribution through the POM redox process. Future work will focus on optimising the loading of the POM for the best specific capacitance and expand the approach to POMs capable of storing multiple electrons, for example Keggin (figure 1.6).

6.5. References

[1] J. Yu, Q. Tan, J. Li, *Journal of Cleaner Production* **2020**, *255*, 120269.
[2] J. Wen, Y. Yu, C. Chen, *Materials Express* **2012**, *2*, 197-212.
[3] G. Heal, *The Economics of Renewable Energy* **2009**.DOI 10.3386/w15081.
[4] J. Winsberg, T. Hagemann, T. Janoschka, M. D. Hager, U. S. Schubert, *Angewandte Chemie International Edition* **2017**, *56*, 686-711.
[5] X. Yu, N. S. Sandhu, Z. Yang, M. Zheng, *Applied Energy* **2020**, *271*, 115169.
[6] aE. Kabir, P. Kumar, S. Kumar, A. A. Adelodun, K.-H. Kim, *Renewable and Sustainable Energy Reviews* **2018**, *82*, 894-900; bA. Demirbaş, *Energy Conversion and Management* **2001**, *42*, 1357-1378.
[7] T. B. Reddy, *Linden's handbook of batteries, Vol. 4*, Mcgraw-hill New York, **2011**.
[8] N. Kularatna, *Energy storage devices for electronic systems: rechargeable batteries and supercapacitors*, *Academic Press*, **2014**.
[9] Y. Nishi, *Journal of Power Sources* **2001**, *100*, 101-106.
[10] A. Jansen, A. Kahaian, K. Kepler, P. Nelson, K. Amine, D. Dees, D. Vissers, M. Thackeray, *Journal of Power Sources* **1999**, *81*, 902-905.
[11] Y. Cheng, S. Lu, R. Zheng, D. Zhang, H. Zhang, *Applied Surface Science* **2019**, *485*, 119-127.
[12] K. Kubota, S. Komaba, *Journal of The Electrochemical Society* **2015**, *162*, A2538.
[13] P. Simon, Y. Gogotsi, *Nature Materials* **2020**, *19*, 1151-1163.
[14] J. Yang, Y. Liu, S. Liu, L. Li, C. Zhang, T. Liu, *Materials Chemistry Frontiers* **2017**, *1*, 251-268.
[15] F. Liu, Q. Q. Li, S. H. Zhang, C. Ma, Q. Z. Ren, X. Y. Tao, J. P. Cheng, X. B. Zhang, in *Advanced Materials Research, Vol. 507*, Trans Tech Publ, **2012**, pp. 48-51.
[16] R. Kötz, M. Carlen, *Electrochimica Acta* **2000**, *45*, 2483-2498.
[17] aL. Dagousset, G. Pognon, G. T. Nguyen, F. Vidal, S. Jus, P.-H. Aubert, *Journal of Power Sources* **2017**, *359*, 242-249; bS. Wang, W. Quan, Z. Zhu, Y. Yang, Q. Liu, Y. Ren, X. Zhang, R. Xu, Y. Hong, Z. Zhang, *Nature Communications* **2017**, *8*, 1-8; cV. Dragunov, D. Ostertak, K. Pelmenev, R. Sinitskiy, E. Dragunova, *Sensors and Actuators A: Physical* **2021**, *318*, 112501.
[18] aK. Ueno, H. Shimotani, H. Yuan, J. Ye, M. Kawasaki, Y. Iwasa, *Journal of the Physical Society of Japan* **2014**, *83*, 032001; bM. Endo, T. Takeda, Y. Kim, K. Koshiba, K. Ishii, *Carbon letters* **2001**, *1*, 117-128.
[19] F. Béguin, V. Presser, A. Balducci, E. Frackowiak, *Advanced Materials* **2014**, *26*, 2219-2251.
[20] Q. Wei, Y. Jiang, X. Qian, L. Zhang, Q. Li, S. Tan, K. Zhao, W. Yang, Q. An, J. Guo, *Iscience* **2018**, *6*, 212-221.
[21] S. Yang, X. Wu, C. Chen, H. Dong, W. Hu, X. Wang, *Chemical Communications* **2012**, *48*, 2773-2775.
[22] V. Augustyn, P. Simon, B. Dunn, *Energy & Environmental Science* **2014**, *7*, 1597-1614.
[23] B. Pal, S. Yang, S. Ramesh, V. Thangadurai, R. Jose, *Nanoscale Advances* **2019**, *1*, 3807-3835.
[24] A. González, E. Goikolea, J. A. Barrena, R. Mysyk, *Renewable and Sustainable Energy Reviews* **2016**, *58*, 1189-1206.
[25] M. V. Reddy, C. M. Julien, A. Mauger, K. Zaghib, *Nanomaterials* **2020**, *10*, 1606.
[26] S. C. Rasmussen, in *100+ Years of Plastics. Leo Baekeland and Beyond*, ACS Publications, **2011**, pp. 147-163.

[27] M. Vangari, T. Pryor, L. Jiang, *Journal of Energy Engineering* **2013**, *139*, 72-79.
[28] J. Hazarika, A. Kumar, *The Journal of Physical Chemistry B* **2017**, *121*, 6926-6933.
[29] A. Borenstein, O. Hanna, R. Attias, S. Luski, T. Brousse, D. Aurbach, *Journal of Materials Chemistry A* **2017**, *5*, 12653-12672.
[30] T. O. Magu, A. U. Agobi, L. HITLER, P. M. Dass, *Journal of Chemical Reviews* **2019**, *1*, 19-34.
[31] J. Zhong, S. Gao, G. Xue, B. Wang, *Macromolecules* **2015**, *48*, 1592-1597.
[32] J. Ghilane, P. Hapiot, A. J. Bard, *Analytical chemistry* **2006**, *78*, 6868-6872.
[33] A. M. Bryan, L. M. Santino, Y. Lu, S. Acharya, J. M. D'Arcy, *Chemistry of Materials* **2016**, *28*, 5989-5998.
[34] A. F. Diaz, J. I. Castillo, J. Logan, W.-Y. Lee, *Journal of Electroanalytical Chemistry and Interfacial Electrochemistry* **1981**, *129*, 115-132.
[35] A. Diaz, J. Bargon, *TA Skotheim Ed* **1986**, *1*, 82-100.
[36] D. Ateh, H. Navsaria, P. Vadgama, *Journal of The Royal Society Interface* **2006**, *3*, 741-752.
[37] M. A. A. M. Abdah, N. H. N. Azman, S. Kulandaivalu, Y. Sulaiman, *Materials & Design* **2020**, *186*, 108199.
[38] E. Håkansson, T. Lin, H. Wang, A. Kaynak, *Synthetic metals* **2006**, *156*, 1194-1202.
[39] R. K. Sharma, A. Rastogi, S. Desu, *Electrochimica Acta* **2008**, *53*, 7690-7695.
[40] X. Liu, L. Zang, C. Liang, Q. Liu, Y. Deng, C. Yang, J. Qiu, *Synthetic Metals* **2021**, *271*, 116654.
[41] Y. Huang, J. Tao, W. Meng, M. Zhu, Y. Huang, Y. Fu, Y. Gao, C. Zhi, *Nano Energy* **2015**, *11*, 518-525.
[42] J. L. Bredas, G. B. Street, *Accounts of Chemical Research* **1985**, *18*, 309-315.
[43] G. A. Snook, P. Kao, A. S. Best, *Journal of Power Sources* **2011**, *196*, 1-12.
[44] M. E. Abdelhamid, G. A. Snook, *Encyclopedia of Polymer Science and Technology* **2002**, 1-20.
[45] S. Ahmad, S. S. Gursoy, S. Kazim, A. Uygun, *Solar Energy Materials and Solar Cells* **2012**, *99*, 95-100.
[46] D. A. Walker, C. D'Silva, *Electrochimica Acta* **2014**, *116*, 175-182.
[47] W. Schuhmann, R. Lammert, M. Hämmerle, H.-L. Schmidt, *Biosensors and Bioelectronics* **1991**, *6*, 689-697.
[48] A. J. Downard, N. A. Surridege, T. J. Meyer, S. Cosnier, A. Deronzier, J.-C. Moutet, *Journal of Electroanalytical Chemistry and Interfacial Electrochemistry* **1988**, *246*, 321-335.
[49] H. KorriáYoussoufi, *Journal of the Chemical Society, Chemical Communications* **1993**, 1550-1552.
[50] M.-M. Titirici, R. J. White, N. Brun, V. L. Budarin, D. S. Su, F. del Monte, J. H. Clark, M. J. MacLachlan, *Chemical Society Reviews* **2015**, *44*, 250-290.
[51] J. Wang, Ü. A. Kirgöz, J.-W. Mo, J. Lu, A. N. Kawde, A. Muck, *Electrochemistry Communications* **2001**, *3*, 203-208.
[52] C. G. Heald, G. G. Wildgoose, L. Jiang, T. G. Jones, R. G. Compton, *ChemPhysChem* **2004**, *5*, 1794-1799.
[53] R. Devi, K. Tapadia, T. Maharana, *Heliyon* **2020**, *6*, e03122.
[54] S.-S. Yao, F.-L. Jin, K. Y. Rhee, D. Hui, S.-J. Park, *Composites Part B: Engineering* **2018**, *142*, 241-250.
[55] C. Zhou, T. Gao, Q. Liu, Y. Wang, D. Xiao, *Electrochimica Acta* **2020**, 135628.
[56] A. T. Lawal, *Biosensors and Bioelectronics* **2019**, *141*, 111384.
[57] K. Li, H. Li, M. Li, C. Li, L. Su, L. Qian, B. Yang, *Composites Science and Technology* **2019**, *175*, 92-99.

[58] S. Z. Hussain, M. Ihrar, S. B. Hussain, W. C. Oh, K. Ullah, *SN Applied Sciences* **2020**, *2*, 1-23.
[59] M. V. Kiamahalleh, S. H. S. Zein, G. Najafpour, S. A. SATA, S. Buniran, *Nano* **2012**, *7*, 1230002.
[60] B. D. Assresahegn, T. Brousse, D. Bélanger, *Carbon* **2015**, *92*, 362-381.
[61] aB. Li, J. Zhao, Z. Zhang, C. Zhao, P. Sun, P. Bai, J. Yang, Z. Zhou, Y. Xu, *Advanced Functional Materials* **2019**, *29*, 1807137; bJ. Yang, Y. Shi, P. Sun, P. Xiong, Y. Xu, *ACS Applied Materials & Interfaces* **2019**, *11*, 42305-42312; cA. Jaffe, A. Saldivar Valdes, H. I. Karunadasa, *Chemistry of Materials* **2015**, *27*, 3568-3571.
[62] K. Jurewicz, S. Delpeux, V. Bertagna, F. Beguin, E. Frackowiak, *Chemical Physics Letters* **2001**, *347*, 36-40.
[63] D. Belanger, J. Pinson, *Chemical Society Reviews* **2011**, *40*, 3995-4048.
[64] M. Deschanels, F. Favier, O. Fontaine, S. Le Vot, *Electrochimica Acta* **2020**, *361*, 137027.
[65] S. B. Sertkol, B. Esat, A. A. Momchilov, M. B. Yılmaz, M. Sertkol, *Carbon* **2017**, *116*, 154-166.
[66] Y. Yang, K. He, P. Yan, D. Wang, X. Wu, X. Zhao, Z. Huang, C. Zhang, D. He, *Electrochimica Acta* **2014**, *138*, 481-485.
[67] aD. Hansen Jr, R. Pappo, R. Garland, *The Journal of Organic Chemistry* **1988**, *53*, 4244-4253; bM. A. Castro, J. M. M. del Corral, M. Gordaliza, P. A. García, A. M. Gamito, S. A. Gualberto, R. Batista, A. San Feliciano, *Synthesis* **2005**, *2005*, 3202-3208.
[68] Z. Wang, A. Li, L. Gou, J. Ren, G. Zhai, *RSC advances* **2016**, *6*, 89827-89835.
[69] M. Shamsipur, A. Siroueinejad, B. Hemmateenejad, A. Abbaspour, H. Sharghi, K. Alizadeh, S. Arshadi, *Journal of Electroanalytical Chemistry* **2007**, *600*, 345-358.
[70] L. Gao, S. Gan, H. Li, D. Han, F. Li, Y. Bao, L. Niu, *Nanotechnology* **2017**, *28*, 275602.
[71] P. Campbell, M. Merrill, B. Wood, E. Montalvo, M. Worsley, T. Baumann, J. Biener, *Journal of Materials Chemistry A* **2014**, *2*, 17764-17770.
[72] Z. Algharaibeh, X. Liu, P. G. Pickup, *Journal of Power Sources* **2009**, *187*, 640-643.
[73] Z. Algharaibeh, P. G. Pickup, *Electrochemistry Communications* **2011**, *13*, 147-149.
[74] aX. Chen, H. Wang, H. Yi, X. Wang, X. Yan, Z. Guo, *The Journal of Physical Chemistry C* **2014**, *118*, 8262-8270; bG. Ma, F. Hua, K. Sun, E. Feng, Z. Zhang, H. Peng, Z. Lei, *Ionics* **2018**, *24*, 549-561.
[75] L. Yang, K. Zhuo, X. Xu, Z. Zhang, Q. Du, G. Bai, J. Wang, *Electrochimica Acta* **2021**, *393*, 139057.
[76] C. Zhu, W. Zhang, G. Li, C. Li, X. Qin, *Journal of Alloys and Compounds* **2021**, *862*, 158472.
[77] T. Ueda, *ChemElectroChem* **2018**, *5*, 823-838.
[78] S. Liu, Z. Tang, *Nano Today* **2010**, *5*, 267-281.
[79] D. L. Long, R. Tsunashima, L. Cronin, *Angewandte Chemie International Edition* **2010**, *49*, 1736-1758.
[80] H. Wang, S. Hamanaka, Y. Nishimoto, S. Irle, T. Yokoyama, H. Yoshikawa, K. Awaga, *Journal of the American Chemical Society* **2012**, *134*, 4918-4924.
[81] M. Samaniyan, M. Mirzaei, R. Khajavian, H. Eshtiagh-Hosseini, C. Streb, *ACS catalysis* **2019**, *9*, 10174-10191.
[82] D. E. Katsoulis, *Chemical Reviews* **1998**, *98*, 359-388.
[83] P. Alotto, M. Guarnieri, F. Moro, *Renewable and Sustainable Energy Reviews* **2014**, *29*, 325-335.
[84] R. G. Compton, C. E. Banks, *Understanding voltammetry*, World Scientific, **2018**.

[85] K. Ngamchuea, S. Eloul, K. Tschulik, R. G. Compton, *Journal of Solid State Electrochemistry* **2014**, *18*, 3251-3257.
[86] F. Cottrell, *Z. phys. Chem* **1903**, *42*, 385-431.
[87] R. Niu, H. Yang, in *2011 IEEE International Conference on Robotics and Automation*, IEEE, **2011**, pp. 1-4.
[88] L. M. Furtado, H. Su, M. Thompson, D. P. Mack, G. L. Hayward, *Analytical chemistry* **1999**, *71*, 1167-1175.
[89] Q. Zhang, M. D. Levi, Y. Chai, X. Zhang, D. Xiao, Q. Dou, P. Ma, H. Ji, X. Yan, *Small Methods* **2019**, *3*, 1900246.
[90] S.-I. Pyun, H.-C. Shin, J.-W. Lee, J.-Y. Go, *Electrochemistry of Insertion Materials for hydrogen and lithium*, *Springer Science & Business Media*, **2012**.
[91] aM. Grossi, B. Riccò, *Journal of Sensors and Sensor Systems* **2017**, *6*, 303-325; bT. J. Freeborn, B. Maundy, A. S. Elwakil, *Materials for Renewable and Sustainable Energy* **2015**, *4*, 1-7; cS. M. Lukic, J. Cao, R. C. Bansal, F. Rodriguez, A. Emadi, *IEEE Transactions on Industrial Electronics* **2008**, *55*, 2258-2267.
[92] S. Fletcher, V. J. Black, I. Kirkpatrick, *Journal of Solid State Electrochemistry* **2014**, *18*, 1377-1387.
[93] K. S. Cole, R. H. Cole, *The Journal of Chemical Physics* **1941**, *9*, 341-351.
[94] B. E. Conway, *Electrochemical supercapacitors: scientific fundamentals and technological applications*, *Springer Science & Business Media*, **2013**.
[95] S. Ernst, L. Aldous, R. G. Compton, *Chemical Physics Letters* **2011**, *511*, 461-465.
[96] E. J. Lawrence, V. S. Oganesyan, G. G. Wildgoose, A. E. Ashley, *Dalton Transactions* **2013**, *42*, 782-789.
[97] E. Lawrence, PhD thesis, University of East Anglia **2015**.
[98] M. V. Reddy, A. Mauger, C. M. Julien, A. Paolella, K. Zaghib, *Materials* **2020**, *13*, 1884.
[99] R. Sneha, K. Vinayaka, K. Rana, in *2020 IEEE International Conference on Power Systems Technology (POWERCON)*, IEEE, **2020**, pp. 1-6.
[100] L. Lu, X. Han, J. Li, J. Hua, M. Ouyang, *Journal of Power Sources* **2013**, *226*, 272-288.
[101] Y. Qin, J. Li, X. Jin, S. Jiao, Y. Chen, W. Cai, R. Cao, *Ceramics International* **2020**.
[102] aE. Mossali, N. Picone, L. Gentilini, O. Rodrìguez, J. M. Pérez, M. Colledani, *Journal of Environmental Management* **2020**, *264*, 110500; bJ. Yang, Z. Wang, Y. Shi, P. Sun, Y. Xu, *ACS Applied Materials & Interfaces* **2020**, *12*, 7179-7185.
[103] aS. Goriparti, E. Miele, F. De Angelis, E. Di Fabrizio, R. P. Zaccaria, C. Capiglia, *Journal of power sources* **2014**, *257*, 421-443; bE. Gavilán-Arriazu, J. Hümöller, O. Pinto, B. L. de Mishima, E. Leiva, O. Oviedo, *Physical Chemistry Chemical Physics* **2020**, *22*, 16174-16183.
[104] S. Holmberg, A. Perebikovsky, L. Kulinsky, M. Madou, *Micromachines* **2014**, *5*, 171-203.
[105] A. J. Wain, G. G. Wildgoose, C. G. Heald, L. Jiang, T. G. Jones, R. G. Compton, *The Journal of Physical Chemistry B* **2005**, *109*, 3971-3978.
[106] S. Y. Rhieu, D. R. Ludwig, V. S. Siu, G. T. R. Palmore, *Electrochemistry Communications* **2009**, *11*, 1857-1860.
[107] M. A. Ghanem, J.-M. Chrétien, A. Pinczewska, J. D. Kilburn, P. N. Bartlett, *Journal of Materials Chemistry* **2008**, *18*, 4917-4927.
[108] M. Kullapere, M. Marandi, V. Sammelselg, H. A. Menezes, G. Maia, K. Tammeveski, *Electrochemistry Communications* **2009**, *11*, 405-408.
[109] M. Kullapere, J.-M. Seinberg, U. Mäeorg, G. Maia, D. J. Schiffrin, K. Tammeveski, *Electrochimica Acta* **2009**, *54*, 1961-1969.

[110] M. Weissmann, O. Crosnier, T. Brousse, D. Bélanger, *Electrochimica Acta* **2012**, *82*, 250-256.
[111] K. Jüttner, C. Ehrenbeck, *Journal of Solid State Electrochemistry* **1998**, *2*, 60-66.
[112] E. S. Lee, J. H. Park, G. G. Wallace, Y. H. Bae, *Polymer International* **2004**, *53*, 400-405.
[113] W. Khan, T. Marew, N. Kumar, *Biomedical Materials* **2006**, *1*, 235.
[114] Y. Wang, C. Zhang, S. Li, L. Liu, *European Journal of Organic Chemistry* **2021**, *2021*, 3837-3849.
[115] C. Su, L. Wang, L. Xu, C. Zhang, *Electrochimica Acta* **2013**, *104*, 302-307.
[116] G. Douglade, B. Fabre, *Synthetic metals* **2002**, *129*, 309-314.
[117] L. Zhang, G. Xia, Z. Guo, X. Li, D. Sun, X. Yu, *International Journal of Hydrogen Energy* **2016**, *41*, 14252-14260.
[118] aJ. R. Lawson, R. L. Melen, *Inorganic chemistry* **2017**, *56*, 8627-8643; bN. L Guernion, W. Hayes, *Current Organic Chemistry* **2004**, *8*, 637-651.
[119] E.-L. Kupila, J. Kankare, *Synthetic metals* **1995**, *74*, 241-249.
[120] G. G. A. Wildgoose, A. E.; Courtney, J. M.; Lawrence, E. J.,, *Appl* **2019**.
[121] N. Mermilliod, J. Tanguy, F. Petiot, *Journal of the Electrochemical Society* **1986**, *133*, 1073.
[122] aG. Garcia-Belmonte, J. Bisquert, *Electrochimica Acta* **2002**, *47*, 4263-4272; bC. Xu, J. Sun, L. Gao, *Journal of Materials Chemistry* **2011**, *21*, 11253-11258; cD. Zhang, X. Zhang, Y. Chen, P. Yu, C. Wang, Y. Ma, *Journal of Power Sources* **2011**, *196*, 5990-5996.
[123] M. D. Ingram, H. Staesche, K. Ryder, *Journal of Power Sources* **2004**, *129*, 107-112.
[124] A. E. Ashley, T. J. Herrington, G. G. Wildgoose, H. Zaher, A. L. Thompson, N. H. Rees, T. Krämer, D. O'Hare, *Journal of the American Chemical Society* **2011**, *133*, 14727-14740.
[125] P. K. Adusei, S. Gbordzoe, S. N. Kanakaraj, Y.-Y. Hsieh, N. T. Alvarez, Y. Fang, K. Johnson, C. McConnell, V. Shanov, *Journal of Energy Chemistry* **2020**, *40*, 120-131.
[126] M. Yang, J. Xu, L. Zhang, Y. Shi, J. Xie, F. Lei, L. Fan, *Materials Letters* **2021**, 130095.
[127] K. Brousse, C. Martin, A. Brisse, C. Lethien, P. Simon, P.-L. Taberna, T. Brousse, *Electrochimica Acta* **2017**, *246*, 391-398.
[128] M. R. Gerhardt, L. Tong, R. Gómez-Bombarelli, Q. Chen, M. P. Marshak, C. J. Galvin, A. Aspuru-Guzik, R. G. Gordon, M. J. Aziz, *Advanced Energy Materials* **2017**, *7*, 1601488.
[129] Q. Wu, Y. Sun, H. Bai, G. Shi, *Physical Chemistry Chemical Physics* **2011**, *13*, 11193-11198.
[130] K. Kalinathan, D. P. DesRoches, X. Liu, P. G. Pickup, *Journal of Power Sources* **2008**, *181*, 182-185.
[131] J. Liu, Q. Wang, P. Liu, *Colloids and Surfaces A: Physicochemical and Engineering Aspects* **2020**, *588*, 124388.
[132] L. Xu, R. Shi, H. Li, C. Han, M. Wu, C.-P. Wong, F. Kang, B. Li, *Carbon* **2018**, *127*, 459-468.
[133] J. Ren, X. Zhao, J. Zhang, Q. Zhang, *International Journal of Electrochemical Science* **2016**, *11*, 2550-2559.
[134] S. Ryu, E. Kim, J. Yoo, *Electrochimica Acta* **2021**, *370*, 137809.
[135] T. J. Carney, S. J. Collins, J. S. Moore, F. R. Brushett, *Chemistry of Materials* **2017**, *29*, 4801-4810.
[136] T. Chen, L. Dai, *Journal of Materials Chemistry A* **2014**, *2*, 10756-10775.

[137] Z. Han, X. Li, Q. Li, H. Li, J. Xu, N. Li, G. Zhao, X. Wang, H. Li, S. Li, *ACS Applied Materials & Interfaces* **2021**, *13*, 6265-6275.
[138] M. Ammam, *Journal of Materials Chemistry A* **2013**, *1*, 6291-6312.
[139] A. Proust, B. Matt, R. Villanneau, G. Guillemot, P. Gouzerh, G. Izzet, *Chemical Society Reviews* **2012**, *41*, 7605-7622.
[140] A. J. Kibler, G. N. Newton, *Polyhedron* **2018**, *154*, 1-20.
[141] S. Herrmann, C. Ritchie, C. Streb, *Dalton Transactions* **2015**, *44*, 7092-7104.
[142] X. Li, K. F. Zhou, Z. B. Tong, X. Y. Yang, C. Y. Chen, X. H. Shang, J. Q. Sha, *Chemistry–An Asian Journal* **2019**, *14*, 3424-3430.
[143] R. Tsunashima, Y. Iwamoto, Y. Baba, C. Kato, K. Ichihashi, S. Nishihara, K. Inoue, K. Ishiguro, Y. F. Song, T. Akutagawa, *Angewandte Chemie* **2014**, *126*, 11410-11413.
[144] aD. P. Dubal, S. H. Lee, J. G. Kim, W. B. Kim, C. D. Lokhande, *Journal of Materials Chemistry* **2012**, *22*, 3044-3052; bS. Ghosh, T. Maiyalagan, R. N. Basu, *Nanoscale* **2016**, *8*, 6921-6947.
[145] A. Müller, E. Krickemeyer, J. Meyer, H. Bögge, F. Peters, W. Plass, E. Diemann, S. Dillinger, F. Nonnenbruch, M. Randerath, *Angewandte Chemie International Edition in English* **1995**, *34*, 2122-2124.
[146] S. Landsmann, C. Lizandara-Pueyo, S. Polarz, *Journal of the American Chemical Society* **2010**, *132*, 5315-5321.
[147] A. Proust, R. Thouvenot, P. Gouzerh, *Chemical Communications* **2008**, 1837-1852.
[148] J. Zhang, F. Xiao, J. Hao, Y. Wei, *Dalton Transactions* **2012**, *41*, 3599-3615.
[149] S. A. Alshehri, A. Al-Yasari, F. Marken, J. Fielden, *Macromolecules* **2020**, *53*, 11120-11129.
[150] A. Al-Yasari, PhD thesis, University of East Anglia **2016**.
[151] aS. Sadki, P. Schottland, N. Brodie, G. Sabouraud, *Chemical Society Reviews* **2000**, *29*, 283-293; bG. G. Wallace, P. R. Teasdale, G. M. Spinks, L. A. Kane-Maguire, *Conductive electroactive polymers: intelligent materials systems*, CRC press, **2002**.
[152] M. V. Rosenthal, T. Skotheim, A. Melo, M. Florit, M. Salmon, *Journal of Electroanalytical Chemistry and Interfacial Electrochemistry* **1985**, *185*, 297-303.
[153] J. R. Reynolds, P. A. Poropatic, R. L. Toyooka, *Macromolecules* **1987**, *20*, 958-961.
[154] S. Kumar, S. Krishnakanth, J. Mathew, Z. Pomerantz, J.-P. Lellouche, S. Ghosh, *The Journal of Physical Chemistry C* **2014**, *118*, 2570-2579.
[155] T. Raudsepp, M. Marandi, T. Tamm, V. Sammelselg, J. Tamm, *Electrochimica Acta* **2008**, *53*, 3828-3835.

Chapter 7

7.1. Conclusion and future work

In chapter 3, surface-immobilized anthraquinone was characterised using electrochemical methods, showing a promising cathodic electrode for energy storage. The anthraquinone/lithium system shows (from GCD) specific capacitance of 59 F/g compared to 21.3F/g using carbon fibre for a 1 cm^2 symmetric anthraquinone-carbon fibre (AQ-CF) supercapacitor.

In chapter 4, different Lewis acidic N-pyrrolyl bis(aryl)boranes were studied to find a suitable anode material for use in the hybrid battery/supercapacitor. Poly**1** (borane = $B(C_6F_5)_2$), poly**2** (-$B(C_6Cl_5)_2$) and poly**3** ($B\{C_6H_3(CF_3)_2\}_2$) were characterised by using electrochemical methods and other techniques. The specific capacitance of poly**1** was excellent (90 F/g by GCD) considering its high molecular weight, which might result from stabilisation of increased positive charge by the pentafluorophenyl groups of the borane. Compared to the other materials, and polypyrrole, Poly**1** also demonstrated a much wider stable operating voltage window when used in a symmetric supercapacitor device of ± 4 V and exhibited a more stable charge storage performance over 6000 charge–discharge cycles.

In chapter 5, a new hybrid battery / supercapacitor has been fabricated using anthraquinone functionalised carbon fibre. It shows an excellent electrochemical stability for long cycle life. The capacitance of the flexible hybrid battery / supercapacitor is maintained 90% after 1000 charge-discharge processes. The capacitance of the hybrid battery / supercapacitor is improved by using the new polypyrrolyl-borane material (poly**1**) which reaching 142 F/g compared to the anthraquinone-carbon fibre system alone (21.3 F/g) and the capacitance retention was 90 % for poly**1**-AQ over 1000 cycles indicating promise for the materials in energy storage.

The capacitance of hybrid battery/ supercapacitor was higher than the capacitance of each material individual material (anthraquinone and poly**1**) used in the hybrid battery supercapacitor. The design of the flexible hybrid battery / supercapacitor shows excellent electrical properties as parallel hybrid battery/ supercapacitor.

The final chapter in this thesis investigates polypyrrole supercapacitors with covalently linked Lindqvist polyoxometalates that are prepared by electropolymerisation, and studied by various electrochemical techniques including cyclic voltammetry, electrochemical impedance spectroscopy (EIS), galvanostatic charge-discharge and electrochemical quartz crystal microscopy (EQCM). These films are the first covalent POM-PPy hybrids, and the first demonstration of electropolymerisation of a POM-derivatised monomer which open new possibilities for construction of POM hybrid materials. The covalent linkage provides access to higher loadings of POM than obtained in non-covalent inclusion films, which can prevent loss of POM in early reduction cycles, and increasing its length increases both the specific capacitance and stability of the film. The capacitance retention is around 95% over 1200 cycles. The polyoxometalate increases specific capacitance by modifying the polypyrrole itself, with reduced charge transfer resistance implying that a more open structure results from the steric bulk of the POMs, and by the contribution of faradaic capacitance through the POM redox process.

Overall, this work has shown anthraquinone can be attached to a carbon surface easily and produce a stable cathode. Introducing lithium ions enhances the performance of the capacitor, probably because ion pairing with anthraquinone facilitates reduction. In addition, the boranes and POM derivatives of polypyrrole both show that adding steric bulk enhances the performance and stability of polypyrrole (at a penalty in mass), likely because this helps provide and stabilize channels for ion transport during charging and discharging. The borane work also suggests that resonance donors may enhance performance in polypyrrole by

stabilizing positive charge. However, uncertainty about the true of specific capacitance of the chloro- and -CF_3 borane derivatives poly**2** and poly**3** means that further investigation is needed here.

There are some suggestions for future work:

Firstly, find a material that can extend to more negative potentials as a cathode, for example formazan derivatives that can provide a wider potential window through a reductive wave between around -0.4 to -2 V. Other more electron rich quinone derivatives with electron donor groups could also be investigated for more negative potentials, and also naphthoquinone or benzoquinone which have lower molecular weight but the same storage capacity and could provide better specific capacitance.

Secondly, with the polyoxometalate-polypyrrole materials, we could improve the specific capacitance and stability of materials by using Bucky paper layer on to the glassy carbon electrode to increase surface area. Indeed, generally the capacitance of the materials presented here may be improved further through use of higher surface area supporting carbon materials such as carbon nanotubes. As mentioned in chapter 6, work can be done optimise the loading of the POM for the best specific capacitance – there may be a point which achieves the best compromise between improved per monomer performance, and added mass. The approach can also be expanded to POMs capable of storing multiple electrons, for example the Keggin anion.

Lastly, because boranes also introduce extra mass, it may be interesting to investigate them by copolymerization with various ratios of pyrrole (Py) to Py-borane to see if there is an optimum amount of borane required to give an effect. Also, the stabilization of positive charge by resonance donor groups could be investigated in other lower molecular weight systems.

7.2. Appendix

List of publications, presentation, posters, and awards

External Publications

1. Covalently-linked Polyoxometalate-Polypyrrole Hybrids: New Electropolymer Materials with Dual Mode Enhanced Capacitive Energy Storage. Sarah A. Alshehri, Ahmed Al-Yasari, Frank Marken, and John Fielden. Macromolecules, 2020, 53, 24, 11120-11129.

External Presentations

1. Developing polymer Battery Materials, Glasgow, Electrochem conference, 2019.

2. Fabrication of Hybrid Battery /Supercapacitor Energy Storage System, Conference of Chemistry of 2-Dimensional materials: Beyond Graphene Faraday Discussion,2020.25-27, 11 ,2020.

3. Modification of Carbon Electrodes using Anthraquinone with Lithium ions for a Hybrid Battery / Supercapacitor, France, ICREN 2020: International Conference on Renewable Energy, 25-30, 11, 2020.

4.Faraday Joint Interest Group Conference 2021, 29-31 March2021. Fabrication of Hybrid Battery / Supercapacitor Energy Storage System using Carbon Fibre and Lewis acid modified Polypyrroles.

UEA Presentations

1. Developing New Cathode Materials for Hybrid Battery Storage Devices: Oral Presentation and poster, Chemistry Research Day, 11/9/2018.

2. Hybrid Carbon-Polyoxometalate Materials for Enhanced Supercapacitor Energy Storage: Poster, Chemistry Research Day, 11/9/2019.

3. Developing new Cathode Materials for Hybrid-Battery Storage Devices, Oral presentation, Chemistry Research Day, 15/9/2020.

UEA Awards

Bronze Award

Silver Award

Gold Award

The UEA Award is recognizes and certifies a range of activities undertaken during a student's time at UEA which build skills and attributes. UEA Gold Award: completed activities involving part-time work as a UEA Guide, being an active member of the Royal society of chemistry (RSC), plus attending various careers events and improving attributes and skills related to my academic work. In my RSC volunteering, I was supported for RSC East Anglia local section including contribution in Top of the Bench competition for school students in Norwich.